Title
Structure and Electronic Property Relationships in Chemically Doped Semiconducting Polymers and Polymer Photovoltaics

Author
Aubry-Komin, Taylor

Publication Date
2019

Peer reviewed|Thesis/dissertation

UNIVERSITY OF CALIFORNIA

Los Angeles

Structure and Electronic Property Relationships in Chemically Doped Semiconducting Polymers and Polymer Photovoltaics

A dissertation submitted in partial satisfaction
of the requirements for the degree
Doctor of Philosophy in Chemistry

by

Taylor Aubry-Komin

2019

ABSTRACT OF THE DISSERTATION

Structure and Electronic Property Relationships in Chemically Doped Semiconducting Polymers and Polymer Photovoltaics

by

Taylor Aubry-Komin
Doctor of Philosophy in Chemistry
University of California, Los Angeles, 2019
Professor Benjamin Joel Schwartz, Chair

This work is focused on understanding how molecular-level structural control can improve charge carrier properties in π-conjugated polymers. Conjugated polymers are characterized by extended conjugation along their backbone, making them intrinsically semiconducting materials that are of interest for a wide variety of flexible, thin-film electronic applications. Polymeric semiconductors possess advantages over inorganic materials such as being lightweight, low-cost and solution processable. However, due the disordered nature of conjugated polymers and their anisotropic transport, charge carrier dynamics can be highly sensitive to structural effects. The first chapter of this dissertation gives an introduction to conjugated polymers and their relevant applications as well as how tuning morphology and doping level can influence their charge carrier properties. The second introduces a technique, known as sequential processing (SqP), that affords control over polymer domain orientation when preparing polymer films as the active layer in optoelectronic devices. We show that conventional processing methods lead to disordered, isotropic polymer networks. By contrast, SqP can be used to preserve the preferred face-on chain orientation seen with some polymer materials, yielding advantages for photovoltaics and other devices via increased vertical hole mobility. Chapter 3 turns to molecular doping of conjugated polymers and studies the effects of a bulky boron cluster dopant used to modify the charge transport properties of conjugated polymers. The design of the dopant is such that it sterically protects core-localized electron density, resulting in shielding of the electron from holes produced on the polymer. This allows the charge carriers to be highly delocalized, as confirmed both spectroscopically and by

AC-Hall effect measurements. The dopants allow for high carrier mobilities to be achieved even for non-crystalline polymers. The implication is that the counterion distance is the most important factor needed to produce high carrier mobility in conjugated polymers. In the last chapter, we study a series of boron cluster dopants in which the redox potential is tuned over a large range but the anion distance is fixed. In the last chapter, we study a series of boron cluster dopants in which the redox potential is tuned over a large range but the anion distance is fixed. This allows us to disentangle the effects of energetic offset in doping on the production of free carriers. We find that the redox potential not only affects the generation of free carriers, but also the infiltration of dopants into the polymer films.

The dissertation of Taylor Aubry-Komin is approved.

Stuart Brown

Paul S. Weiss

Benjamin Joel Schwartz, Committee Chair

University of California, Los Angeles

2019

To my wonderful parents and entire family for making me who I am. To my cherished friends for their endless encouragement. To my beloved fiancé, who I know will continue to support me in any direction life takes us. Without them, none of my success would have been possible.

TABLE OF CONTENTS

1 Introduction **1**

1.1 Charge carrier dynamics in optoelectronic polymer devices 2

1.1.1 Polymer photovoltaics 2

1.1.2 Thermoelectrics 3

1.2 Structural Effects on Charge Transport in Conjugated Polymers 4

1.3 Molecular Doping of Semiconducting Polymers 6

1.4 Overview of Thesis 7

1.4.1 Chapter 2: Processing Methods for Obtaining a Face-On Crystalline Domain Orientation in Conjugated Polymer-Based Photovoltaics. 7

1.4.2 Chapter 3: Dodecaborane-Based Dopants Designed to Shield Anion Electrostatics Lead to Increased Carrier Mobility in a Doped Conjugated Polymer 8

1.4.3 Chapter 4: The effects of dopant electron affinity at fixed counterion distance on the production of free carriers in conjugated polymers. 9

2 Processing Methods for Obtaining a Face-On Crystalline Domain Orientation in Conjugated Polymer-Based Photovoltaics **10**

2.1 Experimental Section 12

2.1.1 Film Fabrication 12

2.1.2 GIWAXS Measurements 13

2.1.3 Device Measurements 14

2.2 Results and Discussion 14

2.2.1 Orientation of PBDTTT-C Crystallites Measured by 2-D GIWAXS 14

2.2.2 Device Performance of Blend-Cast and Sequentially Processed PBDTTT-C:$PC_{71}BM$ BHJs 25

2.3 Conclusions 28

2.4 Supporting Information Available 29

3 Dodecaborane-based Dopants Designed to Shield Anion Electrostatics Lead to Increased Carrier Mobility in a Doped Conjugated Polymer 33

3.1 Introduction 33

3.2 Results & Discussion 37

4 The effects of dopant electron affinity at fixed counterion distance on the production of free carriers in conjugated polymers 47

4.1 Conclusions 63

A Supporting Information for Chapter 2: Processing Methods for Obtaining a Face-On Crystalline Domain Orientation in Conjugated Polymer-Based Photovoltaics 66

A.1 Experimental Details 66

A.2 Polymer crystallite coherence length in pure, blend cast and sequentially processed films 67

A.3 Solvent Effects of Pure PBDTTT-C 68

A.4 Effect of methanol washing on blend-cast PBDTTT-C:$PC_{71}BM$ with and without DIO 69

A.5 Sequentially processed PBDTTT-C:$PC_{71}BM$ (10 mg/mL PCBM concentration) . . 70

A.6 Determination of PBDTTT-C:$PC_{71}BM$ weight ratio in SqP active layer via redissolving 71

A.7 Absorbance of pure, BC and SqP films 71

A.8 SCLC mobilities 72

A.9 Device optimization of SqP with DIO in polymer/fullerene layer 73

B Supporting Information for Chapter 3: Dodecaborane-based Dopants Designed to Shield Anion Electrostatics Lead to Increased Carrier Mobility in a Doped Conjugated

Polymer **74**

B.1 Materials, Synthesis & Characterization 74

B.2 Experimental Methods 78

B.2.1 Cyclic Voltammetry 78

B.2.2 TD-DFT 78

B.2.3 Electron transfer self-exchange rate by NMR 78

B.2.4 Film fabrication 79

B.2.5 Conductivity 79

B.2.6 Sample Imaging 79

B.2.7 XPS 80

B.2.8 GIWAXS 80

B.2.9 Spectroscopy 81

B.2.10 AC-Hall 81

B.3 Electron transfer self-exchange rate by NMR 81

B.4 Cyclic Voltammetry 85

B.5 Conductivity data 86

B.6 Stability measurements on doped films 89

B.7 Optical and SEM images of the Doped Film's Surface 91

B.8 XPS 93

B.9 GIWAXS 96

B.10 Spectroscopic Characterization 99

B.11 Transport mechanisms from temperature dependent behavior of the conductivity . . 100

B.12 AC Hall measurements 103

B.13 Calculation of dopant density based on mass measurements 103

C Supplementary information for: The effects of dopant electron affinity at fixed counterion distance on the production of free carriers in conjugated polymers 106

C.1 Experimental Methods 106

C.1.1 Materials 106

C.1.2 Cyclic Voltammetry 106

C.1.3 Film Fabrication 107

C.1.4 Spectroscopy 107

C.1.5 Conductivity 107

C.1.6 Neutron Reflectometry 108

C.1.7 X-ray Photoelectron Spectroscopy 108

C.1.8 Graxing Incidence Wide Angle X-ray Scattering 108

C.1.9 AC-Hall 109

C.2 Cyclic Voltammetry Measurements 110

C.3 Absorption Spectroscopy Measurements 111

C.4 Conductivity Measurements 112

C.5 Neutron Reflectometry 113

C.6 X-Ray Photoelectron Spectroscopy 114

C.7 GIWAXS of P3HT Thin-Films Doped with DDBs 115

C.8 Solution Doping of P3HT with DDBs 118

C.9 FTIR of DDB-doped P3HT 120

C.10 AC-Hall Measurements 122

C.11 Fits of UV-VIS-FTIR Data (P1 Region) 123

C.12 Fits of UV-VIS-FTIR Data (Full) 124

D Data Fitting in Python: Deconvolution of Multiple Peaks and Background 128

D.1 A simple example: Two overlapping gaussians and an exponential 128
D.2 Fitting the full UV-VIS-FTIR spectrum of a DDB doped P3HT sample. 132
D.2.1 Pure P3HT spectrum only 132
D.2.2 Full fit of DDB doped P3HT 137

E Maintenance and Modifications of Lab Equipment 144
E.1 Ångstrom Thermal Evaporator 144
E.2 The Nitrogen Glovebox 146
E.3 The Seebeck Measurement Set-Up 153

References 155

LIST OF FIGURES

1.1 Cartoon of current generation in a polymer solar cell (left) and corresponding simplified energy diagram (right). (i) Light absorption and exciton creation (ii) Exciton diffusion to donor/acceptor heterojunction interface. (iii) Exciton dissociation via electron transfer to the acceptor. (iv) Charge separation into free carries. (v) The charge carriers transported to respective electrodes. (vi) Charge extraction. 2

1.2 Schematics of thermoelectric effects. (Left) Seebeck effect where an applied temperature difference causes charge carriers to diffuse from the hot side to the cold side, resulting in a current. (Right) Peltier effect in which heat is absorbed at the upper junction and released at the lower junction when a current is applied to the circuit. 4

1.3 Ordered polymer structure. (a) Charge conduction pathways with along the chain axis having the highest mobility followed by through the π stacking direction and hopping between chains in the alkyl direction being the lowest. (b) Polymer chain orientations, with edge-on and face-on being far more prevalent than end-on. . . . 5

1.4 Schematic energy diagram of *p*-doping process with integer charge transfer. A dopant acceptor with a LUMO that lies below the polymer HOMO can remove an electron from the polymer backbone and produce a positive charge carrier known as a hole and also a polaron. Although not every dopant will necessarily undergo charge transfer with the polymer, each CT event should result in a charge carrier, albeit with varying degrees of localization. 6

2.1 Raw GIWAXS diffractograms for pure polymer (a) and pure polymer with DIO (b) showing a face-on polymer orientation. Diffractograms for blend-cast (c,d) and sequentially processed (e,f) BHJs, both with (d,f) and without DIO (c,e) exhibit isotropic fullerene diffraction, but very different polymer chain orientations. Face-on polymer orientation is clearly seen in SqP films, while blend-cast films show more isotropic diffraction. A cartoon of face-on oriented polymer chains as well as cartoons depicting the (100)- and (010)-stacking directions are shown in (g). 15

2.2 (a) Full integration of GIWAXS diffractograms for pure polymer films showing the increase in crystallinity with the addition of DIO, where the black curves are pure polymer, red curves are polymer with 3% DIO, and blue curves are obtained after washing the DIO away with methanol. The face-on orientation shown by the strong (010) diffraction in the out-of-plane direction (b), with much less intensity in-plane direction (c). 17

2.4 Figure 2.4. (a) Full integration of GIWAXS diffractograms for sequentially processed PBDTTT-C:PCBM films, where the orange curves have no additive, and the purple curves have 3% DIO in the polymer-casting solution. Despite the fullerene scattering, strong (010) diffraction can be seen in the out-of-plane scattering in part (b), but not in the in-plane scattering in part (c). Examination of the (010) scattering in (d) in both the out-of-plane and in-plane diffractions is again facilitated by subtraction of all isotropic scattering, which includes the fullerene diffraction. The inset in (d) is a zoom-in of the (010) polymer region and shows strong positive intensities in the out-of-plane direction, indicative of a face-on polymer chain alignment. 23

2.3 (a) Full integrations of GIWAXS diffractograms for 1:1.5 PBDTTT-C:PCBM blend-cast films without DIO (green), with 3% DIO (blue), and methanol washed (red). The films appear to show a preference for an edge-on polymer chain orientation, as seen by the strong (100) scattering in the (b) out-of-plane direction but not in the (c) in-plane direction. Examination of the (010) scattering in (d) in both the out-of-plane and in-plane diffractions is facilitated by subtraction of all isotropic scattering, which includes the fullerene diffraction. The inset in (d) is a zoom-in of the (010) polymer region and shows negative intensities in the out-of-plane direction, which again indicates a lack of face-on polymer chains. 30

2.5 Photoluminescence of pure PBDTTT-C (red squares) as well as BHJ films made via BC with DIO (dark blue circles) and without DIO (light blue squares), SqP with DIO (dark green down triangles) and without DIO (light green up triangles). A methanol wash was performed to remove the DIO in the BC case, while in SqP, we rely on the SqP solvents to remove the DIO. The PL intensities have been normalized by the polymer optical density at the excitation wavelength (630 nm, see Appendix A Figure A.5). All of the BHJs are well-quenched, indicating the domains in the films are well-mixed. 31

2.6 (a) J–V device curves for blend-cast films without additives (light blue squares) and with 3% v/v DIO (blue diamonds). Additional improvement is seen with methanol washing the DIO films (dark blue circles). Sequential processing without the use of additives (light green triangles) shows improvement over the blend-cast films, mainly due to J_{sc} improvement. SqP devices fabricated with 3% v/v DIO (green down triangles) and, subsequently, MeOH washed (dark green stars) are similar in performance to SqP devices without additives. All devices have the structure: ITO/PEDOT:PSS/PBDTTT-C:PC_{71}BM:Ca/Al. (b) External quantum efficiency (EQE) for optimized blend-cast (w/DIO + MeOH wash) and sequentially processed films (no additional processing), showing higher obtainable current with SqP. . . . 32

3.1 (a) Chemical structures and schematic energy diagram of P3HT, F_4TCNQ, and DDB-F_{72} showing $\sim$0.5 V greater offset for DDB-F_{72} than F_4TCNQ. (b) (top) X-ray crystal structure of DDB-F_{72}; (bottom) DDB-F_{72} anion SOMO calculated by TD-DFT showing the electron localized on the DDB core. (c) Conductivities (solid symbols, calculated using the measured thickness) and idealized conductivities (open symbols, calculated using the 120-nm original thickness) of P3HT films doped with F_4TCNQ (red symbols) and DDB-F_{72} (blue symbols) via solution sequential doping. The error bars are the standard deviation calculated from at least three samples. At the same dopant concentration DDB-F_{72} produces conductivities that are an order of magnitude higher than those produced by F_4TCNQ. 35

3.2 Structural characterization of DDB-cluster-doped films. (a) B 1s XPS spectra of the top surface of pure DDB-F_{72} films in the neutral [0, black curve] and anionic [-1, red curve] states, overlaid with that of a DDB-F_{72}-doped P3HT film (blue curve). The overlap of the doped film and anion spectra indicates that the clusters at the top surface of the film are all reduced. (inset) XPS-determined B:S and F:S ratios measured at the top and bottom of DDB-F_{72}-doped P3HT films indicating clusters penetrate the film. (b) Out-of plane (top) and in-plane (bottom) 2D-GIWAXS spectra for films of pure P3HT (green curves) and DDB-F_{72}-doped P3HT (blue curves). (inset) Zoomed in view of the (100) peak. Dopant-induced peaks are denoted by asterisks (*). These data indicate DDB-F_{72} does not enter the crystallites given its large size and at high dopant concentration (dark blue dash-dotted curves), there is significant loss of overall crystallinity. 40

3.3 Delocalized polaron IR-spectrum. (a) Experimental IR absorption spectrum of the polaron in a 1 mM DDB-F_{72}-doped P3HT film. (b) Simulated P3HT polaron absorption spectrum for different anion-polaron distances. The measured spectrum is in excellent agreement with the theoretical spectrum for an anion at infinite distance, indicating that the polarons in the chemically-doped DDB-F_{72} sample are as delocalized as possible. Note: A distance-dependent permittivity for the pure polymer was used for the calculation. Although the use of a different permittivity would change the shape of the spectrum of the more Coulomb-localized polarons, the spectrum calculated for infinite anion distance is invariant with respect to the choice of permittivity. 43

4.1 a) Chemical structures of P3HT polymer and DDB dopants, which have an icosahedral B_{12} core and each vertex is functionalized with R-groups shown in (c). The energy diagram depicts relative offsets between P3HT HOMO and dopant LUMOs based on CV measurements of all dopants (including F_4TCNQ) and scaled to reported P3HT-F_4TCNQ energy offset. b) Measured $E_{1/2}$ for DDB dopants plotted against their Hammett constant showing tunability of dopant redox potential based on substituent electron donating/withdrawing ability. c) UV-VIS-IR spectra of 120-nm thick film of P3HT doped with 1 mM DDB via SqP with an increase in signature polaron peak intensities (P1, P2 and P3) and a bleach of the bandgap transition. 50

4.2 a) Raw neutron reflectivity data for pure and DDB-doped P3HT (symbols) and fits of the model to the data (darkened lines). b) SLD depth profiles obtained from fitting the data in (a) showing substrate SiO_x layer followed by the active layer before reaching the air interface. Profiles show sample SLD and thickness increase with dopant redox potential and confirm nearly uniform dopant infiltration throughout the film. c) XPS-determined sulfur to fluorine (*or bromine) ratios at the top and bottom surfaces of DDB-doped P3HT films supporting that clusters penetrate the film, sample fits shown in (d) & (e). d) F 1s fit (yellow) and e) S 2p fit (green-neutral S, blue-oxidized S, and pink-full S fit) for the top surface of a DDB-F_{36} doped P3HT film (black). 53

4.3 a)Full integration and out-of-plane (inset) integration of P3HT doped with DDB-F_{36} demonstrating phase change from undoped (h00) pahse to expanded (h00)' lamellar strucutre b) Full integration and out-of-plane (inset) of P3HT doped with various DDB dopants at 1 mM concentration showing relationship of redox potential on extent of phase transition to (h00)' structure c) GIWAXS In-plane integration of P3HT doped with 1 mM DDB dopants showing increase in disordered π-stacking region and shift of (010) peak to higher q. d) To-scale Representation of proposed (h00)' lamellar structure in which DDB dopant has intercalated into the lamellar regions of the P3HT crystal structure. 57

4.4 a) Normalized FTIR of DDB-F_{72} doped P3HT showing concentration dependence of P1 peak location. At higher concentrations, we see a blue shift of the P1 peak for films doped with all DDB clusters (see SI Figure C9a-c) indicating closer counterion-polaron distance as more dopant is infiltrated. b) Normalized FTIR of DDB-doped P3HT at P1 intensity matched concentrations showing pinned anion distance (see SI Figure C9d for unnormalized data). c) AC-Hall measured mobility vs fitted P1 peak center showing linear relationship (see SI Figure C9e for fitted FTIR data and S10a-c for fits). F_4TCNQ and DDB-F_{72} data taken from our previous work Refs. 87 and 141, respectively. 61

A.1 2D-GIWAXS of pure PBDTTT-C films after washing with methanol (a) and 1:1 2-chlorophenol:dicholoromethane (b), which was used to deposit the fullerene during sequential processing. Fully integrated diffractograms (c) for pure polymer (black), polymer with DIO (red), and pure polymer washed with methanol (purple) and the SqP solvent blend (orange). An increase in crystallinity over pure is observed with each of the pure solvent washes, however the addition of DIO causes the largest change. 68

A.2 Examination of the role of methanol washing only for BC devices. (a) Full integration of GIWAXS diffractograms for 1:1.5 PBDTTT-C:PCBM blend cast (BC) films without (green), with 3% DIO (blue), and subsequent methanol wash (red). Methanol wash of a blend cast film without DIO (orange) shows little change. Isotropic fullerene orientation is observed by the equal intensity (b) out-of-plane and (c) in-plane. 69

A.3 (a) Full integration of GIWAXS diffractograms for sequentially processed (SqP) PBDTTT-C:PCBM films, where the orange curves have no additive and the purple curves have 3% DIO in the polymer casting solution. The very strong fullerene scattering, makes the (010) diffraction peak invisible in both the (b) out-of-plane and (c) in-plane directions. 70

A.4 Solution-phase absorption spectrum (black circles) of a redissolved optimized sequentially processed device (obtained from the procedure described in Ref. 37), along with its fit to a linear combination of the pure solution-phase PBDTTT-C (blue curve) and $PC_{71}BM$ (pink curve) components. The overall weight ratio obtained from the fitting coefficients was 1:3.5 of polymer to fullerene by weight, indicating a fullerene rich device. This result is consistent with increased fullerene peak in the diffraction and EQE data. 71

A.5 Absorbance of films made from pure PBDTTT-C (red solid), and BHJs made via BC with DIO (dark blue dash), without DIO (light blue dash), SqP with DIO (dark green dot) and SqP without DIO (light green dot). 71

A.6 Current-voltage curves of hole only devices with pure PBDTTT-C (a), optimized sequentially processed PBDTTT-C:$PC_{71}BM$ (no DIO, no MeOH wash) (b), blend cast PBDTTT-C:$PC_{71}BM$ without DIO (c), and optimized blend cast PBDTTT-C:$PC_{71}BM$ (with DIO and MeOH wash). Symbols represent experimental data and the solid lines represent fit of the experimental data, performed for space charge limited current with the Murgatroyd equation: $J=\frac{9}{8}\varepsilon\mu\frac{V^2}{d^3}e^{0.89\beta\sqrt{\frac{V}{d}}}$ 72

A.7 J-V device curves for sequentially processed PBDTTT-C films with DIO additive in the fullerene layer (solid red) the polymer layer (solid black) and both the fullerene and polymer layers (solid blue). Slight improvement is seen with methanol washing the DIO films (dotted). All devices have the structure: ITO/PEDOT:PSS/PBDTTT-C:$BC_{71}BM$:Ca/Al with DIO added in the indicated layers. 73

B.1 ^{1}H NMR of DDB-F_{72}, * residual H_2O. 76

B.2 ^{11}B NMR of DDB-F_{72}. 77

B.3 ^{19}F NMR of DDB-F_{72}. 77

B.4 ^{19}F NMR of the one-electron self-exchange interaction of the [DDB-F_{72}]$^{0/-}$ redox couple with increasing mole fraction of [DDB-F_{72}]$^{-}$ from bottom to top in any given series. Spectra were recorded at 20 °C (bottom), 40 °C (middle), and 60 °C (top) in a 4:1 o-difluorobenzene:benzene mixture and referenced to an internal standard of trifluoroethanol sealed in a capillary tube. 83

B.5 Overlapped solid state structures of [DDB-F_{72}]^{0} (green) and [DDB-F_{72}]$^{-}$ (red) obtained from single crystal X-ray diffraction studies. Left and middle figures highlight the minor structural rearrangement in the core upon a one electron reduction while the right side highlights the capping ligands. Capping benzyl ligands have been omitted for clarity in the left and middle figures while hydrogen and fluorine atoms have been omitted for the right figure. 84

B.6 Cyclic voltammogram of F_4TCNQ (red) and DDB-F_{72} (blue) demonstrating two reversible single-electron oxidation/reductions. 85

B.7 Conductivity over time of DDB-F_{72} (blue) and F_4TCNQ (red) doped P3HT films in the glovebox under inert argon atmosphere (a) and under ambient atmosphere in air (b) as a function of time after film fabrication as measured by 4-point probe. 89

B.8 Conductivity of DDB-F_{72}-doped P3HT film samples measured over 5 days via the Van der Pauw method. The samples were briefly exposed to air for each measurement and then returned for storage under inert atmosphere. The error bars are the standard deviation of measurements on three separate samples. 90

B.9 Optical images of 1mM DDB-F_{72} doped P3HT at 5x (a) and 50x (b) magnification as well as at 50x magnification under polarizers (c). 91

B.10 SEM images of a P3HT film that has been doped with 1 mM DDB-F_{72} at low to high magnification (a-c). 92

B.11 XPS data and S, SO, B, and F peak fits for DDB-F_{72} doped P3HT (bottom), floated back of DDB-F_{72} doped P3HT film (middle), and floated front of DDB-F_{72} doped P3HT (top). 95

B.12 Full integration of GIWAXS diffractogram for pure DDB-F_{72} showing sharp crystallite peaks. 96

B.13 Full 2D-GIWAXS diffractograms for pure undoped P3HT (a), P3HT doped with 0.05 mM (b), 0.3 mM (c), and 1 mM DDB-F_{72} (d). 97

B.14 Combined FTIR and UV-vis-NIR absorption data for pure P3HT (black curve), P3HT doped with different molar concentrations of DDB-F_{72} (colored solid curves), and neutral (yellow dashed curve) and reduced (pink dashed curve) DDB-F_{72} cluster in DCM. 99

B.15 Conductivity of 1 mM DDB-F_{72} doped P3HT as a function of temperature, plotted as a function of inverse temperature raised to various powers that correspond to different transport models. 101

B.16 Logarithmic derivative of the resistivity ($W = -dln(\rho)/dln(T)$) vs. $ln(T)$. The dashed lines are linear fits with the corresponding slopes given in the legend. . . . 102

C.1 CVs of all boron clusters in the 0/1− redox couple region. 110

C.2 UV-Vis of P3HT doped with 0.3 mM solutions of the DDB clusters. 111

C.3 Bromine 3d peak fits for DDB-*p*-Br doped P3HT. 114

C.4 2D diffractograms of representative samples of P3HT doped with each DDB at multiple concentrations (each condition was run in triplicate). 115

C.5 Out-of-plane GIWAXS curves of P3HT doped with DDB clusters demonstrating the conversion to the new (h00)' lamellar phase. 116

C.6 Normalized in-plane GIWAXS curves of P3HT doped with DDB clusters demonstrating an increase in disordered π-stacking peak centered at 1.4 q with both concentration and DDB redox potential. 117

C.7 Solution doping of P3HT with DDBs in ODCB at known DDB:PRU ratios. 118

C.8 Absorbance tracked at P3HT bandgap peak (a), P3HT aggregate peak (b), P2 peak (c), and P1 peak (d). 119

C.9 Concentration dependent FTIR data for DDB-*p*-F (a), DDB-*p*-Br (b), and DDB-F_{36} (c). Unnormalized, intensity matched FTIR data (d). P1 peaks of doped P3HT with corresponding AC-Hall mobility measurements (e). 121

C.10 Fits of P1 region for F_4TCNQ-doped low crystallinity P3HT (a) and high crystallinity P3HT (b) with data taken from Ref. 87. Fits of our 1 mM DDB-F_{36} (c) and DDB-F_{72} doped P3HT (d). 123

C.11 P3HT film fit to the bandgap and three vibrational transitions with a scattering background. 124

C.12 Full fits of 1 mM DDB doped P3HT films. 125

C.13 Full fits of 0.3 mM DDB doped P3HT films. 126

D.1 Plot of sample data to fit 129

D.2 Plot of initial and best fit to sample data (left) and fit components (right). 131

D.3 Plot of pure P3HT film absorbance 133

D.4 Best fit to P3HT data and sum of P3HT components (left) and individual fit components (right). 137

D.5 Plot of 1 mM DDB-*p*-F doped P3HT absorbance. 138

D.6 Initial and best fit to DDB-*p*-F doped P3HT data (left) and individual fit components (right). 143

E.1 a) Chiller water reservoir b) House water supply and return lines c) chiller front panel. 145

E.2 Previous faulty solenoid valve (replaced twice!) 146

E.5 Modified thermoelectric set up with alligator clips for sample voltage measurement. 154

List of Tables

2.1 Summary of J–V Characteristics[a] for the Devices Shown in Figure 2.6a 26

2.2 SCLC Hole Mobilities (μ_{hole})[a,b] 26

3.1 Comparison of carrier density (n), mobility (μ) and conductivity (σ) measured by the AC Hall effect for P3HT films doped with DDB-F_{72} and F_4TCNQ at their respective solubility limits in DCM. Also shown is the number of dopant molecules in the film estimated via mass mesurements (N_{est}), see SI. The F_4TCNQ data is taken from Ref. 88. The idealized conductivity was calculated using the 120-nm pre-cast polymer film thickness instead of the measured doped film thickness; see text. 45

4.1 Summary of calculated neutron SLDs of pure materials and model SLD results of pure P3HT and DDB-doped P3HT films with calculated DDB:P3HT monomer ratio from these values showing increasing dopant loading with higher redox potential DDBs. 54

4.2 Summary of calculated (100) d-spacing based on GIWAXS-measured overtones for 0.3 mM and 1 mM dopant concentrations. There is a transition between the undoped and doped phases, with both phases coexisting at some doping levels. The undoped phase corresponds to the orignal P3HT lamellar d-spacing. 58

4.3 Estimated doping efficiency of DDB dopants based on dopant density calculated from neutron SLD results, mobilities calculated from P1 peak locations allowing for carrier density estimates from measured mobilities. 63

A.1 Summary of (100) peak location, integrated peak area, and coherence length as calculated from the Scherrer equation. 67

A.2 Summary of J-V Characteristics for the PBDTTT-C devices shown in Figure S3. . . 73

B.1 F_4TCNQ Conductivity Measurements 86

B.2 DDB-F_{72} Conductivity Measurements 87

B.3 Conductivity values for F_4TCNQ-doped P3HT from literature. 88

B.4 XPS peak fits 94

B.5 Out-of-plane (100) Peak Fit Information 98

B.6 In-plane (010) Peak Fit Information 98

B.7 Mass measurements of 6 films before and after doping and carrier density of DDB-F_{72}-doped P3HT films based on the measured mass and a film volume of 1.5 cm $\times$ 1.5 cm $\times$ 300 nm 104

B.8 Mass measurements of 6 films before and after doping and carrier density of F_4TCNQ-doped P3HT films based on the measured mass and a film volume of 1.5 cm $\times$ 1.5 cm $\times$ 145 nm 105

C.1 Van der Pauw conductivity measurements of DDB doped P3HT films. 112

C.2 Comparison of carrier density (n), mobility (μ) and conductivity (σ) measured by the AC Hall effect for doped P3HT films. 122

C.3 Summary of git parameters obtained for P1, P2 and P3 peaks from the full fits of the UV-VIS-FTIR data. 127

ACKNOWLEDGMENTS

There are a number of remarkable people who have helped me along the way to this milestone whom I would like to thank. First, my success would not have been possible without the support of my advisor, Ben Schwartz a.k.a. Big Ben, who has really enabled me to grow as a scientist. Thanks for being a constant source of guidance and encouragement, as well as a fountain of and sounding board for all kinds of crazy ideas in countless office chats. I also want to thank Sarah Tolbert who was essentially like a co-advisor for me. I sought advice from her many times on how to to go after the questions we were trying to answer and got many practical suggestions. Ben and Sarah were always there anytime I needed advice on science, careers, and life. I am also extremely grateful to Alex Spokoyny for entrusting me with some of his gold clusters- I mean boron clusters. Our collaboration really took off and has led to most of my thesis work and throughout that time he always been there to offer his advice and support.

I gratefully acknowledge the assistance of Richard Kaner, Paul Weiss, and Stuart Brown for serving on my committee. I am also very grateful to the rest of my collaborators, many of whom significantly contributed to the work presented in this thesis. In particular, KJ Winchell, Jon Axtell, Jeffrey Lindemuth, and Matt Bird have pondered the science with me on a number of occasions.

I am deeply indebted to my undergraduate advisor Chris Barrett who accepted a somewhat frantic undergraduate looking for her first research appointment into his lab. That experience, during which time I was closely mentored by lab members Tom Singleton and Chris Corkery, was what led me to pursue graduate school. Soon after, Bradley Siwick bravely allowed me to pursue the first of my own crazy ideas in his lab and Tomislav Friscic also bolstered my love of materials chemistry during my time at McGill with his personality and encouragement. Special thanks to Paul Weiss, Bill Gelbart and Chris Barrett for opening a door for me and shifting my course.

I am going to go a little further back than most and say that the passion and excitement about science, learning, and/or discovery instilled in me from some of my CEGEP and high school teachers is what kept me going on a scientific career path: Stephen Newbigging, Rhys Adams, Mike Besner, Darlene McRae, Genevieve Cormier, Richard Fortier, Joanna Schreyer, you are all pretty incredible educators.

I cannot forget the Schwartz group members, who were really the people I saw from day to day during my degree. Steve – I'll always remember you as the brilliant person who took me under his wing and tried to teach me everything at a lightning pace before leaving. Jordan, you showed me the soul of the Schwartz group and your wall of board games made me realize I had found the right group to join. Tyler, I am really glad I got to know you better by working on doping together and have been honored to follow in the footsteps of such an upstanding person. Thank you for converting me to the dark side and truly paving the way for many of my experiments. Matt, you could always brighten up the mood in the lab and were probably the most hard-working out of all of us; your students are truly lucky to have such a passionate teacher. Matthew and Erik, thanks for being my office mates, game buddies, friends and experts on all things spectroscopy and politics. As for the younglins, Dane you are now in charge and Omar you are second-in-command. You guys got this! It has been a great pleasure to watch you both grow. Omar, I am really glad you took an interest in the boron cluster doping projects and I am confident about leaving them in your hands. I look forward to hearing and reading about all your new directions and achievements. Mariah, keep on being the darkest ray of sunshine I have ever met. Everyone else, may the Schwartz be with you, always. And remember, if Darth Vader wears PPE so should you.

I am very fortunate to have made some incredible friends throughout the years and to have old friends who have stuck with me despite being on the other side of the continent in Canada. When I came to UCLA I expected it to be very competitive, but instead I was met by Kevin who has been my friend since that first day and I am lucky to have gone through gradschool in parallel with him. Thomas, I would say we made some pretty memorable tracks over the years and John and Nako I am glad I got to spend more time with you both coming to garage training with me. I especially want to thank all of my friends in the Martial Arts program at UCLA for keeping me sane throughout gradschool, for allowing me to meet some really incredible people, and for giving me my two favorite badass ninjas Aryana & Katelyn.

Last but certainly not least, a huge thank you to my family, who have always not only supported me but cheered me on and celebrated my achievements. I know I did not make it easy on my parents by choosing a school so far away, but they always pushed me to be the best I could be and I would certainly not be where I am today without them. They have really taught me so much. Following

suit, my fiancée Robert Boutelle has been my rock throughout gradschool and has supported me in every way in all of my endeavors. I am so lucky to have found someone who makes me a better person and with whom I can grow both personally and scientifically in the next chapter of our lives. Finally, thanks to the furriest member of my family, Toko, to the one who truly kept me company during the writing of this dissertation and who brightened many of my days with his pure joy over the simplest treasures in life.

Chapter 2 and Appendix A are versions of Reference 120, reproduced with permission from Aubry, T. J.; Ferreira, A. S.; Yee, P. Y.; Aguirre, J. C.; Hawks, S. A.; Fontana, M. T.; Schwartz, B. J.; Tolbert, S. H. Processing Methods for Obtaining a Face-On Crystalline Domain Orientation in Conjugated Polymer-Based Photovoltaics. J. Phys. Chem. C 2018, 122 (27), 15078–15089. Copyright 2018 American Chemical Society. Full article is available at http://pubs.acs.org/doi/10.1021/acs.jpcc.8b02859. This work was supported by the National Science foundation under grant CHE-1608957. The X-ray diffraction studies presented in this manuscript were carried out at the Stanford Synchrotron Radiation Lightsource. Use of the Stanford Synchrotron Radiation Lightsource, SLAC National Accelerator Laboratory, is supported by the U.S. Department of Energy, Office of Science, Office of Basic Energy Sciences, under Contract DE-AC02-76SF00515. I performed all final device, SCLC, PL and EQE measurements and played a significant role in writing the manuscript as well as developing its conclusions. Amy Ferreira performed all of the GIWAXS measurements and initial analysis and draft of the manuscript, Patrick Yee performed additional analysis of GIWAXS data to obtain Scherrer widths, Jordan Aguirre developed the SqP device recipe, Steven Hawks helped with EQE measurements, Matthew Fontana helped with experimental planning. The PIs and/or project directors were: Sarah Tolbert and Benjamin Schwartz.

Chapter 3 and Appendix B are versions of Reference 141, Aubry, T. J.; Axtell, J. C.; Basile, V. M.; Winchell, K. J.; Lindemuth, J. R.; Porter, T. M.; Liu, J.; Alexandrova, A. N.; Kubiak, C. P.; Tolbert, S. H.; et al. Dodecaborane-Based Dopants Designed to Shield Anion Electrostatics Lead to Increased Carrier Mobility in a Doped Conjugated Polymer. Adv. Mater. 2019, 31 (11), 1805647, reproduced with permission reproduced with permission from John Wiley and Sons under license number 4695620611380, copyright 2019 WILEY-VCH Verlag GmbH & Co. KGaA,

Weinheim. Full article is available at https://doi.org/10.1002/adma.201805647. This work was supported by the National Science Foundation under awards CHE-1608957 and CBET-1510353. Use of the Stanford Synchrotron Radiation Lightsource, SLAC National Accelerator Laboratory was supported by the U.S. Department of Energy, Office of Science, Office of Basic Energy Sciences under Contract No. DE-AC02-76SF00515. TD-DFT calculations were performed using Extreme Science and Engineering Discovery Environment's (XSEDE) computing resources. I initiated the project, prepared all samples for conductivity, XPS, GIWAXS, AC Hall and temperature dependent conductivity measurements, performed all conductivity and spectroscopic characterization and drafted and revised the manuscript. Jonathan Axtell performed all required synthesis, NMR characterization and electrochemical measurements of DDB-F_{72}. Victoria Basile performed to XPS measurements. K.J. Winchell performed to GIWAXS measurements. Tyler Porter performed electron-transfer rate NMR experiments. Ji-Yuan Liu performed TD-DFT calculations. Jeffrey Lindemuth performed AC Hall Effect and temperature dependent conductivity measurements. All authors contributed to analysis and interpretation of the data that they contributed. The PIs and/or project directors were: Anastassia Alexandrova, Clifford Kubiak, Sarah Tolbert, Alex Spokoyny, and Benjamin Schwartz.

Chapter 4 and Appendix C are versions of work that will be submitted soon after the submission of the dissertation. This work was supported by the National Science Foundation under awards CHE-1608957 and CBET-1510353. Synthetic work on redox-active boron clusters at UCLA was supported as part of the Center for Synthetic Control Across Length-scales for Advancing Rechargeables (SCALAR), an Energy Frontier Research Center funded by the U.S. Department of Energy, Office of Science, Basic Energy Sciences under Award no. DE-SC0019381. Use of the Stanford Synchrotron Radiation Lightsource, SLAC National Accelerator Laboratory was supported by the U.S. Department of Energy, Office of Science, Office of Basic Energy Sciences under Contract No. DE-AC02-76SF00515. Research at ORNL's Spallation Neutron Source was sponsored by the Scientific User Facilities Division, Office of Basic Energy Sciences, U.S. Department of Energy. I prepared all samples for conductivity, Neutron, GIWAXS, XPS and AC Hall measurements, performed all conductivity and spectroscopic characterization and wrote the manuscript. K.J. Winchell performed all GIWAXS and Neutron measurements and developed the

manuscript. Charlene Salamat helped with the Neutron measurements. Victoria Basile performed to XPS measurements. Julia Stauber performed all electrochemical characterization. Jeffrey Lindemuth performed AC Hall Effect and temperature dependent conductivity measurements. All authors contributed to analysis and interpretation of the data that they contributed. The PIs and/or project directors were: Sarah Tolbert, Alex Spokoyny, and Benjamin Schwartz.

Taylor J. Aubry

Department of Chemistry and Biochemistry, University of California, Los Angeles
607 Charles E Young Dr East, Los Angeles, CA 90095

EDUCATION

Ph.D. Chemistry - Materials & Nanoscience Specialization *September 2014 - Present*
University of California, Los Angeles
M.Sc. Awarded December 2015

B.Sc. Joint Honors in Physics & Chemistry *June 2014*
McGill University
Graduated with First-Class Honors

D.E.C. Honours Science, Pure and Applied *May 2011*
Cégep Vanier College

PUBLICATIONS

T. J. Aubry, K. J. Winchell, V. M. Basile, J. C. Axtell, J. R. Lindemuth, S. H. Tolbert, A. M. Spokoyny and B. J. Schwartz, "Tunable Redox-Potential Dodecaborane Dopants" *In prep* **2019**

T. J. Aubry, J. C. Axtell, V. M. Basile, K. J. Winchell, J. R. Lindemuth, T. M. Porter, J.Y. Liu, A. N. Alexandrova, C. P. Kubiak, S. H. Tolbert, A. M. Spokoyny and B. J. Schwartz, "Dodecaborane-based Dopants Designed to Shield Anion Electrostatics Lead to Increased Carrier Mobility in a Doped Conjugated Polymer" *Ad. Mat.* 1805647 **2019**; DOI: 10.1002/adma.201805647

T. J. Aubry, A. S. Ferreira, P. Y. Yee, J. C. Aguirre, S. A. Hawks, M. T. Fontana, B. J. Schwartz and S. H. Tolbert, "Processing Methods for Obtaining a Face-On Crystalline Domain Orientation in Conjugated Polymer-Based Photovoltaics," *J. Phys. Chem. C* 122(27), 15078-89 **2018**; DOI: 10.1021/acs.jpcc.8b02859.

M. T. Fontana, **T. J. Aubry**, D. T. Scholes, S. A. Hawks and B. J. Schwartz, "Rational Development of Polymer Solar Cells Through Sequential Processing: Optimizing Bulk Heterojunctions via Control of Polymer Swelling," in *World Scientific Handbook of Organic Optoelectronic Devices,* B. C. Thompson, ed., pp. 309-48 **2018**; ISBN: 978-981-3239-85-2; DOI: 10.1142/9789813239517_0008.

CONFERENCES & PRESENTATIONS

Brookhaven National Lab - Upton, NY *May 2019*
"Designing Dopants to Shield Anion Electrostatics in Doped Conjugated Polymers to Obtain Highly Mobile and Delocalized Carriers" (Invited Talk)

UCLA Chemistry Department - Los Angeles, CA *May 2019*
"Designing Dopants to Shield Anion Electrostatics in Doped Conjugated Polymers to Obtain Highly Mobile and Delocalized Carriers" (Talk)

MRS Spring Meeting - Pheonix, AZ *April 2019*
"Dodecaborane Clusters as Novel Tunable Dopants for Conjugated Polymers" (Talk)

ACS National Meeting - Boston, MA *August 2018*
"Tailored Dodecaborane Dopants Designed to Shield Anion Electrostatics in Doped Conjugated Polymers" (Talk)

Seaborg Symposium - Los Angeles, CA *November 2017*
"Tailored Dodecaborane Dopants Designed to Shield Anion Electrostatics in Doped Conjugated Polymer" (Poster)

ACS National Meeting - San Fancisco, CA *April 2017*
"Device Physics of the Organic Alloying Effect in High-Efficiency Ternary Blend Polymer/Fullerene Bulk-Heterojunction Solar Cells" (Poster)

ACS National Meeting - San Diego, CA *March 2016*
"Sequential Processing as a Method for Retaining the Face-On Polymer Orientation in PBDTTT-C-based Photovoltaics" (Poster)

Center for Self Assembled Chemical Structures Symposium - Montreal, QC *September 2013*
"Characterizing Small Molecule Optical Sensors for Neurotransmitter Detection" (Poster)

APS Conference for Undergraduate Women in Physics (CUWiP) *January 2013*

RESEARCH EXPERIENCE

University of California, Los Angeles *December 2014 - Present*
Department of Chemistry & Biochemistry, Prof. Benjamin J. Schwartz

Understanding Structure and Electronic Property Relationships in Chemically Doped Semiconducting Polymers and Polymer Photovoltaics

· Initiated new collaboration studying dodecaborane clusters as novel, tunable molecular dopants for semiconducting polymers that can shield anion electrostatics
· Studied dopant size and redox potential effects on thermoelectric and morphological properties using conductivity, Seebeck, CV, UV-VIS, FTIR, XPS, GIWAXS, SEM and EDX measurements
· Effect of device processing methods on polymer orientation and photovoltaic device performance
· Device physics of organic alloys as seen in single donor, two acceptor ternary blend systems

McGill University *September 2013 - April 2014*
Department of Physics, Prof. Bradley J. Siwick

Probing the Transient Structure of Halogenated Azobenzene Crystals using Femtosecond Electron Diffraction

· Femtosecond resolved electron diffraction studies of isomerization in halogenated azobenzene crystals
· K-space analysis of time delayed diffraction patterns for transient crystal structure determination

McGill University *May 2013 - September 2013*
Department of Chemistry, Prof. Christopher J. Barrett

Boronic Acid Functionalized Azobenzene Derivatives as Small Molecule Optical Sensors for Neurotransmitter Detection

· Investigation of boronic acid functionalized azobenzene derivatives for dopamine detection
· Pump-probe spectroscopy studies on the isomerization kinetics of sensor molecules

AWARDS & HONORS

Materials Chemistry Dissertation Award *2019*
Recognizing outstanding research in materials chemistry

UCLA University Fellowship *2014*
In recognition of outstanding promise in research ability

Dean's Multidisciplinary Undergraduate Research Award *2014*
Recognizing substantial and broad undergraduate science research.

Tomlinson Teaching Award *2013*
For teaching the Chemistry of Advanced Materials course

Vanier College Entrance Scholarship *2010*
In recognition of high academic entrance standings

CHAPTER 1

Introduction

Functional materials continue to influence emerging technologies and impact our lives. In the late 1970s, it was found that some polymer (plastic) materials displayed the electrical properties of semiconductors. Since then, the Nobel Prize in Chemistry in the year 2000 was awarded for the discovery[1] and semiconducting polymers have been widely studied for a variety of device applications such as solar cells,[2] light-emitting diodes,[3] field-effect transistors,[4] thermoelectrics,[5] sensors,[6] and more. Conjugated polymers' unique electronic properties originate from their conjugated backbone, which consists of repeating alternated double- and single-bonds that create overlapping p-orbitals and thus a system of delocalized π-electrons. Conjugated polymers possess several advantages over more traditional inorganic semiconductors, such as being flexible, light-weight, and low-cost. The latter is due to their ease of synthesis and processing, as well as their composition containing only earth-abundant elements. Most conjugated polymers are soluble in common organic solvents, enabling the use of industrial solution processing methods such as spin-coating, ink-jet printing and roll-to-roll processing, which is essential for the realization of large-scale manufacture of devices from these materials.[7]

Despite the numerous promising benefits, implementation of semiconducting polymer materials in practical technologies has lagged mainly because their intrinsic electrical properties are inferior to their inorganic counterparts. The key reason for sustained interest in conjugated polymers lies in their potential for extreme tunability – both synthetically and structurally. This work is focused on understanding and controlling properties on the molecular level to improve charge carrier properties in π-conjugated polymers. This chapter will introduce how charge carrier properties can affect device performance in two categories of polymer devices, photovoltaics and thermoelectrics. This is followed by a discussion of two methods to tune the electrical properties of semiconducting

polymers: intrinsically by modification of the polymer structure and via generation of charge carriers with chemical doping.

1.1 Charge carrier dynamics in optoelectronic polymer devices

1.1.1 Polymer photovoltaics

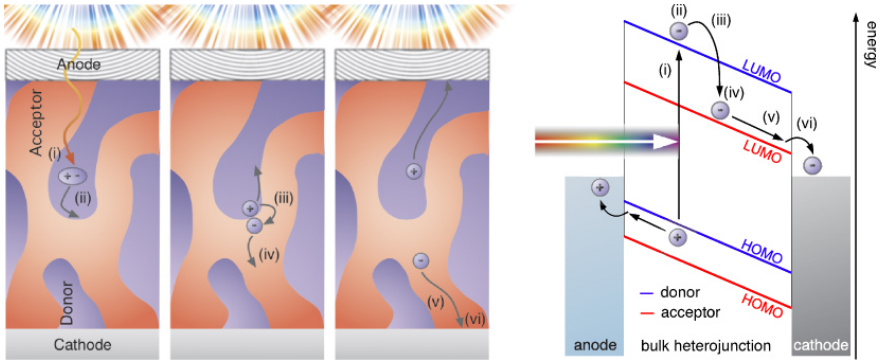

Figure 1.1: Cartoon of current generation in a polymer solar cell (left) and corresponding simplified energy diagram (right). (i) Light absorption and exciton creation (ii) Exciton diffusion to donor/acceptor heterojunction interface. (iii) Exciton dissociation via electron transfer to the acceptor. (iv) Charge separation into free carries. (v) The charge carriers transported to respective electrodes. (vi) Charge extraction.

Polymer solar cells are a type of organic photovoltaic (OPV) that utilize semiconducting polymers as the main light absorber. Upon the absorption of a photon, an electron is excited to the polymer's lowest unoccupied molecular orbital (LUMO), leaving a positive hole in its highest occupied molecular orbital (HOMO); together the electron and hole constitute an exciton (Coulombically bound electron-hole pair). Fundamental to the working principle of a solar cell, these photogenerated charges can be exploited as usable current to generate electricity, however, excitons can only diffuse on the order of 10 nm before recombining, a considerably smaller distance than the $\sim$100 nm-thick active layer in a thin-film device.[8] It is not surprising then that original OPV designs, which relied on a single layer of semiconducting polymer, produced sub 1% efficiencies.[9] Today, the leading device architecture is known as a bulk heterojunction, shown in Figure 1.1,[8] in which the conjugated polymer donor is paired with an electron acceptor, such as fullerene (C_{60}) derivatives or other small molecules, in order to split the excitons into free carriers. The carriers

must then diffuse through contiguous pathways of their respective donor and acceptor material to reach the appropriate electrode in order be collected as photocurrent. The ideal BHJ should have donor and acceptor regions that are well-mixed so that a heterojunction interface is reachable within the diffusion length of generated excitons, but a BHJ also needs to have separate domains that maintain excellent charge-transport so that carriers can reach the electrodes. And both of these requirements must be met for active layers thick enough to adequately harvest incident light. As a result, the efficiency of polymer-based PVs is highly sensitive to the underlying morphology. This leads to one of the primary challenges in this field, as the structural properties of conjugated polymers are nontrivial. The properties of conjugated polymers and their bulk heterojunctions at the molecular scale, mesoscale, and device scale are all fundamentally entangled, and understanding these correlations is crucial for developing high-performance polymer-based electronics.

1.1.2 Thermoelectrics

Another application in which conjugated polymers have recently seen a resurgence in the literature is in the field of thermoelectric devices. Thermoelectric materials enable conversion between thermal and electrical energy via carrier movement in response to energetic gradients and can be used for power generation as well as for heating or cooling. More specifically, in thermoelectric materials, the creation of a voltage from a temperature difference is known as the Seebeck effect, while the reverse process of driving heat flow with an electric current is known as the Peltier effect. The key to creating a thermoelectric module is the pairing of n-type (electron rich) and a p-type (electron deficient) semiconductors, which have opposite majority carriers, to create carrier flow in the same direction and thus allow current to flow in a circuit as shown in Figure 1.2.[10]

The performance of a thermoelectric materials is benchmarked using the thermoelectric figure of merit, ZT:

$$ZT = \frac{S^2\sigma}{\kappa}T \quad \text{where} \quad S = -\frac{\Delta V}{\Delta T} \tag{1.1}$$

where σ is the electrical conductivity, S is the Seebeck coefficient or thermopower, κ is the thermal conductivity and T is the temperature. Therefore, a high electrical conductivity, paired with a low thermal conductivity and an ability to generate a large voltage over a temperature gradient, are

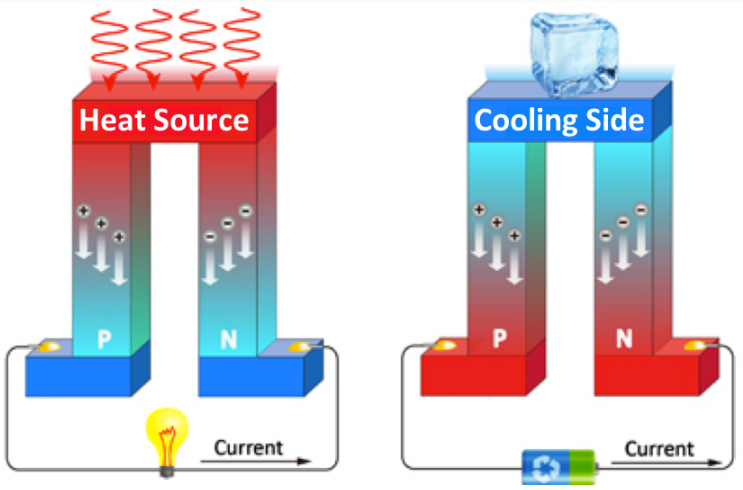

Figure 1.2: Schematics of thermoelectric effects. (Left) Seebeck effect where an applied temperature difference causes charge carriers to diffuse from the hot side to the cold side, resulting in a current. (Right) Peltier effect in which heat is absorbed at the upper junction and released at the lower junction when a current is applied to the circuit.

what is desired from a thermoelectric material. Since polymer materials are expected to have a low thermal conductivity, often only the power factor ($PF = \sigma S^2$) is reported.[10] Semiconducting polymers have recently demonstrated potential as alternative thermoelectric materials with power factors approaching those of inorganic materials, however, all the thermoelectric parameters are strongly correlated, which leads to difficulty in optimizing and improving the figure of merit. The Seebeck coefficient is the average entropy transported per charge carrier and thus decreases with increasing carrier concentration, which boosts conductivity. The thermal conductivity also increases with carrier concentration, as charge carriers can also transport heat. Thus, optimizing doped conjugated polymers for use in thermoelectrics is not a trivial task.

1.2 Structural Effects on Charge Transport in Conjugated Polymers

The electronic properties of conjugated polymers are heavily linked to their underlying structure due to anisotropic charge transport. In semiconducting polymers, charges must not only move along single polymer chains but also between chains in a process known as "hopping" for long-range transport. The highest mobility for charge carriers is along the polymer chain, followed by through the π-stacking direction, and lastly in the alkyl-stacking direction (schematic structure shown in

Figure 1.3a).[11] Device performance can thus be impacted by the local polymer chain orientation, shown in Figure 1.3b,[12] depending on the desired direction of transport. For example, if in-plane charge transport is needed, as in a field effect transistor, then an edge-on domain orientation is preferred so that the higher-mobility pathways (along the chain and through the π-stacks) are in-plane. Polymers most commonly adopt either an edge-on or face-on orientation, as end-on orientation is always energetically unfavorable.[12]

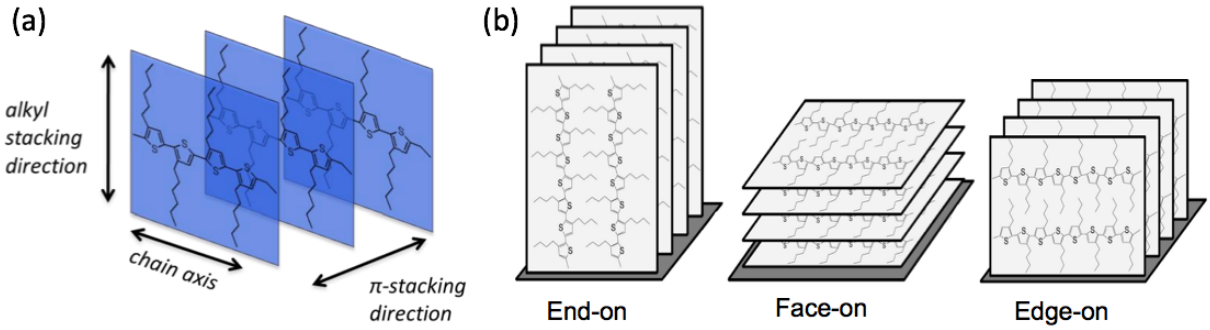

Figure 1.3: Ordered polymer structure. (a) Charge conduction pathways with along the chain axis having the highest mobility followed by through the π stacking direction and hopping between chains in the alkyl direction being the lowest. (b) Polymer chain orientations, with edge-on and face-on being far more prevalent than end-on.

Because of the highly entropic nature of long polymer chains having many possible conformations, ordered regions, as shown in Figure 1.3, only occur in nanometer-scale aggregates embedded in a matrix of largely disordered material. Thus, conjugated polymer films are actually semicrystalline materials with crystallites typically only contributing to a fraction of the bulk volume.[13] Structural disorder in the amorphous region breaks conjugation and leads to energetic traps, thereby limiting charge transport. Therefore, the overall crystallinity of the material is also an important factor for charge transport properties. Although crystalline regions exhibit coherence, long-range order between crystallites is typically not achieved. However, single polymer chains, known as 'tie-chains', can bridge between crystalline regions and allow charge carriers to move from aggregate to aggregate.[13,14] The higher the molecular weight of the polymer, the more inter-crystallite connections are made. Thus, electronic properties of conjugated polymers are highly sensitive to the polymer orientation, molecular weight, crystallinity and overall microstructure. Many factors can affect the resulting microstructure of a conjugated polymer film including: substrate effects,

solvent choice, processing conditions and drying kinetics, etc. It is by studying this relationship between structure and electronic properties that our understanding of these effects can be expanded and guidelines for the design and processing of new materials can be developed.

1.3 Molecular Doping of Semiconducting Polymers

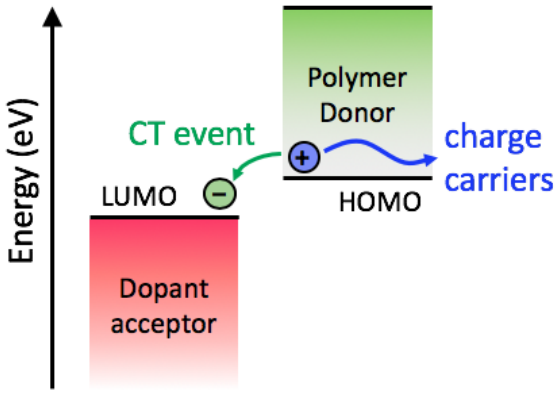

Figure 1.4: Schematic energy diagram of *p*-doping process with integer charge transfer. A dopant acceptor with a LUMO that lies below the polymer HOMO can remove an electron from the polymer backbone and produce a positive charge carrier known as a hole and also a polaron. Although not every dopant will necessarily undergo charge transfer with the polymer, each CT event should result in a charge carrier, albeit with varying degrees of localization.

The introduction of charge carriers via doping can tune the conductivity of conjugated polymers over many orders of magnitude. Low levels of doping can improve the performance of organic photovoltaics by filling trap states and improving charge transport, while more extensive doping can be useful in field-effect transistor or thermoelectric devices. Although doping can be achieved electrochemically or via charge injection, both of these methods require the continuous application of a potential to maintain the doped state. Ground-state charge carriers can be produced by molecular doping, which involves the introduction of a strong electron acceptor (oxidizing agent) or donor (reducing agent) for *p*- or *n*-type doping, respectively. Conjugated polymers are typically most stable as *p*-type materials, and the energy level diagram for this doping process is shown in Figure 1.4: for *p*-type doping, the dopant has a LUMO that lies below the polymer HOMO and thus can undergo ground-state charge transfer (CT) leaving behind a positive charge carrier, known as a polaron, on the polymer backbone.

Although doping of organic semiconducting materials is similar in principle to doping of their inorganic counterparts in that doping increases carrier concentration, there are some significant differences. In inorganic semiconductors, every substitutional impurity creates a free carrier, however, not every dopant molecule creates a free carrier on the polymer backbone due to Coulomb-binding effects and the low permittivity of organic materials. Molecular doping of conjugated polymers is a complex process that also can affect the material's microstructure. This work attempts to disentangle some of the structural effects of the dopant on charge carrier properties and elucidate the mechanisms that govern the doping process in conjugated polymers.

1.4 Overview of Thesis

This thesis contains 4 chapters focused on understanding and controlling structure on the molecular level to improve charge carrier properties in π-conjugated polymers. The following is a brief summary of the subsequent chapters, along with a description highlighting the original results that have contributed to the field.

1.4.1 Chapter 2: Processing Methods for Obtaining a Face-On Crystalline Domain Orientation in Conjugated Polymer-Based Photovoltaics.

The polymer chain orientation and degree of crystallinity within a polymer:fullerene bulk heterojunction (BHJ) photovoltaic can greatly impact device performance. In general, a face-on chain orientation is preferred for charge conduction through sandwich-structure photovoltaic devices, but for many conjugated polymers, an edge-on conformation is energetically favored. In this chapter, we examine the effects of different processing techniques on photovoltaics based on the poly[4,8-bis(2- ethylhexyloxy)-benzol[1,2-b:4,5-b']dithiophene-2,6-diyl-alt-4-(2-ethylhexyloxy-1-one)thieno [3,4-b]thiophene-2,6-diyl] (PBDTTT-C):[6,6]-phenyl-$C_7$1-butyric-acid-methylester ($PC_7$1BM) materials combination. We examine the extent of polymer crystallinity and crystalline domain orientation using both traditional blend-casting (BC), where the polymer and fullerene are cast from a single, codissolved solution, as well as sequential processing (SqP), where the polymer film is deposited first, and then the fullerene is infiltrated into the polymer film in a second solution

processing step. We show using two-dimensional grazing-incidence wide-angle X-ray scattering (GIWAXS) that BC leads to a disordered, isotropic polymer network in the resulting BHJ film with a correspondingly poor device efficiency. By contrast, SqP preserves the preferred face-on chain orientation seen in pure polymer films, yielding higher short-circuit currents that are consistent with the increased hole mobility of face-on oriented polymer chains. We also study the effects of the widely used processing additive 1,8-diiodooctane (DIO) on polymer chain orientation and crystallinity in photovoltaic devices made by both processing techniques. We show that DIO results in increased polymer crystallinity, and in devices made by BC, DIO also causes a partial recovery of the face-on PBDTTT-C domain orientation, improving device performance. The face-on chain orientation in SqP devices produces efficiencies similar to those of optimized BC devices made with DIO but without the need for solvent additives or other postprocessing steps.

1.4.2 Chapter 3: Dodecaborane-Based Dopants Designed to Shield Anion Electrostatics Lead to Increased Carrier Mobility in a Doped Conjugated Polymer

One of the most effective ways to tune the electronic properties of conjugated polymers is to dope them with small-molecule oxidizing agents, creating holes on the polymer and molecular anions. Undesirably, strong electrostatic attraction from the anions of most dopants localize the holes created on the polymer, reducing their mobility. In this chapter, we employ a new strategy utilizing a substituted boron cluster as a molecular dopant for conjugated polymers. By designing the cluster to have a high redox potential and steric protection of the core-localized electron density, we obtain highly delocalized polarons with mobilities equivalent to films doped with no anions present. AC Hall effect measurements show that P3HT films doped with our boron clusters have conductivities and polaron mobilities roughly an order of magnitude higher than films doped with F_4TCNQ, even though the boron-cluster-doped films have poor crystallinity. Moreover, the number of free carriers approximately matches the number of boron clusters, yielding a doping efficiency of $\sim$100%. These results suggest that shielding the polaron from the anion is a critically important aspect for producing high carrier mobility, and that the high polymer crystallinity required with dopants such as F_4TCNQ is primarily to keep the counterions far from the polymer backbone.

1.4.3 Chapter 4: The effects of dopant electron affinity at fixed counterion distance on the production of free carriers in conjugated polymers.

Molecular doping of conjugated polymers produces carriers via charge-transfer between the polymer and dopant. The dopant counterions exhibit distance-dependent Coulomb interactions that limit carrier mobility. Consequently, the effects of energetic offset between polymer and dopant have been difficult to isolate because changing the dopant's redox potential has required changing the entire molecule, which alters where the dopant resides in the polymer crystal structure. Here, we employ dodecaborane (DDB) dopants that intrinsically shield counterion electrostatics via their core-localized electron density and whose redox potential can be varied over nearly 1 V without affecting the dopant size or shape. The doping level increases with redox potential, characterized by higher conductivities and spectroscopic polaron peaks. Using neutron reflectometry to probe vertical dopant distribution, we find that redox potential is a driving force for infiltration. These results are supported by X-ray characterizations, which show a DDB-intercalated phase in the lamellar region that is strongly redox-dependent. This suggest that dopant counterions of any shape and size tend to reside in the lamellar regions as such, polymer crystallinity plays an important role keeping counterions spatially separated from polarons. We find that energetic offset is critical to the production of free carriers as the higher redox potential DDBs result in increased doping efficiencies up to $\sim$100%, while the typical F_4TCNQ dopant traps 95% of carriers.

CHAPTER 2

Processing Methods for Obtaining a Face-On Crystalline Domain Orientation in Conjugated Polymer-Based Photovoltaics

Organic photovoltaics (OPVs) are of interest due to their potentially low cost, ease of processing, and composition containing only earth-abundant elements. These devices typically consist of a semiconducting polymer as the primary photoabsorber and electron donor, paired with a fullerene derivative as the electron acceptor. Although reasonably high power conversion efficiencies (PCEs) can be obtained,[15–17] the overall device performance is highly sensitive to the morphology of the blended system.[18] To obtain optimal performance, the polymer and fullerene must have separated domains to enable efficient charge collection,[19,20] but also must be mixed on length scales of less than $\sim$20 nm to prevent exciton recombination prior to charge separation.[21] The primary way this morphology is achieved is through blend-casting (BC), in which the polymer and fullerene are co-dissolved in solution and spun onto a conductive substrate.[9] In BC, the polymer and fullerene must partially de-mix during film formation to form a bicontinuous interpenetrating network, a process that is often assisted by the use of solvent additives[22–25] or via post-treatment steps involving solvent[26,27] or thermal annealing.[28–30] A more recently introduced method for forming polymer:fullerene BHJs is sequential processing (SqP).[31–39] In SqP, the polymer film is cast first and then the fullerene is infiltrated into the polymer in a second casting step using a quasi-orthogonal solvent or co-solvent blend chosen to swell but not dissolve the polymer underlayer, allowing mass action to drive fullerenes into the amorphous regions of the swollen polymer film.[35,40–45] The fullerene-casting solvent can be rationally selected on the basis of its Flory-Huggins χ parameter, which can be determined via a few simple ellipsometry measurements on solvent-swollen films,

thereby avoiding the need for significant trial-and-error.[44] If necessary, fullerene intercalation in SqP also can be facilitated with a thermal annealing step.[9,42,46–48]

It is well established that the polymer crystallinity in the active layers of BHJ photovoltaics is one of the key factors in determining carrier mobility and carrier extraction in polymer solar cells.[38,39] In addition to the total polymer crystallinity, however, the polymer domain orientation (i.e., 'texture') also plays a major role in hole extraction from the device, which in turn influences both the short-circuit current and fill factor.[49,50] Due to surface energetics, most semiconducting polymers prefer to lie with their side-chains perpendicular to the surface (edge-on orientation of the backbone), requiring holes to hop between polymer chains to be extracted from the top and bottom contact electrodes in a sandwich structure devices.[51–53] Higher mobilities are found for carrier motion either along the polymer backbone or through a π-stacked network of polymer chains. Although it would be ideal to exploit the largest possible hole mobility, which is along the length of a semiconducting polymer chain, this would require a remarkably uncommon end-on polymer chain conformation in an OPV device.[11,12,54–57] Therefore, the best readily-achievable mobility has the holes traveling through a stacked π-conjugation network, which is achieved for OPVs when all of the polymer chains orient face-on with respect to the substrate.[58]

For this reason, there has been much recent interest in determining whether the conjugated polymers used in OPV devices lie either face-on or edge-on with respect to the substrate. Indeed, when conjugated polymers have a face-on orientation in working devices, both hole mobility and extraction are improved.[49,50,59–64] One semiconducting polymer that is known to lie face-on when cast into pure films is poly[4,8-bis-(2-ethylhexyloxy)-benzol[1,2-b:4,5-b']dithiophene-2,6-diyl-alt-4-(2-ethylhexyloxy-1-one)thieno[3,4-b]thiophene-2,6-diyl] (PBDTTT-C), which has been used extensively with blend-cast processing to make reasonably high-performing OPV devices.[65–72] Although the performance of blend-cast PBDTTT-C devices has been well optimized,[65–72] the polymer crystallinity and domain orientation in its BHJ devices has not been studied in depth.

In this paper, we present a detailed study of the crystallinity and orientation of PBDTTT-C polymer chains in both pure films and in BHJs produced by BC and SqP where the polymer is combined with [6,6]-phenyl-C71-butyric-acid-methylester ($PC_{71}BM$). We also examine the effects of the widely used processing additive 1,8-diiodooctane[24,25,68–82] (DIO) in pure and BHJ films, as

optimal blend-cast BHJs fabricated with PBDTTT-C require DIO.[68–72] We employ two-dimensional grazing-incidence wide-angle X-ray scattering (GIWAXS) to understand the extent to which the polymer maintains its face-on orientation in BHJ devices created using these different processing methods. We find that blend-casting leads to a more isotropic orientation of the PBDTTT-C crystalline domains in BHJ active layers but that the use of DIO improves device performance by both partially recovering the naturally preferred face-on orientation and improving overall polymer crystallinity. With SqP, we find that we are better able to preserve PBDTTT-C's intrinsic face-on orientation in BHJ active layers. This is because SqP works by swelling the amorphous regions of a polymer film with the fullerene-casting solvent, leaving the polymer crystalline domains relatively intact.[36,42] With the more favorable face-on orientation of PBDTTT-C in devices fabricated via SqP, we are able to match the device efficiencies of optimized blend-cast devices without the need for solvent additives such as DIO. The increased orientation control achieved with SqP and described in this work provides a further tool for researchers aiming to control multiple aspects of semiconducting polymer structure and domain orientation within functioning devices.

2.1 Experimental Section

2.1.1 Film Fabrication

For GIWAXS and device studies, commercially available PBDTTT-C either was used as received or was combined with commercially purchased $PC_{71}BM$ via blend-casting or sequential processing. All PBDTTT-C solutions (pure and blended) were made at a polymer concentration of 10 mg/mL in o-dichlorobenzene, and all films were deposited by spin-coating. For blend-cast BHJ active layers, the solutions were made with a 1:1.5 wt/wt PBDTTT-C:$PC_{71}BM$ ratio, which when deposited yielded an active layer thickness of $\sim$90 nm. Sequentially processed active layers were fabricated by first spin-coating pure PBDTTT-C and then subsequently depositing the fullerene from a 10 mg/mL solution of $PC_{71}BM$ in a 1:1 v/v blend of 2-chlorophenol:dichloromethane (2CP:DCM) (chosen for optimal swelling of the polymer underlayer[44]), such that the final active layer thickness was also $\sim$90 nm. Some BHJs made by SqP used a 5 mg/mL $PC_{71}BM$ concentration in order to more clearly see the texture of the polymer diffraction peaks in GIWAXS experiments. Where noted,

3% v/v 1,8-diiodooctane (DIO) additive was added to either the blend-cast solution or the pure polymer solution samples. Also where noted, a methanol wash was performed to remove DIO from the films.[78–82] Films made for GIWAXS studies were cast onto silicon substrates (with a 1.8 nm SiO_2 native oxide layer) that were coated with a poly(ethylenedioxythiophene):poly(styrenesulfonic acid) (PEDOT:PSS) layer to replicate the bottom device interface; Si was chosen to minimize substrate diffraction. Active layer films for devices were fabricated from the same solutions as for the GIWAXS studies, and electrodes were evaporated to produce the final device structure: ITO/PEDOT:PSS/PBDTTT-C:PC_{71}BM/Ca/Al. Diodes for space-charge-limited current (SCLC) measurements were fabricated in the same way as the BHJ devices but using an architecture of ITO/PEDOT:PSS/active layer/Au to ensure majority hole carriers. All film thicknesses were measured using a Dektak 150 stylus profilometer. Further fabrication details can be found in the Supporting Information (Appendix A).

2.1.2 GIWAXS Measurements

The two-dimensional GIWAXS measurements were performed at the Stanford Synchrotron Radiation Lightsource (SSRL) on beamline 11-3 using a wavelength of 0.9742 Å. Diffraction patterns were collected on a two-dimensional image plate with a sample to detector distance of 400 mm and a spot size of roughly 150 µm. A helium chamber was utilized to increase the signal-to-noise ratio. For the analysis of the GIWAXS data, the two-dimensional diffraction for each sample was integrated using WxDiff. The limits of the integration were changed on the basis of the orientation information desired. To obtain a full integration of a diffractogram, the integration limits were from 0 to 180°. For in-plane, out-of-plane, and 45° integrations, the limits were 0-10°, 80-90°, and 40-50°, respectively. The intensities on the opposite sides of the diffractogram (90-180°) were also checked to ensure they were the same as the chosen limits. Each integration was background corrected for the substrate scattering. The subtractions were performed on the raw scattering data to ensure that no errors occurred due to background subtraction. To ensure reproducibility in diffraction intensity and shape, all samples were made and measured in triplicate, and if all three samples did not agree, samples were refabricated and rerun.

2.1.3 Device Measurements

Photoluminescence spectra were collected on a Spex Fluorolog 3 spectrofluorometer using a 630 nm excitation wavelength, 5 s integration time, and 5 nm excitation and emission slit widths for all samples. Photovoltaic performance was measured in an argon atmosphere using a Keithley 2400 sourcemeter and AM-1.5 filtered light from a xenon arc lamp source equipped with a liquid light guide (Oriel). The incident light intensity on tested samples was adjusted to be 100 mW/cm^2 using a calibrated Si diode. SCLC measurements were taken on the same setup but without the light source. The dark J–V curves were corrected for series resistance and fit to the Murgatroyd equation[83–85] to extract the steady-state mobilities (details of the fits can be found in Appendix A). EQE measurements were collected using a chopped (23 Hz) monochromatic beam (Newport TLS-300X) measured across a 50 Ω resistor using a SR830 lock-in amplifier. Because the currents are low, the voltage across the resistor and therefore the device is also low, which means that short-circuit conditions are well-maintained at all times. Multiple long-wave-pass filters (90% transmission cut-on at 345, 605, 850, 1030, and 1550 nm) were used during the measurement to remove high-energy light transmitted through the monochromator due to lower-order reflections. Each data point was taken from the amplitude readout of the lock-in and averaged for ∼5 time constants.

2.2 Results and Discussion

2.2.1 Orientation of PBDTTT-C Crystallites Measured by 2-D GIWAXS

Two-dimensional GIWAXS is a powerful tool that allows us to determine both the relative polymer crystallinity and the orientation of the crystalline domains. From the two-dimensional scattering patterns, the extent of polymer orientation can be determined by comparing the intensities of the (100) lamellar-stacking and (010) π-π-stacking peaks in both the conventional out-of-plane and in-plane scattering directions. The out-of-plane scattering reports only on those diffraction planes oriented parallel to the plane of the substrate, while in-plane scattering focuses on diffraction planes oriented perpendicular to the plane of the substrate. To study how the polymer structure changes

with different processing conditions, we measured the two-dimensional X-ray scattering from both blend-cast and sequentially processed PBDTTT-C:$PC_{71}BM$ BHJ active layers in addition to pure PBDTTT-C films with and without DIO, as shown in Figure2.1a–f.

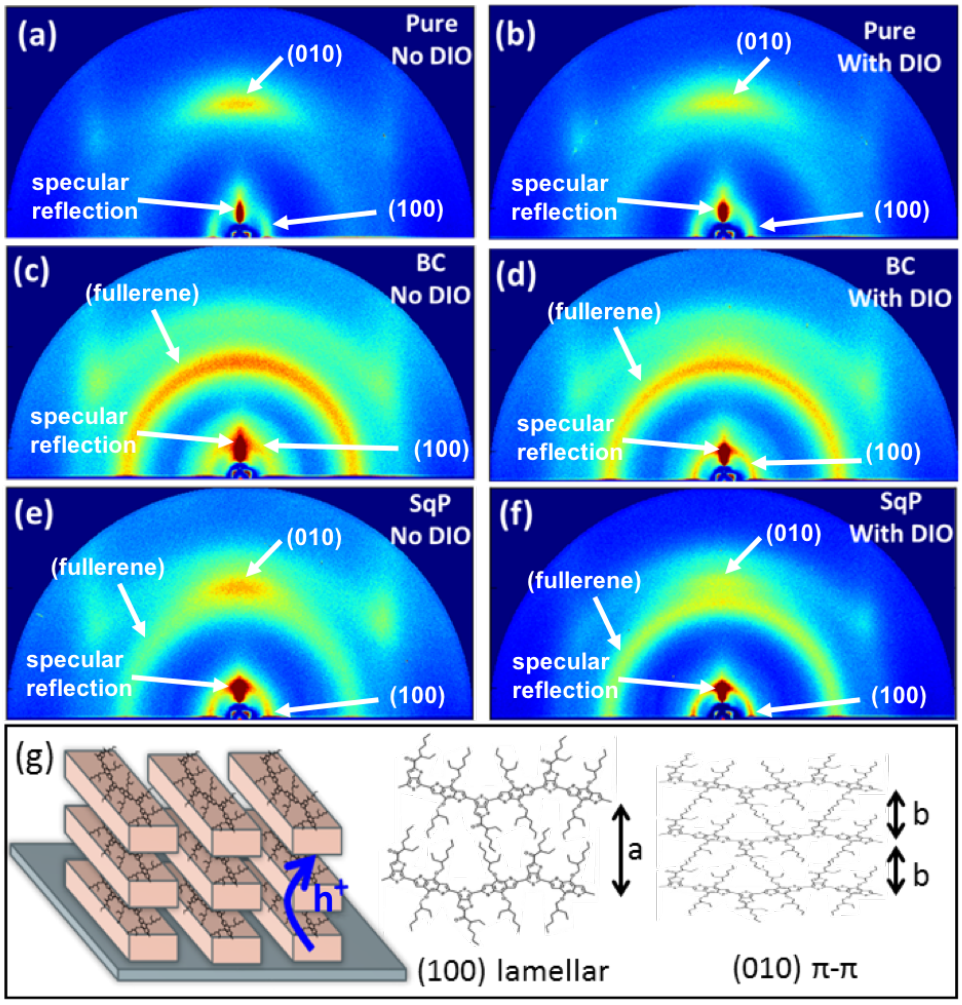

Figure 2.1: Raw GIWAXS diffractograms for pure polymer (a) and pure polymer with DIO (b) showing a face-on polymer orientation. Diffractograms for blend-cast (c,d) and sequentially processed (e,f) BHJs, both with (d,f) and without DIO (c,e) exhibit isotropic fullerene diffraction, but very different polymer chain orientations. Face-on polymer orientation is clearly seen in SqP films, while blend-cast films show more isotropic diffraction. A cartoon of face-on oriented polymer chains as well as cartoons depicting the (100)- and (010)-stacking directions are shown in (g).

2.2.1.1 Face-On Structure of Pure PBDTTT-C Films

From the raw diffractogram of the pure polymer (Figure 2.1a), the preference for face-on orientation of the polymer domains can clearly be seen: the (100) lamellar peak is located primarily in-plane,

and the (010) π-π-stacking peak is seen primarily in the out-of-plane direction, in agreement with the literature.[70] A cartoon depicting this face-on orientation of the PBDTTT-C polymer chains in the pure polymer film is shown in Figure 2.1g.

The addition of the solvent additive DIO to blend-cast solutions of polymers and fullerenes has been shown to improve the power conversion efficiency in a variety of systems[78–82] and in particular has been effective for improving devices made with PBDTTT-C.[68–72] Thus, we also looked at the effects of DIO on the structure of pure PBDTTT-C and sequentially processed BHJ films in addition to the well-studied blend-cast system with $PC_{71}BM$.[65–72] We find that adding DIO to solutions when casting pure polymer films does not change the polymer domain orientation (Figure 2.1b). For blend-cast and sequentially processed BHJ films, however, isotropic scattering from the fullerene is observed near the polymer (010) peak, making it difficult to see the polymer (010) diffraction peak in some cases. Even though the raw data cannot be used to determine polymer chain orientation in all cases, clear (010) scattering can still be seen in the out-of-plane direction for the sequentially processed films, suggesting that this method preserves the face-on orientation of the pure polymer. For a more detailed analysis of the chain orientation across processing conditions, selective integrations of the data are needed, as presented below.

For pure PBDTTT-C films, we radially integrated the two-dimensional diffractograms shown in Figure 2.1 to obtain information on the crystallinity and crystallite size, as depicted in Figure 2.2a. The fitted peak areas and coherence lengths, which give quantitative information about the overall crystallinity and crystallite size, are given in Table A.1 of Appendix A. The pure polymer exhibits characteristic (100) and (010) scattering peaks at 0.33 and 1.57 $Å^{-1}$ respectively. Upon the addition of DIO, a marked increase of over 50% in the overall crystallinity of the pure polymer is observed. It is well-established that, due to its low volatility, DIO tends to remain in polymer films, where it can be detrimental to device performance if it is not properly removed.[80–82] Furthermore, it has been shown that the addition of DIO increases time for crystallite formation in BHJs.[86] Thus, the low volatility of DIO compared to the polymer-casting solvent gives the polymer more time to crystallize and thus increases overall crystallinity.

We further quantified the crystalline domain sizes using the full width at half-maximum (fwhm) of the (100) peaks via the Scherrer equation (details in Appendix A). We note that in conjugated

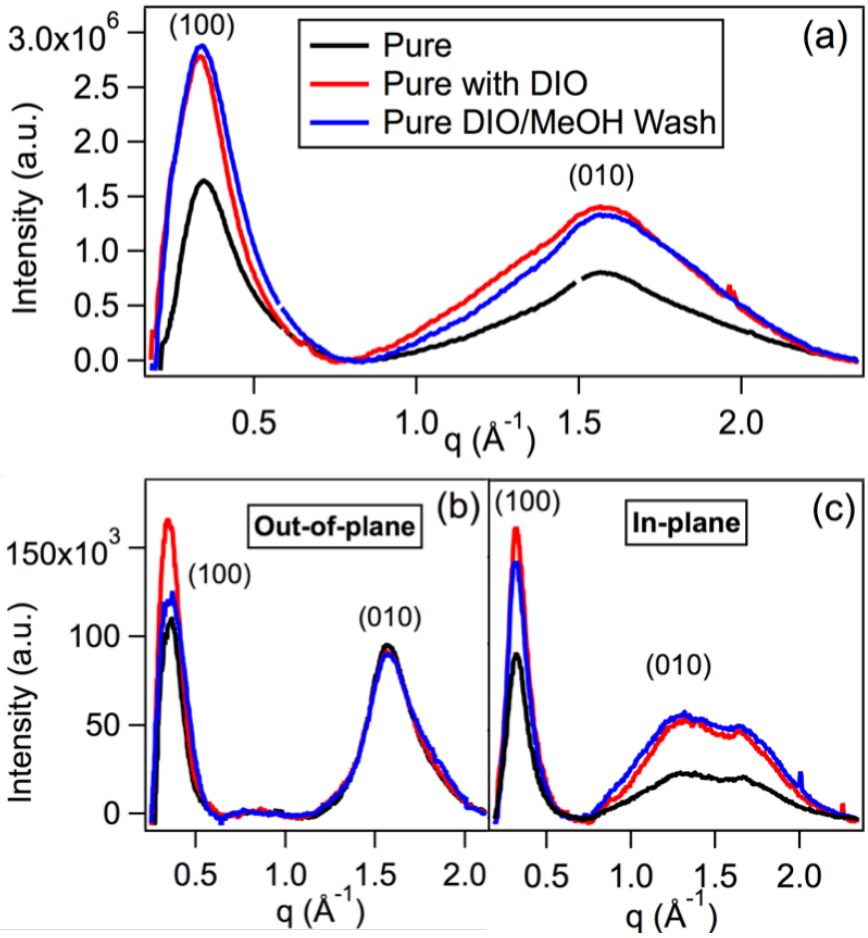

Figure 2.2: (a) Full integration of GIWAXS diffractograms for pure polymer films showing the increase in crystallinity with the addition of DIO, where the black curves are pure polymer, red curves are polymer with 3% DIO, and blue curves are obtained after washing the DIO away with methanol. The face-on orientation shown by the strong (010) diffraction in the out-of-plane direction (b), with much less intensity in-plane direction (c).

polymer systems like those studied here, the broadening of X-ray scattering peaks results from a combination of finite size effects, as seen in traditional crystalline materials, as well as disordered-induced broadening. As a result, domain sizes derived from the fwhm of diffraction peaks using the Scherrer equation correspond to what we call the crystalline coherence length, which is always smaller than or equal to the actual crystallite size because of the effects of chain packing disorder. Although there is an increase in overall crystallinity of the pure polymer upon the addition of DIO, the coherence length is unchanged within the error, going from 4.1 nm for the pure polymer to 3.7 nm with DIO (Table A.1 of Appendix A).

We next examined the results of removing the DIO additive from the pure polymer films. Because it is detrimental to device performance, several groups have investigated removing DIO from BHJ active layers using techniques such as the application of high vacuum[81,82] or methanol washing.[78–82] In particular, Ye and co-workers showed that by monitoring the C–I stretch vibrations from DIO, both techniques can remove DIO from PBDTTT-C:PCBM BHJs with similar efficacy.[81] Here, we remove the DIO from our films via methanol washing, as this provides consistency between our GIWAXS and device active layer samples. For the pure polymer films, we found that methanol washing produced very little change in the structure of films cast with DIO as a solvent additive. The calculated Scherrer length of 3.8 nm is very close to that of the polymer film with DIO and still within the error of the pure polymer. Indeed, neither methanol nor the 2CP:DCM solvent blend that we used for casting the fullerene during SqP significantly changed overall the polymer crystallinity or chain orientation (see Figure A.1 of Appendix A). We next determined the extent of the polymer chain orientation in the pure polymer films by directionally integrating the diffractograms. To look at the orientation, we took 10° integration slices in the out-of-plane (Figure 2.2b) and in-plane (Figure 2.2c) directions. By comparing the out-of-plane and in-plane peaks, it is apparent that the PBDTTT-C chains in pure films lie mostly face-on. The face-on orientation can be determined from the (010) π-π-stacking peak, which appears at 1.57 Å^{-1} in the out-of-plane patterns. The high out-of-plane intensity relative to the in-plane intensity is indicative of a face-on chain orientation. We note that the relative (010) peak intensity is a better measure of chain orientation than the relative (100) peak intensity because of interference from the specular reflection in the (100) peaks. Although we always subtract the specular reflection away before integration, its intensity varies with surface roughness, so perfect background subtractions are not always possible. We note that for all samples, the in-plane (010) peak is much broader than the out-of-plane peak and is dominated by a shoulder shifted to lower q (centered at about 1.3 Å^{-1}). The shoulder indicates the presence of some disordered, edge-on polymer chains that have a significantly larger π-π-stacking distance. Thus, although the chains in the pure film are not perfectly face-on oriented, the data show that PBDTTT-C films do have an excess of face-on domains and that those face-on domains appear to be more ordered.

The orientation of the pure polymer chains is mostly maintained upon addition of DIO, whose

dominant effect is to produce an increase in overall crystallinity, as observed in Figure 2.2b. This increase in crystallinity is likely due to the slower drying kinetics with DIO, since its low vapor pressure causes it to remain in the film.[86] Some decrease in face-on orientation is also observed with DIO addition as indicated by the relative increase in the in-plane (010) scattering intensity. No significant additional changes are observed upon removing the DIO with methanol. Overall, these data suggest that pure PBDTTT-C, without additives, is the most promising candidate for devices that require a face-on polymer orientation but that DIO-containing films still show a significant fraction of face-on polymer chains for such applications.

2.2.1.2 Polymer Orientation in Blend-Cast PBDTTT-C BHJs with PCBM

Now that we have an understanding of the chain conformation in pure PBDTTT-C films, we turn to assessing whether or not this orientation is maintained during blend-casting with PCBM. The fully integrated diffractograms for blend-cast BHJs are shown in Figure 2.3a, which can be compared to the pure polymer patterns in Figure 2.2a. The data show both the (100) lamellar polymer diffraction at 0.36 $Å^{-1}$ and several $PC_{71}BM$ scattering peaks located at 0.66, 1.34, and 1.89 $Å^{-1}$. In addition to increasing the polymer crystallinity, the use of DIO as a solvent additive in BC devices also decreases the lamellar (100) polymer peak width, indicating the formation of larger crystalline PBDTTT-C domains.(49,62) Indeed, the calculated coherence length increases from 2.4 to 3.9 nm upon the addition of DIO to the BC film without a significant change in overall crystallinity. Increased domain size, up to a certain extent, can enable better hole conductivity through the polymer network and is likely partially responsible for the increase in current observed for the DIO-treated blend-cast BHJ devices, whose properties are discussed below.

Unlike the case for the pure polymer films, we do see significant changes in the scattering from DIO-containing blend-cast BHJ films upon washing with methanol. After methanol washing, we are left with higher overall crystallinity and similar Scherrer domain sizes of 3.1 nm. Further, methanol washing causes a significant increase in the fullerene crystallinity as seen by the increase in the intensity of the peak centered at about 1.3 $Å^{-1}$ in Figure 2.3a. The removal of DIO with methanol washing clearly enables the polymer:fullerene system to pack better and form more crystalline

domains, creating a better overall bicontinuous BHJ network. We note that in addition to removing the DIO, the methanol wash likely also removes any residual blend-casting solvent. This conclusion is based on the fact that methanol washing a blend-cast film without any DIO additive (shown in Figure A.2, Appendix A) also produces a slight increase in fullerene crystallinity, though this increase is to a much smaller extent than in BHJ films prepared with DIO.

We also compared the in-plane and out-of-plane diffraction of our blend-cast BHJs to determine the average polymer domain orientation, as plotted in Figure 2.3b,c. In these panels, we see a large out-of-plane (100) lamellar-stacking peak with a correspondingly much smaller in-plane lamellar diffraction. This suggest that the PBDTTT-C polymer in blend-cast BHJs has an orientation that is more edge-on or isotropic, rather than mostly face-on, as observed for the pure polymer. Because of potential interference form the specular reflection, however, it would make sense to confirm this conclusion using the (010) diffraction peak. Unfortunately, the (010) π-π-stacking peak in these BHJs is largely obscured by the presence of the strong, isotropic fullerene scattering centered at 1.34 $Å^{-1}$. For the sample with DIO, the (010) peak is observed as a small shoulder, but the intensity in both samples is too small for quantitative analysis. To extract the (010) π-π-stacking peak from the fullerene peak, we took a 10° radial segment from the diffractogram centered at 45°, which contains scattering from any peaks with an isotropic orientation. Since the fullerene diffraction is isotropic, we subtracted the 45° segment from both the out-of-plane and in-plane data in Figure 2.3b,c, respectively. This procedure should leave only the nonisotropic polymer diffraction. The results of this subtraction procedure are shown in Figure 2.3d, where we see that the (100) lamellar peak for the blend-cast film now lies entirely out-of-plane. This indicates that no polymer domains show a preference for face-on orientation and that indeed most of the blend-cast sample is isotropic.

We next focus on the (010) π-π-scattering region; here, the subtracted data are quite complex. In the in-plane direction, little nonisotropic scattering is observed. In the out-of-plane direction, by contrast, we see a derivative-shaped peak. The negative intensity of this peak indicates a lack of face-on oriented polymer chains relative to the isotropic scattering, and the overall derivative shape indicates that those chains that do orient face-on have a slightly different lattice spacing than the isotropic chains. As discussed above, we frequently observe this trend with a smaller π-stacking distance in face-on chains that are flattened by interaction with the substrate. The combination of

increased out-of-plane lamellar diffraction and decreased out-of-plane π-stacking intensity thus indicates that for blend-cast films without DIO, the polymer no longer has a net face-on orientation.

Finally, we can compare the blend-cast BHJ films with and without the DIO additive. When DIO is used in the casting solution, the (100) lamellar peak intensity increases in both the in-plane and out-of-plane directions, indicating greater overall crystallinity, as discussed above. A small out-of-plane (010) peak can also be seen between the two fullerene diffraction peaks at $\sim$1.6 Å^{-1}, which was not visible in the blend-cast sample without DIO. The existence of this out-of-plane (face-on) (010) peak is confirmed in the 45°-subtracted curve, which again shows no signal in the in-plane direction, but now shows some positive intensity in the out-of-plane direction (Figure 2.3c). This indicates a slightly larger population of a face-on oriented polymer chains for the films cast with DIO. A loss of out-of-plane isotropic (010) scattering and an increase in face-on out-of-plane (010) scattering are also observed for methanol-washed samples, this time accompanied by a relative increase in the in-plane (100) scattering, indicating even further recovery of the face-on orientation in the methanol washed samples and the highest overall crystallinity out of all our conditions. The recovery of face-on orientation and increased coherence length, in combination with the increased overall crystallinity, explains the higher current and increased overall performance observed in blend-cast devices made with DIO (removed by methanol washing) as discussed in more detail below.

2.2.1.3 Polymer Orientation in Sequentially Processed PBDTTT-C BHJs with PCBM

One goal in using naturally face-on oriented polymers is to be able to preserve the favorable polymer orientation in BHJ devices blended with fullerene. We have shown above, however, that the face-on morphology is not always well-preserved by blend-casting; the presence of fullerene during film formation can kinetically frustrate crystallization, leading to isotropic polymer orientation. The use of low-vapor-pressure solvents like DIO leaves the film wet with solvent for an extended period of time, partly alleviating the frustration. But an alternative to preserving face-on polymer domain orientation in BHJs is to use sequential processing, where a pure polymer layer is deposited first with a face-on orientation, and then, the fullerene is infiltrated in a second step using a solvent that

swells but does not dissolve the underlying polymer film. We have argued in previous work that SqP preserves much of the morphology of the original polymer film,[37,38,44,87,88] so it is entirely possible that the method could better preserve the native polymer orientation producing real differences in the net orientation of blend-cast and sequentially processed BHJs of the same materials.

Figure 2.4a shows radially integrated two-dimensional GIWAXS diffractograms for sequentially processed films with and without DIO additive in the polymer-casting solution. It should be noted that the PCBM concentration used for these films was 5 mg/mL, whereas the optimal PCBM concentration for sequentially processed photovoltaic devices is 10 mg/mL. The GIWAXS data for films made with 10 mg/mL PCBM are shown in Figure A.3 (Appendix A), where the large fullerene peaks with the high fullerene concentration make the analysis of these patterns difficult. The increased fullerene peak intensity is consistent with the fact that the optimized SqP device has a PBDTTT-C:$PC_{71}BM$ weight ratio of 1:3.5 (see Appendix A, Figure A.4), much higher than the BC ratio of 1:1.5. Therefore, we choose to analyze the GIWAXS data for the 5 mg/mL PCBM sequentially processed samples where the trends in the various peaks are easier to extract.

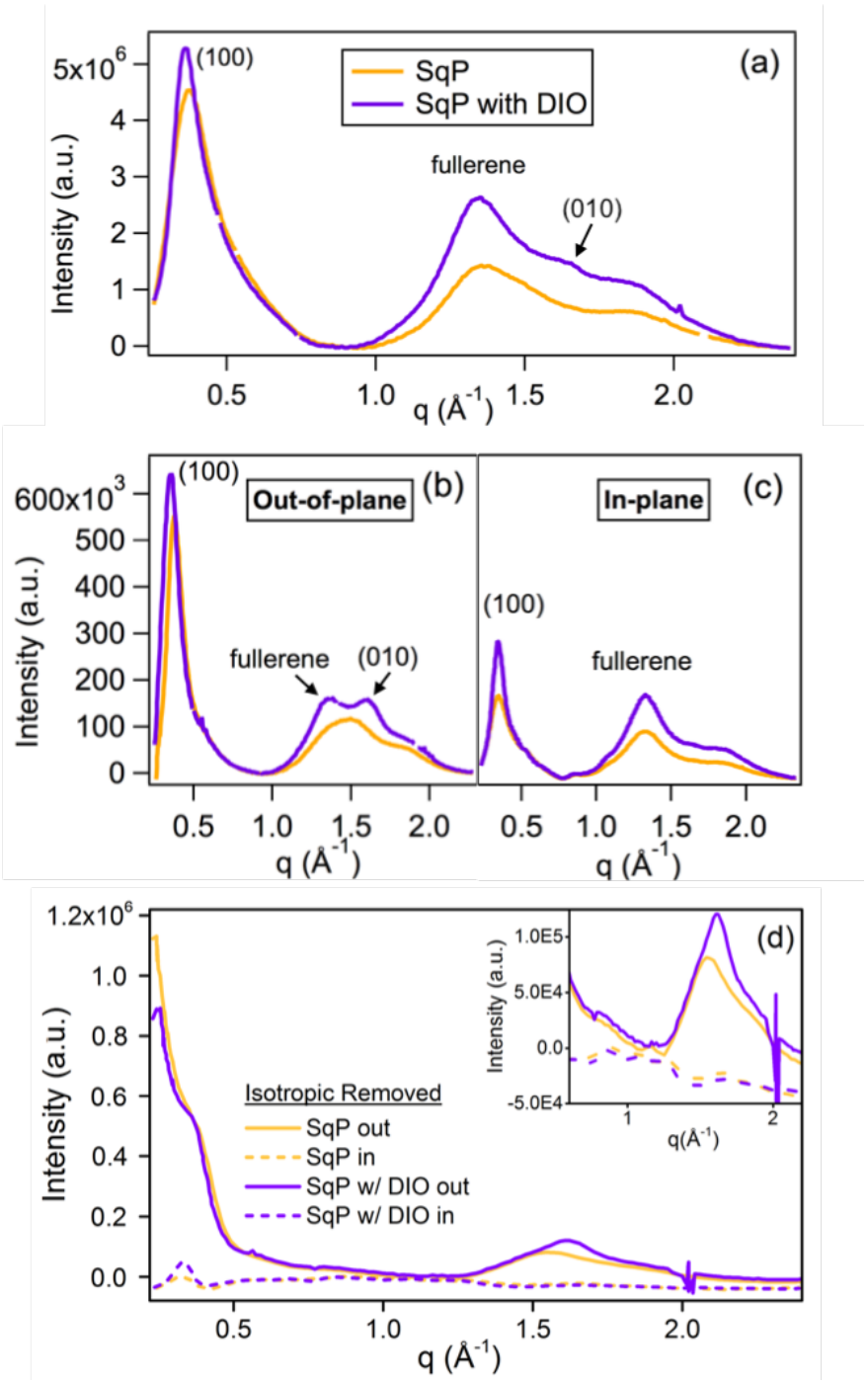

Figure 2.4: Figure 2.4. (a) Full integration of GIWAXS diffractograms for sequentially processed PBDTTT-C:PCBM films, where the orange curves have no additive, and the purple curves have 3% DIO in the polymer-casting solution. Despite the fullerene scattering, strong (010) diffraction can be seen in the out-of-plane scattering in part (b), but not in the in-plane scattering in part (c). Examination of the (010) scattering in (d) in both the out-of-plane and in-plane diffractions is again facilitated by subtraction of all isotropic scattering, which includes the fullerene diffraction. The inset in (d) is a zoom-in of the (010) polymer region and shows strong positive intensities in the out-of-plane direction, indicative of a face-on polymer chain alignment.

We note that in SqP, because the vapor pressure of DIO is low, if DIO is used in the polymer-casting solution, some of it remains in the film during the fullerene deposition stage. Figure 2.4a shows that the addition of DIO to the polymer-casting solution does not significantly change the overall crystallinity; however, it does increase the coherence length from 4.9 to 5.7 nm. Since the coherence lengths are larger than both the pure polymer films and the blend-cast BHJ films, we performed photoluminescence (PL) quenching experiments to verify that the sequentially processed films still were sufficiently mixed to provide good exciton harvesting. Figure 2.5 shows the PL of PBDTTT-C films fabricated via BC and SqP with and without DIO. The intensity was scaled by the polymer absorption at the excitation wavelength (see Figure A.5 in Appendix A), and the data show that in all cases, the BHJ films' PL is more than 90% quenched compared to pure PBDTTT-C. The PL data thus confirms that there is adequate polymer:fullerene mixing for BHJ films made via both processing methods despite the larger domain sizes obtained via SqP. In fact, Figure 2.5 shows that the blend-cast-with-DIO film has the most residual PL, which makes sense as it has the highest overall crystallinity (see Table A.1 of Appendix A).

The presence of DIO in the polymer-casting solution also causes an increase in the intensity of the $PC_{71}BM$ scattering peak centered at 1.34 $Å^{-1}$ as seen in Figure 2.4. This intensity increase suggests that DIO enables $PC_{71}BM$ to diffuse more easily into the polymer, which likely occurs because of the low vapor pressure of DIO,[67,75] resulting in some DIO remaining in the film under ambient conditions.[73] As a result, the film is still partially wet with DIO during the fullerene-casting step in SqP. Favorable mixing between DIO and the SqP-casting solvent then results in DIO-induced polymer swelling.[80] Increased solvent swelling during SqP either allows more fullerene to incorporate into the film or allows whatever fullerene that is present in the film to become more crystalline, both of which result in increased fullerene diffraction and could be beneficial for device performance.

In contrast to the blend-cast BHJ films, the in- and out-of-plane diffractograms for the sequentially processed BHJ films (Figure 2.4b,c) show more pronounced differences in scattering intensity. The data clearly show a (010) scattering peak (shoulder) in the out-of-plane direction but not in the in-plane direction for the sequentially processed films made both with and without DIO. The presence of this strong out-of-plane π-π peak means that PBDTTT-C in the sequentially processed

BHJs is far more face-on than in its blend-cast counterparts. There is also somewhat more (100) lamellar scattering intensity observed in the in-plane direction for the sequentially processed BHJs than was seen with the blend-cast BHJ films, consistent with a more face-on domain orientation.

Although the (010) polymer diffraction peaks can be seen in the sequentially processed samples, strong fullerene diffraction again makes quantitative analysis difficult, so as with the analysis above, Figure 2.4d shows the results of subtracting off the isotropic diffraction measured at 45°. Unlike the blend-cast films, where the subtraction led to a derivative shape, the sequentially processed PBDTTT-C:$PC_{71}BM$ BHJs instead show a distinct peak in the (010) region for out-of-plane scattering (inset of Figure 2.4d). Moreover, the (100) lamellar scattering in the sequentially processed BHJs shows more in-plane intensity than in the blend-cast samples, again indicating a more face-on orientation. Thus, in contrast to blend-cast BHJs, SqP-based devices have stronger face-on polymer orientation both with and without DIO, similar to pure polymer samples.

2.2.2 Device Performance of Blend-Cast and Sequentially Processed PBDTTT-C:$PC_{71}BM$ BHJs

To understand how all of the above structural observations affect actual device performance, we fabricated OPVs with blend-cast and sequentially processed PBDTTT-C:$PC_{71}BM$ active layers, without DIO, with DIO, and with DIO removed via methanol treatment; the results are summarized in Figure 2.6 and Table 2.1. To further correlate performance with variations in mobility as a result of changes in polymer orientation and degree of crystallinity, we fabricated hole-only diodes and fit the corresponding dark J–V curves to the space-charge-limited current (SCLC) model, yielding the hole mobilities listed in Table 2.2. Details of the fitting procedure and corresponding fits to the data are shown in Figure A.6 of Appendix A.

As has been observed in previous work,[70–72] the addition of DIO during blend-casting is necessary for optimal device performance. Our blend-cast photovoltaic device data fits with this expectation, as we observe an increase in overall power conversion efficiency from 4.4 to 5.0% upon the addition of 3% DIO by volume (Figure 2.6a and Table 2.1). The boost in efficiency arises from a slight improvement in the fill factor and a large improvement in the short-circuit current,

Table 2.1: Summary of J–V Characteristics[a] for the Devices Shown in Figure 2.6a

Device		Voc (V)	J_{sc} (mA/cm^2)	FF (%)	PCE (%)
Blend Cast	no DIO	0.775 ± 0.005	-12.7 ± 0.2	45 ± 4	4.4 ± 0.5
	with DIO	0.719 ± 0.004	-15.4 ± 0.4	46 ± 3	5.0 ± 0.4
	with DIO + MeOH wash	0.733 ± 0.005	-14.0 ± 0.5	61 ± 2	6.3 ± 0.3
Sequentially	no DIO	0.701 ± 0.006	-15.1 ± 0.6	59 ± 3	6.3 ± 0.4
Processed	with DIO	0.711 ± 0.003	-16.0 ± 0.8	56 ± 1	6.3 ± 0.2
	with DIO + MeOH wash	0.696 ± 0.005	-16.2 ± 0.6	55 ± 2	6.2 ± 0.3

[a]The device characteristics were averaged over 3 films (12 devices) and are presented with $\pm$ the standard deviation of each set of conditions.

Table 2.2: SCLC Hole Mobilities (μ_{hole})[a,b]

Active layer	μ_{hole} (cm^2/Vs)
Pure PBDTTT-C	$1.07(6) \times 10^{-3}$
Optimized SqP	$2.9(2) \times 10^{-4}$
Optimized BC	$1.26(8) \times 10^{-4}$
Blend Cast no DIO	$2.8(2) \times 10^{-5}$

[a]Representative active layers: pure PBDTTT-C, optimized SqP (without DIO), optimized BC (with DIO and MeOH wash), and BC without DIO.
[b]The results for the pure polymer and optimized blend-cast are in agreement with the literature.[67,72,89]

J_{sc}, from 12.7 to 15.4 mA/cm^2 for devices without and with DIO, respectively. Upon washing the blend-cast-with-DIO films with methanol, the PCE is further increased to 6.3%. These results fit well with the observed SCLC hole mobility increase from 2.8×10^{-5} cm^{2}V^{-1}s^{-1} in the blend-cast active layer to 1.26×10^{-4} cm^{2}V^{-1}s^{-1} in the optimized blend-cast films with DIO and subsequent methanol wash. On the basis of the scattering data in Figures 1 and 3, we associate the improvement in mobility when DIO is added to a combination of increased polymer face-on orientation and an increase in domain size. DIO removal further causes an increase in crystallinity and more favorable rearrangement of the fullerene, as discussed above, and also eliminates any detrimental effects DIO might have on device performance.[80–82]

Although we expected an increase in PCE with the use of DIO for blend-cast systems, surprisingly, we see similarly high PCEs for devices fabricated via SqP, both with and without DIO. Without the use of any additives, SqP produces a higher J_{sc} than the optimized blend-cast devices, which is verified by the external quantum efficiency (EQE) measurements shown in Figure 2.5b; the EQE curves, when integrated, yield the measured short-circuit currents to within a few percent. We note that a similar improvement in J_{sc} with SqP compared to BC has been seen with a related polymer, PBDTTT-C-T.[34] In the case of PBDTTT-C-T, however, the J_{sc} improvement was attributed to improved vertical phase separation with SqP rather than to changes in the polymer domain orientation, as we postulate here. The higher J_{sc} for SqP devices is consistent with the higher hole mobility expected through the stacked π-conjugation. Indeed, the SCLC hole mobility for the optimized SqP active layer (without DIO) is 2.9×10^{-4} $cm^2V^{-1}s^{-1}$, an order of magnitude higher than that of the blend-cast device without DIO and more than twice that of the optimized blend-cast device (with DIO and methanol wash). Since the overall crystallinity is lower in the SqP device compared to the optimized BC, the mobility improvement can be assuredly attributed to polymer orientation effects.

In contrast to the blend-cast films, neither the addition of DIO to the polymer layer nor subsequent methanol washing has a significant effect on the overall performance of sequentially processed devices. As discussed above, the addition of DIO to the polymer-casting solution for SqP devices does lead to slightly larger domain sizes, but the Scherrer domain sizes and extent of face-on orientation remain relatively unchanged, in sharp contrast to the role of DIO in blend-cast devices. The lack of appreciable change in the PCE indicates that this slight increase in fullerene content and/or crystallinity with DIO is not important for device performance. Furthermore, methanol washing is no longer necessary, as it has no significant effect on the device performance, likely because the solvent blend used in the SqP step already washes any excess DIO out of the active layer. Thus, sequentially processed devices do not need processing additives (or a subsequent methanol wash) to match the optimized 6.3% PCE of the blend-cast system, which requires both DIO and a subsequent washing step. Given that all BHJ morphologies are adequately mixed and that the overall crystallinity is lower in sequentially processed samples than in blend-cast devices, the preservation of the face-on orientation of PBDTTT-C in sequentially processed films must be

the main contributor to performance enhancements.

2.3 Conclusions

In this work, we have shown that the face-on orientation of pure PBDTTT-C films is not preserved when standard blend-casting techniques for creating polymer:fullerene BHJs are employed. Although PBDTTT-C shows a preferred face-on orientation in pure films, regardless of the presence of any solvent additive, the interactions of the polymer with $PC_{71}BM$ appear to dominate over polymer–substrate interactions, leading to a loss of the natural face-on polymer orientation upon blended film formation. The addition of DIO helps to restore the face-on tendency of the domains in this material when blend-casting.

By producing BHJ devices from PBDTTT-C using sequential processing, however, the face-on orientation of the pure polymer film can be preserved even without additives. Sequential processing thus enables us to translate pure polymer properties into blended BHJ devices. The benefits of preserving the face-on polymer orientation are seen in improved hole mobility and overall device performance. Face-on orientation enables more efficient hole conduction through the polymer π-system, yielding a higher J_{sc} in OPV devices. Overall, even though the final device performance for this polymer:fullerene combination is similar for blend-cast and sequentially processed devices, the structure of the polymer in the two devices is quite different. We note that although the focus of this work is on the preservation of optimized polymer chain orientations using solvent additives or SqP, an interesting corollary is the observation of the remarkable flexibility of the BHJ morphology: we see that there are a wide range of underlying BHJ architectures that can lead to good device performance, which perhaps explains why the BHJ concept works so well in the first place.[37] In the PBDTTT-C blend-cast system, we see higher overall crystallinity but smaller crystalline domains, whereas SqP produces BHJs with lower overall crystallinity but domains that are larger and more face-on oriented. When optimized, both techniques can lead to good device performance.

Overall, our work emphasizes that these two distinct processing methods for creating OPV active layers can be used to enhance different aspects of polymer structure and nanoscale morphology. By adding SqP alongside BC with solvent additives to the OPV processing toolbox, researchers

now have a larger variety of ways to robustly and reproducibly tune both polymer crystallinity and domain orientation in semiconducting polymer OPV devices.

2.4 Supporting Information Available

See Appendix A for details of device fabrication including electrode deposition, summary table of parameters from GIWAXS, 2D GIWAXS diffractograms, BC redissolved film absorbance, all film absorbance, dark J–V curves with details of SCLC fits for extracting hole mobilities, J–V curves with DIO in different steps of the SqP process.

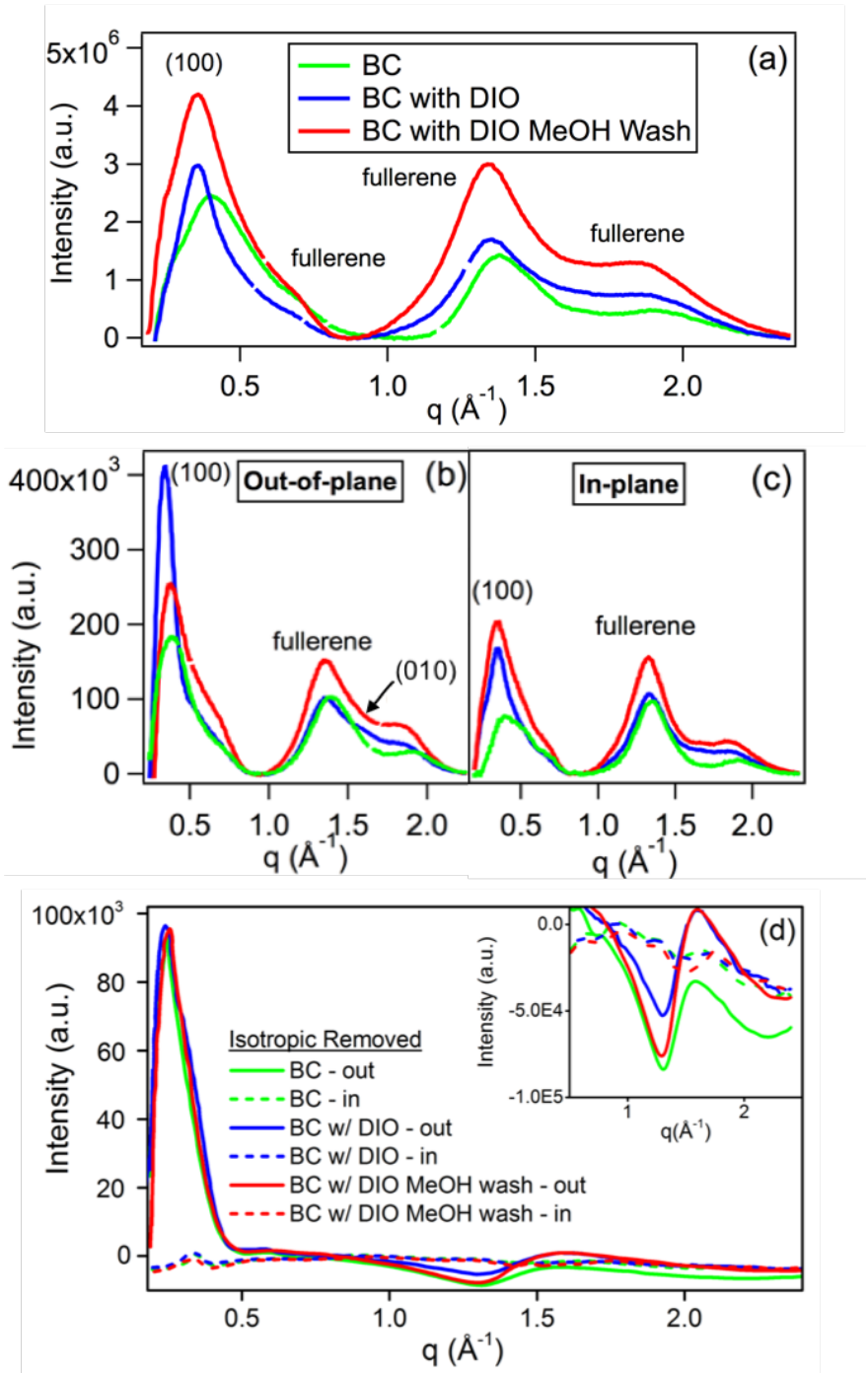

Figure 2.3: (a) Full integrations of GIWAXS diffractograms for 1:1.5 PBDTTT-C:PCBM blend-cast films without DIO (green), with 3% DIO (blue), and methanol washed (red). The films appear to show a preference for an edge-on polymer chain orientation, as seen by the strong (100) scattering in the (b) out-of-plane direction but not in the (c) in-plane direction. Examination of the (010) scattering in (d) in both the out-of-plane and in-plane diffractions is facilitated by subtraction of all isotropic scattering, which includes the fullerene diffraction. The inset in (d) is a zoom-in of the (010) polymer region and shows negative intensities in the out-of-plane direction, which again indicates a lack of face-on polymer chains.

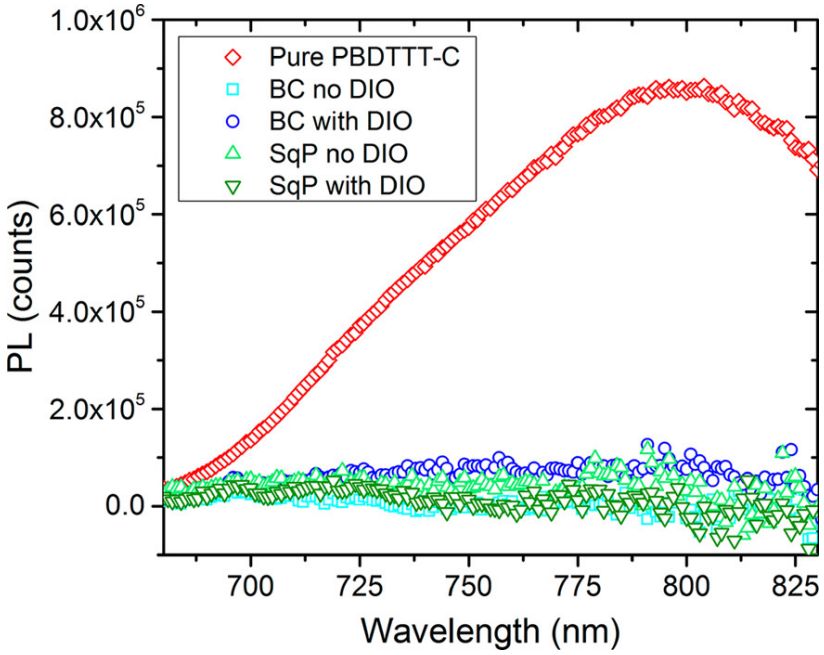

Figure 2.5: Photoluminescence of pure PBDTTT-C (red squares) as well as BHJ films made via BC with DIO (dark blue circles) and without DIO (light blue squares), SqP with DIO (dark green down triangles) and without DIO (light green up triangles). A methanol wash was performed to remove the DIO in the BC case, while in SqP, we rely on the SqP solvents to remove the DIO. The PL intensities have been normalized by the polymer optical density at the excitation wavelength (630 nm, see Appendix A Figure A.5). All of the BHJs are well-quenched, indicating the domains in the films are well-mixed.

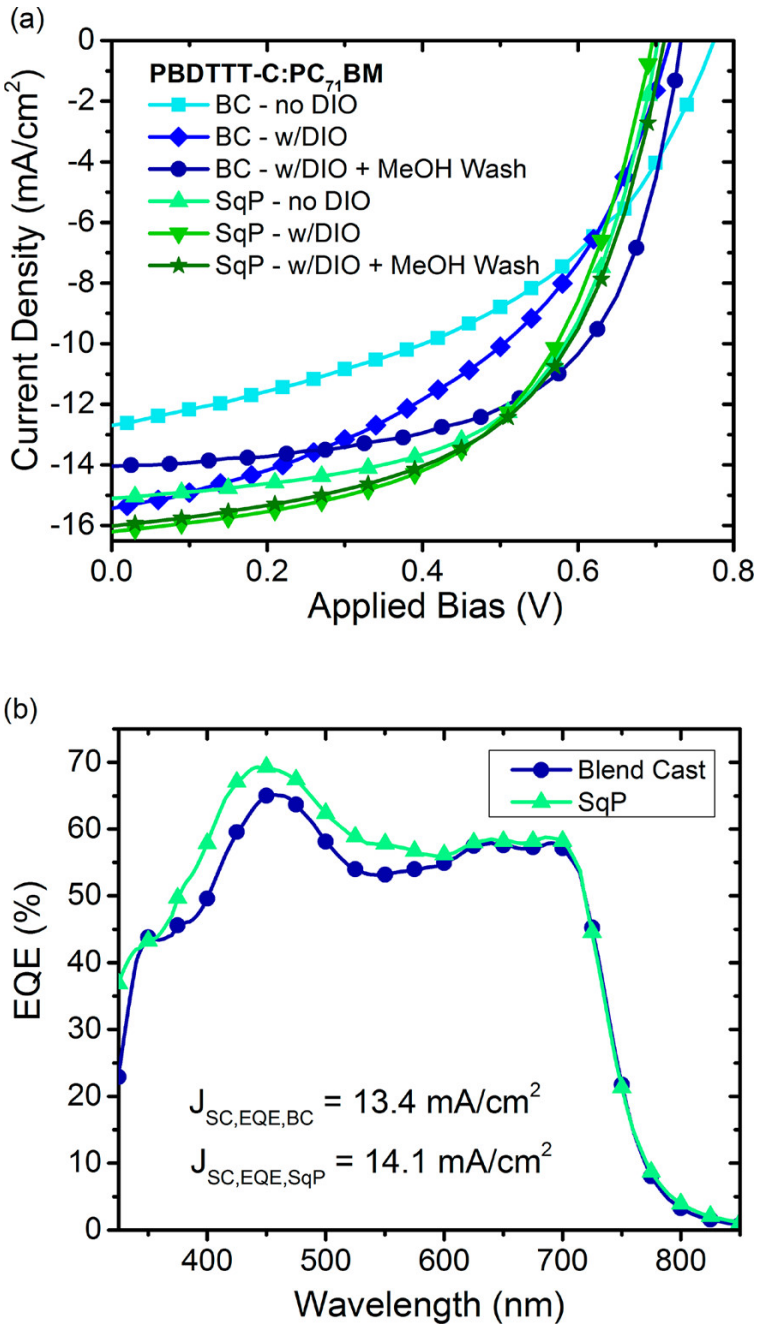

Figure 2.6: (a) J–V device curves for blend-cast films without additives (light blue squares) and with 3% v/v DIO (blue diamonds). Additional improvement is seen with methanol washing the DIO films (dark blue circles). Sequential processing without the use of additives (light green triangles) shows improvement over the blend-cast films, mainly due to J_{sc} improvement. SqP devices fabricated with 3% v/v DIO (green down triangles) and, subsequently, MeOH washed (dark green stars) are similar in performance to SqP devices without additives. All devices have the structure: ITO/PEDOT:PSS/PBDTTT-C:PC_{71}BM:Ca/Al. (b) External quantum efficiency (EQE) for optimized blend-cast (w/DIO + MeOH wash) and sequentially processed films (no additional processing), showing higher obtainable current with SqP.

CHAPTER 3

Dodecaborane-based Dopants Designed to Shield Anion Electrostatics Lead to Increased Carrier Mobility in a Doped Conjugated Polymer

3.1 Introduction

Creating electrical carriers by doping in a controlled fashion enables semiconductors to be used in a wide variety of optoelectronic applications. Indeed, doped conjugated polymers are found in commercially-available organic light-emitting diode (OLED) displays,[90] used to enhance organic solar cells[91] and field-effect transistors,[28] and are receiving increased attention for thermoelectric applications.[92–97] Doping of conjugated polymers can be achieved by electrochemical[98] or electrical charge injection[99] methods, but chemical doping is the best method to produce stable carriers without the need for a continuously applied potential. Chemical doping involves the introduction of a strong electron acceptor (oxidizing agent, for *p*-type doping) or a strong electron donor (reducing agent, for *n*-type doping) that can undergo a charge transfer reaction with the polymer,[100] creating charge carriers on the polymer chain while the dopant molecules remain in the film as counterions. Most conjugated polymers are *p*-type semiconductors, with positive carriers (holes, often referred to as polarons) created by oxidizing dopants.

Some of the earliest molecular dopants for conjugated polymers were halogen vapors,[100] but the instability of the doped films produced this way has led to the design of more stable molecular dopants.[101] One of the most popular molecular dopants for conjugated polymers is 2,3,5,6-tetrafluoro-7,7,8,8-tetracyanoquinodimethane (F_4TCNQ);[87,88,92–97,102–108] see Fig. 3.1a (red) for chemical structure. F_4TCNQ has a low-lying LUMO, (-5.2 eV vs. vacuum)[109] giving it

the ability to *p*-dope a wide variety of conjugated polymers, including poly(3-hexylthiophene-2,5-diyl) (P3HT), whose chemical structure is shown in in Fig. 3.1a (green). Unlike doped inorganic semiconductors, where the interactions of substitutional impurities with the generated charge carriers are screened, the majority of the doping-induced carriers in conjugated polymers remain Coulomb-bound to the dopant counterions due to the low permittivity of organic materials.[102–104] For P3HT doped with F_4TCNQ, it has been estimated that even though the majority of F_4TCNQ molecules undergo integer charge transfer with P3HT, 95% of the holes that are created remain bound to their counterions[102] and thus do not contribute to electrical conduction. Indeed, strong electrostatic interactions between polarons and their counterions are known to localize polarons and reduce their mobilities.[87]

To overcome this issue of carrier localization, in this work we describe a perfunctionalized dodecaborane cluster that was designed to spatially separate the anions created when doping conjugated polymers. Dodecaborane (DDB) clusters are robust and kinetically stable due to their 3-dimensional aromaticity, which allows for electron delocalization around the boron scaffold.[110–114] Certain perfunctionalized clusters of the type $B_{12}(OR)_{12}$ (R = alkyl, aryl, H) behave as reversible, redox-active species with multiple accessible oxidation states.[113–117] Recent advances have led to the rational and rapid synthesis of such substituted dodecaboranes with tunable redox potentials.[115] We have designed a DDB cluster with a very high ground-state redox potential, which when combined with the cluster's intrinsic stabilization of electron density in its well-shielded core, makes it an outstanding candidate to molecularly dope conjugated polymers.

The conventional processing method to dope polymeric semiconductors, known as blend doping, involves mixing the polymer and dopant in solution prior to casting the doped polymer onto a substrate. The solvents for most conjugated polymers, however, are non-polar, such that at high doping levels the charges produced on the polymer and dopant render them insoluble during solution processing, yielding very poor doped film quality. This problem has been overcome by sequential doping,[87,88,93–97,105–108,118,119] which relies on exposing a pre-cast polymer film to the dopant, either in the vapor phase[93–96,106,108,118,119] or in solution.[88] Solution sequential processing uses a semi-orthogonal solvent to swell but not dissolve the polymer underlayer, allowing mass action to drive the dopant into the swollen polymer film.[87,88,93,94,96,97,105–107] Doping by solution sequential

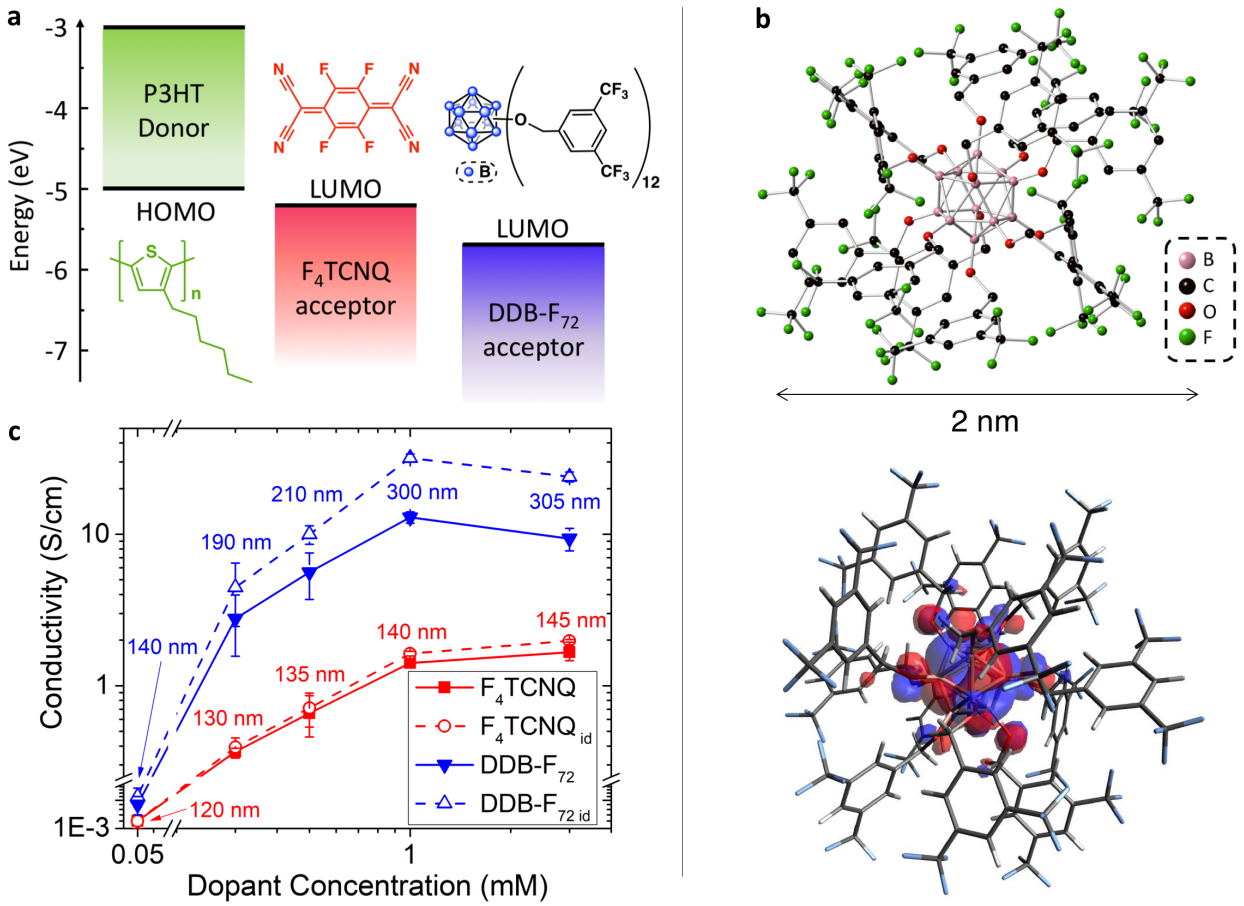

Figure 3.1: (a) Chemical structures and schematic energy diagram of P3HT, F_4TCNQ, and DDB-F_{72} showing ∼0.5 V greater offset for DDB-F_{72} than F_4TCNQ. (b) (top) X-ray crystal structure of DDB-F_{72}; (bottom) DDB-F_{72} anion SOMO calculated by TD-DFT showing the electron localized on the DDB core. (c) Conductivities (solid symbols, calculated using the measured thickness) and idealized conductivities (open symbols, calculated using the 120-nm original thickness) of P3HT films doped with F_4TCNQ (red symbols) and DDB-F_{72} (blue symbols) via solution sequential doping. The error bars are the standard deviation calculated from at least three samples. At the same dopant concentration DDB-F_{72} produces conductivities that are an order of magnitude higher than those produced by F_4TCNQ.

processing (SqP) maintains all of the advantages of solution-based processing methods, producing high-quality films with conductivities that are significantly better than those produced by blend doping.[88,105] We expect that SqP should be amenable for use with dodecaborane clusters given that it is routinely used to infiltrate large molecules such as fullerenes and large dopants into films of conjugated polymers.[37,44,120–122]

Here, we report the use of a newly-synthesized, strongly-oxidizing perfunctionalized DDB cluster as a dopant for the conjugated polymer P3HT. The chemical structure of our new cluster,

shown in Fig. 3.1a (blue), depicts the pseudo-icosahedral dodecaborane core with each vertex functionalized with a 3,5-bis(trifluoromethyl)benzyloxy substituent. We refer to this molecule as DDB-F_{72} because of the 72 electron-withdrawing F atoms placed on the periphery of the cluster. Using SqP to dope identical films of P3HT with both DDB-F_{72} and F_4TCNQ, we find that at equimolar doping concentrations, DDB-F_{72} produces doped films with conductivities that are an order of magnitude higher. We verify using NMR spectroscopy techniques that there is negligible electron transfer between DDB-F_{72} clusters, so that the conductivity improvement we see comes solely from the increased mobility of polarons on the conjugated polymer.

To understand this increased conductivity, we structurally characterize our doped polymer films by using X-ray Photoelectron Spectroscopy (XPS) and 2-dimensional grazing-incidence wide-angle X-ray scattering (2D-GIWAXS) to show that DDB-F_{72}-doped P3HT films are remarkably non-crystalline, likely due to the fact that the DDB cluster cannot intercalate into the crystalline polymer domains due to its large size. This is in sharp contrast to dopants such as F_4TCNQ, which reside within the polymer crystallites[87,97] in closer proximity to the polarons. In addition to residing farther from the polymer crystallites, the steric footprint associated with DDB-F_{72}'s peripheral substitutions, in combination with the delocalization of the unpaired electron within the shielded boron cluster core, allows for greatly reduced electrostatic interactions between DDB-F_{72} anions and the holes on the polymer chains.

With this reduced electrostatic interaction, we show using combination of AC Hall effect and IR spectroscopy measurements that the polarons on P3HT doped with DDB-F_{72} have mobilities that are an order of magnitude higher than those created by doping with F_4TCNQ; the carrier mobilities with DDB-F_{72} are comparable to those created by charge modulation with no anions present at all.[99] We calculate idealized conductivities in our DDB-F_{72}-doped P3HT films of 32 S/cm, despite the lack of crystallinity in our doped material. These findings highlight the importance of polaron delocalization effects and the corresponding need to electrostatically screen the anion from the holes. Reducing the polaron/counterion Coulomb interaction is clearly important for electrical conduction. We suspect the reason that high crystallinity is important with dopants such as F_4TCNQ is also to reduce the Coulomb interaction by placing the dopant counterion into a precise location in the polymer crystallite far from the polymer backbone where the polaron resides. Even though F_4TCNQ

enters the crystallite, it still resides in the lamellar regions a distance away from the backbone. By contrast our tailored DDB dopants are so large that they can only infiltrate amorphous regions, but electrostatic shielding is taken care of by the dopant itself so that polymer crystallinity is no longer required.

3.2 Results & Discussion

We chose P3HT for this study as it is a model conjugated polymer that has become an important reference material for the study of optoelectronic processes in organic semiconductors. The offset between the HOMO of the polymer and LUMO of the dopant gives the energetic driving force for doping via integer charge transfer.[102] Figure 3.1a shows these energy levels for P3HT, F_4TCNQ, and DDB-F_{72} based on cyclic voltammetry (CV) measurements of the dopants (see Figure B.6 of Appendix B) and literature values for P3HT.[123] Our CV measurements indicate a 0/1- redox potential of 0.16 V vs. F_c/F_c^+ for F_4TCNQ, in excellent agreement with literature values.[124] The redox potential of DDB-F_{72} is 0.67 V vs. F_c/F_c^+, thus producing a 0.5 eV greater energetic driving force for doping compared to F_4TCNQ.

The X-ray crystal structure of DDB-F_{72} is shown in Fig. 3.1b (top) (see the SI online for CIF file). The diameter of DDB-F_{72} is approximately 2 nm, nearly twice that of a C_{60} molecule. The B_{12}-based core lies deep in the center, surrounded by the corona of twelve bulky substituents, so if the additional unpaired electron on the reduced cluster is confined to the core as expected,[115,117] we should be able to achieve increased spatial separation of the electron from the polaron. Indeed, our TD-DFT calculations reveal that the SOMO of the DDB-F_{72} anion is delocalized only on the core, as shown in Fig. 3.1b (bottom).

To dope conjugated polymer films via SqP, we started by spinning 120-nm-thick P3HT films out of 1,2-dichorobenzene at 1000 rpm for 60 seconds. We then spun the dopant (F_4TCNQ or DDB-F_{72}) out of solutions with different concentrations in dichloromethane (DCM) at 4000 rpm for 10 seconds on top of the pre-cast polymer film. We measured the electrical conductivity of the doped films using the Van der Pauw method,[125] a type of four-point-probe measurement, with the electrodes placed at the corners of a 1.5 cm $\times$ 1.5 cm square (see Appendix B for details). The

results are shown in Fig. 3.1c.

The filled points/solid curves in Fig. 3.1c show that for the same molar concentration of dopant, the conductivities of P3HT films doped with DDB-F_{72} (blue down-pointing triangles) are about an order of magnitude higher than the F_4TCNQ-doped samples (red squares). For example, at 1 mM dopant concentrations we achieve P3HT conductivities of 12.9 S/cm when doped with DDB-F_{72} but only 1.4 S/cm when doped with F_4TCNQ. We were unable to explore SqP doping concentrations higher than a few mM because of the solubility limit of both dopants in DCM. The drop in conductivity observed for 3-mM DDB-F_{72} solutions is due to their colloidal nature, which is above the molecular solubility limit; the colloidal solutions do not effectively deliver dopant in the P3HT film, as documented in the spectroscopy section of Appendix B. The DDB-F_{72} doped films are stable under inert atmosphere for days (see Appendix B), suggesting the films would remain stable indefinitely if packaged appropriately.

One interesting feature of SqP is that so much of the large DDB-F_{72} dopant can be intercalated that the polymer films change thickness after doping.[37] Starting with 120-nm-thick pre-cast P3HT films, we find that doping with a 1-mM solution yields 140-nm-thick films doped with F_4TCNQ but 300-nm-thick films doped with DDB-F_{72}. Since SqP relies on swelling of the polymer followed by infiltration of the dopant into the swollen polymer matrix,[44] we worried about whether or not DDB-F_{72} was fully penetrating into the P3HT film. Given the large size of the DDB-F_{72} molecule and that fact that some large dopants in have shown limited film penetration in previous work,[126] it is possible that the large increase in thickness we observe results from an overlayer of excess DDB-F_{72} on top of the P3HT film rather than uniform intercalation throughout the film.

To investigate the penetration of the dopant into the film, we used XPS, which has a penetration depth of only a few nm, to examine the oxidation state of boron near the top surface of the film. Figure 3.2 shows the B 1s XPS spectra of both the neutral DDB-F_{72} cluster (black curve) and the DDB-F_{72} anion (red curve), along with one of our DDB-F_{72}-doped P3HT films (blue curve). The data make clear that the boron on the top surface of our films is reduced, suggesting that there is no excess overlayer of neutral clusters on top of the film, and that the clusters have indeed penetrated well into the P3HT layer. Further evidence that there is no continuous cluster overlayer is that XPS is able to pick up considerable signal from the sulfur of P3HT on the top surface of this doped film

(see Table B.4 in Appendix B). In addition, we imaged the top surface of the films using both optical and scanning electron microscopies (SEM) (see Figs. B.9 and B.10 of Appendix B). In the optical images, we see sparse crystallites of DDB-F_{72} that certainly do not form a contiguous overlayer. The SEM images reveal a sharp crack pattern, which we attribute as resulting from the expansion and contraction of the film upon swelling and deswelling during the SqP process.

To further our understanding of the degree of cluster penetration, we also examined the elemental composition of both the top and bottom surfaces of our DDB-F_{72}-doped P3HT films using XPS; we accessed the bottom surfaces by floating doped films off the substrate,[37] as described in more detail in Appendix B. Since sulfur is unique to P3HT while boron and fluorine are unique to DDB-F_{72}, the sulfur 2p:boron 1s and sulfur 2p:fluorine 1s peak-integrated ratios, shown in the inset to Fig. 3.2, give a good measure of the film composition at each surface. The data make clear that the B:S and F:S ratios on the top and bottom of the DDB-F_{72}-doped films are similar, suggesting that the clusters are roughly evenly distributed throughout the film. Indeed, recent work has shown that other fairly large dopant molecules also are able to penetrate well into pre-cast P3HT films.[121] Moreover, the XPS peak position for boron on both the top and bottom film surfaces indicate the cluster is reduced throughout the film (see Appendix B for detailed XPS peak fit assignments and additional information).

It is important to note that the calculation of electrical conductivity from the measured sheet resistivity scales inversely with the thickness of a material. Given the large thickness change of our DDB-F_{72}-doped films, this makes the conductivities we measure all the more remarkable because electrical conduction takes place only on the polymer, but polymer comprises only $\sim$1/3 of the material in the DDB-F_{72}-doped films. To verify the conduction mechanism, we investigated the kinetics of electron self-exchange between $[\text{DDB-F}_{72}]^0$ and $[\text{DDB-F}_{72}]^{-1}$ by dynamic NMR line broadening experiments, described in more detail in Appendix B. Using ^{19}F NMR across a range of 40 °C, we observed no coalescence of the peaks corresponding to the neutral and anionic forms of DDB-F_{72} in solution, indicating an electron self-exchange rate slower than that of the experimental timescale ($k_{ET} < 1.2 \times 10^3$ s^{-1} or $\tau_{ET} > 0.84$ ms), which is orders of magnitude longer than the typical collision time between clusters. This indicates that there is a high intrinsic barrier to electron transfer between DDB-F_{72} clusters, most likely the result of small electronic couplings due to poor

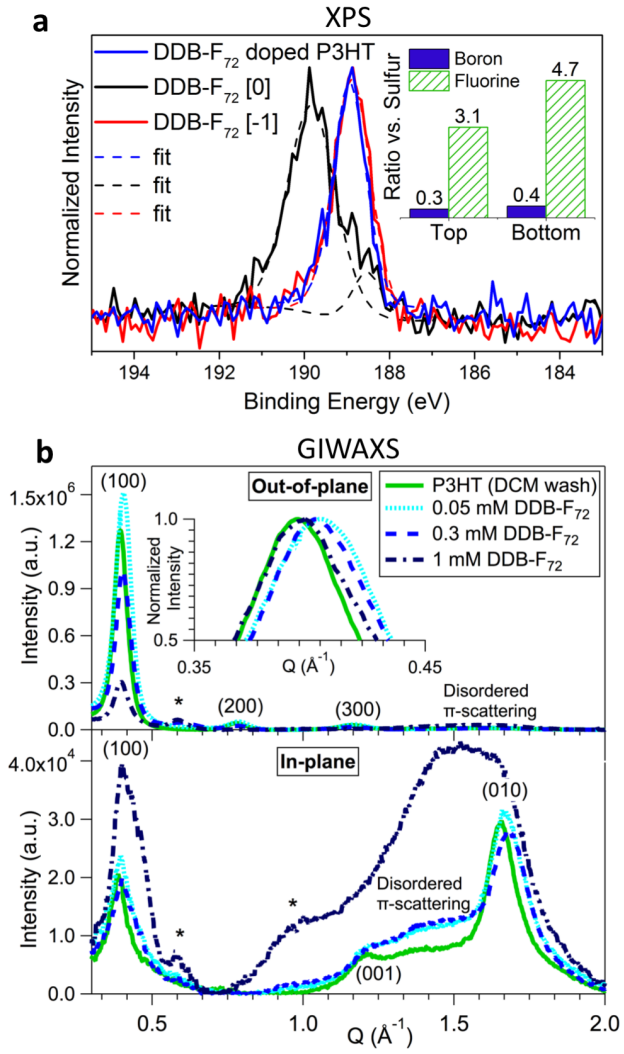

Figure 3.2: Structural characterization of DDB-cluster-doped films. (a) B 1s XPS spectra of the top surface of pure DDB-F_{72} films in the neutral [0, black curve] and anionic [−1, red curve] states, overlaid with that of a DDB-F_{72}-doped P3HT film (blue curve). The overlap of the doped film and anion spectra indicates that the clusters at the top surface of the film are all reduced. (inset) XPS-determined B:S and F:S ratios measured at the top and bottom of DDB-F_{72}-doped P3HT films indicating clusters penetrate the film. (b) Out-of plane (top) and in-plane (bottom) 2D-GIWAXS spectra for films of pure P3HT (green curves) and DDB-F_{72}-doped P3HT (blue curves). (inset) Zoomed in view of the (100) peak. Dopant-induced peaks are denoted by asterisks (*). These data indicate DDB-F_{72} does not enter the crystallites given its large size and at high dopant concentration (dark blue dash-dotted curves), there is significant loss of overall crystallinity.

orbital overlap between self-exchanging pairs.[127–129] Indeed, the idea of poor electron transfer between DDB clusters is in agreement with our DFT calculations in Fig. 3.1b, which show strong localization of the electron in the cluster interior, likely due to stabilization from the aromaticity of the B_{12} cluster. Overall, our NMR measurements strongly imply that electron hopping between

DDB clusters does not occur on any reasonable timescale, and therefore the electrical conduction of our doped films takes place only through the polymer network.

Given that the doped films are 300-nm thick but that there is only an initially 120-nm thickness of polymer material in the doped film to conduct, we calculated “idealized conductivities" based on the initial polymer thickness of 120 nm rather than using the measured doped film thickness. These idealized conductivities, which represent the limit of conductivity that could be achieved with the same carrier mobility if there were no swelling of the film during doping, are shown by the dotted lines and open symbols in Figure 3.1c. The difference between the idealized conductivity and the conductivity is larger for the DDB-F_{72}-doped films due to their larger thickness increase. At the 1-mM dopant concentration, we achieve idealized conductivities of $\sim$32 S/cm for the DDB-F_{72} doped films, whereas the idealized conductivity of F_4TCNQ-doped films reaches only 2.0 S/cm.

To better understand the structure of our DDB-F_{72}-doped films, we used 2-D GIWAXS. Figure 3.2b shows the out-of-plane (top) and in-plane (bottom) scattering patterns of P3HT (green solid curves) and P3HT doped with DDB-F_{72} from low-to-high concentration (light-to-dark blue curves). As expected for pure P3HT, which is well known to have a preferential edge-on orientation,[96,105,106] we see that the intensity of the π–π stacking (010) peak is largely in-plane, while strong peak intensity is observed in the out-of-plane direction for the lamellar (h00) peaks, indicating edge-on orientation with respect to the substrate.

Upon doping with DDB-F_{72} with low-to-mid concentration solutions (0.05 mM and 0.3 mM), we see that the edge-on orientation of P3HT’s crystallites is maintained as the (010) peak is still largely in-plane, consistent with the fact that SqP is known to preserve domain orientation.[87,88,120] The in-plane data reveals a shift in the (010) peak to higher Q, reminiscent of what has been previously reported for F_4TCNQ,[87,97] but with some significant differences.

In F_4TCNQ-doped-P3HT, a much larger shift of the (010) π-stacking peak, out to 1.8 Q, is observed upon doping compared to what is seen here. Despite the large peak shift, the change in the π-stacking distance is actually quite small as the structural change is mainly due to reorientation of the unit cell: F_4TCNQ intercalation into the side-chain regions of the P3HT crystallites causes an adjustment of the chain angle relative to the unit cell axes.[97] DDB-F_{72} only causes a small shift of

the P3HT (010) peak from 1.66 to 1.68 Q, indicating that this intercalation-induced phase transition does not take place. Additionally, for our DDB-F_{72}-doped films, we observe a small shift in the P3HT (100) lamellar peak to higher Q (see inset), which is in the opposite direction of what is typically seen with F_4TCNQ doping.[87,97] This provides a clear indication that, unlike F_4TCNQ, DDB-F_{72} does not intercalate into the P3HT lamellar regions. The lack of intercalation of large molecular structures into the polymer crystallites is not surprising as their size does not allow them to fit between P3HT side chains. Furthermore, previous work has shown that addition of bulky groups on fullerenes can inhibit their intercalation into the lamellar regions of conjugated polymers,[130] and molecules of DDB-F_{72} have approximately twice the diameter of a typical fullerene. Overall, the observed peak shifts suggest that for DDB-F_{72}, the structural changes induced by doping are solely due to the delocalization of charges within a crystallite,[87,97] likely accompanied by counterions situated around the edge of each doped crystallite.

At high (1 mM) DDB-F_{72} dopant solution concentration, we see a significant loss of crystallinity and a broadening of the P3HT (100) peak rather than a shift. Since GIWAXS only reports on crystalline regions in the doped films, the broadening we observe suggests that at this high doping concentration, most of the doped regions have become amorphous and the only remaining P3HT crystallites seen via GIWAXS are those that remain un-doped. The large increase in disordered P3HT π-stacking intensity seen between 1.2 and 1.5 Q further supports the idea that these high-concentration-doped films are much more disordered than those doped using solutions with lower concentrations of DDB-F_{72}.

Interestingly, we also observe the appearance of new peaks at 0.6 and 1.0 Q (marked by asterisks in Fig. 3.2b) when P3HT is doped with DDB-F_{72}. These new peaks are broadened to the same extent and show a very similar texture as the P3HT peaks. The new peaks do not at all resemble those seen for DDB-F_{72} crystallites (see). Therefore, we hypothesize that these new peaks either result from a new polymorph of P3HT that preferentially forms in the presence of DDB-F_{72} or a P3HT polymorph that is stable only at very high doping levels.

To characterize the extent of charge carrier delocalization in DDB-F_{72}-doped films, we turn to spectroscopic measurements. Spano and co-workers have argued theoretically that the degree of delocalization of holes on P3HT is directly reflected in the shape and position of the polaron's IR

absorption spectrum.[87,107,131–133] Their predictions for how the spectral shape changes when the polarons are localized by proximity to an anion, reproduced from Ref. 87, are shown in Fig. 3.3b, where the blue curve shows the spectrum of a fully delocalized P3HT polaron with no confinement by an anion. We have shown previously using F_4TCNQ-doped P3HT films with different crystallinities that the spectrum of polarons with different degrees of delocalization matches well with Spano and co-workers' theory, and indeed correlates strongly with the experimentally-measured polaron mobility.[87]

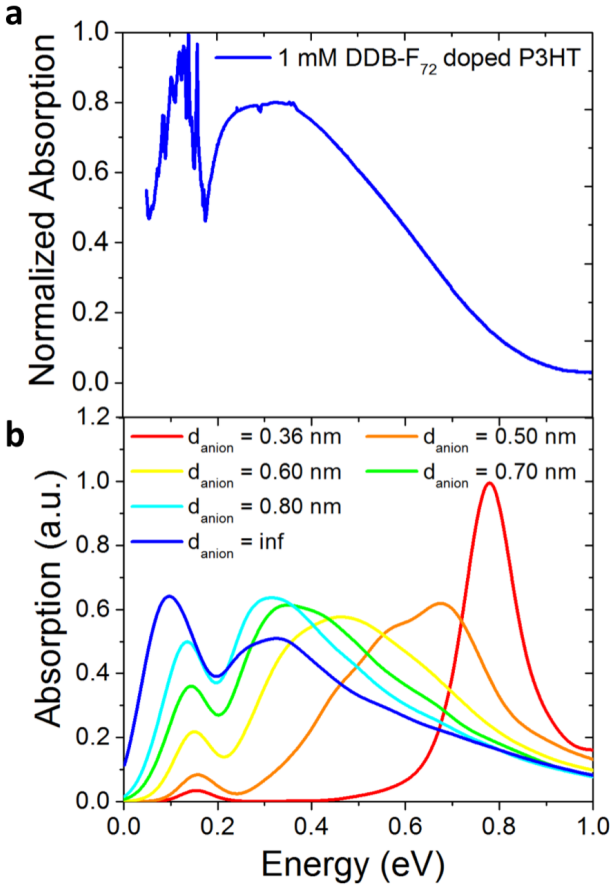

Figure 3.3: Delocalized polaron IR-spectrum. (a) Experimental IR absorption spectrum of the polaron in a 1 mM DDB-F_{72}-doped P3HT film. (b) Simulated P3HT polaron absorption spectrum for different anion-polaron distances. The measured spectrum is in excellent agreement with the theoretical spectrum for an anion at infinite distance, indicating that the polarons in the chemically-doped DDB-F_{72} sample are as delocalized as possible. Note: A distance-dependent permittivity for the pure polymer was used for the calculation. Although the use of a different permittivity would change the shape of the spectrum of the more Coulomb-localized polarons, the spectrum calculated for infinite anion distance is invariant with respect to the choice of permittivity.

Figure 3.3a shows the measured IR spectrum of our DDB-F_{72}-doped P3HT films. The shape and

position of the spectrum we measure is essentially identical to that predicted for a fully delocalized polaron that has no Coulombic interaction with an anion. Indeed, similar IR spectra have been measured in P3HT films doped by charge modulation with no anion present (i.e., doped by the presence of a large applied voltage).[99] A similar polaron spectrum also has been observed in recent work doping P3HT with large molybdenum dithiolene complexes, although the conductivities were much lower than we see here, likely due to low carrier densities, and carrier mobilities were not reported.[122] This indicates that the electron on the DDB-F_{72} anion is sufficiently isolated to have no effect on the polaron, despite the relatively low dielectric constant of P3HT. This is because the electron is localized entirely in the cluster interior, which by Gauss' law means that it effectively behaves as a point charge at the center of the cluster. The steric bulk associated with the substituted DDB cluster means that at no point can the polaron-anion distance be less than the radius of the cluster, which is $\sim$1 nm. We believe that it is the combination of electron localization to the dopant interior shielded by the bulky substituents with the fact that the dopants sit outside the P3HT crystallites that leads to this unusual but highly favorable situation where the polaron is entirely unaffected by the dopant counterion.

To further characterize the extent of delocalization of the polarons in our DDB-F_{72}-doped P3HT films, we performed AC Hall effect measurements,[134–137] the results of which for identically-prepared F_4TCNQ- and DDB-F_{72}-doped P3HT films[88] are summarized in Table 3.1. The concentrations chosen for both dopants were their solubility limits in DCM. We note that for low-mobility materials such as doped conjugated polymers, screening effects can cause Hall effect measurements to slightly overestimate the mobile carrier concentration and thus slightly underestimate the free carrier mobility,[137] as discussed in more detail in .

* 3.6 mM = 1 mg/mL F_4TCNQ

In our sample doped with 1-mM DDB-F_{72}, we measure a mobile carrier concentration that is roughly twice that of the F_4TCNQ-doped sample. We believe that this results from a higher ratio of integer charge transfer due to the greater energetic driving force for doping with DDB-F_{72}, summarized in Fig. 3.1a, and an increase in free carrier (as opposed to trapped carrier) generation due to less Coulomb interaction with DDB-F_{72}. In fact, we have estimated the overall concentration of dopant clusters in the film by directly measuring the change in mass upon doping the films (see

Table 3.1: Comparison of carrier density (n), mobility (μ) and conductivity (σ) measured by the AC Hall effect for P3HT films doped with DDB-F_{72} and F_4TCNQ at their respective solubility limits in DCM. Also shown is the number of dopant molecules in the film estimated via mass mesurements (N_{est}), see SI. The F_4TCNQ data is taken from Ref. 88. The idealized conductivity was calculated using the 120-nm pre-cast polymer film thickness instead of the measured doped film thickness; see text.

Dopant	n (1/cm^3)	μ (cm^2/Vs)	σ (S/cm)	N_{est} (1/cm^3)
1 mM DDB-F_{72}	7.9×10^{20}	0.10	12.8	$6.9(6)\times10^{20}$
3.6 mM* F_4TCNQ[88]	4.3×10^{20}	0.02	1.5	$4.8(9)\times10^{21}$

for details). For F_4TCNQ, the dopant density is $4.8(9)\times10^{21}$ cm^{-3} yielding a doping efficiency of $\sim$10% (slightly higher then the reported 5% value determined by Pingel and Neher[102,103] likely due to the fact that we are in a much higher doping regime and/or to the potential overestimation of the free carrier concentration via AC Hall measurements[137]). For DDB-F_{72}, the carrier concentration is $6.9(6)\pm1.2\times10^{20}$ cm^{-3}, which agrees within error with the carrier concentration we measure via the AC Hall effect (which we also expect to be slightly overestimated[137]). This strongly suggests that essentially every DDB-F_{72} dopant molecule gives rise to a free polaron on P3HT, a full order of magnitude improvement over the $\sim$5–10% free carrier yield estimated for F_4TCNQ.

Perhaps more importantly, the carrier mobility of 0.1 cm^2/Vs is five times higher for DDB-F_{72} than F_4TCNQ, a direct reflection of the higher degree of polaron delocalization with DDB-F_{72}. Moreover, the polaron mobility in the DDB-F_{72}-doped P3HT films is comparable to mobilities seen only in charge-modulation-doped films with no anions present[99] or in highly-crystalline doped 100% regioregular P3HT.[87] Finally, the large degree of polaron delocalization is also supported by the results of temperature-dependent conductivity experiments, which are discussed in .

Overall, we have demonstrated that by using a functionalized dodecaborane dopant, we can achieve spatial separation of the conjugated polymer polaron and counterion leading to highly delocalized and mobile charge carriers even in poorly crystalline polymer material. The dodecaborate cluster anions cannot infiltrate into P3HT crystallites, resulting in a substantial loss in crystallinity upon doping. Thus, the counterions reside outside any remaining P3HT crystallites, and the unpaired electron on the DDB-F_{72} anion is further separated from the polarons on the polymer by being confined to the cluster core. The shielding provided by the cluster's physical and electronic structure

relaxes the crystallinity constraints typically needed to achieve high conductivities and mobilities in conjugated polymer materials. Thus, with other dopants such as F_4TCNQ, crystallinity is important both for improving the delocalization of the polarons and for keeping the anion as far from the polymer backbone as possible. With our dodecaborane cluster dopant, on the other hand, we see that reducing the polaron localization by the anion is at least as important as delocalization due to crystallinity in determining polaron mobility and thus overall conductivity. We achieve conductivities of 12.8 S/cm and mobilities of 0.1 cm^2/Vs with our DDB-F_{72}-doped P3HT, values that are an order of magnitude higher than those obtained with comparable doping by F_4TCNQ. Since the DDB-F_{72}-doped P3HT films significantly increase in thickness upon doping and the DDB clusters themselves do not conduct, this means that the idealized P3HT hole conductivities reach 32 S/cm. Thus, by carefully designing new molecular dopants, we can produce stable molecularly-doped conjugated polymer films with polaron mobilities limited only by intrinsic materials properties, rather than being limited by electrostatic attraction to the proximal dopant anion.

CHAPTER 4

The effects of dopant electron affinity at fixed counterion distance on the production of free carriers in conjugated polymers

Introduction

Modern electronics rely heavily on semiconductor technology for everything from transistors and light-emitting diodes (LEDs) to renewable power-generating photovoltaic and thermoelectric devices.[138] One of the key properties of semiconductors is that they can be doped to improve conductivity or adjust interfacial band alignment via tuning of the Fermi level.[139] The expense of processing precisely-doped inorganic semiconductors has resulted in the emergence of conjugated polymers as potential alternatives that have the advantages of being low-cost, lightweight, solution processable, earth-abundant and compatible with flexible substrates.[7,140] Despite these promising benefits, implementation of semiconducting polymer materials in practical technologies has lagged mainly because their intrinsic electrical properties are inferior to their inorganic counterparts. Unlike inorganic semiconductors, where the packing structure is largely unaffected by substitutional or interstitial dopant atoms, doping of conjugated polymers causes significant disruption to the polymer morphology. Moreover, the relatively low dielectric constant of conjugated polymers typically results in strong Coulomb binding of the charge carriers and the counterions that balance the charge, such that the doped charge carriers have varying degrees of localization depending on the strength of the Coulomb interaction.[87,107,133,141,142] A further consequence of the localization of carriers is the need for a high density of dopants in order to increase the conductivity of organic materials. The very introduction of these dopants into the polymer matrix as well as the electrostatic

changes they impart leads to the disruption of the polymer's microstructure. Understanding the relationship between the chemical nature of the dopant, the way the dopant counterion interacts with the carrier on the doped polymer backbone, and the polymer morphology is crucial for developing high-performance polymer-based electronics.

Multiple methods for doping polymer thin-films exist, including electrical gate and electrochemical doping,[98,99,143] but molecular doping is the only method that produces equilibrium carriers via a ground state charge transfer process without the application of a potential. Molecular doping of conjugated polymers involves the addition of an electron donor (reducing agent) or an electron acceptor (oxidizing agent) for *n*- or *p*-type doping, respectively.[144] For *n*-type doping, a low ionization potential (IP) donor is used to add electrons to the lowest unoccupied molecular orbital (LUMO) of the polymer whereas for *p*-type doping a high electron affinity (EA) acceptor removes electrons from the highest occupied molecular orbital (HOMO), producing conductive holes. The traditional approach for chemical doping of conjugated polymers is to simply mix the polymer and dopant in solution. Unfortunately, the solvents used to process conjugated polymers are typically non-polar, so the charged species that form upon the addition of a dopant crash out of solution at high doping concentrations. This leads to poor film quality and thus limits the types of measurements and applications possible with doped films.[88,105] To overcome film quality issues at high doping levels, new processing methods have been developed in which the dopant is applied to a pre-cast film of the undoped semiconducting polymer. Such methods include vapor phase infiltration of the dopant[93,96,106,108,118,119,145] as well as solution phase infiltration via a second spin-coating step in which a semi-orthogonal solvent that swells but does not dissolve the polymer is used.[87,88,93,96,97,105–107,141,145] These sequential processing (SqP) methods enable preservation of the original undoped polymer film morphology and allow for conductivity measurements on cm length scales as well as AC-Hall effect measurements[134,136] that provide a way to determine the doped carrier concentration and mobility in these materials.[88,135,137,141,146]

A dominant idea in the literature has been that highly crystalline polymer films are necessary to achieve good charge transport properties, with many molecular doping papers focusing on improving polymer solid state order.[87,88,93,96,106,108,135,145] In our previous work, we showed that for the widely used poly(3-hexylthiophene-2,5-diyl) (P3HT) and 2,3,5,6-tetrafluoro-7,7,8,8-

tetracyanoquinodimethane (F_4TCNQ) materials combination, SqP could be used to preserve relative crystallinity upon doping with higher carrier mobilities achieved in more crystalline films. More recently, we employed a substituted icosahedral dodecaborane (DDB) cluster as a novel dopant molecule, and obtained high mobility for P3HT (0.1 cm^2/Vs) in exceptionally disordered films.[141] We attribute the increased polaron delocalization to the DDB's steric protection of core-localized electron density. Since boron exhibits aromaticity across boron scaffolds,[110,147] substituted DDB clusters tend to stabilize electron density on their core.[115,117,141] This means that for our bulky 2 nm diameter DDB dopant, the counterion effectively behaves as a point charge in its center by Gauss' law and is at least $\sim$1 nm from any carrier. Moreover, we estimated that the doping efficiency (number of free carriers produced per dopant molecule) for our DDB doped P3HT films was 100%. This is in sharp contrast to the doping efficiency of F_4TCNQ doped P3HT which is only 5-10%.[102,141,148] The low doping efficiency despite nearly every F_4TCNQ being capable of charge transfer with the polymer[102] implies the majority of generated carriers are trapped. We suspect that these localization effects are a result of F_4TCNQ's closer distance to the polarons. F_4TCNQ infiltrates the lamellar regions of P3HT crystallites at a distance of 6-8 Åfrom the backbone and can likely get even closer in the amorphous regions.[87] We hypothesize that the reason high crystallinity is important for good conductivity with small molecule dopants like F_4TCNQ is that crystallinity helps reduce Coulombic interactions by keeping the dopant counterions at greater distances from the polymer backbone where the polaron resides.

Doping efficiency is expected to increase with the energetic offset between the polymer HOMO and dopant LUMO.[122,139,149] Yet, to date few papers have studied the effects of this thermodynamic driving force and none have directly pinned down how the electronic offset affects doping efficiency largely due to the aforementioned problems of disentangling structural effects from electronic ones. In past studies, either only slight tuning of the dopant EA was possible (while maintaining an energetic offset large enough to dope),[78,93] significant structural changes of the dopant were necessary,[122,141,150] or quantification of charge carrier properties (mobility and carrier density) were not carried out nor the main focus.[151] In this paper, we directly attack the question of the effect of electronic offset on doping efficiency by employing a series of DDB dopants for which the redox potential is tuned over nearly 1 V via modification of the substituents without changing

the dopant's size or shape. We find that not only is the redox potential of the dopant critical for the production of free carriers, it also drives dopant into the film and into the crystallites. Just like many other albeit much smaller and more planar molecular dopants, these DDBs are found to infiltrate the lamellar region of P3HT crystallites. This observation suggests that one of the reasons partial charge-transfer complexes are so rare in polymeric systems is dopants preferentially pack in their lamellar regions rather than breaking apart the π-stacks due to enthalpic effects dominating over entropic ones. Unlike in charge transfer salts where the dopants sit close to the organic material being doped, polymers have a crystalline structure which help situate the counterions farther from the polymer backbone leading to integer rather than partial charge transfer (in which the charge can be shared between a proximal donor and acceptor).

Results & Discussion

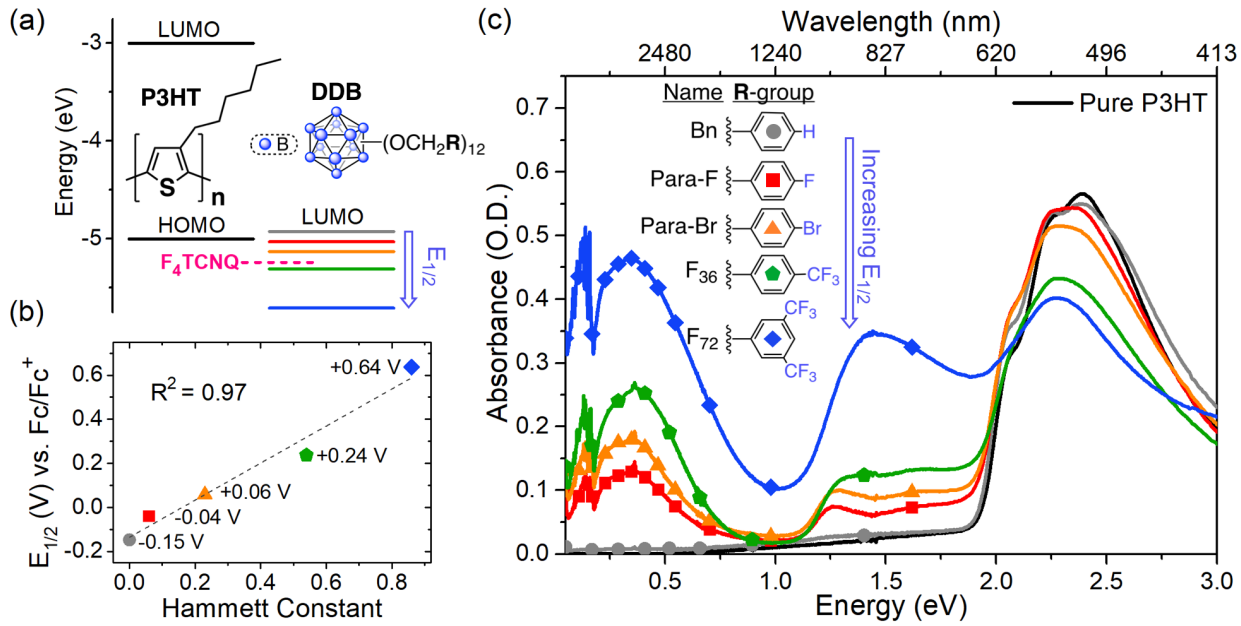

Figure 4.1: a) Chemical structures of P3HT polymer and DDB dopants, which have an icosahedral B_{12} core and each vertex is functionalized with R-groups shown in (c). The energy diagram depicts relative offsets between P3HT HOMO and dopant LUMOs based on CV measurements of all dopants (including F_4TCNQ) and scaled to reported P3HT-F_4TCNQ energy offset. b) Measured $E_{1/2}$ for DDB dopants plotted against their Hammett constant showing tunability of dopant redox potential based on substituent electron donating/withdrawing ability. c) UV-VIS-IR spectra of 120-nm thick film of P3HT doped with 1 mM DDB via SqP with an increase in signature polaron peak intensities (P1, P2 and P3) and a bleach of the bandgap transition.

The effects of energetic offset between polymer and dopant has been difficult to study because significantly changing the redox potential has required modifying the dopant's entire molecular structure. In this work, we take advantage of DDB clusters whose redox potentials can be rationally tuned via their substituents.[117,152,153] The clusters have an icosahedral dodecaborane core with a substituent on each boron atom in the form $B_{12}OCH_2R_{12}$ where R is a functionalized aryl group (see Figure 4.1a for core structure and 4.1c for R-group substituents). By tuning the Hammett parameter of the R-group, which captures its electron-donating/withdrawing ability, the redox potential of the cluster is correspondingly tuned as shown in Figure 4.1b. A more positive Hammett parameter corresponds to a more electron-withdrawing functional group, generating a more oxidizing DDB with a lower lying LUMO. To identify the different DDB clusters, we give them shorthand names based on the structures of these substituents (Bn for benzyl, *p*-F for *para*-fluoro, *p*-Br for *para*-bromo and F_{36} and F_{72} representing the total number of fluorines on the DDB molecule). In this work, we choose to dope the semiconducting polymer P3HT shown in Figure 4.1a since the P3HT and F_4TCNQ dopant system is currently one of the most widely studied in the field. The redox potentials of all the DDBs were measured alongside F_4TCNQ under the same conditions as reported in Figure C.1 of Appendix C so that the offsets shown in Figure 4.1a are drawn to scale, and the P3HT/F_4TCNQ offset is estimated based on the literature values of the P3HT HOMO (-5 eV vs vacuum) and F_4TCNQ LUMO (-5.2 eV vs vacuum).

As a first order test of the effect of redox potential on doping, we can look at the absorption spectra and conductivity of the films, both of which report on the formation of carriers via doping. We fabricated sequentially doped thin films of P3HT using equimolar dopant solutions. In our previous work, we showed that despite the large size of our DDB-F_{72} dopant, it can intercalate throughout the depth of the pre-cast polymer film.[141] In our doped films, we find that, as expected, both the absorption from polaronic transitions and conductivity increase with redox potential. The UV-VIS-FTIR spectra of P3HT films SqP doped with 1 mM DDB solutions are shown in Figure 4.1c and 0.3 mM DDB solutions are shown in Figure C.2. As the DDB dopant redox potential is increased, we see an increase in the signature P1, P2, and P3 polaron peaks at around 0.3 eV, 1.3 eV, and 1.6 eV, respectively.[154] Our lowest redox potential cluster, DDB-Bn, has a redox potential that is too low to dope and no polarons are visible in the UV-VIS. Unlike with F_4TCNQ, the P2

and P3 peaks are resolvable until they coalesce at higher doping levels (as with DDB-F_{72}) since the DDB neutral and anion peaks are under the broad polymer bandgap absorption.[141,152] This is why the HOMO-LUMO transition appears not to bleach even for high doping levels. The film quality of our SqP doped films is maintained such that we can measure conductivity over macroscopic length scales. The electrodes are placed at the corners of our 1.5 cm $\times$ 1.5 cm samples, and the conductivity is measured using the Van der Pauw method.[125] The measured conductivities at multiple concentrations are shown in Table C.1 and for all DDBs at a given concentration we see higher conductivity for the higher redox potential clusters, reflecting our spectroscopic observations. For the 1 mM doped films, the conductivities are as follows: DDB-Bn 0 S/cm, DDB-*p*-F 0.2 S/cm, DDB-*p*-Br 0.4 S/cm, DDB-F_{36} 2.3 S/cm, and DDB-F_{72} 12.9 S/cm. Curiously, we find that film thickness also increases with increasing redox potential of the dopant, indicating that the dopant infiltration may be redox driven.

Because of the sequential doping method and the different chemical nature of the DDBs, it is possible that different amounts of cluster are able to infiltrate the film despite the SqP concentrations being held constant. Although we have previously shown successful intercalation of DDB-F_{72},[141] others have demonstrated limited vertical intercalation for large dopants.[126,155] Furthermore, there is a the lack of clear mechanism for infiltration in films in which diffusion through the polymer layer is achieved.[121,122,130] To the best of our knowledge, no prior work has accurately quantified the amount or the vertical phase distribution of the dopant in a sequentially doped polymer film. To this end, we employ neutron reflectometry (NR) which is a non-destructive technique that can measure the vertical distribution of materials within a thin film. Contrast between materials for NR must come from differences in their scattering length density (SLD), which is calculated as an average of the SLDs of each of the nuclei in the molecule. The calculated SLDs are summarized in Table 4.1. There is adequate contrast for NR between the DDB-dopants and P3HT polymer without deuteration since the DDB dopants have a smaller H-to-heavy-atom ratio and thus higher SLD than P3HT. The experimental reflectivity patterns are shown in Figure 4.2a. We have chosen to use films doped with 0.3 mM DDB to balance both a doping level that leads to measurable conductivity while maintaining sufficiently low surface roughness for NR. The data is fit using a layered model in which the thickness, roughness, and SLD of the layers are varied to produce the best fit SLD values

as a function of distance from the substrate.

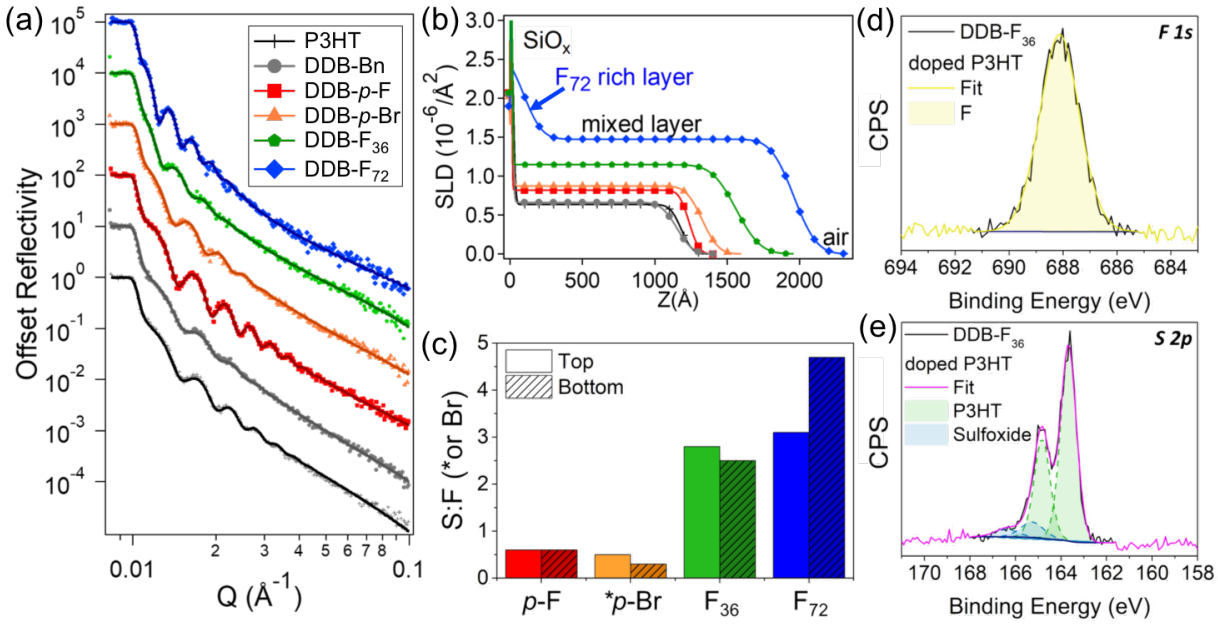

Figure 4.2: a) Raw neutron reflectivity data for pure and DDB-doped P3HT (symbols) and fits of the model to the data (darkened lines). b) SLD depth profiles obtained from fitting the data in (a) showing substrate SiO_x layer followed by the active layer before reaching the air interface. Profiles show sample SLD and thickness increase with dopant redox potential and confirm nearly uniform dopant infiltration throughout the film. c) XPS-determined sulfur to fluorine (*or bromine) ratios at the top and bottom surfaces of DDB-doped P3HT films supporting that clusters penetrate the film, sample fits shown in (d) & (e). d) F 1s fit (yellow) and e) S 2p fit (green-neutral S, blue-oxidized S, and pink-full S fit) for the top surface of a DDB-F_{36} doped P3HT film (black).

The layered models that generate the best fits to the data are shown in Figure 4.2b, which show the SLD as a function of distance from the bottom of the sample (Z = 0 Å). As expected, the undoped P3HT film fits to two layers: substrate and pure polymer. The SiO_x layer is present on the bottom due to the oxidized surface of the silicon substrate and the active layer has roughness at the air-polymer interface, as demonstrated by the gradual change from active layer SLD to air. The measured active layer SLD for pure P3HT is $0.56 \times 10^{-6}/\text{Å}^2$ which is in good agreement with our calculation as well as previously measured values.[156–158] For DDB-Bn, which does not dope the polymer, there is only a slight change in the active layer SLD indicating little infiltration of this molecule. As the redox potential of the DDB dopants increase, so does the measured SLD of the active layer (summarized in Table 4.1). This observation is suggestive of an increase in DDB

content in the film with redox potential of the dopant, however, because the SLDs of each dopant vary slightly, we must further deconvolute their contributions to the mixed layer SLD. The active layer SLD is simply the weighted average of the pure SLDs of the individual components allowing for determination of the P3HT monomer to DDB dopant ratio (see SI for details). This calculation confirms that the trend in SLDs corresponds to an increase in dopant:monomer ratio as summarized in Table 4.1. The increasing dopant:monomer ratio clearly shows that the chemical charge-transfer reaction that occurs upon the introduction of a redox-active dopant drives intercalation. The non-doping cluster, DDB-Bn, provides an excellent control for this hypothesis as it infiltrates 3 times less than the next lowest redox potential dopant (DDB-*p*-F) and approximately an order of magnitude less than the others.

Table 4.1: Summary of calculated neutron SLDs of pure materials and model SLD results of pure P3HT and DDB-doped P3HT films with calculated DDB:P3HT monomer ratio from these values showing increasing dopant loading with higher redox potential DDBs.

	Calculated SLD (pures) (10^{-6}/Å^2)	Measured SLD (films) (10^{-6}/Å^2)	DDB:P3HT monomers
P3HT	0.6	0.56	-
DDB-Bn	1.6	0.63	1:106
DDB-*p*-F	1.8	0.81	1:30
DDB-*p*-Br	1.3	0.87	1:11
DDB-F_{36}	1.9	1.17	1:11
DDB-F_{72}	2.0	1.43	1:7

The neutron reflectometry data demonstrates that within the active layer of the doped polymer film, the dopant is uniformly distributed throughout. The only exception to this is DDB-F_{72}, in which there is a small layer with excess dopant at the bottom of the film. These results are corroborated by the X-ray photoelectron spectroscopy (XPS) data shown in Figure 4.2c-e. Though XPS cannot accurately depth-profile in the same manner as NR, it can be used to check for dopant penetration through the film by using a delamination technique to access both the top and bottom surfaces of the film as previously reported.[141] Relative dopant quantities can be assessed by comparing the atomic

ratio of sulfur to fluorine (or bromine in the case of DDB-*p*-Br) since sulfur is unique to the P3HT polymer, while fluorine (or bromine) is unique to the DDB dopants (see structures in Figure 4.1 and Appendix C Figure C.3. According to the XPS results, the sulfur to fluorine (or bromine) ratios are similar for both the top and bottom of the DDB-*p*-F, DDB-*p*-Br, and DDB-F_{36} films (Figure 4.2c) suggesting uniform infiltration, while DDB-F_{72} has excess dopant on the bottom of the film as we saw in NR (Figure 4.2c).

While NR and XPS give insight into the vertical distribution of dopants throughout the film and reveals redox-driven infiltration, many previous works have demonstrated the importance of understanding the interaction of the dopant molecule with the crystalline regions of the polymer film. In general semiconducting polymers like P3HT have two characteristic crystalline features: a lamellar spacing relating to the length of the side chains and a π-stacking distance. These crystalline features in doped polymer films have been extensively studied using 2D-Grazing-incidence wide angle X-ray scattering (GIWAXS). In general, for small molecule dopants the counteranion resides in the lamellar region causing an expansion in this lattice direction. Intercalation of the dopant into the crystal structure in this way causes a reorientation of the unit cell which decreases the π-stacking distance. This structural change has been observed for a wide variety of dopants including F_4TCNQ, $FeCl_3$, polyoxometalate dopants and others.[87,97,126,132,159]

In order to understand the effect of these much larger, three dimensional dopants on the crystalline regions of P3HT, we studied the P3HT films doped DDB dopants via GIWAXS. 2D diffractograms for all sample conditions are shown in Figure C.4 of Appendix C. Figure 4.3a shows the progression of structural changes in the lamellar (h00) region of the polymer as the doping level is increased for a representative DDB. The original P3HT (100) and corresponding overtones appear at 16 Å. As the doping level increases, the original peaks corresponding to crystalline P3HT decrease and a new phase denoted as (h00)' begins to appear. At the highest doping level, the original P3HT peaks have disappeared entirely and have been replaced with peaks at 0.44, 0.66. 0.88 and 1.10 q. These overtones correspond to a (100) distance of 0.22 q or 2.85 nm, indicating a highly expanded lamellar region. The (100) peak is not fully visible in our GIWAXS experiment due to the beam stop blocking the lowest-q region in which the (100) peak would appear. We hypothesize that this new (h00)' phase is indicative of the structure shown in Figure 4.3d, in which

the DDB dopant has intercalated into the P3HT lattice much in the same way that F_4TCNQ and other small molecule dopants do.

Figure 4.3b demonstrates that all other DDB dopants undergo a similar phase change as the doping level increases. DDB-*p*-F, which dopes P3HT only slightly shows the beginning of a phase change with the increase in intensity at 0.66 q, shown in the inset of Figure 4.3b. With increasing redox potential to DDB-*p*-Br, the peaks corresponding to the doped phase continue to increase until full conversion to the new phase with DDB-F_{36}. DDB-F_{72} undergoes a similar change but to a slightly larger d-spacing in the lamellar regions. Doping with DDB-F_{72} causes a new phase with peaks at 0.40, 0.60, and 0.80 corresponding to a (100) peak of 0.20 q, or 31 Å. These results demonstrate that for P3HT, and likely semiconducting polymers in general, molecular dopants of all sizes, shapes and surface energies tend to reside in the crystalline region of the polymer, thus ensuring spatial separation for the polaron and anion.

The summary of the results relating to this new phase change are shown in Table 4.2 and Figure C.5. The presence or lack thereof of the new doped phase and the original undoped P3HT phase for each dopant at different concentrations demonstrates the different redox-dependent rates at which the crystalline region has converted to the new phase. For example, even at the highest concentration of DDB-*p*-F, there is very little presence of the new doped phase. However, for DDB-*p*-Br, at 1 mM dopant concentration, there is clear 2-phase coexistence such that both peaks can be fit clearly (also shown in Figure 4.3b). However, for DDB-F_{36} this clear two-phase coexistence occurs at only 0.3 mM with full conversion to the expanded doped phase at 1 mM. As can be seen in the NR results in Table 4.1,there are similar amounts of DDB-*p*-Br and DDB-F_{36} in the film at 0.3 mM yet the ratio of the doped crystalline phases at 0.3 mM is very different. This indicates that the driving force for DDB intercalation into the P3HT crystallite is even more redox-driven than the infiltration of dopant into the film. Due to peak overlap with the original phase, it is not possible to fully deconvolute the DDB-F_{72} doped regions from the undoped P3HT. With this new phase change and the anion localized on the DDB core, in the crystalline regions, the anion and the hole are separated by approximately 14 Å for DDB-*p*-F, DDB-*p*-Br, and DDB-F_{36} and 15 Å when P3HT is doped with DDB-F_{72}. This anion-hole spatial separation is approximately twice as large as what is seen in the crystalline regions of films doped with F_4TCNQ.

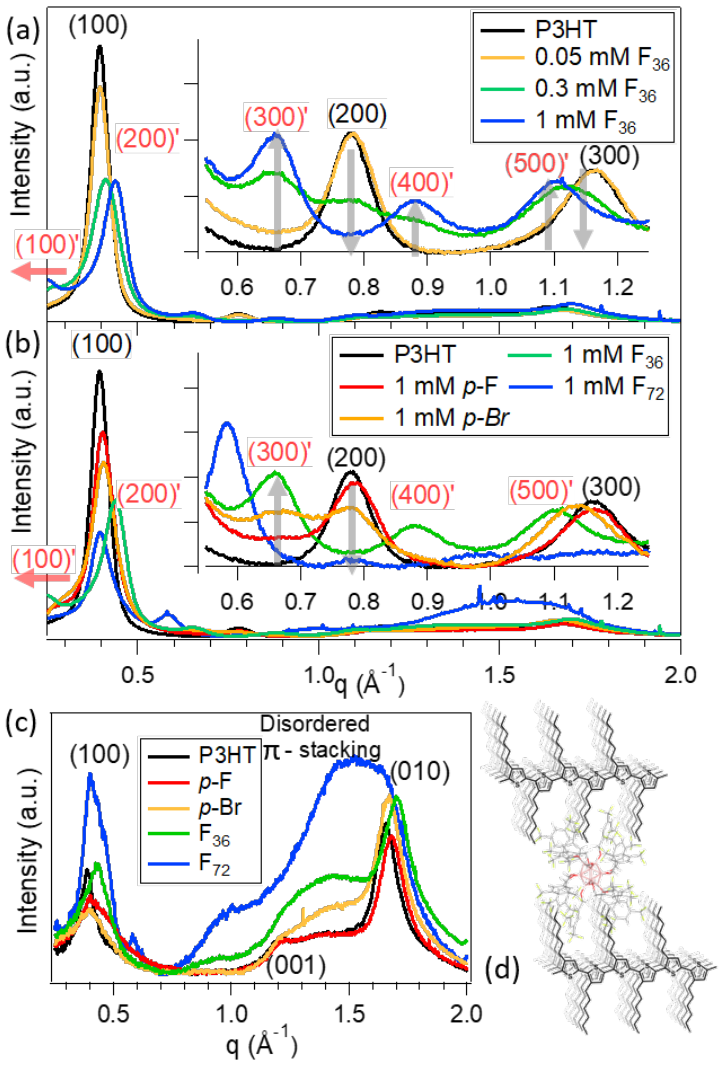

Figure 4.3: a)Full integration and out-of-plane (inset) integration of P3HT doped with DDB-F_{36} demonstrating phase change from undoped (h00) pahse to expanded (h00)' lamellar strucutre b) Full integration and out-of-plane (inset) of P3HT doped with various DDB dopants at 1 mM concentration showing relationship of redox potential on extent of phase transition to (h00)' structure c) GI-WAXS In-plane integration of P3HT doped with 1 mM DDB dopants showing increase in disordered π-stacking region and shift of (010) peak to higher *q*. d) To-scale Representation of proposed (h00)' lamellar structure in which DDB dopant has intercalated into the lamellar regions of the P3HT crystal structure.

These results demonstrating that the dopant anion lies in the lamellar region are important for understanding the effect of polymer crystallinty on doping and resulting conductivity. The location of the dopant anion in the lamellar regions has proven critical for conductivity because the spatial separation of the anion and hole directly relates to extent of integer charge transfer and the delocalization of the resulting polaron.[131,142] Conversely, anions that are able to reside in the amorphous regions result in much more localized carriers because the anion is so much closer to the hole. These results suggests that for semiconducting polymers, crystallinity is key in creating the spatial separation between the anion and hole required to create mobile carriers and that even dopants of very large size are able to infiltrate the lamellar region.[87] This is supported by the fact that charge-transfer complexes in polymers are difficult to make because they need to be kinetically trapped.[160]

Table 4.2: Summary of calculated (100) *d*-spacing based on GIWAXS-measured overtones for 0.3 mM and 1 mM dopant concentrations. There is a transition between the undoped and doped phases, with both phases coexisting at some doping levels. The undoped phase corresponds to the orignal P3HT lamellar *d*-spacing.

	DDB-*p*-F doped *d*-spacing (Å)		**DDB-*p*-Br doped *d*-spacing (Å)**		**DDB-F_{36} doped *d*-spacing (Å)**		**DDB-F_{72} doped *d*-spacing (Å)**	
(h00) phase	*undoped*	*doped*	*undoped*	*doped*	*undoped*	*doped*	*undoped*	*doped*
0.3 mM DDB-doped	15.5	-	16	-	16	28	-	31
1 mM DDB-doped	15.5	-	16	28	-	28	-	31

Conversely, the in-plane integrations show that the π-stacking region does not undergo a phase change as with the lamellar region and the morphology is largely preserved. There is a slight shift of the (010) π-stacking peak to higher q, due to the delocalization of the hole across multiple polymer chains. In this region is it also clear that there is a large increase in the broad, disordered π-stacking peak centered 1.4 q. Figure C.6 shows that this broad peak grows in for both higher concentration and higher redox potential DDBs, likely because both factors result in more DDB cluster content in the films This indicates that in addition to the population of DDB anions integrated into the lamellar crystal structure, the dopant anions also populate the more disordered regions of the film in which the anion-hole separation would be determined only by the side chains of the DDB dopants. We hypothesize that these results indicate that the DDB dopants first reside in the lamellar regions as

seen by in the increase in new (h00)' phase at fairly low doping, and only dope the more disordered regions once the crystalline regions are full.

Lastly, we also observe that the intensity in the (100) region at 0.40 q decreases significantly both with increase in redox potential and DDB concentration in 4.3a and 4.3b. This drop in intensity can be attributed to two factors. First, as can be seen in 4.3c, the disorder of the film increases greatly at higher doping which could correspond to a decrease in crystallinity. Second, in the new (h00)' phase the peak centered near 0.40 q is a (200) peak as compared to the original P3HT (100) peak, which is inherently more intense than higher order overtones.

The intercalated phase we observe from GIWAXS, with DDBs in the lamellar regions of P3HT crystallites, means the center of a DDB cluster is 14-15 Åfrom the polymer backbone as shown in Figure 4.3d. Since the DDBs localize electron density on their core, and by Gauss law should behave as a point charge on the center of the cluster, this means that the counteranion is 14-15 Åfrom the polaron. This physical separation, which is approximately double the 6-8 Åwe have previously reported for F_4TCNQ, should result in highly delocalized polarons. FTIR spectroscopy can be used to probe polaron delocalization as it has been shown that the shape and location of the polaron P1 peak reports on and is highly sensitive to inter- and intrachain coherence as well as distance-dependant counterion binding effects.[87,131–133,142] In our previous work, we showed that in order to reproduce the peak shifts we saw in the P1 peak location, the anion separation was a critical factor that needed to be accounted for.[87] In general, polaron localization decreases with red-shifting of the P1 peak and an enhanced ratio of IRAV peaks (located around 0.1 eV) to main P1 band absorption.

The concentration dependence of the P1 peak is shown in Figure 4.4a for DDB-F_{72} and for all other DDB dopants in Figure C.9a-c. For all dopants we observe a blue shoulder growing in at higher dopant loadings. It makes sense that as we add more dopant molecules they are forced to organize closer P3HT backbone. We suspect the increased proximity occurs primarily in the amorphous regions. Unlike in crystalline parts of the film where the DDB dopant is held in the lamellar region of the crystallite, in the amorphous regions, a section of polymer backbone (and therefore polaron) could be located right next to or slightly inside in the edge of the cluster. The IR concentration effects are correlated with an increase in the intensity of disordered regions in

the GIWAXS centered at 1.4 q with higher dopant concentration as shown in Figure C.6. The concentration effect is more pronounced for higher redox potential DDBs which is also supported by GIWAXS given that Figure 4.3c shows increased disorder with redox potential at fix concentration and by far the most disorder for DDB-F_{72}.

For the highest concentration of DDB-F_{72} in particular, we see the most broadening of the P1 peak, which we attribute to the sample's lack of overall crystallinity yielding a wider range of configurations and therefore possible polaron-counterion distances. In fact, in previous work, Gosh and coworkers fit the P1 peak for this sample and found a distribution of counterion separations corresponding to 18 and 8 Å (in a 3:1 ratio). The 18 Å distance coincides well with the 15 Å distance we find for the DDB in the lamellar spacing. The 8 Å distance therefore must only in non-crystalline regions in which the anion is not separated from the holes by the P3HT side chains. Still, we achieve this minimum spacing of 8 Å and the P1 peaks are much more red-shifted than in F_4TCNQ doped P3HT, owing to the DDB structure's ability to spatially separate the counterion.

To use the P1 peak to compare polaron-counterion separation distance between all DDB clusters, we chose concentrations for which the P1 intensities are best matched (see Figure C.9d. Normalization of this data yields Figure 4.4b for which all DDB doped P3HT polarons have nearly identical P1 shapes, indicating the capability of the DDBs to truly pin the anion distance. This confirms that all dodecaborane dopants spatially separate the counterion by approximately the same distances and further supports the separations found in GIWAXS. Despite the varying oxidation potential of the dopants, all DDBs produce relatively delocalized carriers and are working the way we intended. Thus, we are able to tune the electronic offset without affecting the polaron-counterion distance. Since the FTIR indicates largely delocalized polarons, the higher conductivities we observe with the higher redox potential dopants must be a direct effect of an increase in the number of free carriers produced and thus higher doping efficiencies.

The ratios obtained from NR can allow us to estimate the number of dopants in our films based on the density of P3HT. This means that to calculate the doping efficiency, all we need is an estimate of the carrier density. We suspected that the P1 peak location could give us a rough handle on the mobility (μ) in our films, with which we could calculate the carrier density (n) via the equation $\sigma = ne\mu$ where σ is the conductivity and e is the elementary charge. Indeed, by fitting the P1 peak

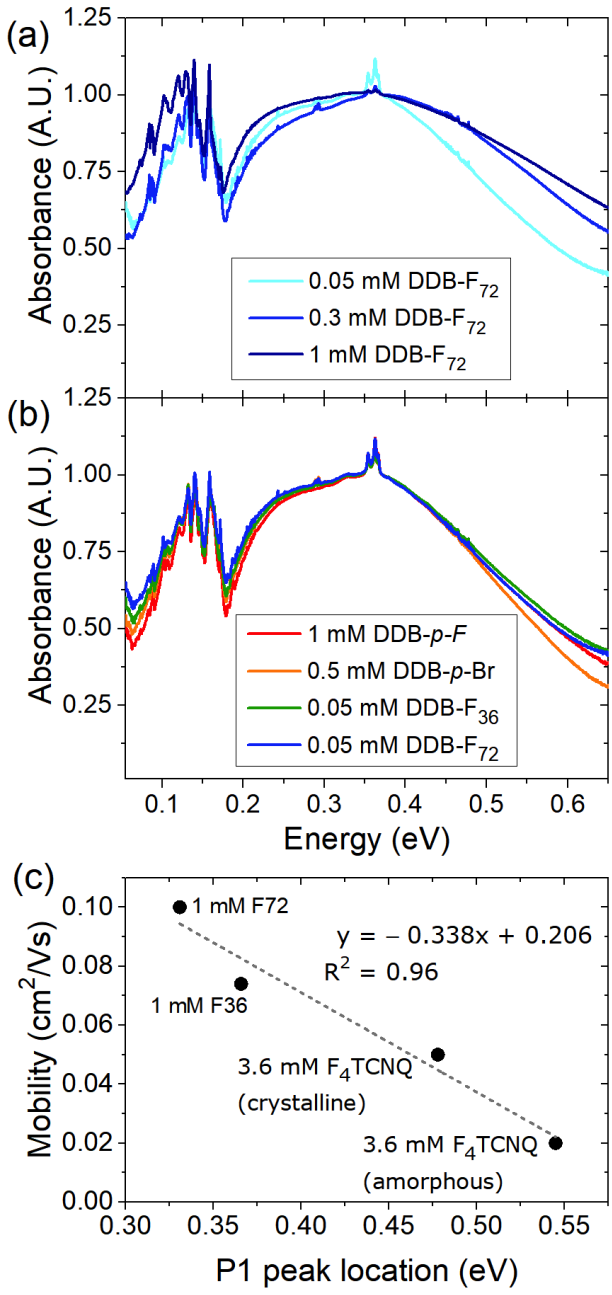

Figure 4.4: a) Normalized FTIR of DDB-F_{72} doped P3HT showing concentration dependence of P1 peak location. At higher concentrations, we see a blue shift of the P1 peak for films doped with all DDB clusters (see SI Figure C9a-c) indicating closer counterion-polaron distance as more dopant is infiltrated. b) Normalized FTIR of DDB-doped P3HT at P1 intensity matched concentrations showing pinned anion distance (see SI Figure C9d for unnormalized data). c) AC-Hall measured mobility vs fitted P1 peak center showing linear relationship (see SI Figure C9e for fitted FTIR data and S10a-c for fits). F_4TCNQ and DDB-F_{72} data taken from our previous work Refs. 87 and 141, respectively.

locations for all doped P3HT samples for which we have corresponding AC-Hall data (from the same polymer batch of the same MW and regioregularity, see Figure C.10 of Appendix C) we find

that the P1 peak centers track linearly with the AC-Hall measured mobility as shown in Figure 4.4c. For the DDB-doped films, we fit the full UV-Vis spectra as well as the FTIR region only and found that for this region, the fit parameters are largely unchanged (see Figures C.12 and C.13 and Table C.3 in Appendix C). This gives us a good indication that fitting the P1 region only is accurate and give us an important handle with which we can estimate the mobility of carriers in our doped films. With this information, we calculate the estimated free carrier density and compare to dopant densities determined by NR and calculate the doping efficiency of our DDB clusters.

The doping efficiency is simply the ratio of free carriers produced to the number of dopants in the film. To estimate the doping efficiency, the amount of DDB in the doped films is calculated from the neutron DDB:P3HT monomer ratios based on a P3HT density of 1.1 g/cm^2 and are reported in Table 4.3. The fits of the corresponding FTIR peaks give us an estimate of the mobility based on the linear relationship reported in Figure 4.4c. This allows us to calculate the carrier density from our conductivity measurements (summarized in Table C.1 of Appendix C). We thus estimate the doping efficiency of our DDB dopants, and find that indeed as the redox potential of the dopant is increased, so is the doping efficiency. It is important to note that the doping efficiency by definition takes into account all dopant molecules despite whether or not they have undergone charge transfer. By using the cross section of F_4TCNQ anions, Pingel and Neher estimated that F_4TCNQ undergoes CT with the polymer approximately 50-70% of the time, and that 95% of those CT events led to trapped polarons, yielding a doping efficiency of less than 5%.[102,148] Here, we cannot directly probe the number of CT events spectroscopically because of the difficulty of resolving the neutral and anion peaks in the DDB-doped systems (shown in Figures C.12 and C.13 of Appendix C) and the difficulty in obtaining accurate cross sections from solution to film environments. However, given that the intrinsic counterion separation of DDBs leads to free carriers, supported by both our AC-Hall and FTIR measurements, the differences we observe are likely due to differences in the number of CT events. For our DDB-F_{36} dopant, which has the redox potential that is closest to F_4TCNQ (higher by only $\sim$70 mV), we find a doping efficiency of 16%. Thus, there appears to be a trade off: our similar redox potential has a lower yield. This begs the question of distance dependent effects on electron transfer and calls for isolation of the effect of counterion distance which could be accomplished by changing the size of the DDB substituents while holding the redox

potential constant.

Table 4.3: Estimated doping efficiency of DDB dopants based on dopant density calculated from neutron SLD results, mobilities calculated from P1 peak locations allowing for carrier density estimates from measured mobilities.

	Dopant Density (cm^{-3})	P1 center (eV)	μ ($cm^2V^{-1}s^{-1}$)	σ (Scm^{-1})	n_{est} (cm^{-3})	Doping efficiency %
DDB-*p*-F	1.3×10^{20}	0.339	0.092	0.016 ± 0.003	1.09×10^{18}	0.8 (0.3)
DDB-*p*-Br	3.7×10^{20}	0.328	0.095	0.11 ± 0.01	7.20×10^{18}	1.9 (0.3)
DDB-F_{36}	3.6×10^{20}	0.369	0.082	0.75 ± 0.02	5.74×10^{19}	16 (1)
DDB-F_{72}	5.3×10^{20}	0.363	0.084	6.8 ± 0.5	5.08×10^{20}	96 (10)

With our highest redox potential dopant, DDB-F_{72} that has nearly 0.5 eV greater offset compared to F_4TCNQ, we calculate a doping efficiency of 96%, which is within the error of our previously estimated 100% and highlights the importance of energetic offset for the generation of free carriers. We believe all of the structural data we have obtained points towards the reason DDB-F_{72} dopes so well; the high redox potential gives it enough driving force to dope any of the conformations of P3HT that can occur in a semicrystalline thin film. This is supported by our doping experiments carried out in solution for which only DDB-F_{72} can dope the P3HT aggregates that form during the doping process,[161] and can continue to dope well past the level of DDB-F_{36}, see section C.8 of Appendix C for details. Therefore, the high electron affinity combined with spatial separation of the carriers leads to the generation of 100% free carriers in P3HT.

4.1 Conclusions

In this work, we isolated the effects of electron affinity on the generation of charge carriers in P3HT by employing a unique molecular dopant system, dodecaboranes, whose redox potential can be tuned while maintaining a constant size and shape. Indeed, by tuning the redox potential of the DDB and keeping the SqP doping solution concentration constant, we can tune the doping level of the sample. Remarkably, the higher doping levels are not only caused by the dopant's electron affinity, but also by redox driven infiltration of the DDB dopants. Here, for the first time, we characterized the vertical distribution and amount of dopants in sequentially doped films using

neutron reflectometry. We observe mostly uniform dopant distribution throughout the film, with increasing dopant density for higher redox potential clusters. Redox-driven infiltration is also corroborated by both our XPS and GIWAXS studies. Our GIWAXS characterizations show that doping leads to a new phase that is strongly redox-dependent; its structure corresponds to the DDB cluster intercalating into the lamellar region of the polymer, just like F_4TCNQ.

The greater the infiltration of our large DDB clusters, which is higher for higher redox potential clusters, the greater the loss of crystallinity we observe with a notable observable decrease of the (100) and increase in scattering due to disordered π-stacking. Still, both our AC-Hall and FTIR measurements indicate delocalized polarons, highlighting the importance of anion separation to reduce Coulomb binding. The closest distance polaron on the P3HT backbone could get to our DDB counterion is $\sim$1 nm owing to the built-in steric protection of the DDB core. With DDBs in the lamellar region, we calculate an anion-polaron distance of 1.4-1.5 nm, which correspond well with recently reported fits of DDB doped P3HT in the literature.[142] Further, the shape and location of the polaron peak in the FTIR spectra confirm that all DDBs can effectively spatially separate the counterion.

Both our FTIR and AC-HAll measurements suggest virtually no trapped carriers, indicating that the differences we observe in doping level most likely comes from different amounts of charge transfer. By combining the dopant densities we can calculate from NR with estimates of the the carrier density from our empirically derived FTIR-AC Hall mobility relationship, we indeed find that the doping efficiency increases with redox potential. Thus, we are able to tune the number of integer charge transfer events per dopant with offset. With our highest redox potential dopant, DDB-F_{72}, we achieve a doping efficiency of 96%. We find that the electron affinity of DDB-F_{72} is what allows it to dope so efficiently due to an ability to dope different P3HT conformations in the thin-film.

The fact that the DDBs are interspersed in the lamellar regions despite their large size is an indication that any dopants, regardless of their size or shape, will pack into the lamellar regions of polymer crystallites first. This result gives insight as to why conjugated polymers primarily undergo integer charge transfer, as opposed to partial charge transfer. In charge transfer salts, the dopants can pi-stack with the organic material being doped, whereas the crystalline structure of polymers

forces dopants to be in the lamellar regions. This means dopants are further from the backbone making partial charge transfer in which the charge is shared between donor an acceptor much more rare and likely only in amorphous regions where dopants can get closer to the polymer backbone. Therefore, the reason high crystallinity is important for good conductivity with small molecule dopants like F_4TCNQ is that it reduces Coulombic interactions by keeping the dopant counterions at greater distances from the polymer backbone where the polaron resides.

APPENDIX A

Supporting Information for Chapter 2: Processing Methods for Obtaining a Face-On Crystalline Domain Orientation in Conjugated Polymer-Based Photovoltaics

A.1 Experimental Details

The polymer poly[4,8-bis-(2-ethylhexyloxy)-benzol[1,2-b:4,5-b']dithiophene-2,6-diyl-alt-4-(2-ethylhexyloxy-1-one)thieno[3,4-b]thiophene-2,6-diyl] (PBDTTT-C) and [6,6]-phenyl-C_{71}-butyric-acid-methylester ($PC_{71}BM$) were purchased from Solarmer and used as received. All devices were fabricated on indium tin oxide (ITO) substrates (150 nm, 20 ω/□) that were sequentially sonicated in baths of detergent, water, acetone, and isopropyl alcohol followed by UV ozone treatment for 20 minutes. Subsequently, 35 nm of poly(ethylenedioxythiophene): poly(styrenesulfonic acid) (PEDOT:PSS Clevios PVP AI 4083) was deposited onto the ITO to form the hole collection layer and baked at 150 °C for 20 minutes. For the blend-cast devices, the 1:1.5 wt/wt PBDTTT-C:$PC_{71}BM$ solution was deposited at 1800 rpm for 60 s. For sequentially processed devices, the polymer solution was spun at 2500 rpm for 60 s followed by deposition of the fullerene solution onto the fully dry polymer layer at 2000 rpm for 60 s. Pure polymer films for grazing-incidence wide-angle X-ray scattering (GIWAXS) and space-charge limited current (SCLC) studies were deposited at the same conditions as the first SqP step. Methanol (MeOH) washing of devices containing 3% v/v 1,8-diiodooctane (DIO) was performed at 4000 rpm for 10 s. After deposition of the active layer, both blend-cast and sequentially-processed films were fabricated into devices by thermally evaporating 10 nm of Ca and 70 nm of Al as cathodes at a pressure of 1×10^{-6} Torr using an Ångstrom Engineering NexDep evaporator. The Ca layer was deposited at a rate of 0.5 Å/s to a

thickness of 10 nm, and the Al layer was deposited at a rate of 1.5 Å/s to a thickness of 80 nm. Before exposing the devices to the metals, ∼10 nm of Ca was evaporated onto the shutter to ensure layer purity. For SCLC diodes Au was evaporated at a rate of 0.5 Å/s for the first 10 nm and then at 1 Å/s to a final thickness of 60 nm.

A.2 Polymer crystallite coherence length in pure, blend cast and sequentially processed films

Table A.1: Summary of (100) peak location, integrated peak area, and coherence length as calculated from the Scherrer equation.

Sample	100 Location ($Å^{-1}$)	Relative Peak Area	Error	Coherence length (nm)	Error	
Pure PBDTTT-C	no DIO	0.34	1.0	0.3	4.1	0.1
	w/ DIO	0.32	1.6	0.3	3.7	0.4
	w/ DIO + MeOH wash	0.33	1.5	0.4	3.8	0.4
Blend Cast BHJ	no DIO	0.36	2.0	0.6	2.4	0.1
	w/ DIO	0.36	1.4	0.4	3.9	0.8
	w/ DIO + MeOH wash	0.39	2.8	0.4	3.1	0.1
Sequentially Processed BHJ	no DIO	0.35	2.1	0.3	4.9	0.3
	w/ DIO	0.34	1.7	0.5	5.7	0.1

The (100) crystallite coherence lengths were calculated by peak fitting the fully integrated diffractograms and using the Scherrer equation $\tau=\frac{K\lambda}{\beta\cos\theta}$ where τ is the coherence length, K is the dimensionless shape factor taken to be 0.9, λ is the X-ray wavelength 0.9742 Å, β is the FWHM of the fit and θ is the peak location.

A.3 Solvent Effects of Pure PBDTTT-C

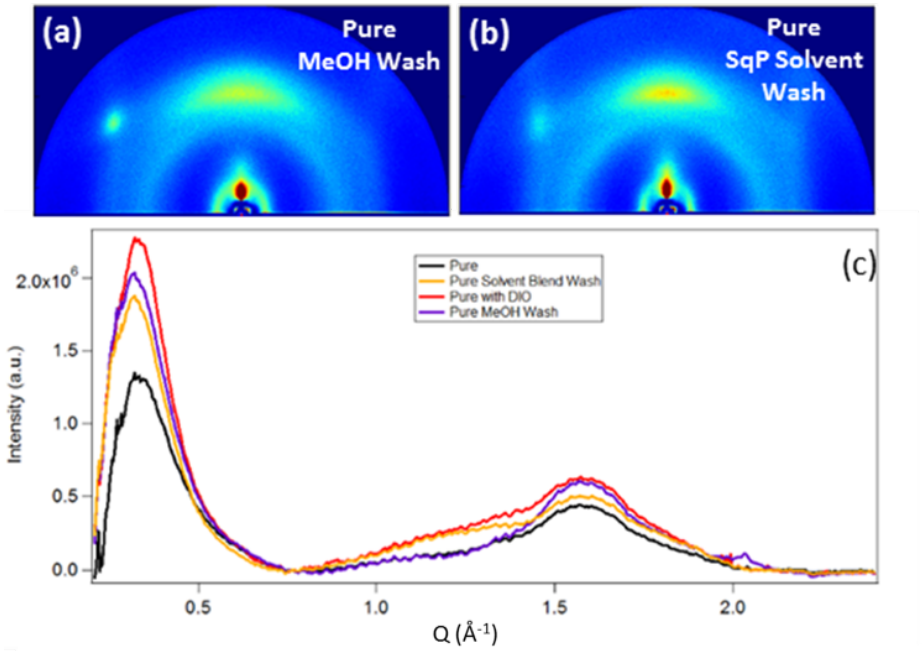

Figure A.1: 2D-GIWAXS of pure PBDTTT-C films after washing with methanol (a) and 1:1 2-chlorophenol:dicholoromethane (b), which was used to deposit the fullerene during sequential processing. Fully integrated diffractograms (c) for pure polymer (black), polymer with DIO (red), and pure polymer washed with methanol (purple) and the SqP solvent blend (orange). An increase in crystallinity over pure is observed with each of the pure solvent washes, however the addition of DIO causes the largest change.

A.4 Effect of methanol washing on blend-cast PBDTTT-C:$PC_{71}BM$ with and without DIO

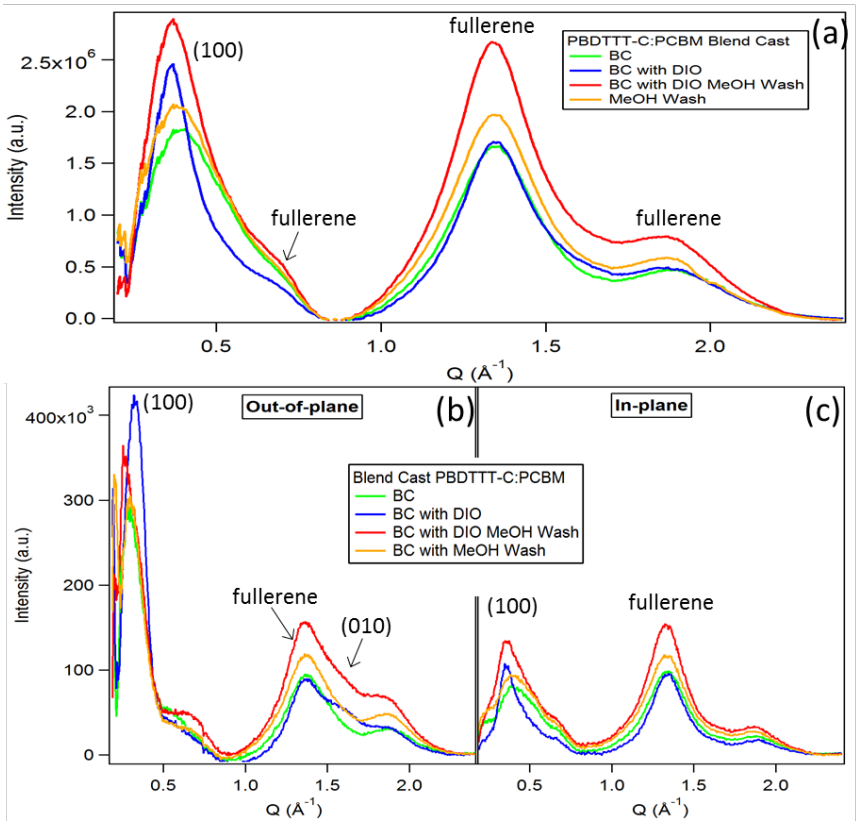

Figure A.2: Examination of the role of methanol washing only for BC devices. (a) Full integration of GIWAXS diffractograms for 1:1.5 PBDTTT-C:PCBM blend cast (BC) films without (green), with 3% DIO (blue), and subsequent methanol wash (red). Methanol wash of a blend cast film without DIO (orange) shows little change. Isotropic fullerene orientation is observed by the equal intensity (b) out-of-plane and (c) in-plane.

A.5 Sequentially processed PBDTTT-C:$PC_{71}BM$ (10 mg/mL PCBM concentration)

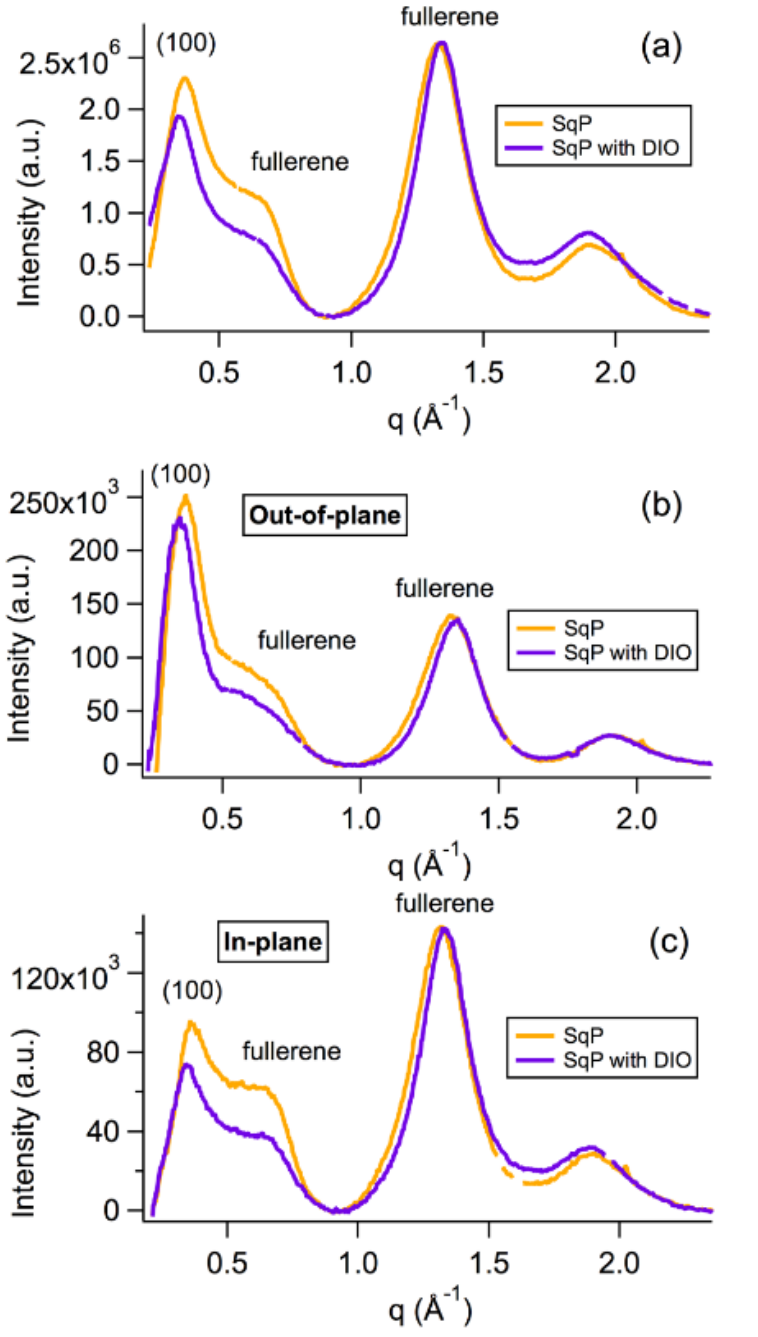

Figure A.3: (a) Full integration of GIWAXS diffractograms for sequentially processed (SqP) PBDTTT-C:PCBM films, where the orange curves have no additive and the purple curves have 3% DIO in the polymer casting solution. The very strong fullerene scattering, makes the (010) diffraction peak invisible in both the (b) out-of-plane and (c) in-plane directions.

A.6 Determination of PBDTTT-C:$PC_{71}BM$ weight ratio in SqP active layer via redissolving

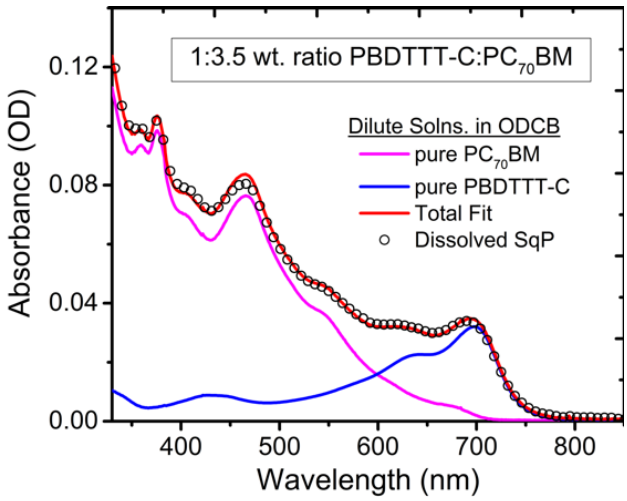

Figure A.4: Solution-phase absorption spectrum (black circles) of a redissolved optimized sequentially processed device (obtained from the procedure described in Ref. 37), along with its fit to a linear combination of the pure solution-phase PBDTTT-C (blue curve) and $PC_{71}BM$ (pink curve) components. The overall weight ratio obtained from the fitting coefficients was 1:3.5 of polymer to fullerene by weight, indicating a fullerene rich device. This result is consistent with increased fullerene peak in the diffraction and EQE data.

A.7 Absorbance of pure, BC and SqP films

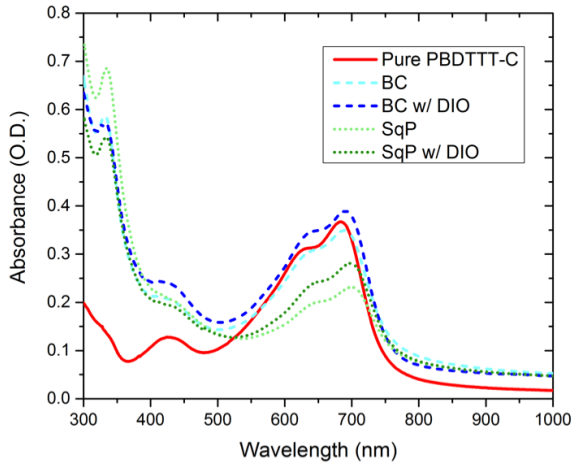

Figure A.5: Absorbance of films made from pure PBDTTT-C (red solid), and BHJs made via BC with DIO (dark blue dash), without DIO (light blue dash), SqP with DIO (dark green dot) and SqP without DIO (light green dot).

A.8 SCLC mobilities

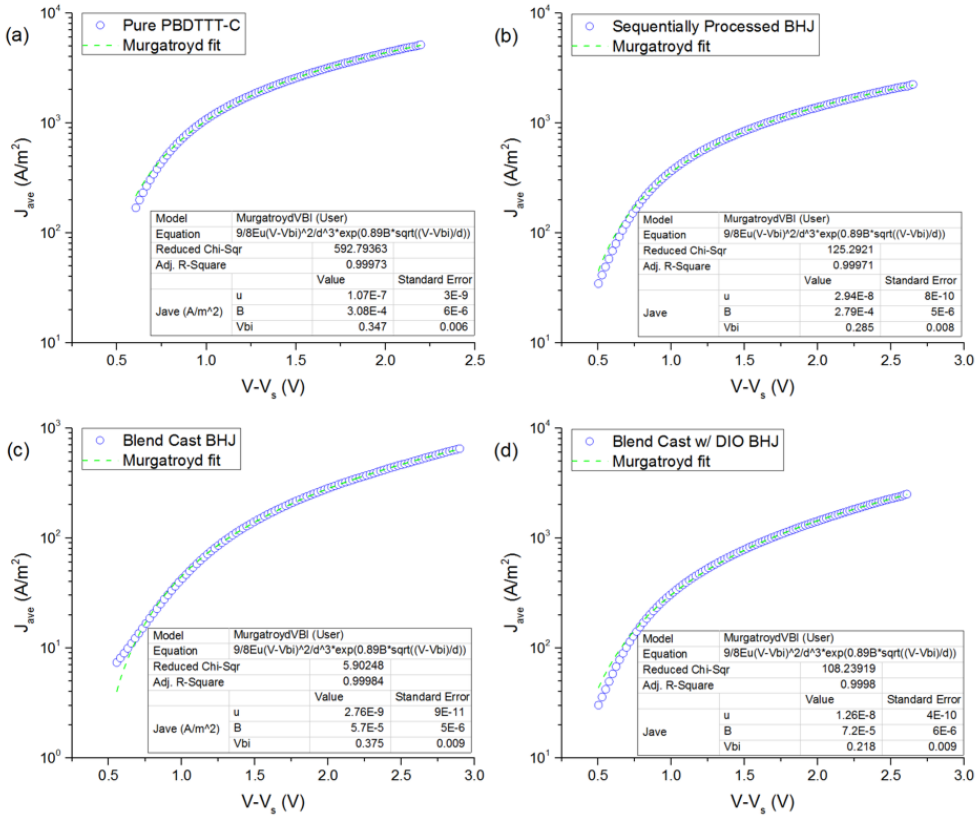

Figure A.6: Current-voltage curves of hole only devices with pure PBDTTT-C (a), optimized sequentially processed PBDTTT-C:$PC_{71}BM$ (no DIO, no MeOH wash) (b), blend cast PBDTTT-C:$PC_{71}BM$ without DIO (c), and optimized blend cast PBDTTT-C:$PC_{71}BM$ (with DIO and MeOH wash). Symbols represent experimental data and the solid lines represent fit of the experimental data, performed for space charge limited current with the Murgatroyd equation: J=$\frac{9}{8}\varepsilon\mu\frac{V^2}{d^3}e^{0.89\beta\sqrt{\frac{V}{d}}}$

A.9 Device optimization of SqP with DIO in polymer/fullerene layer

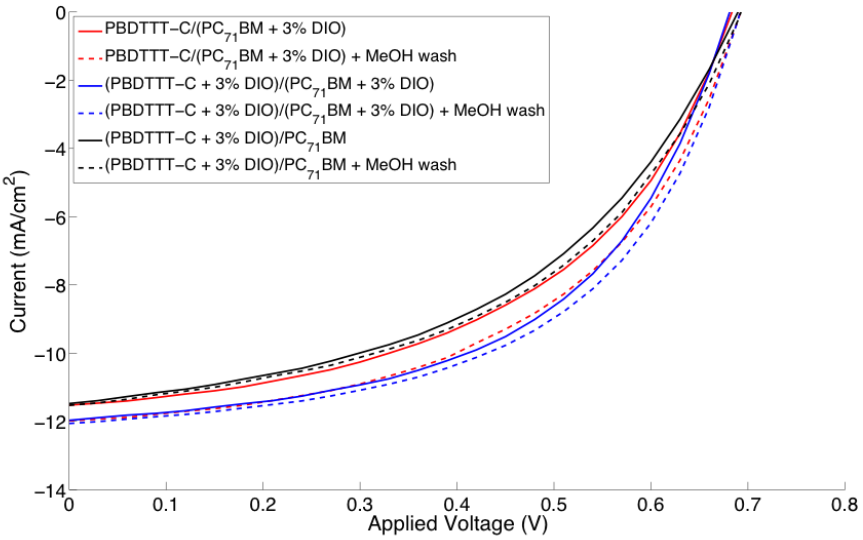

Figure A.7: J-V device curves for sequentially processed PBDTTT-C films with DIO additive in the fullerene layer (solid red) the polymer layer (solid black) and both the fullerene and polymer layers (solid blue). Slight improvement is seen with methanol washing the DIO films (dotted). All devices have the structure: ITO/PEDOT:PSS/PBDTTT-C:BC$_{71}$BM:Ca/Al with DIO added in the indicated layers.

Table A.2: Summary of J-V Characteristics for the PBDTTT-C devices shown in Figure S3.

Device	Voc (V)	J_{sc} (mA/cm^2)	FF (%)	PCE (%)
PBDTTT-C / (PC$_{71}$BM + 3% DIO)	0.684 ± 0.002	-11.5 ± 0.4	49 ± 1	3.9 ± 0.2
PBDTTT-C / (PC$_{71}$BM + 3% DIO) + MeOH wash	0.692 ± 0.005	-12.0 ± 0.4	51 ± 1	4.3 ± 0.2
(PBDTTT-C + 3% DIO) / (PC$_{71}$BM + 3% DIO)	0.681 ± 0.02	-12.0 ± 0.3	53 ± 2	4.5 ± 0.2
(PBDTTT-C + 3% DIO) / (PC$_{71}$BM + 3% DIO) + MeOH wash	0.691 ± 0.008	-11.5 ± 0.2	53.8 ± 0.4	4.4 ± 0.2
(PBDTTT-C + 3% DIO) / PC$_{71}$BM	0.690 ± 0.003	-11.5 ± 0.2	47.0 ± 0.7	3.7 ± 0.1
(PBDTTT-C + 3% DIO) / PC$_{71}$BM + MeOH wash	0.693 ± 0.007	-11.5 ± 0.2	48 ± 2	3.9 ± 0.2

APPENDIX B

Supporting Information for Chapter 3: Dodecaborane-based Dopants Designed to Shield Anion Electrostatics Lead to Increased Carrier Mobility in a Doped Conjugated Polymer

B.1 Materials, Synthesis & Characterization

P3HT (Rieke metals inc., 4002-EE, M_n = 50-70 kg/mol, regioregularity 91-94%) and F_4TCNQ (TCI Chemicals) were purchased and used as received. $NBu_4[DDB\text{-}F_{72}]$ and $[NBu_4]_2[B_{12}(OH)_{12}]$ were synthesized following similar methods to previously reported procedures.[152]

Microwave reactions were performed using a CEM Discover SP microwave synthesis reactor. The reactions were conducted in glass 10 mL microwave reactor vials purchased from CEM with silicone/PTFE caps equipped with a stirbar. 3,5-bis(trifluoromethyl)benzyl bromide (97 %) was purchased from Oakwood Chemicals and used as received. N,N-diisopropylethylamine (>99 %) was purchased from Sigma Aldrich and used as received. Reagent grade hexanes, acetone, and ethyl acetate used for column chromatography were purchased from Sigma Aldrich and used as received. The CH_3CN (anhydrous, 99.8 %) used for the synthesis of $DDB\text{-}F_{72}$ was purified using a solvent purification system and was stored in a nitrogen-filled glovebox over activated 3 Å molecular sieves. NMR spectra were recorded using Bruker AV500 or Bruker AV300 spectrometers at 300 or 500 MHz (^1H), 161 MHz (^{11}B), and 282 MHz (^{19}F) reported in δ (parts per million) relative to tetramethylsilane (^1H), $BF_3{\cdot}Et_2O$ (^{11}B) or C_6H_5F (^{19}F), respectively, and referenced to residual ^1H signals of the deuterated solvent (^1H (δ) $CDCl_3$ 7.26; ^{11}B (δ) $BF_3{\cdot}Et_2O$ 0.00 ppm; ^{19}F (δ) C_6H_5F -113.15 ppm). Deuterated solvents (Cambridge Isotope Laboratories) for NMR spectroscopic analyses were stored over 3 Å molecular sieves.

$B_{12}(OCH_2((3,5\text{-}CF_3)_2C_6H_3))_{12}$ (**DDB-F**$_{72}$) : $[NBu_4]_2B_{12}(OH)_{12}$ (200mg, 0.244 mmol) was charged to a 10 mL glass CEM microwave vial equipped with a stirbar. 3 mL of CH_3CN was added, followed by N,N-diisopropyl-N-ethylamine (0.81 mL, 4.64 mmol) and 3,5-bis(trifluoromethyl)benzyl bromide (2.69 mL, 14.7 mmol). The mixture was heated to 140 °C in a microwave for 45 min. Upon cooling, the purple mixture was concentrated under reduced pressure and was subjected to column chromatography. The purple mixture was loaded with 65/35 hexanes/ethyl acetate (some of the material did not fully dissolve) and the excess benzyl bromide was eluted. The column was flushed with acetone and the eluent was collected. The acetone fraction was dried *in vacuo*. The resulting residue was charged to a vial equipped with a stirbar and brought into the glovebox, where it was dissolved in $\sim$ 5 mL CH_3CN and was charged with $NOBF_4$ (71 mg, 0.607 mmol). The resulting mixture, which gradually developed an orange precipitate, was stirred for 12 h. The orange mixture was placed in the freezer (~ -30 °C) overnight and was then isolated by filtration on a glass frit and washed three times with cold (~ -30 °C) CH_3CN. The resulting orange powder was dried *in vacuo* and was used without further purification. (448 mg, 60%) ^{1}H NMR (500 MHz, $CDCl_3$) 7.77 (s, 12H, Ar), 7.52 (s, 24H, Ar), 5.47 (s, 24H, CH_2); ^{11}B NMR (161 MHz): 41.28 (s); ^{19}F NMR (282 MHz): 63.73 (s).

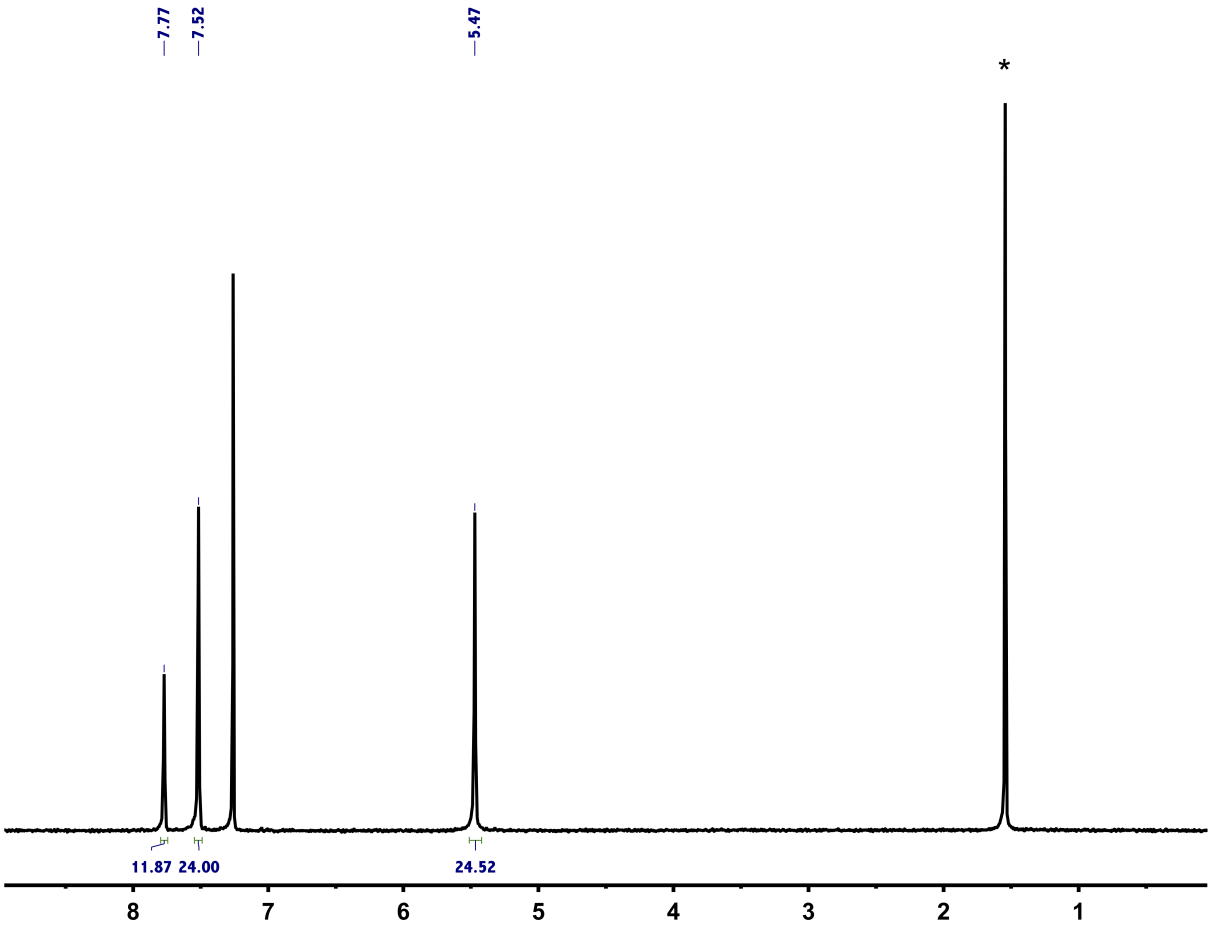

Figure B.1: ^{1}H NMR of DDB-F_{72}, * residual H_2O.

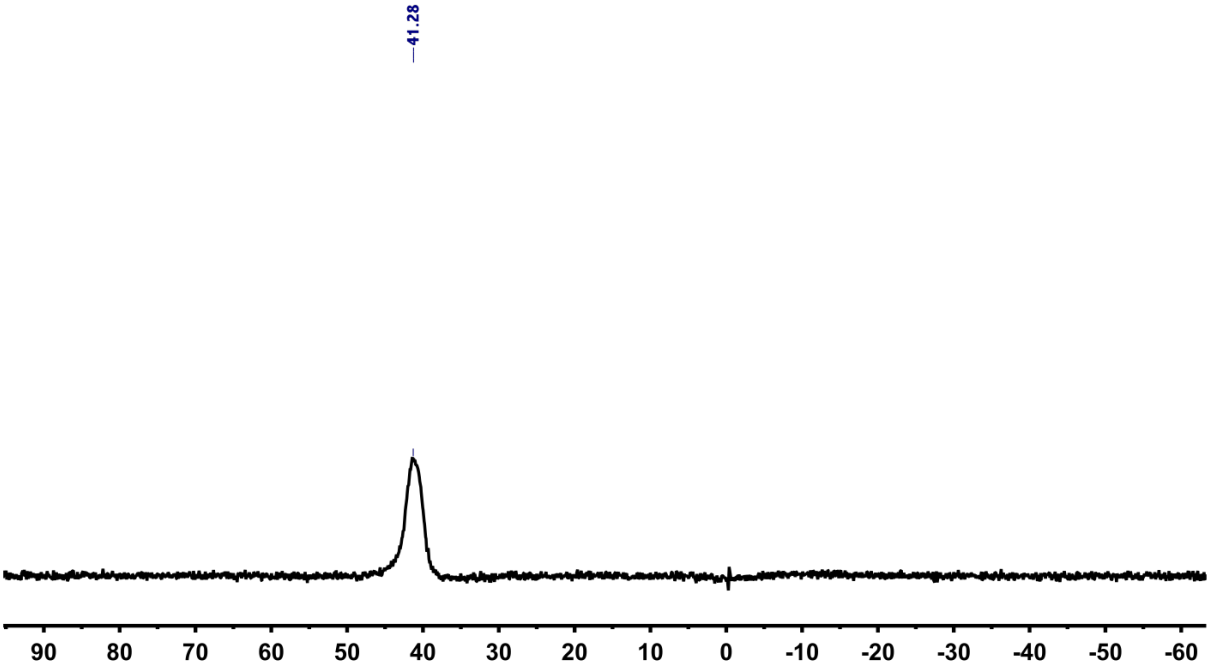

Figure B.2: ^{11}B NMR of DDB-F$_{72}$.

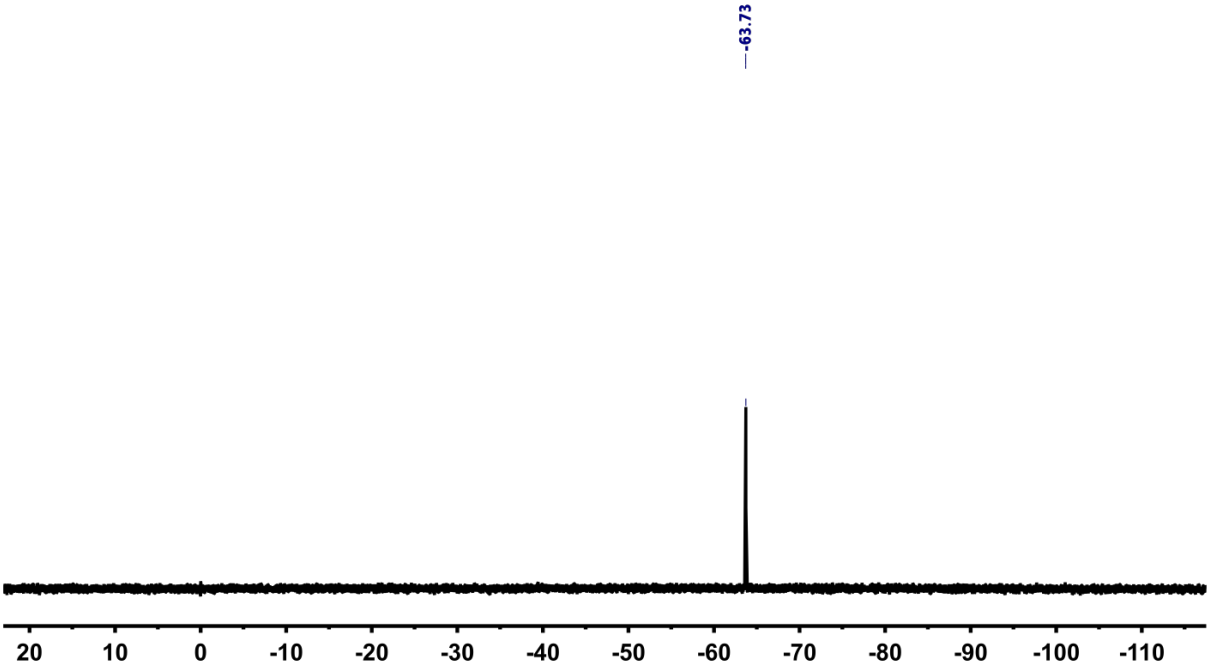

Figure B.3: ^{19}F NMR of DDB-F$_{72}$.

B.2 Experimental Methods

B.2.1 Cyclic Voltammetry

The redox potentials of F_4TCNQ and DDB-F_{72} were measured in-house by cyclic voltammetry using a CH Instruments CHI630D potentiostat with a glassy carbon disc working electrode, Pt wire counter electrode, and Ag/Ag^+ wire pseudoreference. All experiments were conducted at a 0.5 mM analyte concentration in 0.1M $[N^nBu_4]PF_6/CH_2Cl_2$ at a scan rate of 0.1 mV/s and referenced to an internal ferrocene standard. The solution was degassed by bubbling Ar, and the CV measurements were performed under Ar gas.

B.2.2 TD-DFT

Ground state geometry optimization of the neutral DDB-F_{72} molecule was performed using Turbomole[162] for which the initial coordinates were adopted from the single crystal X-ray structure. The τ-dependent gradient-corrected functional of Tao, Perdew, Staroverov, and Scuseria (TPSS)[163] with the def2-TZVP[164,165] basis set was used. In order to access the energies of the anion SOMO, the TD-DFT formalism was used with the hybrid functional of TPSS(TPSSh)[163,166] with cc-pvdz[167,168] basis set. Gaussian 09[169] was used for the excited state calculation and Avogadro was used for visualization.

B.2.3 Electron transfer self-exchange rate by NMR

Under an inert atmosphere, 0.1 mM stock solutions of $[DDB\text{-}F_{72}]^0$ and $[DDB\text{-}F_{72}]^-$ were prepared using 4:1 o-difluorobenzene:benzene as the solvent. Five aliquots of the oxidized species were then added to separate J-Young NMR tubes giving volumes of 0 L, 200 L, 400 L, 600 L, and 800 L respectively. To these samples, aliquots of the reduced species were added such that the final sampled volume totaled 800 L. This afforded five samples whose mole fraction of reduced species was near 1, 0.75, 0.5, 0.25, and 0 respectively. All samples were analyzed immediately on a Bruker 300 MHz NMR spectrometer and analyzed using iNMR software. A total of 64 scans of 65536 data points (2.04 Hz resolution) were collected from +20.0 to -216.0 ppm.

B.2.4 Film fabrication

Substrates were cleaned by sequential sonication in alconox detergent solution, deionized water, acetone, and isopropanol. Subsequent film preparation steps were carried out in nitrogen glove box atmosphere. P3HT films were spin-coated at a rate of 1000 rpm for 60 seconds from a 20 mg/mL polymer solution in orthodichlorobenzene, producing $\sim$120-nm thick films. The films were doped in a second step in which the dopant solution was deposited on the pre-cast polymer film and spin-coated at 4000 rpm for 10 seconds. All DDB-F_{72} and F_4TCNQ dopant solutions were prepared in dichloromethane at the concentrations stated in text. Film thicknesses were measured using a Dektak 150 stylus profilometer. Mass measurements were taken with a Mettler AT20 analytical microbalance. Dodecaborane clusters are stored in air and show no signs of degradation. The cluster is also structurally stable in solution, however, it can undergo a redox reaction wiht the solvent if left for too long. Solutions were used within a few days of making them. Doped films are stable under inert atmosphere for days.

B.2.5 Conductivity

Devices for conductivity measurements were fabricated on 1.5 cm $\times$ 1.5 cm glass substrates. Following film fabrication, electrodes were placed on the corners of the sample using PELCO conductive silver paint. The Van der Pauw method was used to measure conductivities in-house as well as the values reported in Table 1 of the main text, which were measured independently at Lake Shore Cryotronics on samples prepared for AC-Hall measurements (described below). Our Van der Pauw measurements were performed using a custom-made apparatus in ambient atmosphere using a Kiethley 2400 Sourcemeter controlled by Labview software where the maximum current sourced was held to 1 mW total power. All reported values were averaged over multiple measurements taken on at least 3 samples.

B.2.6 Sample Imaging

Optical images were taken using a Carl Zeiss Axiotech 100HD microscope. Scanning Electron Microscopy (SEM) images of the 1 mM DDB-F_{72} doped films have been studied using a JEOL

7500F HRSEM with a 5 kV accelerating voltage.

B.2.7 XPS

XPS was performed using a Kratos Axis Ultra DLD spectrometer with a monochromatic Al Kα radiation source and a charge neutralizer filament was used to control charging of the sample. A pass energy of 20 eV was used for all spectra with a 0.1 eV step size and 300 ms dwell time. All spectra were calibrated to the advantageous carbon 1s peak at 284.8 eV. Films for standard XPS were fabricated on sapphire substrates to minimize interference from the silicon 2s plasmon peaks with the boron 1s signal. In order to analyze dopant infiltration, spectra of the top (front) and bottom (back) of the films were obtained by floating films off glass substrates and placing them on copper tape. Floating was accomplished by cutting a grid pattern into the film using the free edge of a razor, and applying deionized water. No sacrificial layers such as poly(3,4-ethylenedioxythiophene) polystyrene sulfonate or polyacrylic acid were used as they were difficult to remove completely, which affected the obtained surface sensitive ratios. Analysis was performed using CasaXPS software and the relative sensitivity factors used were from the CASAXPS library.

B.2.8 GIWAXS

Films for 2-D GIWAXS measurements were prepared on silicon substrates. Measurements were performed at the Stanford Synchrotron Radiation Lightsource on beamline 11-3 using a wavelength of 0.9742 Å with an incidence angle of 0.12°. Diffraction patterns were collected in a helium chamber to increase signal-to-noise with a sample to detector distance of 250 mm and a spot size of $\sim$150 μm on the image plate. The 2-D diffractograms were radially integrated from to 0-10° and 80-90° to obtain the in-plane and out-of-plane diffraction patterns. The software package WxDiff was used to reduce the GIWAXS data and subsequent analysis was performed in IgorPro. The intensities on the opposite sides of the diffractogram (90-180°) were also checked to ensure they matched the chosen limits. Each integration was background corrected for substrate scattering. The subtractions were performed on the raw scattering data to ensure that no errors occurred due to background subtraction. To ensure reproducibility in diffraction intensity and shape, all samples were made and measured in triplicate.

B.2.9 Spectroscopy

UV-VIS-NIR absorption spectra were acquired from 300-2500 nm using a Shimadzu UV3101PC UV-VIS-NIR Scanning Spectrophotometer for films prepared on both glass substrates and KBr pellets (cleaned in chlorobenzene and acetone). FTIR data was acquired from 220-7000 cm^{-1} for films on KBr plates using a Jasco FT/IR-420 spectrometer.

B.2.10 AC-Hall

Devices for AC-Hall effect measurements were prepared on 1 cm $\times$ 1 cm glass substrates. Following film fabrication, silver electrodes were deposited on the corners of the samples with an Angstrom Engineering, Inc. evaporator at a pressure of $< (1\times10^{-6}$ Torr). The silver layer was deposited at a rate of 0.5 Å/s up to 10 nm, followed by 1 Å/s to a final total thickness of 60 nm. Samples were packaged in scintillation vials under argon atmosphere before being sent to Lakeshore Cryotronics for testing. AC magnetic field Hall measurements were performed with a Lake Shore model 8400 series AC Hall probe system at a field strength of 0.6484 T and a current of 1.00×10^{-5}. Nitrogen was flowed continuously over the samples to reduce error from sample degradation. The technique is similar to DC Hall Effect, but with an oscillating magnetic field at a certain frequency such that the hall voltage (resulting from the Lorentz force) becomes time dependent. This allows the hall voltage to be distinguished from the static misalignment offset voltage, which is large in low mobility materials.

B.3 Electron transfer self-exchange rate by NMR

According to Marcus-Hush theory of electron transfer (ET), the rates of electron self-exchange (k_{et}) can be directly related to rates of *intermolecular* ET with other redox species and the total reorganization energy (λ_{tot}) for ET.[170] The kinetics of electron self-exchange in DDB-F_{72} were investigated by dynamic NMR through the application of line broadening experiments. The NMR spectrum was recorded for samples in which the mole fraction of the reduced species ([DDB-F_{72}]$^{-}$) was varied relative to the oxidized species ([DDB-F_{72}]^{0}). The NMR line shape is highly

sensitive to the rate of exchange and when exchange is in the fast regime $k(C_{tot}) >> 2\pi(\Delta\nu)$, the chemical shifts of the exchanging species are found to be the averages of the diamagnetic and paramagnetic chemical shifts weighted by their respective mole fractions.[171] Rate constants can then be determined by equation B.1 after spectral deconvolution:[171]

$$k_{et} = \frac{4\pi\chi_{red}\chi_{ox}(\Delta\nu)^2}{(w_{ro} - \chi_{red}w_{red} - \chi_{ox}w_{ox})C_{tot}} \tag{B.1}$$

Here, χ_{red} and χ_{ox} are the mole fractions of reduced and oxidized species, $\Delta\nu$ is the difference in chemical shift between reduced and oxidized species in Hertz, w_{ro} is the peak width at half maximum of the mixture in question, w_{red} and w_{ox} are the peak widths at half maximum of the pure reduced and oxidized species, and C_{tot} is the total concentration in moles per liter. Although any NMR active nucleus may be used to determine the rates of self-exchange, in this present study, ^{19}F NMR was used to determine the rates of self-exchange as the large number of fluorine atoms present offered an excellent spectroscopic handle.

The NMR scans taken for five mole fractions of [DDB-F_{72}]$^{0/-}$ at 20 °C (bottom), 40 °C (middle), and 60 °C (top) in a solution of 4:1 o-difluorobenzene:benzene are shown in Fig. B.4. The lack of coalesced spectra across a 40 °C temperature range suggest that intermolecular self-exchange for the [DDB-F_{72}]$^{0/-}$ redox couple occurs much slower than the NMR time-scale[172] ($k_{et} < 1.2 \times 10^3$ s^{-1} or $t_{et} < 0.84$ ms). This timescale is orders of magnitude slower than the expected collision time for two clusters. The concentration of DDB-F_{72} used was 0.1 mM, which means there are $\sim$10 particles in a 550 nm^3 volume, or an average distance between clusters of $\sim$8 nm. According to the Stokes-Einstein equation, the diffusion constant of 2-nm spherical particles in a typical organic liquid at room temperature is $\sim 1.8\times10^{-10}$ m^2/s. This means one of our DDB-F_{72} clusters should diffuse far enough to encounter each other on a 60 ns time scale, which is much faster than the 840 μs timescale of the NMR experiment. Thus, even after over 1000 collisions between particles, there is no sign of motional narrowing and thus ET between the clusters. These results support high intrinsic barriers to ET most likely attributed to small electronic couplings (H_{ab}) and poor orbital overlap between self-exchanging pairs.[127–129]

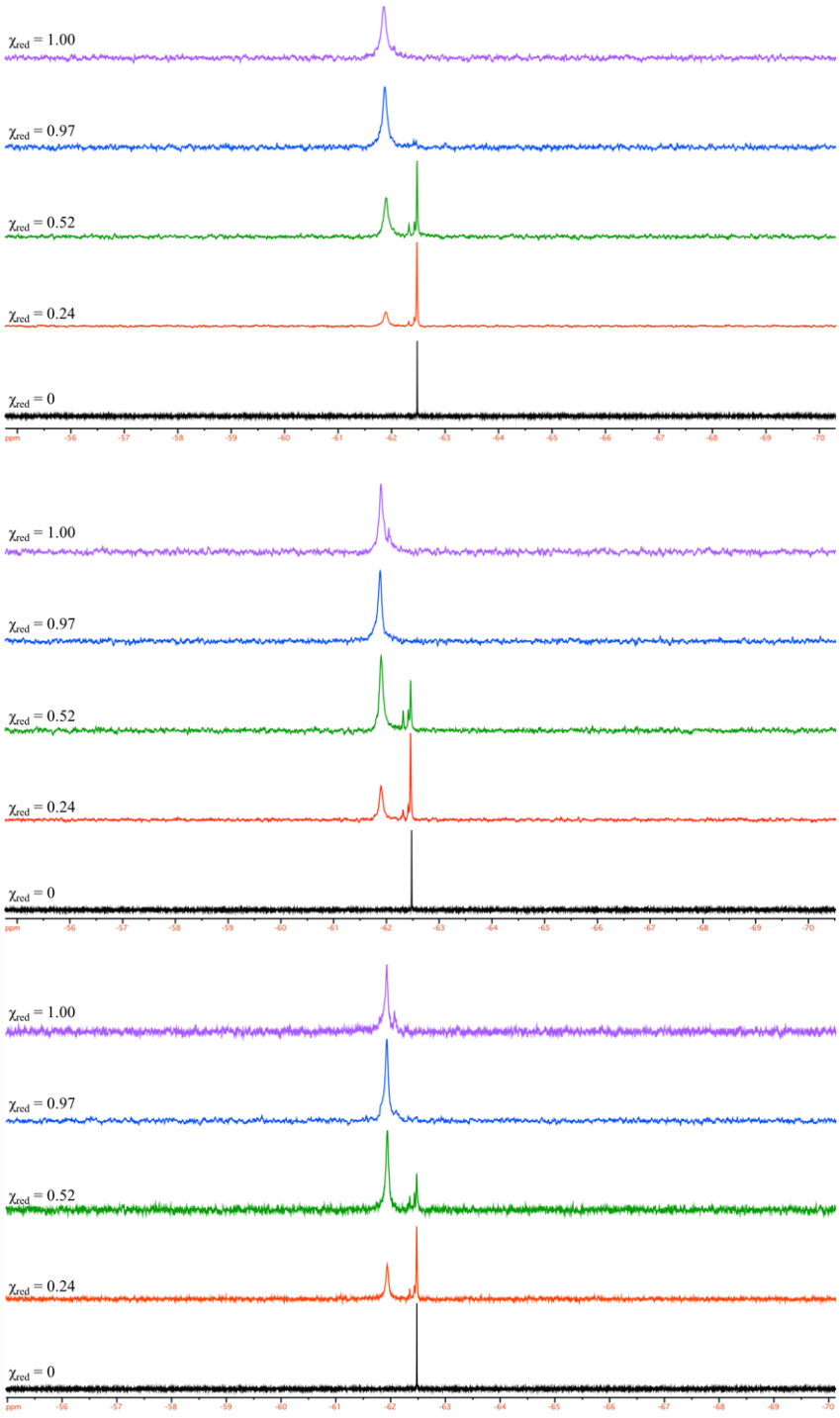

Figure B.4: ^{19}F NMR of the one-electron self-exchange interaction of the [DDB-F_{72}]$^{0/-}$ redox couple with increasing mole fraction of [DDB-F_{72}]$^{-}$ from bottom to top in any given series. Spectra were recorded at 20 °C (bottom), 40 °C (middle), and 60 °C (top) in a 4:1 o-difluorobenzene:benzene mixture and referenced to an internal standard of trifluoroethanol sealed in a capillary tube.

The minimal distortion observed between the solid state structures of $[DDB\text{-}F_{72}]^0$ and $[DDB\text{-}F_{72}]^-$ shown in Fig. B.5 suggests that reorganization energies do not contribute significantly to the electron self-exchange barrier in these systems. The largest observed distortion is found in the capping benzyl ligands, which most likely arises from packing in the solid state as they are believed to be freely rotating in solution. Instead, the lack of a large chemical shift between the ^{19}F signals in these two oxidation states suggests that the benzyl capping ligands experience minimal electron-density and that the odd electron in $[DDB\text{-}F_{72}]^-$ is primarily localized in the core of the borane clusters (see DFT results). The capping ligands effectively screen the core and prevent donor-acceptor overlap from occurring. This ultimately leads to negligible electronic coupling and slow rates of electron self-exchange.

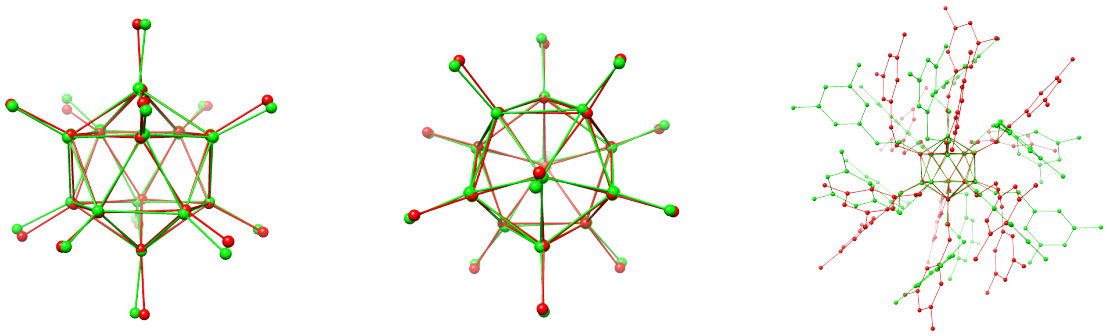

Figure B.5: Overlapped solid state structures of $[DDB\text{-}F_{72}]^0$ (green) and $[DDB\text{-}F_{72}]^-$ (red) obtained from single crystal X-ray diffraction studies. Left and middle figures highlight the minor structural rearrangement in the core upon a one electron reduction while the right side highlights the capping ligands. Capping benzyl ligands have been omitted for clarity in the left and middle figures while hydrogen and fluorine atoms have been omitted for the right figure.

B.4 Cyclic Voltammetry

In order to characterize the offset between the HOMO of the polymer and the LUMO the dopants, we performed side-by-side cyclic voltammetry on F_4TCNQ and DDB-F_{72}. The 2-/1- transition occurs at -0.48 V for F_4TCNQ and -0.07 V for DDB-F_{72}, while the 1-/0 transition occurs at $+0.16$ V for F_4TCNQ and $+0.67$ V for DDB-F_{72}. All potentials are referenced to an internal ferrocene standard. The redox potential of DDB-F_{72} is therefore $\sim$0.5 V higher than F_4TCNQ giving it a much higher energetic driving force for doping.

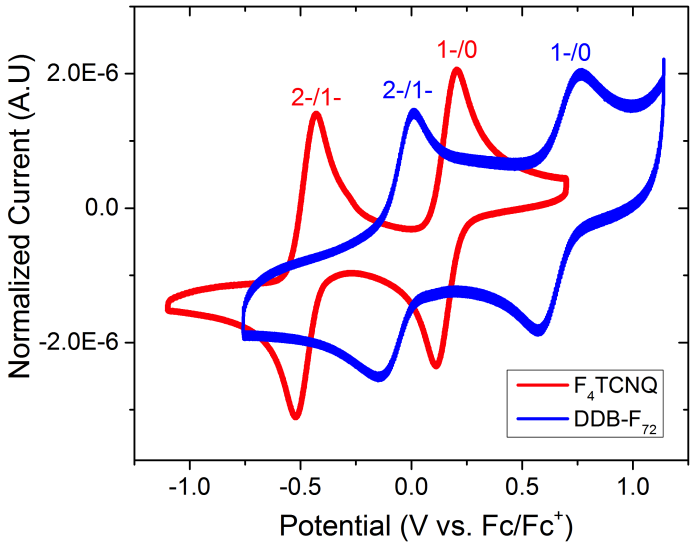

Figure B.6: Cyclic voltammogram of F_4TCNQ (red) and DDB-F_{72} (blue) demonstrating two reversible single-electron oxidation/reductions.

B.5 Conductivity data

Devices were fabricated as described in the main text on 1.5 cm $\times$ 1.5 cm glass substrates with silver paste applied as electrical contacts. The Van der Pauw technique[125] was used to measure conductivity, a type of four-point probe method in which current is flowed from negative to positive along one edge of the sample and the voltage is measured across the opposite edge. The sample is then rotated 90°, and the measurement is repeated. The resistance values obtained from the slope of the $I-V$ curves are fit to the Van der Pauw equation to obtain the sheet resistance ($R_\square$). The thickness (t) of the samples was obtained in three locations using a Dektak 150 stylus profilometer. The reported values for $R_\square$ and t in Table B.1 and Table B.2 are averaged over all measured values for all samples while the reported conductivities (σ) are averaged over the values obtained for each sample (i.e., the average $R_\square$ and t for each sample were used to calculate the conductivity of that sample, and the obtained conductivities were averaged over the samples to yield the values reported.) The ideal conductivities (σ_{id}) were calculated using the initial polymer thickness of 120 nm. In each case, the reported error is the standard deviation of the measurements. The calculation of idealized conductivity makes a bigger difference for the DDB-F_{72} samples due to the large thickness increase due to incorporation of the dopant, which does not conduct as shown by the self-exchange experiments and the p-type conductivity found using AC hall measurements.

Table B.1: F_4TCNQ Conductivity Measurements

[ ] (mM)	$R_\square$ ($\Omega/\square$)	t (nm)	σ (S/cm)	σ_{id} (S/cm)
0.05	$(7.11 \pm 1.1) \times 10^7$	122 ± 2	0.0012 ± 0.0002	0.0012 ± 0.0002
0.3	$(2.16 \pm 0.39) \times 10^5$	129 ± 4	0.37 ± 0.06	0.39 ± 0.06
0.5	$(1.23 \pm 0.35) \times 10^5$	130 ± 5	0.7 ± 0.2	0.7 ± 0.2
1	$(5.12 \pm 0.19) \times 10^4$	139 ± 3	1.41 ± 0.06	1.63 ± 0.06
3	$(4.22 \pm 0.10) \times 10^4$	143 ± 3	1.66 ± 0.04	1.98 ± 0.04

Table B.2: DDB-F_{72} Conductivity Measurements

[ ] (mM)	$R_\square$ ($\Omega/\square$)	t (nm)	σ (S/cm)	σ_{id} (S/cm)
0.05	$(4.0 \pm 1.0) \times 10^7$	141 ± 5	0.0018 ± 0.0004	0.0022 ± 0.0006
0.3	$(2.11 \pm 0.77) \times 10^4$	190 ± 22	2.8 ± 0.9	4 ± 2
0.5	$(8.5 \pm 1.2) \times 10^3$	213 ± 27	5.6 ± 0.5	10 ± 1
1	$(2.63 \pm 0.21) \times 10^3$	296 ± 12	12.9 ± 0.7	32 ± 3
3	$(3.50 \pm 0.27) \times 10^3$	306 ± 16	9.4 ± 0.4	24 ± 2

Although the conductivity values we report do not represent an all-time record, to the best of our knowledge, the 12.7 S/cm we report is the highest achieved for solution doping of a film of commercially-available P3HT. It is important to note that all of the highest conductivities reported for F_4TCNQ-doped P3HT in the literature were achieved for films where the order was carefully preserved (e.g., by vapor doping, by using 100% regioregular P3HT, keeping the films very thin ($\leq$25 nm) to enhance their crystallinity/crystalline domain orientation, or by casting the polymer onto a rub-aligned substrate). Table B.3 below shows some of these leading conductivity values for F_4TCNQ-doped P3HT from the literature. Given that our DDB-F_{72}-doped films are $\sim$300-nm thick and have almost no crystallinity, the conductivities and mobilities we achieve are completely unprecedented, demonstrating the importance of anion interactions on the conductivity.

Table B.3: Conductivity values for F_4TCNQ-doped P3HT from literature.

Journal	Year	Corr. Author	Conductivity (S/cm)	Method
Chem. Mater.	2018	Chabinyc	50	Vapor (atmospheric pressure, 80 °C polymer)
RSC Adv.	2018	Muller	12	Vapor (atmospheric pressure, 60 °C polymer)
Macromolecules	2017	Muller	12	Vapor (atmospheric pressure, 60 °C polymer)
Ad. Fun. Mater.	2017	Schwartz	9	Solution (100% RR P3HT)
JPC Lett	2015	Schwartz	5.5	Solution
Adv. Fun. Mater.	2017	Brinkmann	22 $\parallel$, 3 $\perp$	Solution (Rub aligned)

B.6 Stability measurements on doped films

In order to assess the stability of our doped films we measured the conductivity of P3HT films doped with both DDB-F_{72} and F_4TCNQ as a function of time in both an inert environment (argon glovebox) and in air. Figure B.7 shows that the doped films are quite stable under inert atmosphere for 24 hours (panel a), but show signs of degradation over the same time period in air (panel b), with a reduction in conductivity of about 25% for the DDB-F_{72} doped film and about 50% for the F_4TCNQ doped film. Interestingly, the DDB-F_{72}-doped film only decreases from its initial conductivity after 6 hours of air exposure, whereas the conductivity of the F_4TCNQ-doped sample decreases from the beginning of the measurement. Thus, the stability of DDB-F_{72}-doped P3HT films is comparable to but slightly better than that of F_4TCNQ-doped P3HT films.

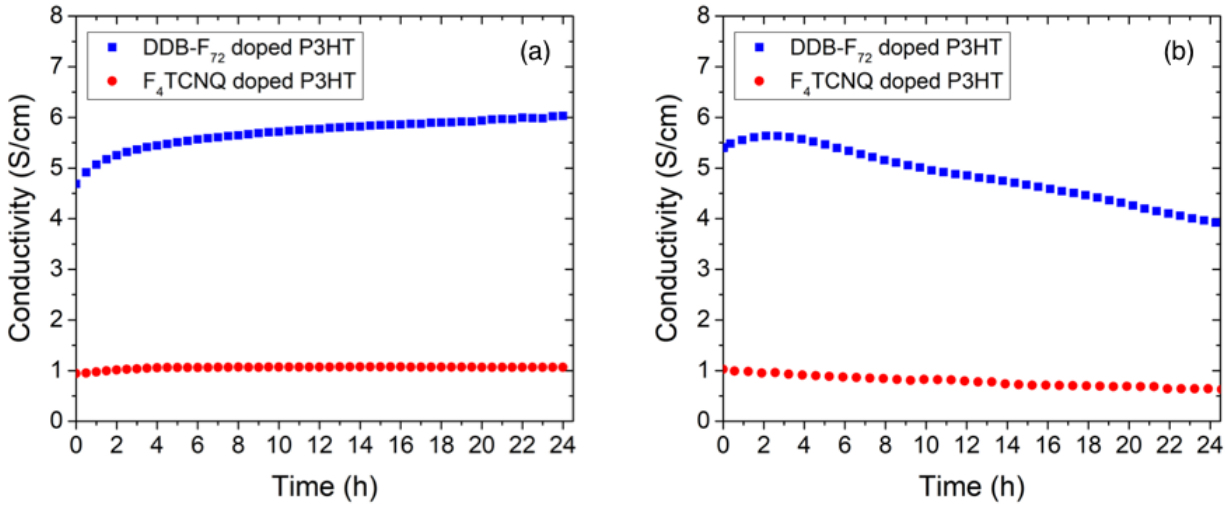

Figure B.7: Conductivity over time of DDB-F_{72} (blue) and F_4TCNQ (red) doped P3HT films in the glovebox under inert argon atmosphere (a) and under ambient atmosphere in air (b) as a function of time after film fabrication as measured by 4-point probe.

To see how robust the stability of the DDB-F_{72} films are under inert atmosphere, the conductivity of three samples were also measured on a daily basis. Over a period of 5 days, the conductivity stayed constant within an error of 2 standard deviations. These results suggest that the DDB-F_{72}-doped films would be stable essentially indefinitely if packaged appropriately.

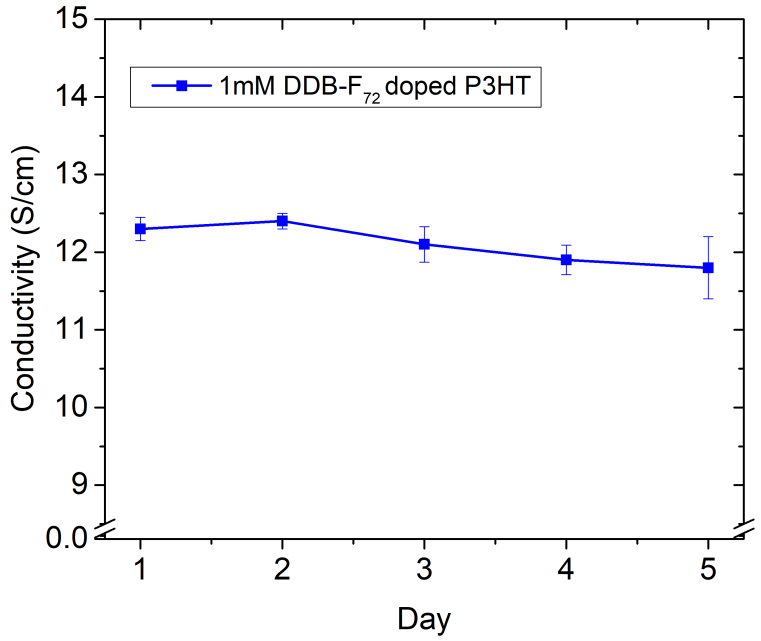

Figure B.8: Conductivity of DDB-F_{72}-doped P3HT film samples measured over 5 days via the Van der Pauw method. The samples were briefly exposed to air for each measurement and then returned for storage under inert atmosphere. The error bars are the standard deviation of measurements on three separate samples.

B.7 Optical and SEM images of the Doped Film's Surface

Given the large film thickness increase observed following doping P3HT with DDB-F_{72}, we took optical and SEM images of the surface of the films to examine the possibility of formation of an overlayer of boron clusters. Figure B.9 shows images of the clusters at 5× (a) and 50× (b,c) showing the appearance of a few particles on the surface of the film. The particles light up under polarized light in (c) indicating that they are likely crystalline in nature; we conclude that these must be small crystallites of boron clusters on top of the film. The particles are sparsely distributed, which indicates that there is not an overlayer of boron cluster crystallites on top of the film.

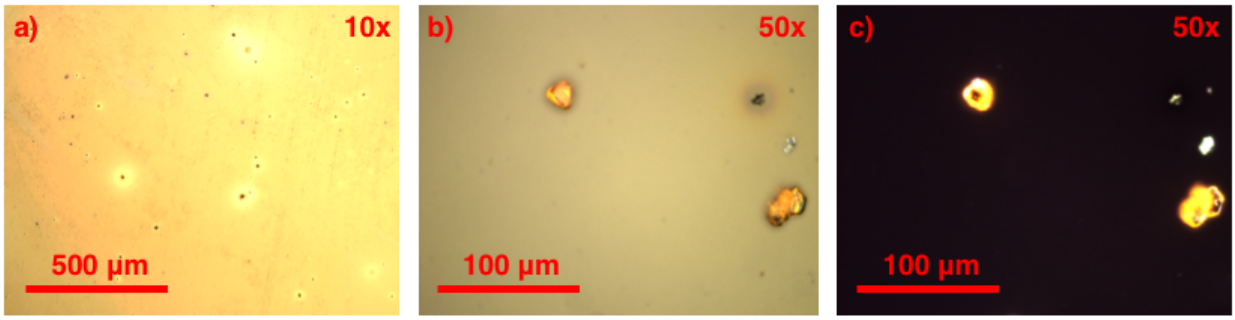

Figure B.9: Optical images of 1mM DDB-F_{72} doped P3HT at 5x (a) and 50x (b) magnification as well as at 50x magnification under polarizers (c).

Figure B.10 shows SEM images of a 1 mM DDB-F_{72} doped film of P3HT. The images show a clear pattern of sharp cracks, which are likely due to the expansion and contraction of the film upon swelling and deswelling during the solution sequential doping process. We believe that during SqP doping, the peak thickness of the film is greater than the final 300-nm thickness, so that as the solvent evaporates and the film shrinks to its final (albeit still highly swollen size), the strain from drying opens these sharp crack-like features. The sharp features are not what one would expect if the DDB-F_{72} clusters were immiscible with the P3HT and formed a dewetting layer on top, as a dewetting layer would have smooth interfaces to minimize the surface tension between the immiscible phases. Thus, the optical and SEM images both confirm the conclusion from the XPS data in the main text that SqP mixes the DDB-F_{72} clusters throughout the P3HT underlayer.

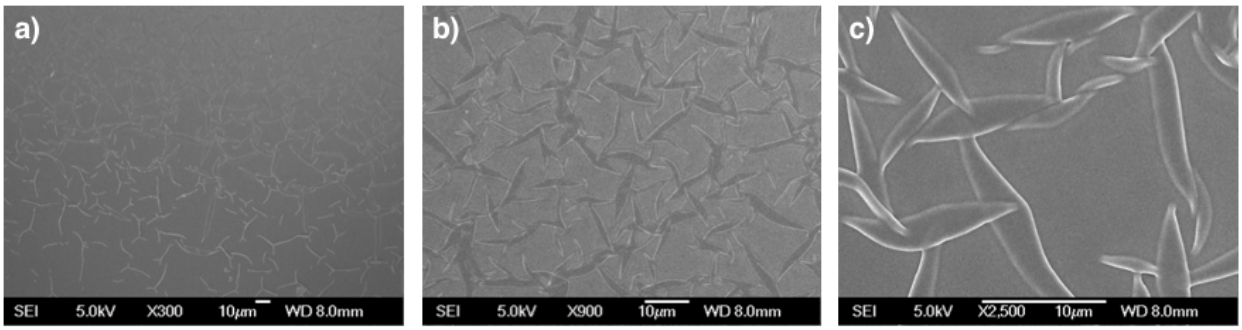

Figure B.10: SEM images of a P3HT film that has been doped with 1 mM DDB-F_{72} at low to high magnification (a-c).

B.8 XPS

Table B.4 shows all of the peak fit information for pure DDB-F_{72}, DDB-F_{72} [1-], a 1 mM DDB-F_{72} doped P3HT film on sapphire substrate and the front and back of a 1 mM DDB-F_{72} doped P3HT as well as an undoped P3HT films obtained via the floating procedure described in the methods section. Figure B.11 shows the data and peak fits for each of the doped films. Floating the films off the substrate allowed us to obtain information about the cluster content at both the top (front) and bottom (back) surfaces of the films. The sulfur signal comes only from P3HT whereas the B and F signals come only from DDB-F_{72}. Integrated peak areas were used to calculate the B:S and F:S ratios reported in the main text. The drop in relative B:S and F:S peak intensity ratios for the doped film on sapphire compared to the floated films indicates that some clusters gets washed off during the floating process, but this does not prohibit us from obtaining relative information about the cluster content at the top and bottom surfaces. As discussed in the main text, the B:S and F:S ratios are roughly similar at the top and bottom of the film (and if anything slightly higher at the bottom of the film), indicating that the clusters do indeed penetrate throughout the polymer film. To ensure that cluster was not somehow being added to the films during the floating process, we floated a pure P3HT film in the same wash used for the doped film. As shown by the peak fit information in Table B.4, no boron, fluorine or sulfur peaks were found, indicating that the floating process indeed cannot add clusters to the films. Finally, based on the boron peak positions, the doped films contain only the DDB-F_{72} anion, indicating that the cluster effectively dopes the film and no neutral clusters are in the film or form an excess overlayer on top of the film.

Table B.4: XPS peak fits

	B			S					F		
	Position (eV)	FWHM (eV)	Area (CPS*eV)	Position S (eV)	FWHM (eV)	Position SO (eV)	FWHM (eV)	Area (CPS*eV)	Position (eV)	FWHM (eV)	Area (CPS*eV)
Pure [0]	189.83	1.33	465.36	-	-	-	-	-	687.78	1.82	5939.64
Pure [1-]	188.88	1.03	310.44	-	-	-	-	-	687.7	1.61	2933.86
Doped film On substrate	188.93	0.91	392.1	163.50/ 164.66	0.88	164.37/ 165.53	1.78	259.36	687.79	1.67	4485.36
Doped film Float top	189.05	0.95	118.19	163.79/ 164.95	0.77	165.05/ 166.21	1.95	366.25	688.38	1.58	1149.69
Doped film Float bottom	189.2	1.28	143.23	163.75/ 164.91	0.79	165.30/ 166.46	1.67	326.13	688.38	1.61	1545.56
Control Float top	-	-	-	163.69/ 164.85	0.78	-	-	588.79	-	-	-
Control Float bottom	-	-	-	163.72/ 164.88	0.76	-	-	569.68	-	-	-

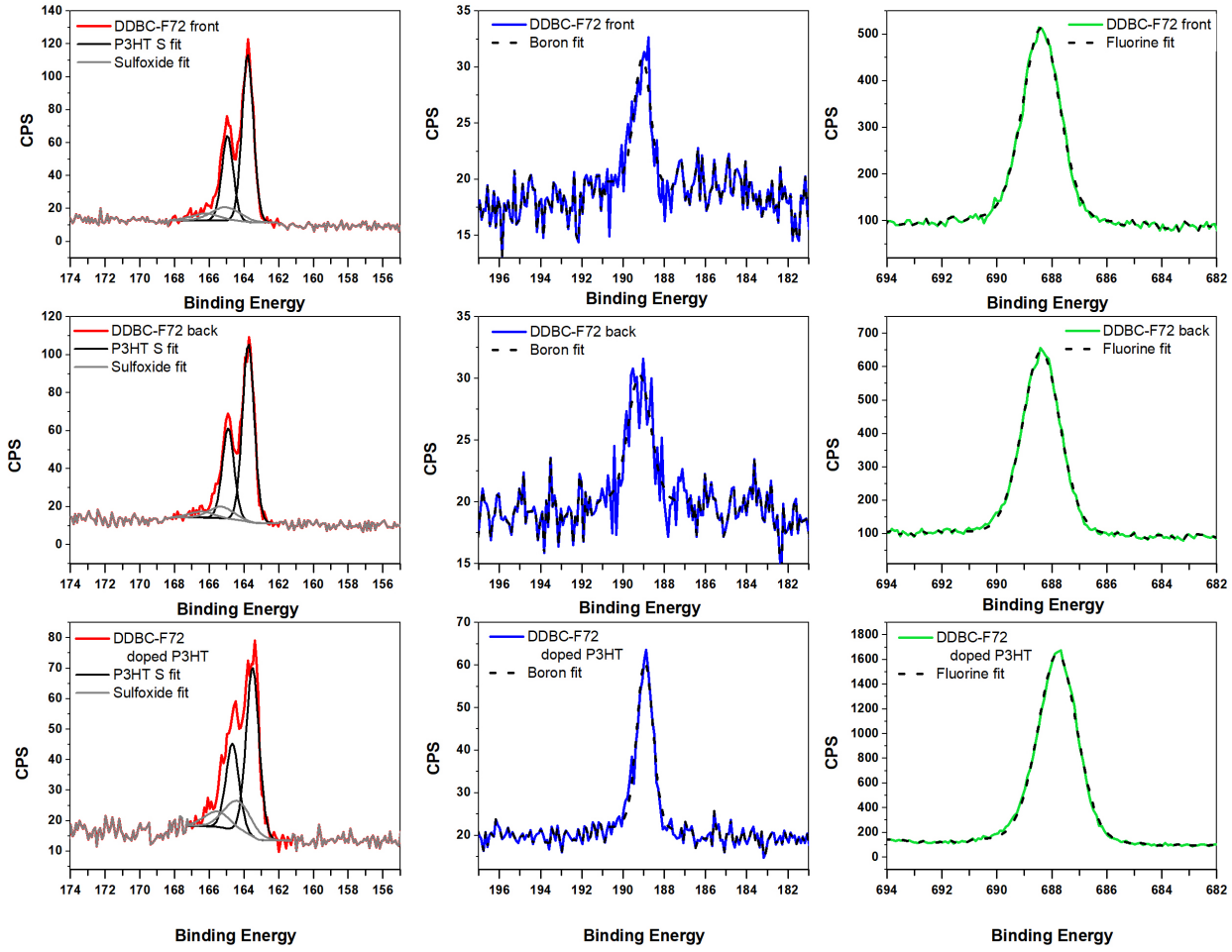

Figure B.11: XPS data and S, SO, B, and F peak fits for DDB-F_{72} doped P3HT (bottom), floated back of DDB-F_{72} doped P3HT film (middle), and floated front of DDB-F_{72} doped P3HT (top).

B.9 GIWAXS

The full integration of the diffractogram for a drop-cast film of pure DDB-F_{72} out of DCM is shown in Figure B.12. The diffractogram displays sharp peaks with no broadening, as is typically seen for small crystallites. The dopant induced peaks indicated by (*) in Figure 2 of the main text therefore must involve the polymer as they have the same broadening and texture as the polymer peaks.

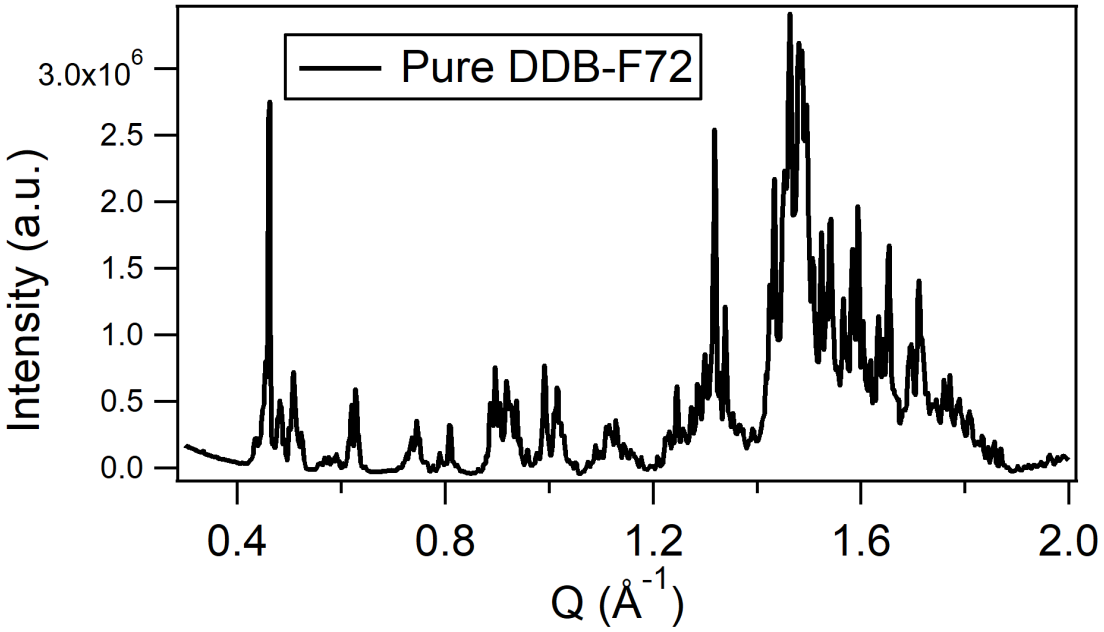

Figure B.12: Full integration of GIWAXS diffractogram for pure DDB-F_{72} showing sharp crystallite peaks.

Figure B.13 shows the full 2D-GIWAXS diffractograms for pure P3HT and P3HT doped with different concentrations of DDB-F_{72}. The out-of-plane and in-plane integrations are shown in the main text and the peak fit information for the out-of-plane (100) and in-plane (010) are shown in Table B.5 and Table B.6, respectively. No peak fit information is reported for the in-plane (010) 1 mM DDB-F_{72} doped sample due to high amounts of amorphous π-scattering making definition of this peak difficult.

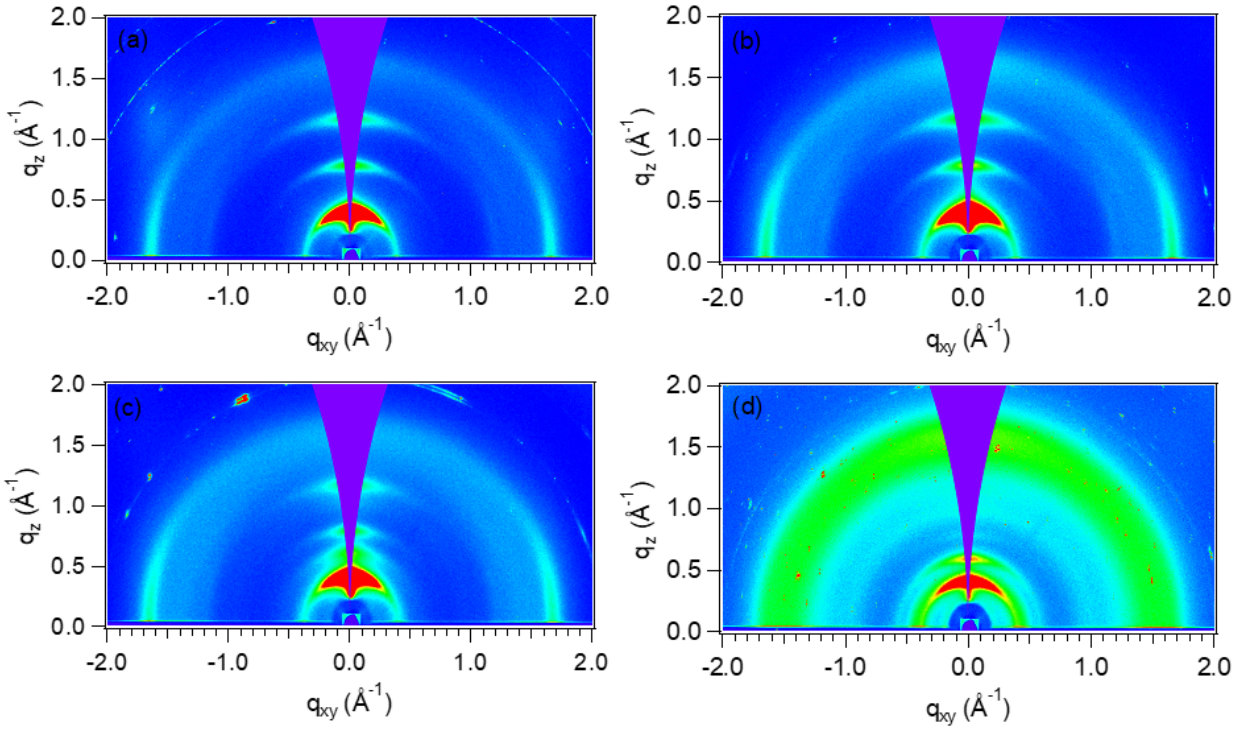

Figure B.13: Full 2D-GIWAXS diffractograms for pure undoped P3HT (a), P3HT doped with 0.05 mM (b), 0.3 mM (c), and 1 mM DDB-F_{72} (d).

Table B.5: Out-of-plane (100) Peak Fit Information

Sample	Location (Q)	d-spacing (Å)	Height	Area	FWHM
Undoped P3HT	0.396	15.9	3.75×10^6	2.04×10^5	0.051
0.05 mM DDB-F_{72}	0.403	15.6	3.48×10^6	1.99×10^5	0.054
0.3 mM DDB-F_{72}	0.398	15.8	1.36×10^6	1.72×10^5	0.119
1 mM DDB-F_{72}	0.396	15.9	9.98×10^5	5.20×10^5	0.049

Table B.6: In-plane (010) Peak Fit Information

Sample	Location (Q)	d-spacing (Å)	Height	Area	FWHM
Undoped P3HT	1.66	3.79	1.84×10^4	1.82×10^3	0.093
0.05 mM DDB-F_{72}	1.67	3.76	1.72×10^4	1.93×10^3	0.106
0.3 mM DDB-F_{72}	1.68	3.73	1.56×10^4	1.83×10^3	0.110
1 mM DDB-F_{72}	-	-	-	-	-

B.10 Spectroscopic Characterization

Figure B.14 shows the absorption spectra for films of pure and doped P3HT with different concentrations of DDB-F_{72} in DCM. The inset shows the standard energy band diagram for the formation of polarons. In the doped films, we see spectroscopic signatures of the P1, P2, and P3 transitions and a bleach of the neutral polymer absorption. The absorption in the 2.3-eV region contains contributions from the neutral (dashed yellow curve) and anionic (dashed pink curve) forms of DDB-F_{72} as well as any residual undoped P3HT (black curve), making it difficult to deconvolute the individual contributions of each component in the doped films. The intensity of the polaron bands increase monotonically up to 1 mM, but at at the 3 mM concentration, there is a slight decrease in optical density for these transitions. This indicates that less cluster is infiltrating into the film despite the higher dopant concentration. We suspect, given the colloidal nature of the 3-mM DDB-F_{72} solution, that there may actually be fewer free solubilized clusters in solution due to an equilibrium with clusters of DDB-F_{72} clusters. Additionally, the morphology of the 3-mM doped film is likely worse due to the colloidal nature of the solution, resulting in the observed slight drop in conductivity.

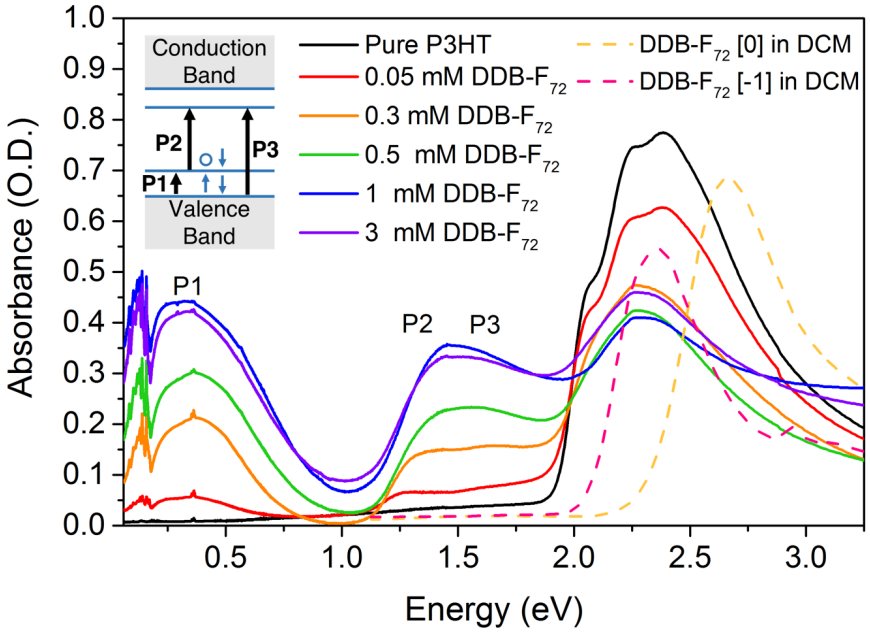

Figure B.14: Combined FTIR and UV-vis-NIR absorption data for pure P3HT (black curve), P3HT doped with different molar concentrations of DDB-F_{72} (colored solid curves), and neutral (yellow dashed curve) and reduced (pink dashed curve) DDB-F_{72} cluster in DCM.

B.11 Transport mechanisms from temperature dependent behavior of the conductivity

The dominant charge transport mechanisms can be determined from the temperature dependence of the conductivity.[173–176] We looked at the conductivity of our 1 mM DDB-F_{72}-doped P3HT films over a 50 K to 300 K temperature range. Figure B.15 shows the conductivity plotted against the temperature raised to various fractional powers, allowing us to visualize agreement with the power laws as straight lines. At low temperatures, the $T^{1/2}$ plot yields a straight line, indicating the temperature dependence of the low temperature region can be described by the Efros Shklovskii Variable Range Hopping (VRH) model,[173] which means that Coulomb interactions still dominate. At higher temperature, the charge transport mechanism transitions over to a traditional Mott VRH model[174] with a $T^{1/4}$ temperature dependence, which disregards Coulomb interactions and suggests more diffusive transport. A more analytical approach to extract transport mechanisms is to perform logarithmic differentiation to linearize the temperature-dependent conductivity,[175,176] as shown in Figure B.16. By fitting the different slopes, we again find Efros Shklovskii VRH at low temperatures and Mott VRH at high temperatures. As we approach room temperature there is a drastic decrease in the T-dependence of the conductivity, indicating a regime that deviates from hopping-dominated transport and is approaching a diffusive mechanism of charge transport. This is very similar to behavior we observed in a previous study that compared P3HT of different crystallinity doped with F_4TCNQ.[87] Only in the most crystalline 100% regioregular samples was the $T^{1/4}$ temperature dependence observed over the same temperature range. By contrast, we know from our GIWAXS measurements that the crystallinity of the DDB-F_{72} doped P3HT is very low, exposing the importance of counterion shielding for better charge transport. In the F_4TCNQ samples, due to the proximity of the counterion, the only way to achieve diffusive transport is through the P3HT crystallites.

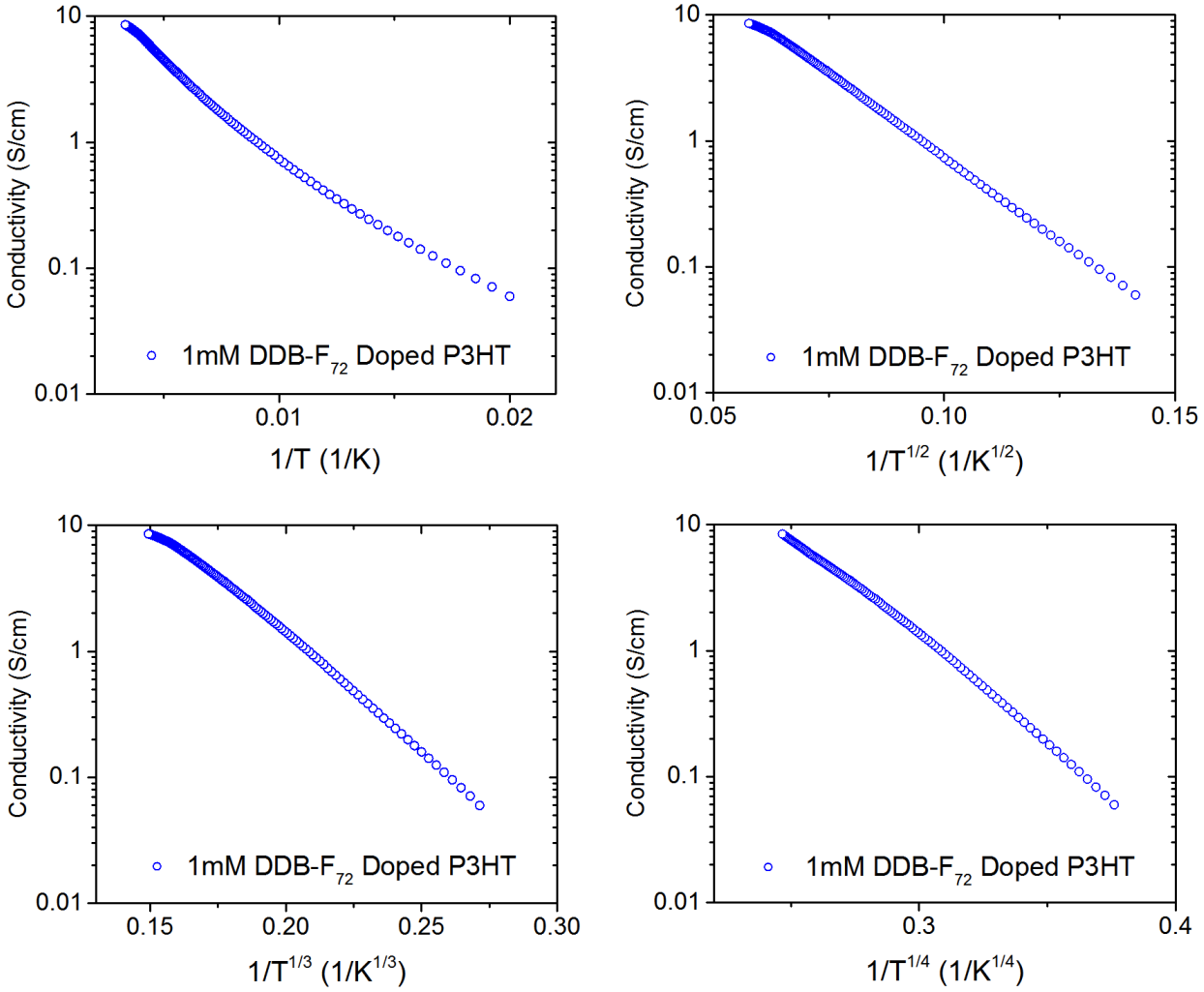

Figure B.15: Conductivity of 1 mM DDB-F_{72} doped P3HT as a function of temperature, plotted as a function of inverse temperature raised to various powers that correspond to different transport models.

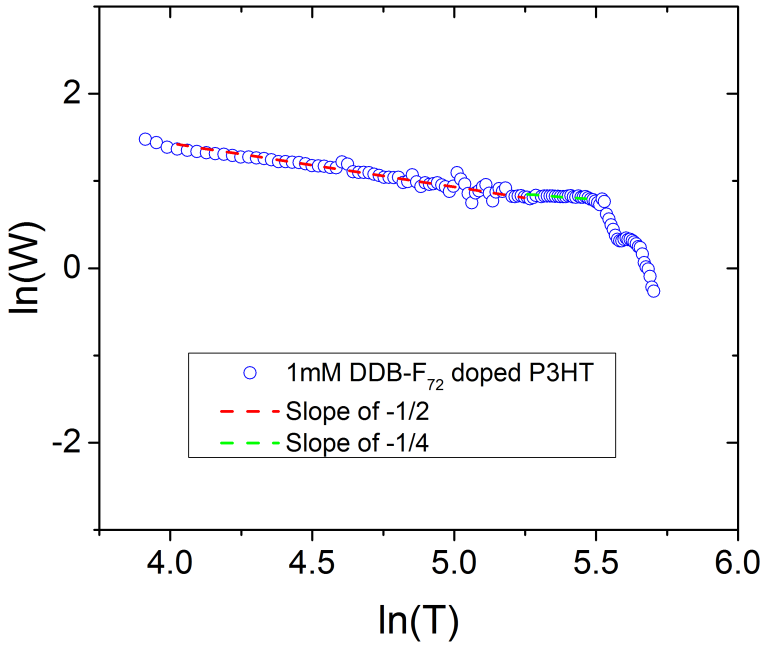

Figure B.16: Logarithmic derivative of the resistivity ($W = -dln(\rho)/dln(T)$) vs. $ln(T)$. The dashed lines are linear fits with the corresponding slopes given in the legend.

B.12 AC Hall measurements

The carrier concentrations we report were obtained through AC Hall measurements using the traditional Hall coefficient equations, which assume band-like transport. However, as we have just shown in the previous section, band-like transport is only beginning to occur at room temperature and carrier transport in our films still likely consists of both band-like and hopping-type mechanisms. As Podzorov and coworkers have shown[137] and noted in the main text, Hall effect measurements in organic semiconductors likely result in an overestimate of the carrier density due to different behavior of these carriers. Although any band-like carriers will experience both the Lorentz and electric forces, the hopping carriers only respond to the electric forces, resulting in carriers being moved to opposite sides of the channel and thus a reduced hall voltage, which is inversely proportional to the reported carrier density. The reported mobilities are calculated from both an independent measurement of the sample conductivity as well as the Hall voltage, this time in a direct proportionality, thus resulting in an underestimate of the mobility. We therefore note that the mobilities we report are likely underestimated, with correspondingly overestimated carrier densities, but this is true for both the F_4TCNQ- and DDB-F_{72}-doped P3HT samples that we use comparison.

B.13 Calculation of dopant density based on mass measurements

One simple method to obtain an estimate of the doping efficiency (the number of free carriers produced over the dopant molecules) is to combine our AC-Hall measurements with an estimate of the dopant density by measuring the change in mass after doping. Using the measured mass increase and film volume (1.5 cm $\times$ 1.5 cm $\times$ 300 nm for DDB-F_{72} and 1.5 cm $\times$ 1.5 cm $\times$ 145 nm for F_4TCNQ), the density of dopant molecules in the film can be approximated. For these measurements, precisely cut ITO was used as the substrate for its uniformity in size and the samples were weighed on an analytical microbalance. The samples were placed under rough-pump vacuum before the measurements were taken to remove any residual solvent. A set of 6 repeats were measured for each dopant and the results are shown in Tables B.7 and B.8.

For DDB-F_{72}, the average dopant density is 6.9×10^{20} cm^{-3} with a standard deviation (σ) of

0.6×10^{20} cm^{-3}. Therefore, the carrier density we obtain via our AC Hall measurements (7.9×10^{20} cm^{-3}) lies well within the 95% confidence limits (2σ) of this data (5.7 to 8.1×10^{20} cm^{-3}), as discussed in the main text. This means that we have about as many carriers as we do dopants and a doping efficiency of $\sim$100%, supporting the notion that the majority of carriers in DDB-F_{72} doped films are free due to the reduced Coulomb interaction between the shielded anion and the polaron. Finally, the fact that the carriers measured via the AC Hall effect fall at the upper limit of this range is likely due to the tendency of Hall measurements to overestimate the number of free carriers due to screening effects, as discussed above.

For F_4TCNQ, the average dopant density is $4.8(9)\times10^{21}$ cm^{-3} while the carrier density found via AC-Hall is 4.3×10^{20} cm^{-3}, yielding a doping efficiency of $\sim$10%, an order of magnitude lower than for DDB-F_{72}. It should be noted that the 10% value we measure is slightly higher then the 5% value determined in careful previous work by Pingel and Neher.[102,103] The reasons for this could be two-fold. One is that we are in a much higher doping regime than the previous work and therefore have started to saturate traps and thus have increaed the proportion of free carriers. The other is that, as mentioned in the main text, the AC Hall effect has the potential to overestimate the free carrier density due to screening of the applied magnetic field by the low-mobility carriers, so that the ratio of free carriers to dopants could be slightly lower than what we report.

Table B.7: Mass measurements of 6 films before and after doping and carrier density of DDB-F_{72}-doped P3HT films based on the measured mass and a film volume of 1.5 cm $\times$ 1.5 cm $\times$ 300 nm

Glass + P3HT (g)	Glass + P3HT + 1 mM DDB-F_{72} (g)	Mass DDB-F_{72} (μg)	n DDB-F_{72} (/cm^3)
0.399808(5)	0.400019(5)	211	6.2E+20
0.389582(5)	0.389830(5)	248	7.3E+20
0.399402(5)	0.399622(5)	220	6.4E+20
0.390810(5)	0.391028(5)	218	6.4E+20
0.385742(5)	0.386002(5)	260	7.6E+20
0.391792(5)	0.392044(5)	252	7.4E+20
			6.9(6)E+20

Table B.8: Mass measurements of 6 films before and after doping and carrier density of F_4TCNQ-doped P3HT films based on the measured mass and a film volume of 1.5 cm $\times$ 1.5 cm $\times$ 145 nm

Glass + P3HT (g)	Glass + P3HT + 3.6 mM F_4TCNQ (g)	Mass F_4TCNQ (μg)	n F_4TCNQ (/cm^3)
0.389934(5)	0.389996(5)	62	4.1E+21
0.391344(5)	0.391430(5)	86	5.7E+21
0.360448(5)	0.360504(5)	56	3.7E+21
0.360234(5)	0.360316(5)	82	5.5E+21
0.397418(5)	0.397502(5)	84	5.6E+21
0.384942(5)	0.385002(5)	60	4.0E+21
			4.8(9)E+21

APPENDIX C

Supplementary information for: The effects of dopant electron affinity at fixed counterion distance on the production of free carriers in conjugated polymers

C.1 Experimental Methods

C.1.1 Materials

P3HT (Rieke metals inc., 4002-EE, M_n = 50-70 kg/mol, regioregularity 91-94%) and F_4TCNQ (TCI Chemicals) were purchased and used as received. The DDBs were synthesized following previously reported microwave based procedures.[141,152] Microwave reactions were performed using a CEM Discover SP microwave synthesis reactor. The reactions were conducted in glass 10 mL microwave reactor vials purchased from CEM with silicone/PTFE caps equipped with a stirbar. Benzyl bromides were purchased from Oakwood Chemicals and used as received. N,N-diisopropylethylamine (>99 %) was purchased from Sigma Aldrich and used as received. Reagent grade hexanes, acetone, and ethyl acetate used for column chromatography were purchased from Sigma Aldrich and used as received. The CH_3CN (anhydrous, 99.8 %) used for the synthesis of DDB-F_{72} was purified using a solvent purification system and was stored in a nitrogen-filled glovebox over activated 3 Å molecular sieves.

C.1.2 Cyclic Voltammetry

Measurements were performed with a Gamry Instruments Interface 1010E potentiostat using a glassy carbon disc working electrode, platinum wire counter electrode and a fritted Ag/AgCl

reference electrode (fill solution: saturated KCl in MeCN). All experiments were conducted at 2 mM analyte concentration with $[NnBu_4]PF_6$ (0.1 M) supporting electrolyte in anhydrous DCM at a scan rate of 100 mV/s and referenced to an internal Fc/Fc^+ standard.

C.1.3 Film Fabrication

Substrates (either glass or silicon wafers) were cleaned by sequential sonication in alconox detergent solution, deionized water, acetone, and isopropanol. This was followed by treatment in a harrick plasma cleaner PDC-32G set to low RF level for 10 minutes. Subsequent film preparation steps were carried out in nitrogen glove box atmosphere. P3HT films were spin-coated at a rate of 1000 rpm for 60 seconds from a 20 mg/mL polymer solution in 1,2-dichlorobenzene (ODCB, Sigma aldrich, anhydrous, 99%) producing films that are $\sim$120-nm thick. The DDBs were infiltrated in a second spin-coating step out of CH_3CN (anhydrous, 99.8 %) at the stated concentrations in which the solution was deposited on the pre-cast polymer film and spun at 4000 rpm for 10 seconds. Film thicknesses were measured using a Dektak 150 stylus profilometer. The DDBs are stable in air and structurally stable in solution, however, can undergo a redox reaction with the solvent if left for too long, therefore solutions were used on the same day they were made.

C.1.4 Spectroscopy

UV-VIS-NIR absorption spectra were acquired from 300-2500 nm using a Shimadzu UV3101PC Scanning Spectrophotometer for films prepared on glass substrates. FTIR data was acquired from 220-7000 cm^{-1} for matched samples on KBr plates using a Jasco FT/IR-420 spectrometer.

C.1.5 Conductivity

Devices for conductivity measurements were fabricated on 1.5 cm $\times$ 1.5 cm glass substrates. Following film fabrication, electrodes were placed on the corners of the sample using PELCO conductive silver paint. The Van der Pauw measurements were performed using a custom-built apparatus using a Kiethley 2400 Sourcemeter controlled by Labview software where the maximum current sourced was held to 1 mW total power. For lower conductivity samples, the only low power

region was fit. All reported values were averaged over multiple measurements taken on at least 3 samples.

C.1.6 Neutron Reflectometry

Films for neutron reflectometry were made on 2 cm $\times$ 2 cm silicon substrates at 0.3 mM dopant concentrations to increase signal (by maximizing size and decreasing surface roughness). Neutron measurements were carried out at Oak Ridge National Lab on beamline 4b at the sample-air interface. Raw data was fit to multi-layer model using Refl1D.[177] Fits were performed by multiple people independently to ensure reproducibility. Relative contribution of DDB and polymer to the active layer SLD was calculated as a weighted average of the measured P3HT SLD and the calculated SLD for DDB dopants. Percentages were then normalized by atomic nuclei per monomer in both the dopant and P3HT monomer. DDB SLDs were calculated using the NIST Neutron activation and scattering calculator.

C.1.7 X-ray Photoelectron Spectroscopy

XPS was performed using a Kratos Axis Ultra DLD spectrometer with a monochromatic Al Kα radiation source and a charge neutralizer filament was used to control charging of the sample. A pass energy of 20 eV was used for all spectra with a 0.1 eV step size and 300 ms dwell time. All spectra were calibrated to the advantageous carbon 1s peak at 284.8 eV. In order to analyze dopant infiltration, spectra of the top and bottom of the films were obtained via previously described methods.[141] Analysis was performed using CasaXPS software and the relative sensitivity factors used were from the CASAXPS library.

C.1.8 Graxing Incidence Wide Angle X-ray Scattering

Films for 2-D GIWAXS measurements were prepared on 1.5 cm $\times$ 1.5 cm silicon substrates. Measurements were performed at the Stanford Synchrotron Radiation Lightsource on beamline 11-3 using a wavelength of 0.9742 Å with an incidence angle of 0.12°. Diffraction patterns were collected in a helium chamber to increase signal-to-noise with a sample to detector distance of

250 mm and a spot size of $\sim$150 μm on the image plate. The 2-D diffractograms were radially integrated from to 0-10° and 80-90° to obtain the in-plane and out-of-plane diffraction patterns. The IgorPro macro, Nika was used to calibrate and reduce the GIWAXS data and subsequent analysis was performed in IgorPro. The intensities on the opposite sides of the diffractogram (90-180°) were also checked to ensure they matched the chosen limits. Each integration was background corrected for substrate scattering. The subtractions were performed on the raw scattering data to ensure that no errors occurred due to background subtraction. To ensure reproducibility in diffraction intensity and shape, all samples were made and measured in triplicate.

C.1.9 AC-Hall

Ac-Hall effect measurements were carried out at Lakeshore Cryotronics. Devices were made on 1 cm $\times$ 1 cm glass substrates. Following film fabrication, silver electrodes were deposited on the corners of the samples with an Angstrom Engineering, Inc. evaporator at a pressure of $< (1\times10^{-6}$ Torr). The silver layer was deposited at a rate of 0.5 Å/s up to 10 nm, followed by 1 Å/s to a final total thickness of 60 nm. Samples were packaged in scintillation vials under argon atmosphere before being sent for testing. AC magnetic field Hall measurements were performed with a Lake Shore model 8400 series AC Hall probe system at a field strength of 0.6484 T and a current of 1.00×10^{-5}. Nitrogen was flowed continuously over the samples to reduce error from sample degradation. The technique is similar to DC Hall Effect, but with an oscillating magnetic field at 0.1 Hz such that the hall voltage (resulting from the Lorentz force) becomes time dependent. This allows the hall voltage to be distinguished from the static misalignment offset voltage, which is large in low mobility materials.

C.2 Cyclic Voltammetry Measurements

The redox potentials of all dopants, including F_4TCNQ, were measured in-house by cyclic voltammetry under the same conditions to properly ascertain their relative offsets. The results for the $0/1-$ redox couple are shown in Figure C.1. The offset vs. P3HT shown in the main text was estimated based on literature values for P3HT HOMO (-5.0 eV vs vacuum) and F_4TCNQ LUMO (-5.24 eV vs vacuum).[109, 124, 144]

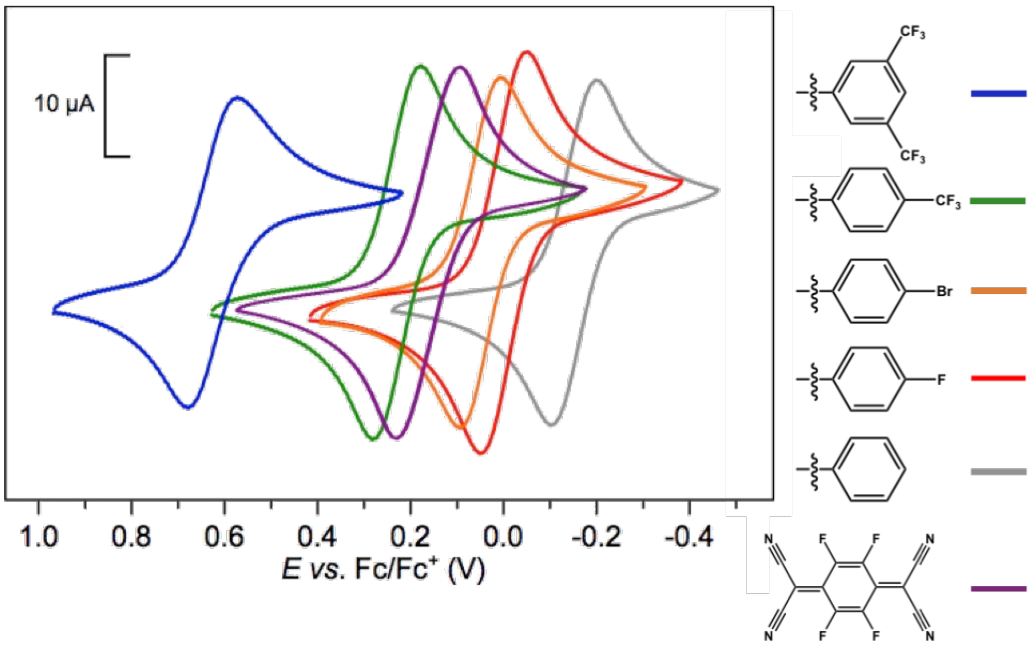

Figure C.1: CVs of all boron clusters in the $0/1-$ redox couple region.

C.3 Absorption Spectroscopy Measurements

Figure C.2 shows the UV-VIS-IR absorption spectra for 0.3 mM DDB sequentially doped P3HT (with the 1 mM data shown in Figure 1 of the main text.) The inset shows the standard energy band diagram for the formation of polarons. Indeed, in the DDB doped P3HT spectra we see the evidence of polarons via these signatures for all dopants with redox potentials above DDB-Bn. We do not see a significant / full bleach of the band to band transition, even in the 1 mM films, due to the absorption of the neutral and anionic DDBs under this peak.

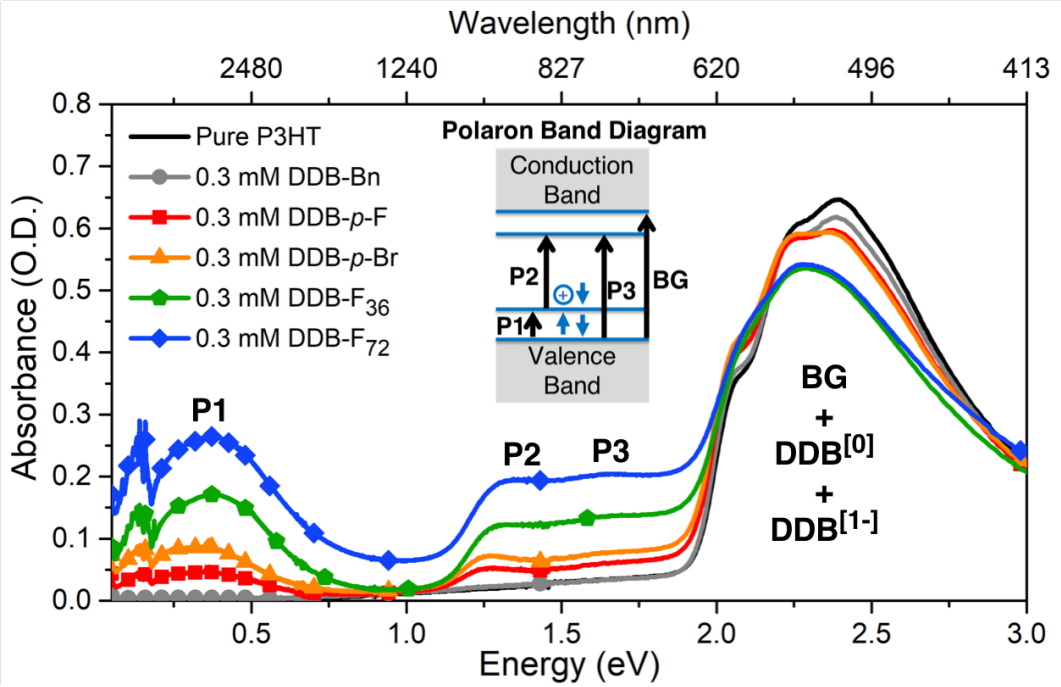

Figure C.2: UV-Vis of P3HT doped with 0.3 mM solutions of the DDB clusters.

C.4 Conductivity Measurements

To characterize the electrical conductivity of P3HT films doped with DDB clusters of varying redox potential, we fabricated samples doped with equimolar DDB solutions. The measured conductivities are shown in Table C.1.

Table C.1: Van der Pauw conductivity measurements of DDB doped P3HT films.

Cluster	[ ] mM	$R_{\square}$ ave ($\Omega/\square$)	t_{ave} (nm)	Conductivity (S/cm)
	0.3	$(4.87 \pm 0.77) \times 10^6$	131 ± 4	0.016 ± 0.003
DDB-*p*-F	0.5	$(8.02 \pm 0.72) \times 10^5$	137 ± 4	0.09 ± 0.01
	1	$(2.35 \pm 0.63) \times 10^5$	149 ± 5	0.29 ± 0.08
	0.3	$(6.74 \pm 0.50) \times 10^6$	139 ± 2	0.11 ± 0.01
DDB-*p*-Br	0.5	$(4.03 \pm 0.24) \times 10^5$	150 ± 3	0.17 ± 0.01
	1	$(1.00 \pm 0.07) \times 10^5$	177 ± 2	0.56 ± 0.04
	0.3	$(8.28 \pm 0.11) \times 10^4$	161 ± 3	0.75 ± 0.02
DDB-F_{36}	0.5	$(5.49 \pm 0.13) \times 10^4$	182 ± 3	1.00 ± 0.03
	1	$(2.80 \pm 0.18) \times 10^4$	213 ± 8	1.7 ± 0.1
	0.3	$(7.56 \pm 0.46) \times 10^3$	195 ± 5	6.8 ± 0.5
DDB-F_{72}	0.5	$(4.65 \pm 0.54) \times 10^3$	226 ± 8	9 ± 1
	1	$(2.89 \pm 0.99) \times 10^3$	305 ± 10	12 ± 2

Devices were fabricated via sequential processing on 1.5 cm $\times$ 1.5 cm glass substrates. The Van der Pauw technique was used to measure the sheet resistance as follows; four probes are placed on each corner of the square sample geometry and current is flowed along one edge of the sample while the voltage is measured across the opposite edge. The contacts are rotated 90°, and the measurement is repeated. The resistance values obtained from the slope of the I-V curves are fit to the Van der Pauw equation to obtain the sheet resistance ($R_{\square}$). The thickness (t) of the samples was obtained in three locations using a Dektak 150 stylus profilometer. The reported values are averages and standard deviations of at least three samples and this errors were propagated in the calculation of conductivity ($1/R_{\square}t$).

C.5 Neutron Reflectometry

Active layer SLDs are a weighted average of the SLDs of the contributing materials; P3HT and DDB dopant. A sample calculation to obtain the P3HT monomer:DDB-F_{36} dopant is presented here. From our measurements and calculations we have:

Measured P3HT SLD = 0.56

Calculated DDB-F_{36} SLD = 1.9

Measured Active Layer SLD = 1.17

Let x be the weighted fraction of P3HT in the film. Then $1-x$ is the weighted fraction of DDB-F_{36} and their relative contributions to the average SLD follows the relationship:

$$0.56x + 1.9(1-x) = 1.17 \tag{C.1}$$

The solution is $x = 0.544$, thus $1-x = 0.456$ and the nuclear ratio of P3HT:DDB is 544:456. To turn this into a monomer to monomer ratio, we must divide by the number of atoms in each material.

P3HT ($C_{10}H_{14}S$) has 25 atoms per monomer

DDB-F_{36} ($C_{96}H_{72}B_{12}F_{36}$) has 228 atoms per monomer

$$\frac{544}{25} = 21.76 \text{ P3HT monomers to } \frac{456}{228} = 2 \text{ DDB monomers} \tag{C.2}$$

Therefore the DDB-F_{36}:P3HT monomer ratio is 1:11

C.6 X-Ray Photoelectron Spectroscopy

To obtain information about the infiltration of the dodecaborane clusters, XPS measurements were carried out on the top and bottom surfaces of the films. The signal from the halogens on the DDB clusters can be referenced to the sulfur signal which comes only from P3HT and integrated peak areas were used to calculate the reported ratios. Sample fits for the resolvable fluorine and sulfur spectra are shown in the main text Figure 2d,e and fits for bromine are shown here in Figure C.3. We were unable to use such a reference on DDB-Bn because the signal from boron is too weak to be used accurately and the DDB-Bn cluster has no halogenated functional groups.

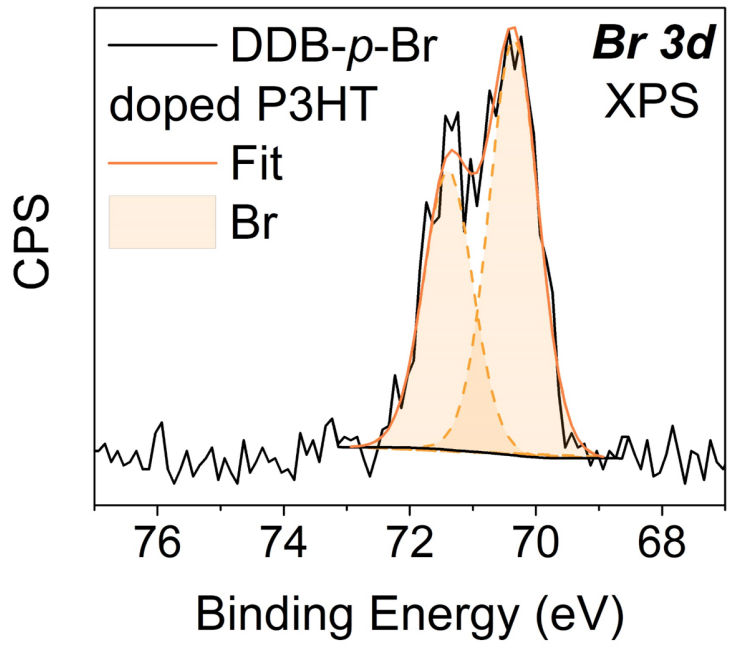

Figure C.3: Bromine 3d peak fits for DDB-*p*-Br doped P3HT.

C.7 GIWAXS of P3HT Thin-Films Doped with DDBs

Representative 2D diffractograms for DDB doped P3HT are shown in Figure C.4. The clear edge-on orientation of the polymer with respect to the substrate is observed in which the lamellar (h00) overtones appear out-of-plane and the (010) peak appears in-plane.

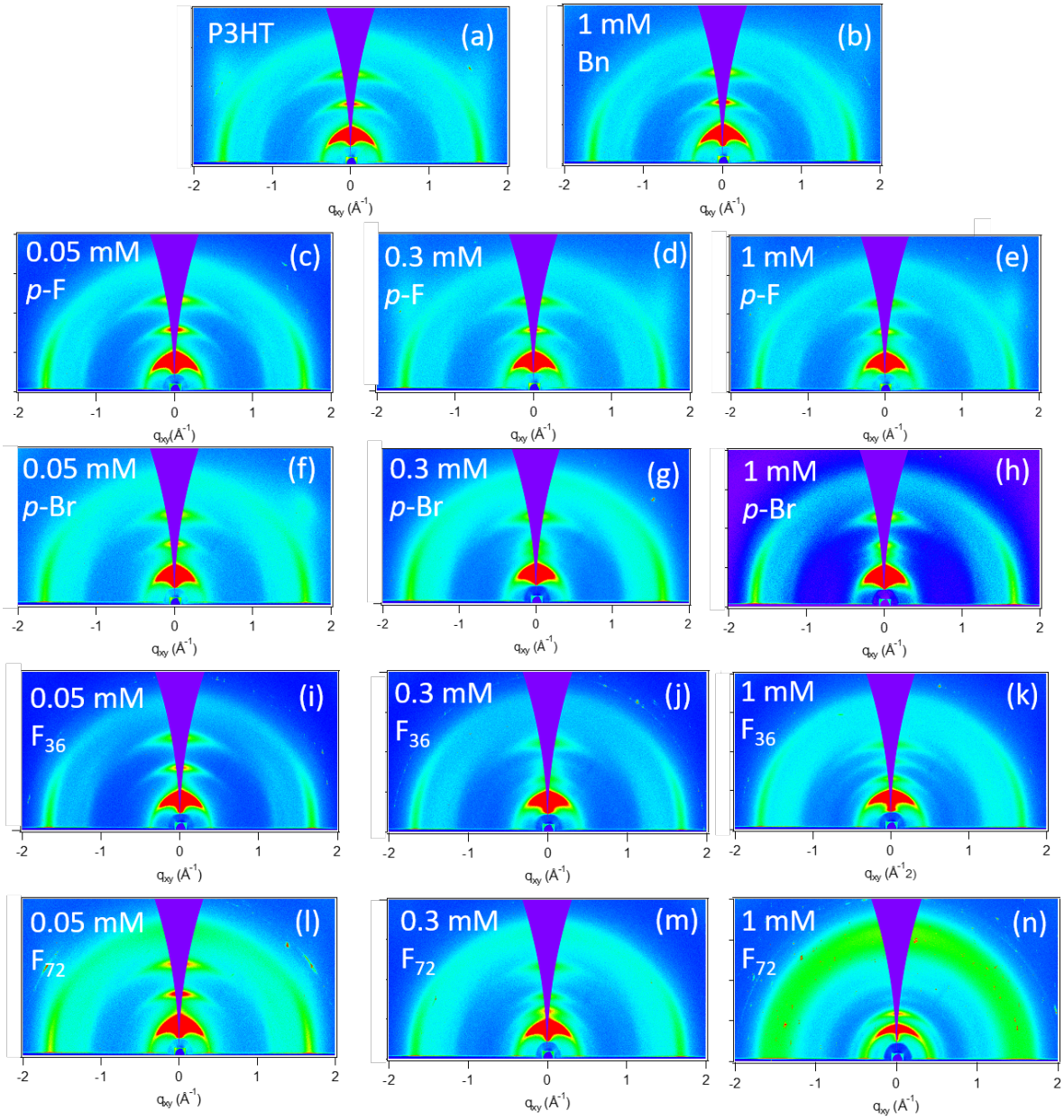

Figure C.4: 2D diffractograms of representative samples of P3HT doped with each DDB at multiple concentrations (each condition was run in triplicate).

The out-of-plane GIWAXS curves for each DDB (with DDB-F_{36} shown in Figure 3 of the main text) shows the concentration effects of each dopant and the gradual formation of a new phase. DDB-Bn, the non-doping control, shows no structural changes. DDB-*p*-F increases the crystallinity of the P3HT at the lowest doping concentration before causing the beginnings of the new phase at 1 mM. It has been previously observe that the introduction of positive charges can increase the order of the film through the delocalization of the positive charge.[159] 1 mM DDB-*p*-Br shows clear coexistence of both (h00) phases as the original phase is being converted to the new one. Co-existence of phases in films doped with DDB-F_{72} cannot be clearly determined due to the overlap of the original (h00) and (h00)' peaks, however, the appearance of the new phase is still clear from the higher order peaks.

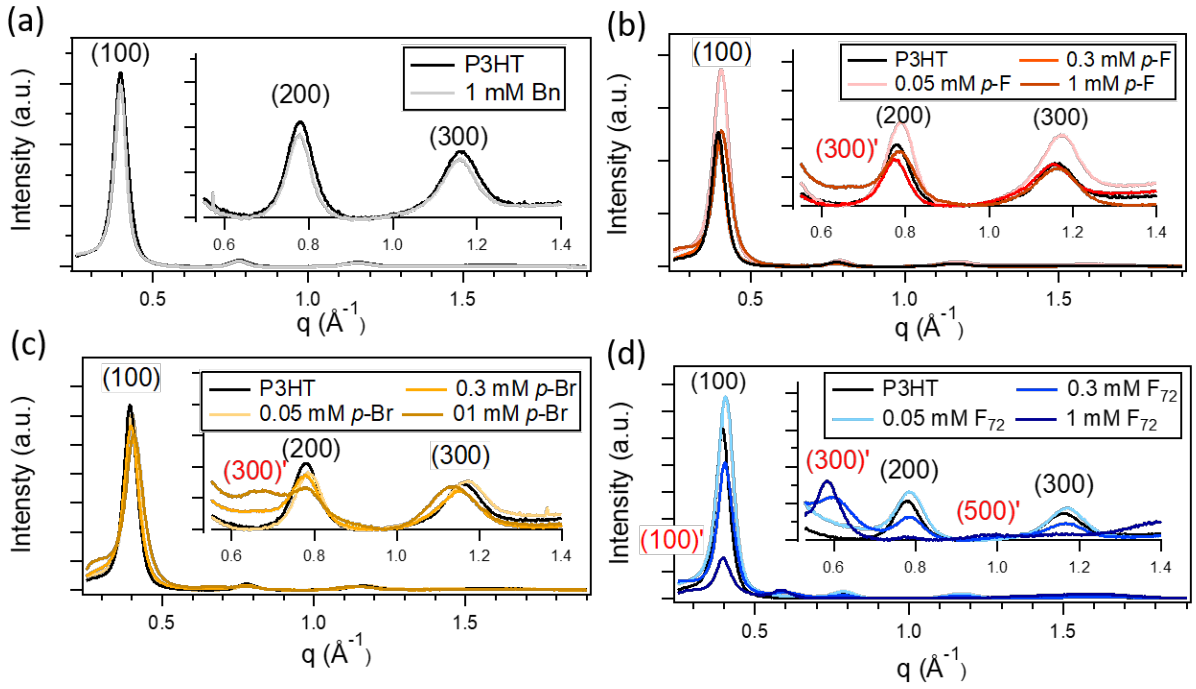

Figure C.5: Out-of-plane GIWAXS curves of P3HT doped with DDB clusters demonstrating the conversion to the new (h00)' lamellar phase.

The in-plane GIWAXS data for each DDB dopant at three concentrations is shown in Figure C.6 and has been normalized to the (010) peak. This reveals that a disordered π-stacking peak centered at 1.4 q grows in with increasing DDB concentration. Further, we see more of this disordered peak for the higher redox potential DDBs. It is expected that there is more DDB cluster in the film for both increasing concentration as well as redox-potential (based on NR), which would cause the increased structural disorder that is observed here.

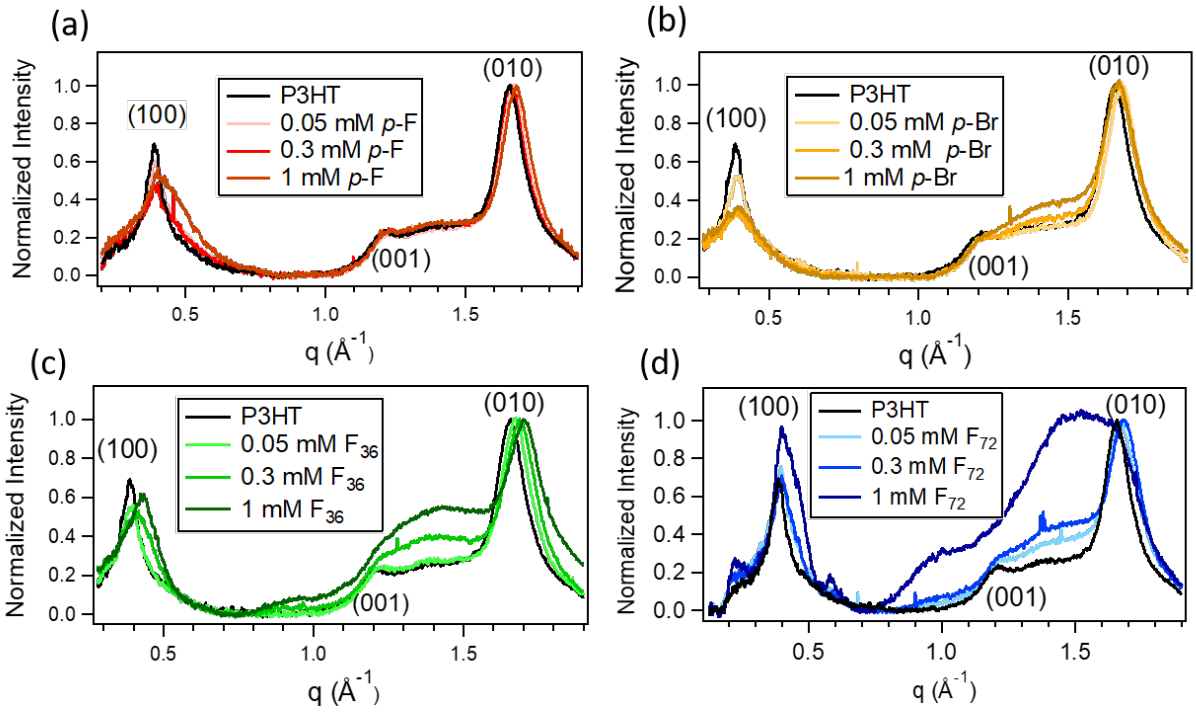

Figure C.6: Normalized in-plane GIWAXS curves of P3HT doped with DDB clusters demonstrating an increase in disordered π-stacking peak centered at 1.4 q with both concentration and DDB redox potential.

C.8 Solution Doping of P3HT with DDBs

Solution doping experiments were carried out as another method to compare the effect of redox potential on the formation of polarons in P3HT. Here, the volume and concentration (2.5 mL of 0.1 mM) of P3HT was controlled, as well as the amount of 0.1 mM dopant solution via a syringe. Both materials were dissolved in ODCB and at these low concentrations and the doped materials remain soluble even at the highest dopant aliquots. The solution UV-VIS-NIR spectra are shown in Figure C.2. The advantage of this method is that the amount of dopant can be controlled precisely and is known.

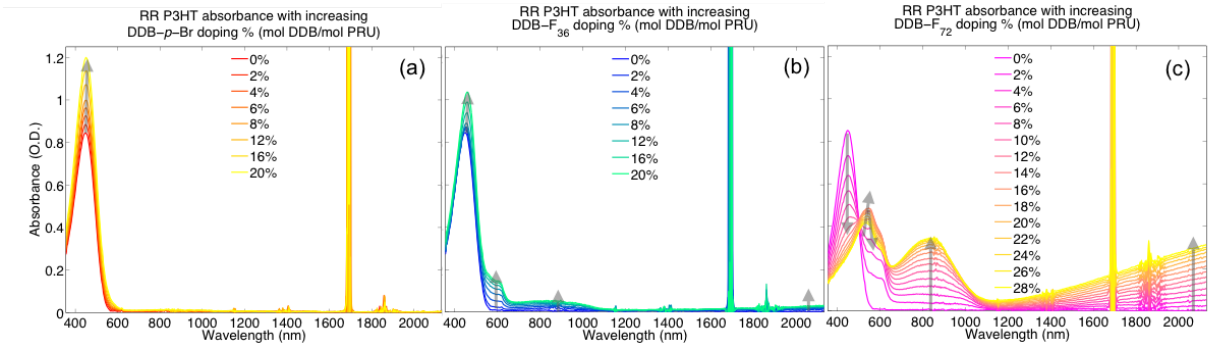

Figure C.7: Solution doping of P3HT with DDBs in ODCB at known DDB:PRU ratios.

To further elucidate trends in this data, the relevant peaks are tracked in Figure C.8. We see that although DDB-*p*-Br is able to dope P3HT in film here the reorganization energy is likely too high in solution and we get no bleach of the P3HT peak at 450 nm (tracked in Figure C.8a) and no notable increase in either the P1 or P2 peaks (tracked in Figure C.8c,d). Still the relative doping ability is as we expect with DDB-F_{36} being able to dope in solution and DDB-F_{72} being by far the best dopant. For DDB-F_{36} we see a bleach of the P3HT peak up to 10% dopant after which the peak increases due to absorption from the cluster itself. Similarly, P1 and P2 increase up to 10%, after which they stay relatively constant and there is a clear change in slope. By contrast, DDB-F_{72} is able to continue to dope well past 10% and obtain a nearly full bleach of the P3HT bandgap transition and larger increases in the P1 and P2 peaks that only begin to level off near 30% dopant. For both DDB-F_{36} and DDB-F_{72}, we see the formation of P3HT aggregates, indicated by the peak at 600 nm[161] (tracked in Figure C.8b). For DDB-F_{72} only we see a decrease in intensity in the

P3HT aggregate peak upon further doping. These experiments support the ideas that the very high electron affinity of DDB-F_{72} contributes to its ability to dope many structureal conformations of P3HT, even those that occur upon doping.

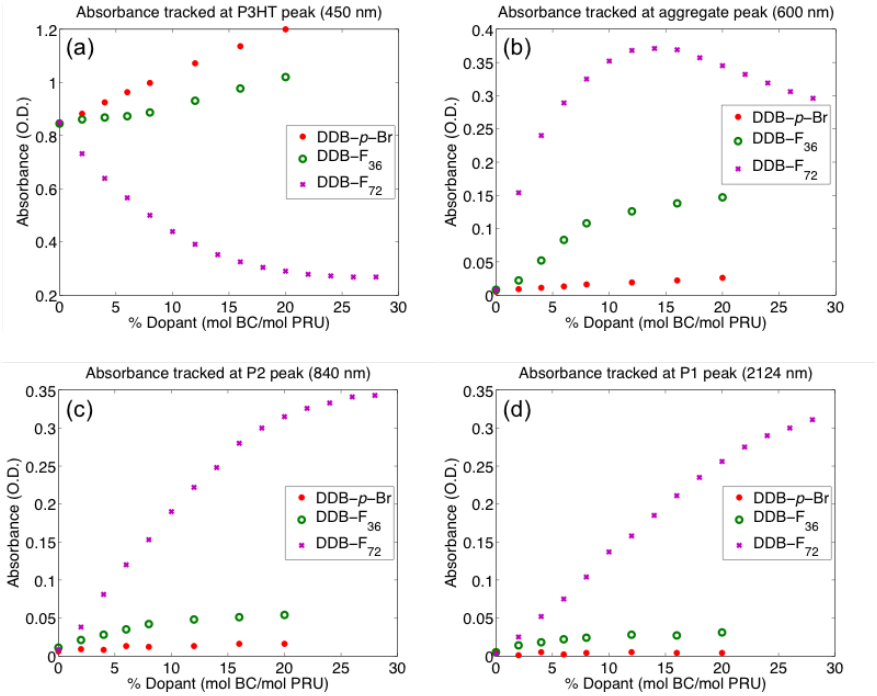

Figure C.8: Absorbance tracked at P3HT bandgap peak (a), P3HT aggregate peak (b), P2 peak (c), and P1 peak (d).

C.9 FTIR of DDB-doped P3HT

Concentration dependent FTIR data for P3HT doped with each DDB cluster is shown in Figure C.9a-c (with DDB-F_{72} shown in Figure 4a of the main text). In all cases, we see that as the concentration of DDB dopant is increased, there is a slight blue shift of the P1 peak, which we attribute to the DDB clusters packing slightly closer to the P3HT backbone as more clusters are loaded into the polymer network. Because of this concentration dependence, we compare the closest intensity matched P1 peaks for which the raw data is shown in Figure C.9d (normalized data is shown in Figure 4b of the main text). Finally the P1 peaks for all doped commercially obtained P3HT for which we have AC Hall measurements are shown in C.9e. The AC-Hall measurements are summarized on the following page, Section C.10, in Table C.2 and the fits to this data are shown in Section C.11, yielding a linear correlation between peak position and mobility (shown in Figure 4c of the main text).

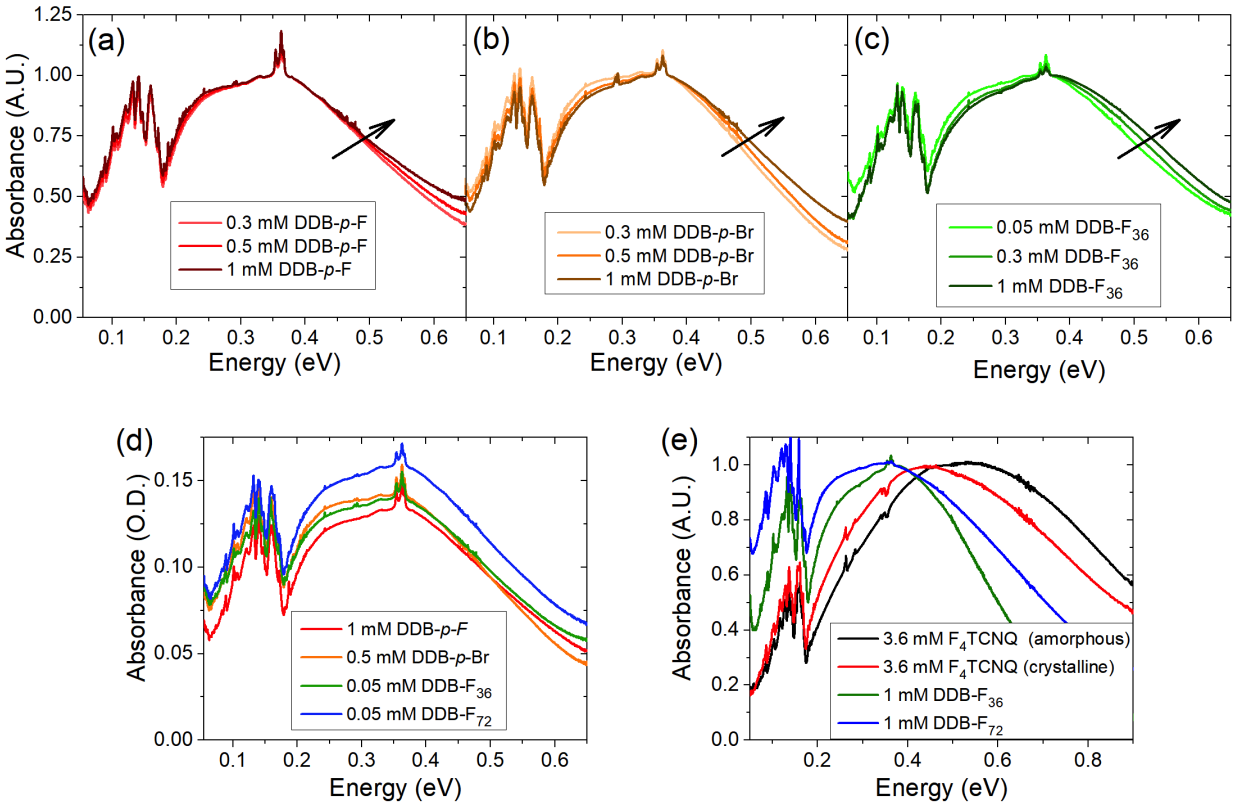

Figure C.9: Concentration dependent FTIR data for DDB-*p*-F (a), DDB-*p*-Br (b), and DDB-F_{36} (c). Unnormalized, intensity matched FTIR data (d). P1 peaks of doped P3HT with corresponding AC-Hall mobility measurements (e).

C.10 AC-Hall Measurements

AC-Hall measurements were obtained for DDB-F_{36} and compared to our previously obtained measurements for DDB-F_{72}[141] and F_4TCNQ.[87] Films with conductivities under 1 S/cm are below the limits that can be accurately measured with AC-Hall. All samples compared were prepared with commercial P3HT (MW 50-70 kg/mol and regiogregularity 91-94%). We see that doping with the DDB clusters result in higher mobilities than even the high crystallinity P3HT doped with F_4TCNQ. DDB-F_{72} results in the highest carrier density, likely due to its $\sim$0.5 eV greater energetic compared to the other dopants. The F_4TCNQ films still have relatively high carrier densities likely due to the higher dopant solution concentration and potentially greater infiltration of the small molecule. We note that the mobility tracks with the peak positions of the corresponding FTIR peaks (shown in Figure C.9). We fit the P1 region in the following section and report the obtained correlation with mobility in Figure 4c of the main text.

Table C.2: Comparison of carrier density (n), mobility (μ) and conductivity (σ) measured by the AC Hall effect for doped P3HT films.

Sample	n (1/cm^3)	μ(cm^2/Vs)	σ (S/cm)
1 mM DDB-F_{72}	7.90×10^{20}	0.1	12.9
1 mM DDB-F_{36}	1.40×10^{20}	0.074	1.6
3.6 mM F_4TCNQ (crystalline P3HT)	7.10×10^{20}	0.05	5.7
3.6 mM F_4TCNQ (amorphous P3HT)	5.90×10^{20}	0.02	1.4

C.11 Fits of UV-VIS-FTIR Data (P1 Region)

To determine the peak centers of the P1 peaks in doped P3HT films, we fit the P1 region of the absorbance data to a Gaussian as shown in equation C.3 where A is the Amplitude, c is the center, and ω is the width.

$$g(x;A,c,\omega) = \frac{A}{\omega\sqrt{2\pi}} e^{-(x-c)^2/2\omega^2} \tag{C.3}$$

The values we obtain agree with the full fits for the DDB-doped films we present in Section C.12, justifying this simplified method for fitting the data. For F_4TCNQ films we fit the region between 0.18 and 0.8 eV and for DDB doped films we fit from 0.18 to 0.6 eV to best encompass the center of the peak. The fitting was performed in python using lmfit's built in Gaussian model. The resulting fits are shown in Figure C.10 and the fit parameters are reported in the inset tables. The errors on the fit parameters are smaller than the last reported significant digit. The F_4TCNQ peaks are both more blue shifted than the DDB peaks with the following order of peak centers:

(blue)$-$ F_4TCNQ (amorphous) $>$ F_4TCNQ (crystalline) $>$ DDB-F_{36} $>$ DDB-F_{72} $-$(red)

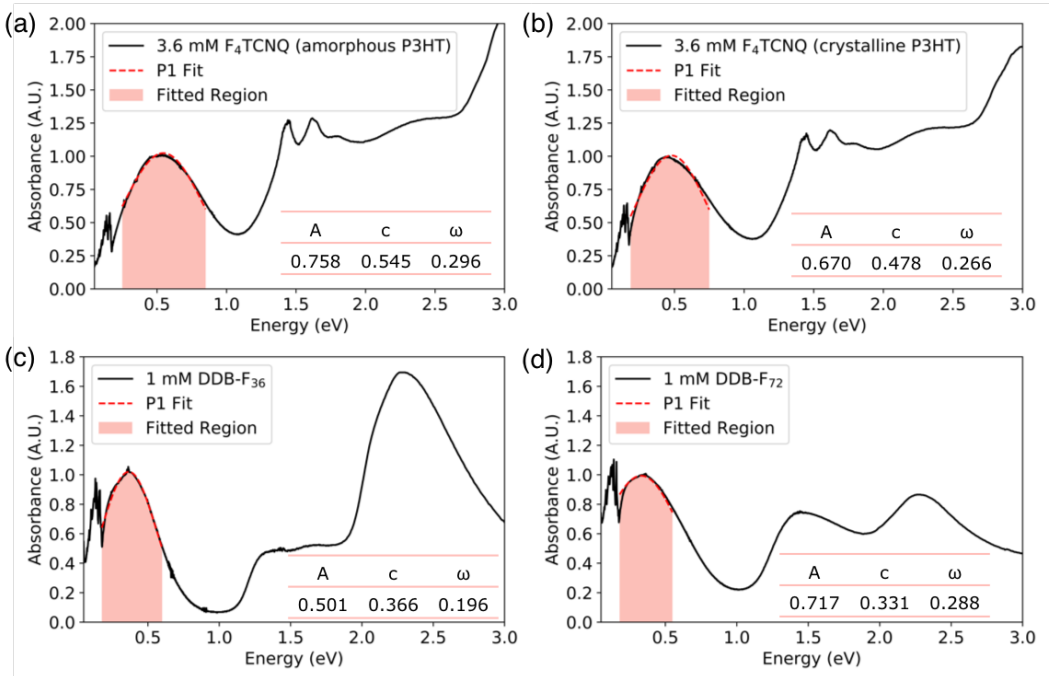

Figure C.10: Fits of P1 region for F_4TCNQ-doped low crystallinity P3HT (a) and high crystallinity P3HT (b) with data taken from Ref. 87. Fits of our 1 mM DDB-F_{36} (c) and DDB-F_{72} doped P3HT (d).

C.12 Fits of UV-VIS-FTIR Data (Full)

To fit the full DDB doped P3HT spectra, we began with the absorption spectrum of a pure P3HT film. Since P3HT has many vibronic transitions and both the anion and neutral spectra of the DDBs absorb under P3HT's peak, we will not try to pull out any quantitative information from this region. However, since there is overlap between this region and the tail of the P3 polaron peak, it is important for the rest of the fitting to get this region qualitatively right.

We implement four gaussians to fit P3HT: one for the main band-to-band transition and three for the vibronic transitions associated with the crystalline π-stacking structure of P3HT. We find that in order to reproduce the P3HT spectrum, we need to add a Rayleigh scattering term. Rayleigh scattering occurs if a sample contains particles smaller than the wavelength of light such as the crystalline aggregates that exist in our thin films and is proportional to λ^{-4}. Since the scattered light will not reach the detector, it will be interpreted as absorption. Therefore, the equation used for this scattering term is as follows (in terms of energy) where k is a constant fit parameter:

$$Scat(x;k) = \log_{10} \frac{1}{1 - k(\frac{hc}{x})^{-4}} \tag{C.4}$$

The peak centers obtained correspond well to previously reported values for the bandgap transition (E_g = 2.78 eV) as well as the singlet exciton (S_0 = 2.05 eV), exciton +1 phonon (S_1 = 2.22) , and exciton +2 phonons (S_2 = 2.43).[178]

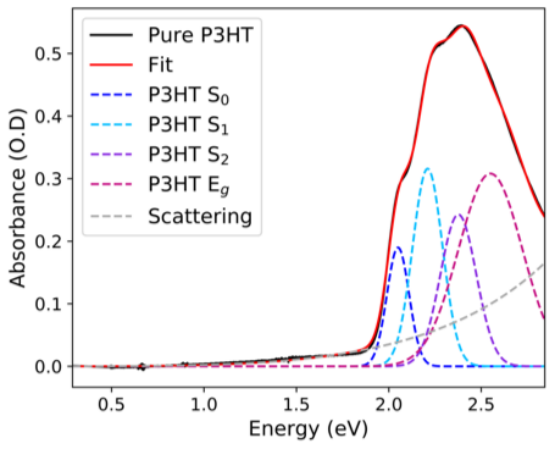

Figure C.11: P3HT film fit to the bandgap and three vibrational transitions with a scattering background.

To fit the full DDB doped P3HT spectra, we fix the obtained centers of the P3HT transitions to +/- 0.1 eV and let their widths and amplitudes vary freely. We also add a gaussian for the DDB neutral and DDB anion at their approximate locations (+/- 0.25 eV). We use one gaussian per polaron transition, and unlike the region under P3HT these are well resolved. Thus, our final fitting model is as follows:

$$f(x) = g_{P_1} + g_{P_2} + g_{P_3} + g_{S_0} + g_{S_1} + g_{S_2} + g_{E_g} + g_{DDB^0} + g_{DDB^{1-}} + Scat \tag{C.5}$$

The full fits with their decompositions are shown in Figures C.12 and C.13 and the obtained fit parameters are summarized in Table C.3 for which again the errors obtained are smaller than the last reported significant digit.

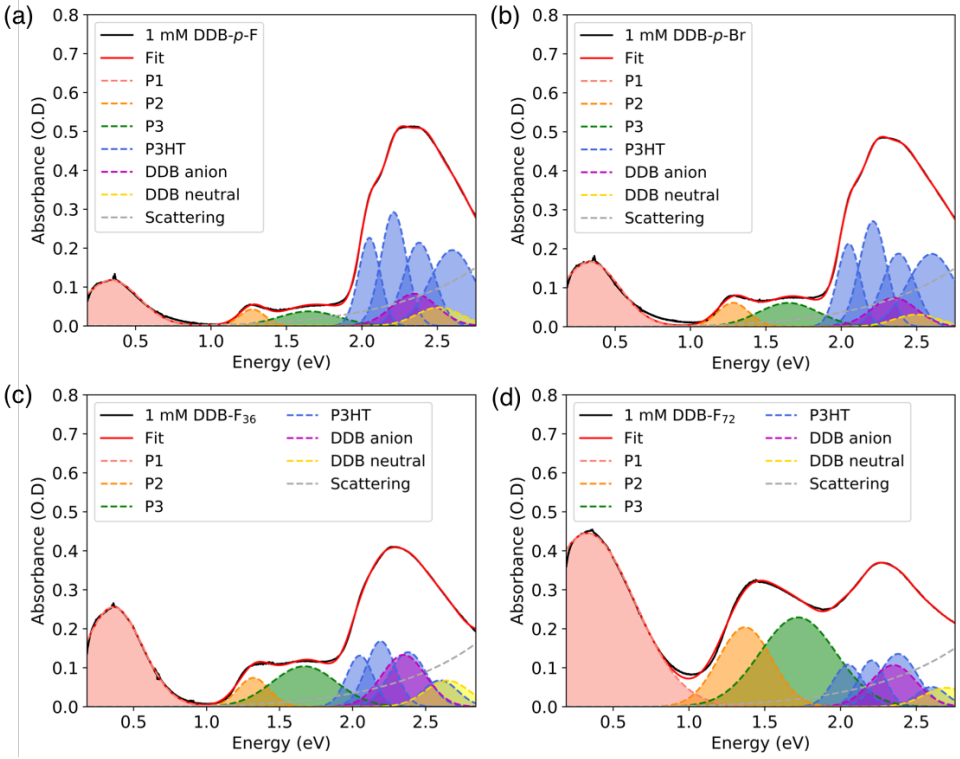

Figure C.12: Full fits of 1 mM DDB doped P3HT films.

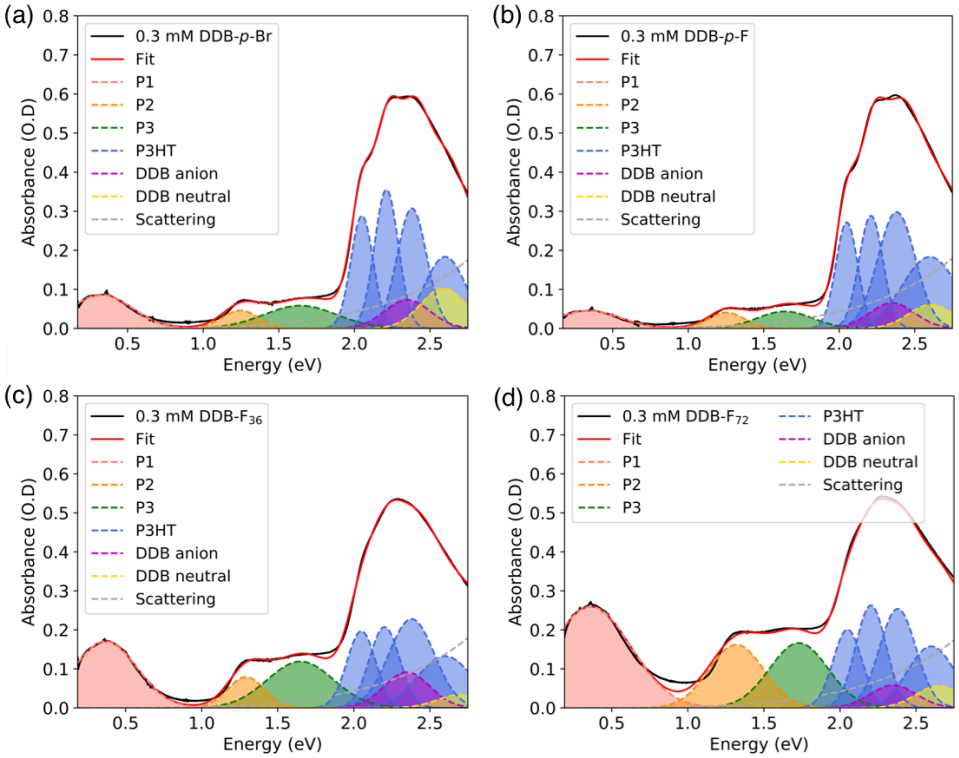

Figure C.13: Full fits of 0.3 mM DDB doped P3HT films.

Table C.3: Summary of git parameters obtained for P1, P2 and P3 peaks from the full fits of the UV-VIS-FTIR data.

		0.3 mM Concentration			1 mM Concentration		
		P1	**P2**	**P3**	**P1**	**P2**	**P3**
DDB-*p*-F	A	0.0237	0.0121	0.0199	0.0547	0.00896	0.0187
	c	0.339	1.25	1.64	0.340	1.27	0.165
	ω	0.206	0.119	0.430	0.185	0.0839	0.199
DDB-*p*-Br	A	0.0436	0.0137	0.035	0.0817	0.0160	0.0305
	c	0.328	1.25	1.64	0.334	1.28	1.65
	ω	0.201	0.120	0.240	0.196	0.104	0.0201
DDB-F_{36}	A	0.0878	0.0237	0.0649	0.127	0.0201	0.0573
	c	0.369	1.29	1.65	0.363	1.32	1.67
	ω	0.205	0.120	0.218	0.199	0.108	0.221
DDB-F_{72}	A	0.170	0.073	0.0799	0.348	0.0898	0.143
	c	0.363	1.32	1.73	0.330	1.37	1.72
	ω	0.261	0.180	0.192	0.312	0.176	0.250

APPENDIX D

Data Fitting in Python: Deconvolution of Multiple Peaks and Background

D.1 A simple example: Two overlapping gaussians and an exponential

To make sure our code is working correctly, let us begin with a simple example of two overlapping gaussians and an exponential with known model parameters. This section is adapted from Example 3 of https://lmfit.github.io/lmfit-py/builtin_models.html but with more detail and is based on fitting data from NIST's website. Download the Gauss2 data file from https://itl.nist.gov/div898/strd/nls/data/gauss2.shtml and save only the xy data values as Gauss2.dat in the same directory as you Python notebook.

Step 1: Import packages. At the start of every python script, we import relevant packages and can give them names (using "as") to make it easier to call upon them later.

```
import numpy as np #math package
import matplotlib.pyplot as plt #plotting package
from lmfit.models import ExponentialModel, GaussianModel #built in models
```

Step 2: Load data. Next load the data we want to fit (again make sure Gauss2.dat is in the same directory as your python code), create x and y variables from the dataset, and plot the data to see what it looks like:

```
dat = np.loadtxt('Gauss2.dat')
x = dat[:, 1]
y = dat[:, 0]
plt.plot(x, y, 'b')
```

The output should look like this:

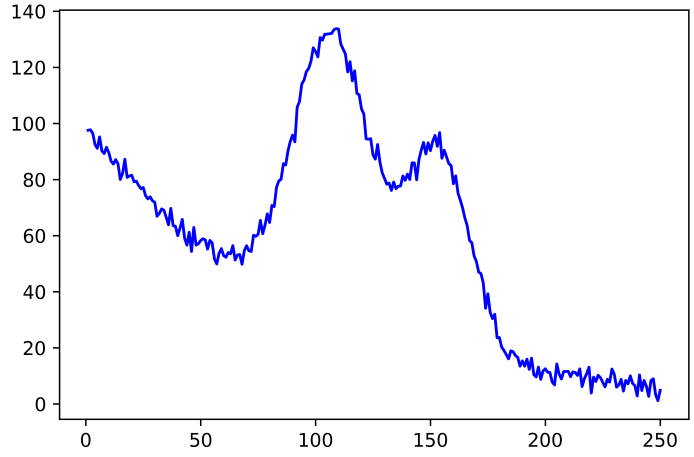

Figure D.1: Plot of sample data to fit

Step 3: Define the fitting model. Now it is time to define the model. We can see from the data that this looks like two convoluted gaussians with an exponential background. Python's LMFIT package has predefined exponential and gaussian models that we will use here. (In the next section, we will go through how to define our own model.) The definitions of the built in models are well documented here: https://lmfit.github.io/lmfit-py/builtin_models.html. The benefit of using LMFIT over SCIPY is the ability to define prefixes and set constraints for the model parameters. This makes dealing with many parameters MUCH easier. Further, in order to obtain a good fit, the initial guesses must be reasonable. Sometimes, this takes several guesses to get right, but plotting the initial guess (as done here) can help.

```
8  #Create EXPONENTIAL model with prefix exp_
9  exp_mod = ExponentialModel(prefix='exp_')
10 #Let LMFIT make initial guess of parameters using xy data
11 pars = exp_mod.guess(y, x=x)
12
13 #Create GAUSSIAN model with prefix g1_
14 gauss1 = GaussianModel(prefix='g1_')
15 #Create parameters
```

```
pars.update(gauss1.make_params())
#Set inital guesses and constraints
pars['g1_center'].set(value=105, min=75, max=125)
pars['g1_sigma'].set(value=15, min=3)
pars['g1_amplitude'].set(value=2000, min=10)

#Create another GAUSSIAN model with prefix g2_
gauss2 = GaussianModel(prefix='g2_')
#Create parameters
pars.update(gauss2.make_params())
#Set inital guesses and constraints
pars['g2_center'].set(value=155, min=125, max=175)
pars['g2_sigma'].set(value=15, min=3)
pars['g2_amplitude'].set(value=2000, min=10)

#Define model as the sum of two gaussians and an exponential
mod = gauss1 + gauss2 + exp_mod
```

Step 4: Run the fit, print and plot the results. Evaluate the model with our initial parameters and run the fit. Depending on the complexity of the fitting function, this step may take a while. Finally, it is important to plot the initial guess and best fit, as well as the components of the fit.

```
init = mod.eval(pars, x=x) #evaluate the model using our initial parameters
out = mod.fit(y, pars, x=x) #fit the model
print(out.fit_report(min_correl=0.5)) #print fit statistics

#Plot data, initial guess, and best fit on left plot
fig, axes = plt.subplots(1, 2, figsize=(12.8, 4.8))
axes[0].plot(x, y, 'b')
axes[0].plot(x, init, 'k--', label='initial fit')
```

```
axes[0].plot(x, out.best_fit, 'r-', label='best fit')
axes[0].legend(loc='best')

#Plot individual components on right plot
comps = out.eval_components(x=x)
axes[1].plot(x, y, 'b')
axes[1].plot(x, comps['g1_'], 'g--', label='Gaussian component 1')
axes[1].plot(x, comps['g2_'], 'm--', label='Gaussian component 2')
axes[1].plot(x, comps['exp_'], 'k--', label='Exponential component')
axes[1].legend(loc='best')
plt.show()
```

The output should look like this:

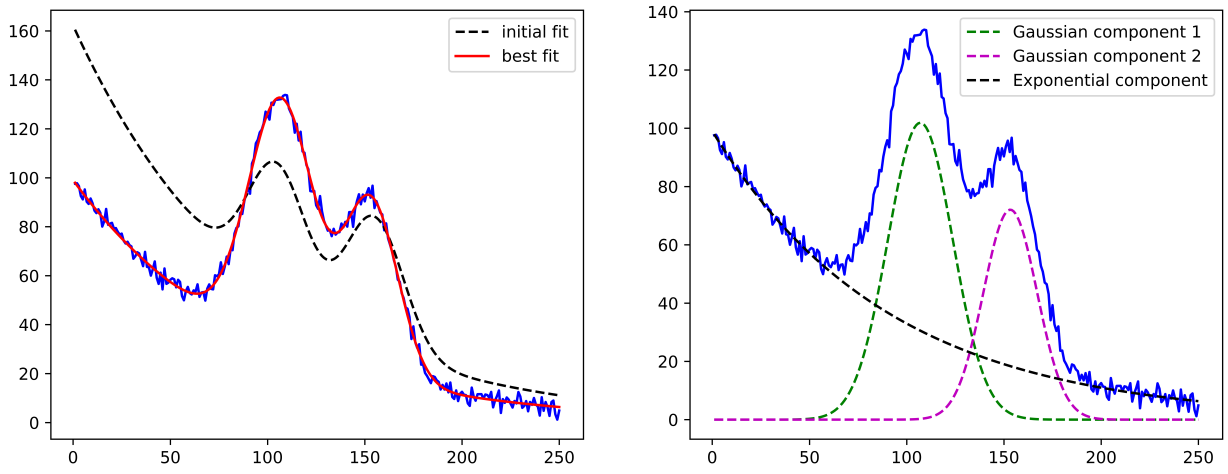

Figure D.2: Plot of initial and best fit to sample data (left) and fit components (right).

The best fit parameters and fit statistics will also print in the Python notebook. We obtain a good fit to this data and can see that the obtained values of the parameters match those on the NIST website from which the data was obtained. In general, we want to make sure that the final fit closely matches the data and that none of the parameter values are at the bounds that we set, which will be stated explicitly in the output. If the best fit did not match the data well, often the fit can be improved by giving a better initial guess (which can be done iteratively). Otherwise, it may be that the model is

not a good representation of the data and should be changed.

D.2 Fitting the full UV-VIS-FTIR spectrum of a DDB doped P3HT sample.

D.2.1 Pure P3HT spectrum only

Step 1: Import packages. Now we will move on to fitting actual DDB doped P3HT data, however, since the P3HT region itself is so complicated, let us first begin with that region alone. As before the first step is to import necessary packages:

```
import pandas as pd #convenient data structures package
import numpy as np
from numpy import exp, sqrt, pi
import matplotlib.pyplot as plt
import matplotlib.colors as mcolors #purely cosmetic for plots
import lmfit
from lmfit.models import GaussianModel
```

Step 2: Load data. Next we import the data. Since we are loading an excel file, it is convenient to use the pandas package. Simply replace PATHTOFILE with the path to you data file including the file name. This will load the data into a data frame. I have selected the relevant regions of the data using iloc and the last step since we're still in the data frame structure is to select the values. Finally we plot the data.

```
#import and select xy data to fit
data = pd.read_excel (r'PATHTOFILE.xlsx')
energy = pd.DataFrame(data, columns= ['XDATA'])
x = energy.iloc[1000:3950,:] #selected data
P3HT = pd.DataFrame(data, columns= ['YDATA'])
y = P3HT.iloc[1000:3950,:] #selected data
x=x.values[:,0]
y=y.values[:,0]
```

```
16
17 #plot data
18 plt.plot(x,y,'k',label='Pure P3HT')
19 plt.legend(loc='best',fontsize=14)
20 plt.xlabel('Energy (eV)', fontsize=14)
21 plt.ylabel('Absorbance (O.D)', fontsize=14)
22 plt.xticks(fontsize=14)
23 plt.yticks(fontsize=14)
24 plt.margins(x=0)
25 plt.ylim(0,0.6)
```

In this case the output of the pure P3HT spectrum looks as follows:

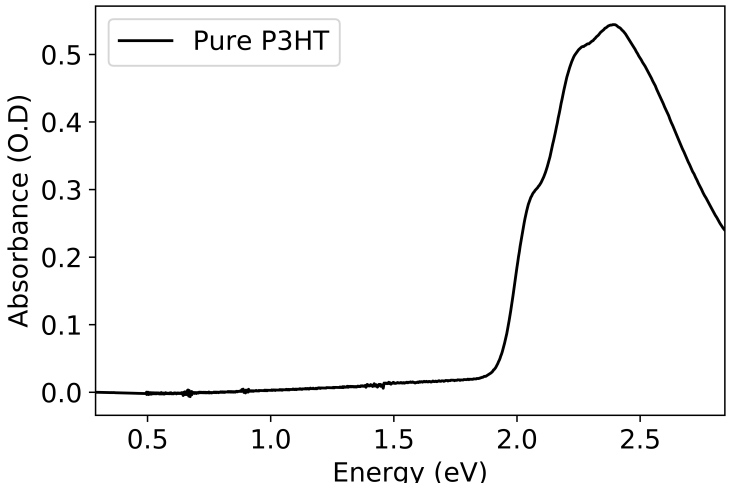

Figure D.3: Plot of pure P3HT film absorbance

Step 3: Define the fitting model. We can clearly see the vibronic structure of P3HT, however, additionally there is a background which we attribute to Rayleigh scattering. Our model therefore includes four gaussians, one for the main band-to-band transition and three for the vibronic transitions associated with the crystalline π-stacking structure of P3HT,[178] and a Rayleigh scattering that we define ourselves taking the form:

$$S(x;k) = \log_{10} \frac{1}{1 - k(\frac{hc}{x})^{-4}} \tag{D.1}$$

```
#Create GAUSSIAN model with prefix g1_
gauss1 = GaussianModel(prefix='g1_')
pars = gauss1.guess(y, x=x)
pars['g1_center'].set(value=2.05, min=2.0, max=2.1)
pars['g1_sigma'].set(value=0.09, min=0.06, max=0.1)
pars['g1_amplitude'].set(value=0.027, min=0.01, max=0.04)

#Create GAUSSIAN model with prefix g2_
gauss2 = GaussianModel(prefix='g2_')
pars.update(gauss2.make_params())
pars['g2_center'].set(value=2.21, min=2.21, max=2.27)
pars['g2_sigma'].set(value=0.09, min=0.07, max=0.1)
pars['g2_amplitude'].set(value=0.05, min=0.02, max=0.1)

#Create GAUSSIAN model with prefix g3_
gauss3 = GaussianModel(prefix='g3_')
pars.update(gauss3.make_params())
pars['g3_center'].set(value=2.38, min=2.35, max=2.45)
pars['g3_sigma'].set(value=0.09, min=0.07, max=0.1)
pars['g3_amplitude'].set(value=0.14, min=0.05, max=0.2)

#Create GAUSSIAN model with prefix g4_
gauss4 = GaussianModel(prefix='g4_')
pars.update(gauss4.make_params())
pars['g4_center'].set(value=2.65, min=2.55, max=2.8)
pars['g4_sigma'].set(value=0.14, min=0.1, max=0.4)
```

```
pars['g4_amplitude'].set(value=0.05, min=0.01, max=0.3)

#Define rayleigh scattering function
def rayleigh(x, const):
    return np.log10(1/(1-const*(1240/x)**-4))

#Create model from function
scat = lmfit.Model(rayleigh)
pars.update(scat.make_params())
pars['const'].set(value=5e9, min=4e9, max=5e10)

mod = gauss1 + gauss2 + gauss3 + gauss4 + scat
```

In order to fit a custom function, first we define the function and then create a model based on that function which makes the function variables into parameters for our model.

Step 4: Run the fit, print and plot the results. As before, we run the fit and plot the results. The plot is more detailed with colors for clarity.

```
init = mod.eval(pars, x=x)
out = mod.fit(y, pars, x=x)
print(out.fit_report(min_correl=0.5))

fig, axes = plt.subplots(1, 2, figsize=(12.8, 4.8))
axes[0].plot(x, y, 'k', label='Pure P3HT')
axes[0].plot(x, out.best_fit, 'r', label='Fit')

axes[0].set_xlabel('Energy (eV)', fontsize=14)
axes[0].set_ylabel('Absorbance (O.D)', fontsize=14)
axes[0].tick_params(axis="both", labelsize=12)

```

```
comps = out.eval_components(x=x)
axes[1].plot(x, y, 'k', label='Pure P3HT')
axes[1].plot(x, out.best_fit, 'r', label='Fit')
axes[1].plot(x, comps['g1_'],'--', color="blue", label='P3HT S$_0$')
axes[1].plot(x, comps['g2_'], '--', color="deepskyblue", label='P3HT S$_1$')
axes[1].plot(x, comps['g3_'], '--', color="blueviolet", label='P3HT S$_2$')
axes[1].plot(x, comps['g4_'], '--', color="mediumvioletred", label='P3HT E$_g$
    ')
axes[1].plot(x, rayleigh(x,out.params['const'].value), '--', color="darkgrey",
     label='Scattering')
axes[1].legend(loc='best',fontsize=14)
axes[1].set_xlabel('Energy (eV)', fontsize=14)
axes[1].set_ylabel('Absorbance (O.D)', fontsize=14)
axes[1].tick_params(axis="both", labelsize=12)

P3HTaggregates = comps['g1_'] + comps['g2_'] + comps['g3_'] + comps['g4_']
axes[0].plot(x, P3HTaggregates, 'b--', label='P3HT aggregates')
axes[0].legend(loc='best',fontsize=14)
axes[0].margins(x=0)
axes[1].margins(x=0)
plt.show()
```

Fit to the P3HT data :

The peak centers obtained correspond well to previously reported values for the bandgap transition (E_g = 2.78 eV) as well as the singlet exciton (S_0 = 2.05 eV), exciton +1 phonon (S_1 = 2.22) , and exciton +2 phonons (S_2 = 2.43)[178] and give us good initial guesses for the more complicated full fit of the DDB spectra.

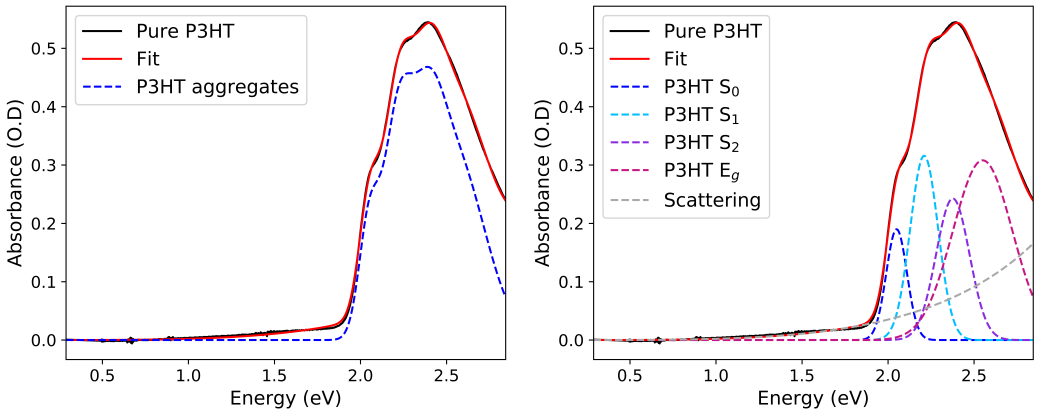

Figure D.4: Best fit to P3HT data and sum of P3HT components (left) and individual fit components (right).

D.2.2 Full fit of DDB doped P3HT

Let us use the 1 mM DDB-*p*-F doped P3HT spectrum as an example.

Step 1: Import packages. Begin by importing necessary packages:

```
import pandas as pd
import numpy as np
from numpy import exp, sqrt, pi
import matplotlib.pyplot as plt
import lmfit
import matplotlib.colors as mcolors
from lmfit.models import GaussianModel
```

Step 2: Load data. Load data and plot doped P3HT absorption spectrum:

```
data = pd.read_excel (r'PATHTOFILE.xlsx')
energy = pd.DataFrame(data, columns= ['XDATA'])
energy = energy.iloc[1100:5820,:]
pF = pd.DataFrame(data, columns= ['YDATA'])
pF = pF.iloc[1100:5820,:]
x=x.values[:,0]
```

```
y=y.values[:,0]


plt.plot(x,y,"k",label='para-F')
plt.legend(loc='best',fontsize=14)
plt.xlabel('Energy (eV)', fontsize=14)
plt.ylabel('Absorbance (O.D)', fontsize=14)
plt.xticks(fontsize=14)
plt.yticks(fontsize=14)
plt.margins(x=0)
plt.ylim(0,0.6)
```

The full spectrum we are fitting looks as follows:

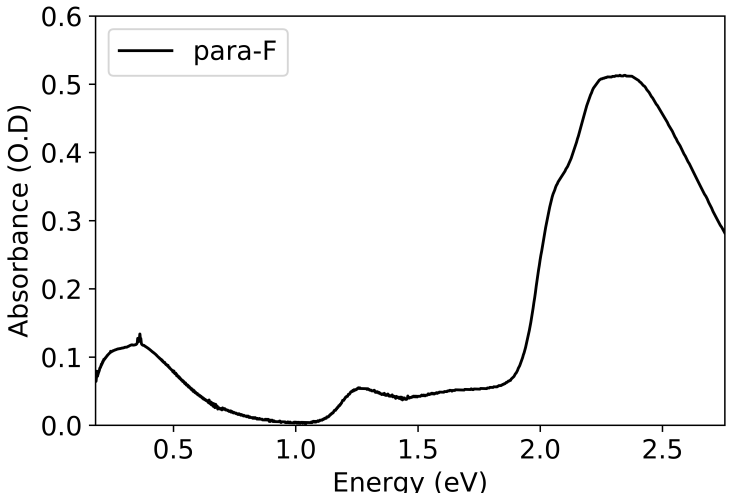

Figure D.5: Plot of 1 mM DDB-*p*-F doped P3HT absorbance.

Now in addition to the 4 gaussians under the broad P3HT absorption and our scattering background, we will add a gaussian for the P1, P2 and P3 polaron peaks. Additionally, the neutral and anionic form of DDBs absorb under the P3HT peak at around 2.3 and 2.6 eV, respectively. While we will add a gaussian for each of these, because of how many peaks overlap in that region, it will be impossible to obtain useful information from this region. Still, it is important to get the peak shape correct since these peaks overlap with the P3. Therefore, our model and our fit will be defined

as follows:

Step 3: Define the fitting model.

```
p1 = GaussianModel(prefix='p1_')
pars = p1.guess(y, x=x)
pars['p1_center'].set(value=0.35, min=0.2, max=0.4)
pars['p1_sigma'].set(value=0.21)
pars['p1_amplitude'].set(value=0.06, min=0.01)

p2 = GaussianModel(prefix='p2_')
pars.update(p2.make_params())
pars['p2_center'].set(value=1.25, min=1.2, max=1.3)
pars['p2_sigma'].set(value=0.12, min=0.05, max=0.15)
pars['p2_amplitude'].set(value=0.015, min=0.008)

p3 = GaussianModel(prefix='p3_')
pars.update(p3.make_params())
pars['p3_center'].set(value=1.63, min=1.6, max=1.65)
pars['p3_sigma'].set(value=0.12, min=0.05, max=0.2)
pars['p3_amplitude'].set(value=0.015, min=0.01)

gauss1 = GaussianModel(prefix='g1_')
pars.update(gauss1.make_params())
pars['g1_center'].set(value=2.05, min=2.045, max=2.055)
pars['g1_sigma'].set(value=0.09, min=0.04, max=0.1)
pars['g1_amplitude'].set(value=0.036, min=0.02, max=0.05)

gauss2 = GaussianModel(prefix='g2_')
pars.update(gauss2.make_params())
pars['g2_center'].set(value=2.21, min=2.15, max=2.25)
```

```
pars['g2_sigma'].set(value=0.08, min=0.05, max=0.1)
pars['g2_amplitude'].set(value=0.056, min=0.045, max=0.07)

gauss3 = GaussianModel(prefix='g3_')
pars.update(gauss3.make_params())
pars['g3_center'].set(value=2.38, min=2.37, max=2.39)
pars['g3_sigma'].set(value=0.1, min=0.08, max=0.15)
pars['g3_amplitude'].set(value=0.07, min=0.05, max=0.1)

gauss4 = GaussianModel(prefix='g4_')
pars.update(gauss4.make_params())
pars['g4_center'].set(value=2.6, min=2.59, max=2.61)
pars['g4_sigma'].set(value=0.16, min=0.1, max=0.2)
pars['g4_amplitude'].set(value=0.08, min=0.06, max=0.11)

gaussn = GaussianModel(prefix='gn_')
pars.update(gaussn.make_params())
pars['gn_center'].set(value=2.35, min=2.3, max=2.4)
pars['gn_sigma'].set(value=0.15, min=0.1, max=0.2)
pars['gn_amplitude'].set(value=0.01, min=0.01, max=0.04)

gaussa = GaussianModel(prefix='ga_')
pars.update(gaussa.make_params())
pars['ga_center'].set(value=2.6, min=2.5, max=2.7)
pars['ga_sigma'].set(value=0.15, min=0.1, max=0.2)
pars['ga_amplitude'].set(value=0.01, min=0.01, max=0.04)

def rayleigh(x, const):
    return np.log10(1/(1-const*(1240/x)**-4))
```

```
scat = lmfit.Model(rayleigh)
pars.update(scat.make_params())
pars['const'].set(value=1.1e10, min=1e10, max=1.2e10)

mod = p1 + p2 + p3 + gauss1 + gauss2 + gauss3 + gauss4 + gaussn + gaussa +
    scat
```

Step 4: Run the fit, print and plot the results.

```
init = mod.eval(pars, x=x)
out = mod.fit(y, pars, x=x)
print(out.fit_report(min_correl=0.5))

fig, axes = plt.subplots(1, 2, figsize=(12.8, 4.8))
axes[0].plot(x, y, 'k', label='1 mM DDB—$\mathit{p}$—F')
axes[0].plot(x, init, 'b——', label='initial fit')
axes[0].plot(x, out.best_fit, 'r—', label='Fit')
axes[0].legend(loc='best',fontsize=13)
axes[0].set_xlabel('Energy (eV)', fontsize=14)
axes[0].set_ylabel('Absorbance (O.D)', fontsize=14)
axes[0].tick_params(axis="both", labelsize=14)
axes[0].set_ylim(0,0.75)

comps = out.eval_components(x=x)
axes[1].plot(x, y, 'k',label='1 mM DDB—$\mathit{p}$—F')
axes[1].plot(x, out.best_fit, 'r', label='Fit')
axes[1].plot(x, comps['p1_'], '——', color="salmon", label='P1')
axes[1].fill_between(x, comps['p1_'], facecolor="salmon", alpha=0.5)
axes[1].plot(x, comps['p2_'], '——', color="darkorange", label='P2')
axes[1].plot(x, comps['p3_'], 'g——', label='P3')
```

```
axes[1].fill_between(x, comps['p3_'], facecolor="g", alpha=0.5)
axes[1].fill_between(x, comps['p2_'], facecolor="darkorange", alpha=0.5)
axes[1].plot(x, comps['g4_'], '--',color="royalblue", label='P3HT')
axes[1].fill_between(x, comps['g4_'], facecolor="royalblue", alpha=0.5)
axes[1].plot(x, comps['g5_'],'--', color="royalblue")
axes[1].fill_between(x, comps['g5_'], facecolor="royalblue", alpha=0.5)
axes[1].plot(x, comps['g6_'], '--',color="royalblue")
axes[1].fill_between(x, comps['g6_'], facecolor="royalblue", alpha=0.5)
axes[1].plot(x, comps['g7_'], '--',color="royalblue")
axes[1].fill_between(x, comps['g7_'], facecolor="royalblue", alpha=0.5)
axes[1].plot(x, comps['g8_'], 'm--', label='DDB anion')
axes[1].fill_between(x, comps['g8_'], facecolor="m", alpha=0.5)
axes[1].plot(x, comps['g9_'], '--', color="gold", label='DDB neutral')
axes[1].fill_between(x, comps['g9_'], facecolor="yellow", alpha=0.5)
axes[1].plot(x, rayleigh(x,out.params['const'].value), '--', color="darkgrey",
    label='Scattering')
axes[1].legend(loc='upper left',fontsize=13,ncol=1)
axes[1].set_xlabel('Energy (eV)', fontsize=14)
axes[1].set_ylabel('Absorbance (O.D)', fontsize=14)
axes[1].tick_params(axis="both", labelsize=14)
axes[1].set_ylim(0,0.8)
plt.show()
```

And our result is as follows:

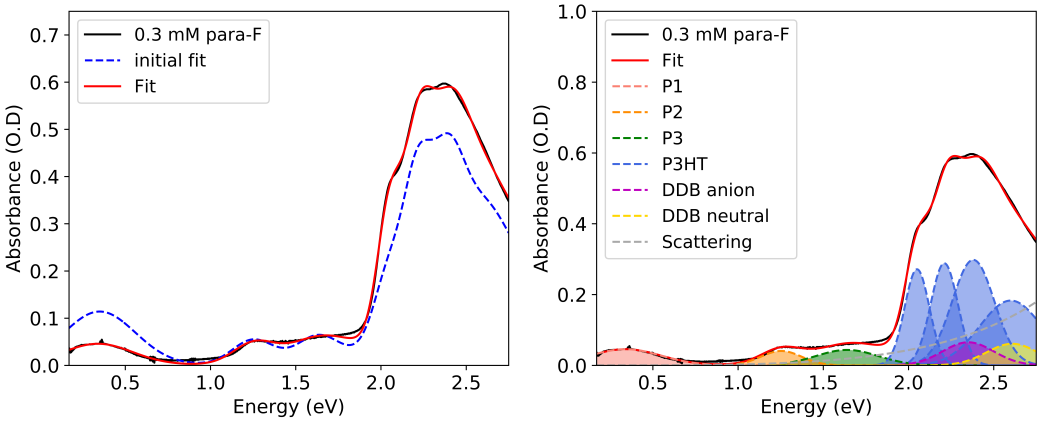

Figure D.6: Initial and best fit to DDB-*p*-F doped P3HT data (left) and individual fit components (right).

APPENDIX E

Maintenance and Modifications of Lab Equipment

E.1 Ångstrom Thermal Evaporator

The water cooling for the sample stage in the Angstrom thermal evaporator was modified to run off a heat exchanger system for separation from the house water cooling line. The change was implemented after it was discovered that the water in the house line caused corrosion of the entire ferrofluidic rotary (which allows the sample stage to turn) causing it to seize as well as another corrosion of another blank. The cause of the damage was attributed to the poor house water quality with excess iron oxide content. With the addition of a heat exchanger water cooling system, the following SOP should be followed when running an evaporation. Note that this focuses on the instrumentation and not the details of running a specific evaporation program.

Procedure for running an evaporation:

1. **Make sure the reservoir (see Figure E.1a) is filled with water (50% tap water, 50% DI water).**

2. **Open the valves for the house water (see Figure E.1b).**
   This will allow cold water from the house line to run through the heat exchanger. There are five valves total (circled in red in Figure E.1b) but we typically operate one set on the supply and return lines (in this case the white ones).

3. **Turn on the chiller (see Figure E.1c).**
   If a horrid alarm sounds, go back to step 1 and fill the reservoir. The pump moves the reservoir water through the heat exchanger and allows it to cool via contact with the house water.

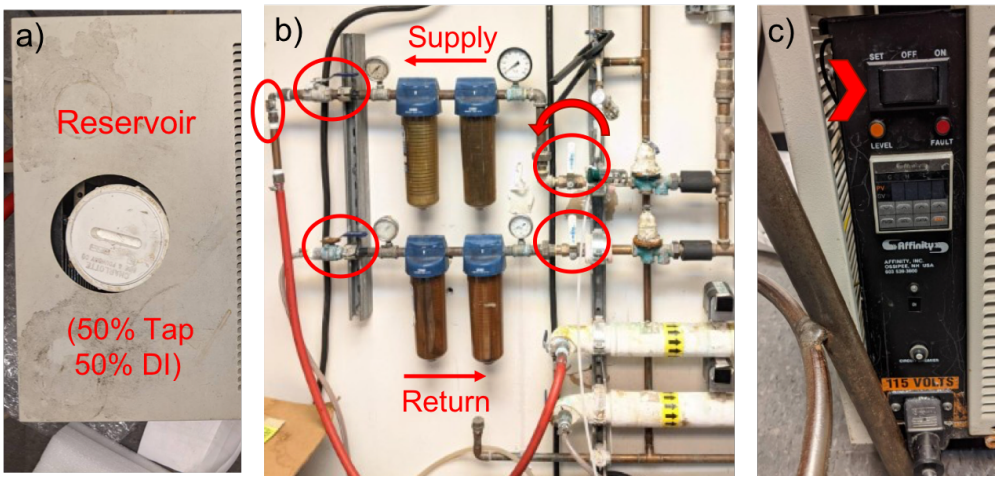

Figure E.1: a) Chiller water reservoir b) House water supply and return lines c) chiller front panel.

4. **Let the chiller run for 20 minutes before starting your evaporation.**

   This gives enough time for the water in the heat exchanger to cool.

5. **Run the evaporation.**

   Once the pressure has reached $< 1 \times 10^{-6}$ Torr, you can run the evaporation.

6. **Turn off the heat exchanger system.**

   When finished, allow 20 minutes for samples to cool before turning off the heat exchanger system. To turn off the cooling system, simply turn off the heat exchanger and then close the two valves you opened (one supply and one return) on the house line.

Things to check to ensure proper operation (and how to troubleshoot them):

- *When you start pumping down the evaporator,* first the rough pump will run, followed by the turbo pump. It should only take about 10 minutes for the turbo pump to kick in (indicated by a higher wattage on the top right of the Inficon display and a whirring sound) and 20 minutes for the system to reach base pressure. Always listen for happy pumps. If the rough pump sounds really bad, it probably needs to have the pump oil changed. The turbo pump is happy if it sits around 8W once base pressure is achieved and does not make noise. If the system takes a long time to pump down, or cannot reach 1×10^{-8} Torr after a weekend of pumping down, first clean the inner plates. If still no improvement, this might indicate a leak in the system.

- *After step 4,* check that cool water is flowing through the water lines going to the evaporator. When placing your hand on the lines, it should feel cool to the touch and a slight vibration indicates flow. If it appears not to be cool, check that the house water lines are fully open and running and you have properly followed previous steps. If there appears to be no flow, but everything is correct, there may be a blockage in the line (although this has been pretty rare). You can remove one of the small hose attachments from the heat exchanger and rinse the line with water.

- *As you are running an evaporation,* take a look through the window in back of the evaporator. You should be able to see that the sample stage is turning and, once you have reached a high enough power, that the area near your chosen source is glowing red with heat. If the stage is not turning, make sure the speed control on the front panel is on at least level 2. If there is no red source, there might be something wrong with the settings or type of metal you have chosen. Double check your source, pocket, and metal settings. Also check that your resistive boat is still in place.

- If these trouble shooting steps do not work and you are having problems, contact Ångstrom, they are extremely helpful.

E.2 The Nitrogen Glovebox

The solenoid valves that were connected to the purge and vacuum lines near the small antechamber were problematic for a long time. So much so that the following step was a regular part of the procedure that will forever be immortalized here:

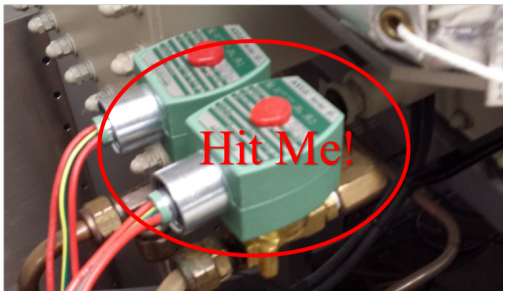

Figure E.2: Previous faulty solenoid valve (replaced twice!)

Solenoid valves rely on an electromagnet to lift a plunger against a spring when energized, and go back to closed position when de-energized via the spring action. The problem is that there is no good way to ensure the valve is either open or closed and since regeneration of the purifier material releases caustic fluid, the purge valve would corrode and stop working. Therefore, these were replaced with manual ball valves, however, since the regeneration runs on a timed program IT IS VERY IMPORTANT THAT YOU BE THERE WHEN THE VALVES NEED TO BE OPENED OR CLOSED! The full regeneration procedure is now as follows:

Procedure for Nitrogen Glovebox Regeneration

1. Perform a quick purge of the glove box for 30-60 min. Do this by attaching the clear tube located at the fume hood to the valve that allows outside air back into the small antechamber. This tube should be attached to an oil bubbler in the nearest fume hood. Open the small antechamber refill valve and the valve that opens the antechamber to outside air that now has the hose attached to it. Increase the pressure of the glovebox until a steady flow of nitrogen is seen leaving the box (bubbles in the bubbler). Let flow for desired time, then lower the pressure and close all valves of the antechamber and remove hose.

2. Switch the circulation toggle to the OFF position (center) on the side of the glovebox. You should hear the fan stop.

3. Close the ball valves leading to and from the cylinder containing the regeneration material (molecular sieves and charcoal) located on the outside of the glove box.

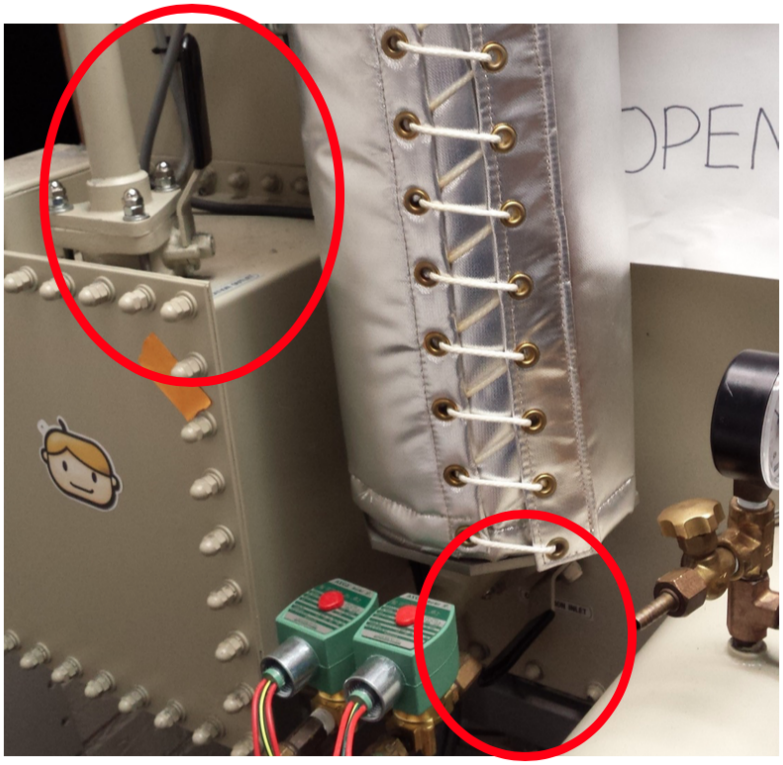

4. Check to make sure the timer on the side of the glove box is in the vacuum position. (Should be at the end of the purge step. DO NOT hold it down to vacuum or it will open all the valves and pull vacuum on everything!)

5. Switch the circulation toggle to the REGENERATE position and open the ball valve to the vacuum line (circled in red). This will open only the cylinder to the vacuum. Let it pump down for 30-60 min. Switch the circulation toggle back to the OFF position, and slowly open

the ball valves as the cylinder will be under vacuum.

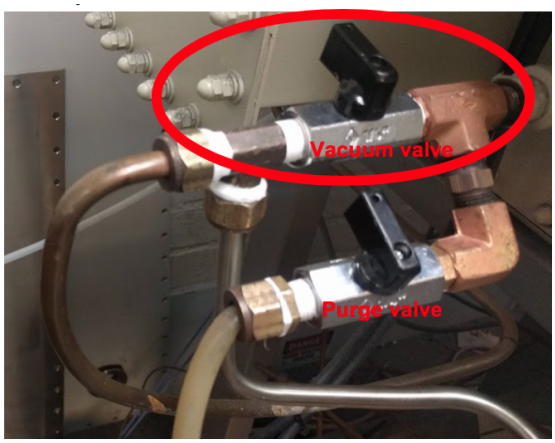

6. Check the level of the N2 forming gas cylinder attached to the rear of the glove box. One regeneration cycle requires approximately 30 cubic feet. Obtain a new cylinder of N2 forming gas if needed and attach to glovebox. Open the cylinder and close the ball valves again.

7. Remove the dessicant and molecular sieve filled solvent trap (aka coffee pot, circled) attached to the top of the inlet that leads to the cylinder from the inside of the glove box. Also remove the small filter from the outlet on the inside of the glovebox (also circled). Every other regen: remove the next charcoal filled cylinder and take it out of the box through the large antechamber. Place in our largest pyrex dish and bake overnight in the oven in MCTP at max temperature (270 °C) and fully opened vacuum. This will regenerate the charcoal. Be careful of fumes. You can also replace every so often as it is quite cheap.

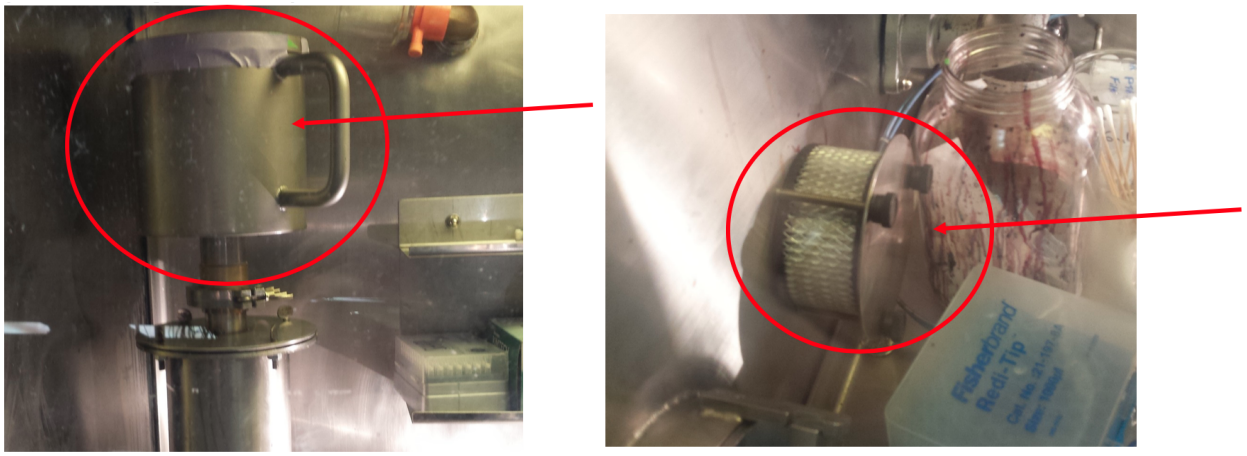

8. Place both the filter and the solvent trap (coffee pot) in the large antechamber. Close the large antechamber and begin pumping down. Do this by opening the valve labeled vent attached to the evacuation outlet on the outside of the large antechamber. Make sure the valve leading to the refill is closed or you will pull vacuum on the box.

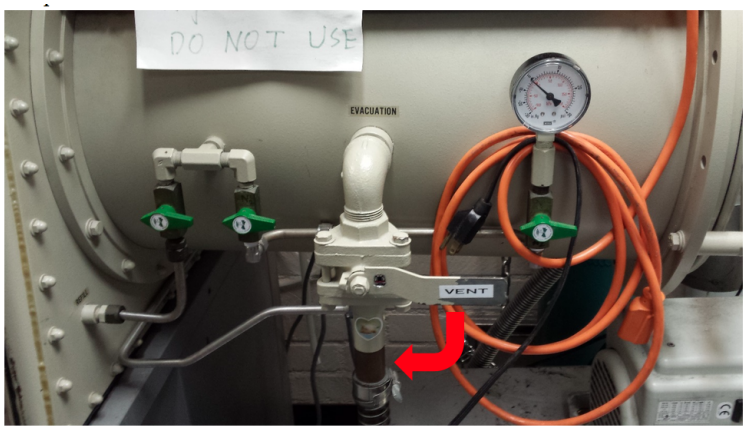

9. Remove the stopper from the purge hose (hose next to the small antechamber) and place the end of the hose in the yellow safety bucket hanging inside the fume hood. Hot, solvent-loaded steam will be exiting this hose. You don't want it anywhere near you.

10. Now begin the timed regeneration cycle. BE SURE TO READ AND UNDERSTAND ALL FOLLOWING SUBSTEPS BEFORE PROCEEDING:

    (a) Turn the timer clockwise to the START position and switch the circulation toggle to the REGENERATE position. The cylinder will now begin to heat up for the next 3 hours. SET A TIMER FOR 2.5 HOURS AND RETURN TO THE LAB WITHIN THAT TIME.

(b) Return to the lab before the timer reaches the PURGE position (∼2.5 hrs). Make sure the purge hose is unstoppered and in the yellow bucket in the fume hood. SIMULTANEOUSLY: manually ADVANCE the timer to the PURGE step and OPEN the PURGE VALVE. The forming gas will begin to flow through the cylinder and out the hose. DO NOT LET THE TIMER TO ADVANCE TO THE PURGE STEP WHILE THE BALL VALVE IS CLOSED OR THE HOSE IS STOPPERED AS THIS WILL LEAD TO PRESSURE BUILD UP IN THE PURIFIER SYSTEM.

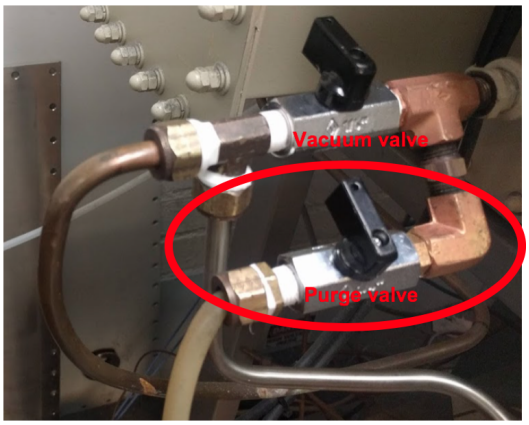

(c) Adjust the flow rate according to the directions on the side of the glovebox next to the circulation toggle (20 CFH for N2). The gas will continue to flow for 1 hour. SET ANOTHER TIMER FOR 45 MINUTES AND BE SURE TO RETURN TO THE LAB WITHIN THAT TIME.

(d) When the purge cycle is nearly finished but BEFORE it ends, SIMULTANEOUSLY: manually ADVANCE the timer to the VACUUM step and CLOSE the PURGE VALVE and CLOSE the VACUUM VALVE. At this point, no more steam should be flow through the purge ball valve and the hot cylinder should now be under vacuum. Now the hot cylinder will pump down. Let it go down for as long as possible, at least 8 hours, overnight is better, weekend is best.

11. Once finished pumping on the cylinder, switch the circulation toggle back to the OFF position.

12. Close the valves on the tank of forming gas.

13. Close the valve leading to the back of the vacuum. Turn on the vacuum pump heater by plugging it in. Make sure it is plugged in on both ends (the extension cord goes up through the ceiling and back down to the fume hood outlet). Let the oil heat for $\sim$3 hours.

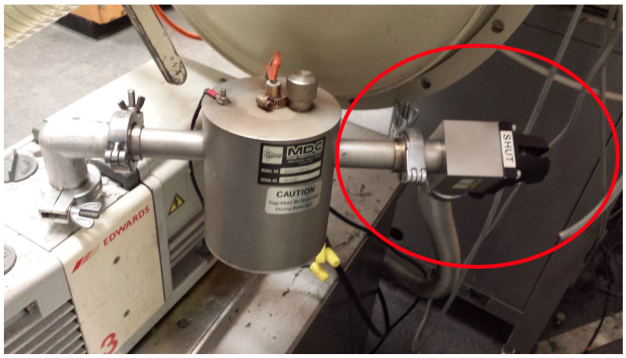

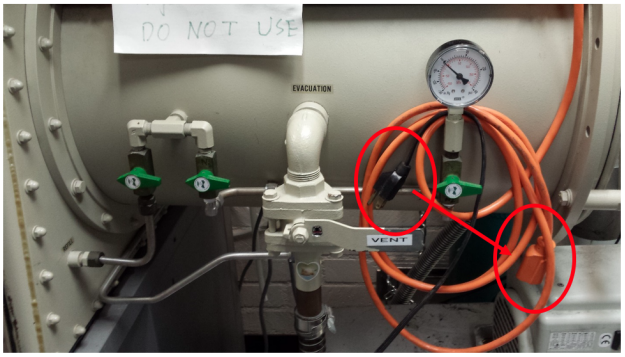

14. Unplug the heater. Turn off the vacuum pump. Change the pump oil. This oil will be pretty gross. USE A RESPIRATOR.

15. Turn the pump back on and open the valve at the back of the vacuum pump.

16. Refill the large antechamber.

17. Return the solvent trap and small filter to their appropriate places.

18. Slowly open the ball valves (under vacuum again).

19. Switch the circulation toggle to CIRCULATE.

20. Let the box circulate for 1 day before preforming a light bulb test to allow the atmosphere time to circulate through the now clean purifying material.

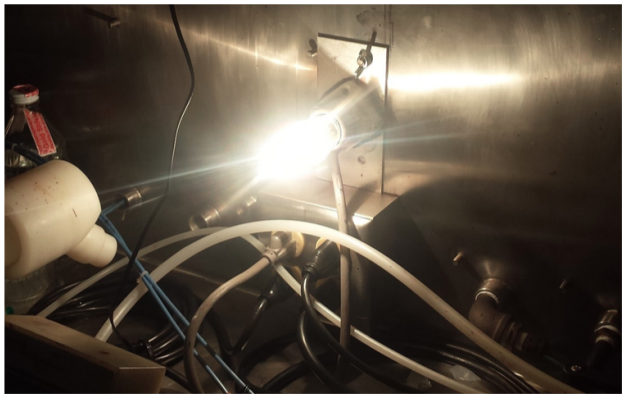

Troubleshooting (for gloveboxes in general):

- *If your lightbulb test fails* (i.e. the bulb lasts less than 20 minutes while it should ideally last for hours) double check that you performed all regeneration steps properly. If you think something went wrong, perform another regen. Otherwise, this may be indicative of a leak or that the catalyst material needs to be replaced (every 5ish years depending on use and presence of solvents, last replaced in 2015 for the Nitrogen box).
- *To check if you have a leak* increase the low pressure setpoint, let the box pressurize, and then decrease the setpoint. Record the pressure vs. time. Anything over 0.1 mbar/min is a significant leak.
- *To find the origin of a leak* use soap and water bubbles along any pieces that are connected and especially the gloves. If a leak is present, the bubbles will enlarge noticeably.

E.3 The Seebeck Measurement Set-Up

The Seebeck measurement set up originally employed two resistance temperature detectors (RTDs) to measure temperature difference and two prongs from a 3M clip to measure the voltage difference over a sample placed across a hot and cold thermoelectric module. The main issue with this set up

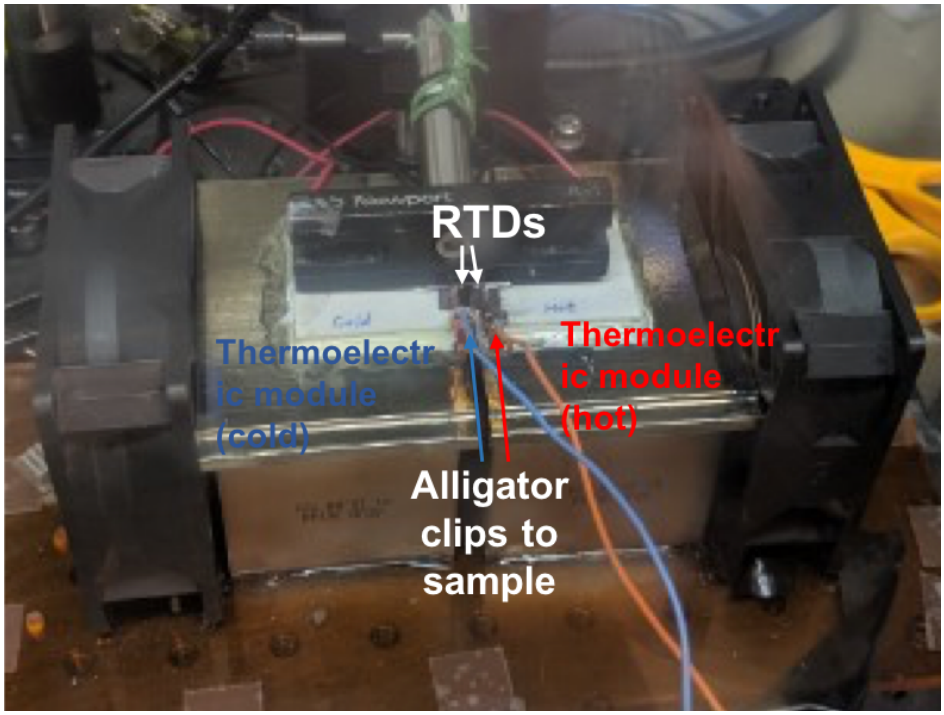

Figure E.5: Modified thermoelectric set up with alligator clips for sample voltage measurement.

was achieving contact with the metal prongs from the 3M clip to the sample, which often were not aligned or needed a lot of pressure resulting in scratches on the sample. The prongs were replaced with two alligator clips that can now easily be clipped on to the sample. The rest of the set-up is still exactly as before, with the voltage measurement taken from the BNC cable labeled "To sample wires".

REFERENCES

[1] B. Norden and E. Krutmeijer, "Advanced Information - The Nobel Prize in Chemistry, 2000: Conductive polymers," tech. rep., 2000.

[2] J. Nelson, "Polymer: Fullerene bulk heterojunction solar cells," *Materials Today*, vol. 14, no. 10, pp. 462–470, 2011.

[3] J. Liang, L. Li, X. Niu, Z. Yu, and Q. Pei, "Elastomeric polymer light-emitting devices and displays," *Nature Photonics*, vol. 7, no. 10, pp. 817–824, 2013.

[4] M. Li, D. K. Mangalore, J. Zhao, J. H. Carpenter, H. Yan, H. Ade, H. Yan, K. Müllen, P. W. Blom, W. Pisula, D. M. De Leeuw, and K. Asadi, "Integrated circuits based on conjugated polymer monolayer," *Nature Communications*, vol. 9, no. 1, 2018.

[5] B. Russ, A. Glaudell, J. J. Urban, M. L. Chabinyc, and R. A. Segalman, "Organic thermoelectric materials for energy harvesting and temperature control," *Nature Reviews Materials*, vol. 1, no. 10, 2016.

[6] D. T. McQuade, A. E. Pullen, and T. M. Swager, "Conjugated Polymer-Based Chemical Sensors," *Chemical Reviews*, vol. 100, pp. 2537–2574, jul 2000.

[7] A. C. Arias, J. D. MacKenzie, I. McCulloch, J. Rivnay, and A. Salleo, "Materials and applications for large area electronics: Solution-based approaches," *Chemical Reviews*, vol. 110, no. 1, pp. 3–24, 2010.

[8] C. Deibel and V. Dyakonov, "Polymer–fullerene bulk heterojunction solar cells," *Reports on Progress in Physics*, vol. 73, p. 096401, sep 2010.

[9] G. Yu, J. Gao, J. C. Hummelen, F. Wudl, and A. J. Heeger, "Polymer Photovoltaic Cells: Enhanced Efficiencies via a Network of Internal Donor-Acceptor Heterojunctions," *Science*, vol. 270, pp. 1789–1791, dec 1995.

[10] Y. Zhang, Y. J. Heo, M. Park, and S. J. Park, "Recent advances in organic thermoelectric materials: Principle mechanisms and emerging carbon-based green energy materials," *Polymers*, vol. 11, no. 1, 2019.

[11] I. Osaka and K. Takimiya, "Backbone orientation in semiconducting polymers," *Polymer*, vol. 59, pp. A1–A15, feb 2015.

[12] J. Ma, K. Hashimoto, T. Koganezawa, and K. Tajima, "End-on orientation of semiconducting polymers in thin films induced by surface segregation of fluoroalkyl chains," *Journal of the American Chemical Society*, vol. 135, no. 26, pp. 9644–9647, 2013.

[13] R. Noriega, J. Rivnay, K. Vandewal, F. P. V. Koch, N. Stingelin, P. Smith, M. F. Toney, and A. Salleo, "A general relationship between disorder, aggregation and charge transport in conjugated polymers," *Nature Materials*, vol. 12, pp. 1038–1044, aug 2013.

[14] S. A. Mollinger, B. A. Krajina, R. Noriega, A. Salleo, and A. J. Spakowitz, "Percolation, Tie-Molecules, and the Microstructural Determinants of Charge Transport in Semicrystalline Conjugated Polymers," *ACS Macro Letters*, vol. 4, no. 7, pp. 708–712, 2015.

[15] M. A. Green, K. Emery, Y. Hishikawa, W. Warta, and E. D. Dunlop, "Solar cell efficiency tables (version 43)," *Progress in Photovoltaics: Research and Applications*, vol. 22, pp. 1–9, jan 2014.

[16] Z. He, C. Zhong, S. Su, M. Xu, H. Wu, and Y. Cao, "Enhanced power-conversion efficiency in polymer solar cells using an inverted device structure," *Nature Photonics*, vol. 6, pp. 593–597, aug 2012.

[17] J. Zhao, Y. Li, G. Yang, K. Jiang, H. Lin, H. Ade, W. Ma, and H. Yan, "Efficient organic solar cells processed from hydrocarbon solvents," *Nature Energy*, vol. 1, p. 15027, jan 2016.

[18] B. A. Collins, J. R. Tumbleston, and H. Ade, "Miscibility, Crystallinity, and Phase Development in P3HT/PCBM Solar Cells: Toward an Enlightened Understanding of Device Morphology and Stability," *The Journal of Physical Chemistry Letters*, vol. 2, pp. 3135–3145, dec 2011.

[19] J. J. M. Halls, C. A. Walsh, N. C. Greenham, E. A. Marseglia, R. H. Friend, S. C. Moratti, and A. B. Holmes, "Efficient photodiodes from interpenetrating polymer networks," *Nature*, vol. 376, pp. 498–500, aug 1995.

[20] S. E. Shaheen, C. J. Brabec, N. Serdar Sariciftci, F. Padinger, T. Fromherz, and J. C. Hummelen, "2.5% efficient organic plastic solar cells," *Hummelen Citation: Applied Physics Letters J. Appl. Phys*, vol. 78, pp. 841–843, feb 2001.

[21] P. E. Shaw, A. Ruseckas, and I. D. W. Samuel, "Exciton Diffusion Measurements in Poly(3-hexylthiophene)," *Advanced Materials*, vol. 20, pp. 3516–3520, jul 2008.

[22] J. Peet, C. Soci, R. C. Coffin, T. Q. Nguyen, A. Mikhailovsky, D. Moses, and G. C. Bazan, "Method for increasing the photoconductive response in conjugated polymer/fullerene composites," *Applied Physics Letters*, vol. 89, p. 252105, dec 2006.

[23] J. Peet, J. Y. Kim, N. E. Coates, W. L. Ma, D. Moses, A. J. Heeger, and G. C. Bazan, "Efficiency enhancement in low-bandgap polymer solar cells by processing with alkane dithiols," *Nature Materials*, vol. 6, pp. 497–500, jul 2007.

[24] J. K. Lee, W. L. Ma, C. J. Brabec, J. Yuen, J. S. Moon, J. Y. Kim, K. Lee, G. C. Bazan, and A. J. Heeger, "Processing Additives for Improved Efficiency from Bulk Heterojunction Solar Cells," *Journal of the American Chemical Society*, vol. 130, pp. 3619–3623, feb 2008.

[25] S. Kwon, H. Kang, J.-H. Lee, J. Lee, S. Hong, H. Kim, and K. Lee, "Effect of Processing Additives on Organic Photovoltaics: Recent Progress and Future Prospects," *Advanced Energy Materials*, vol. 7, p. 1601496, may 2017.

[26] Y. Zhao, Z. Xie, Y. Qu, Y. Geng, and L. Wang, "Solvent-vapor treatment induced performance enhancement of poly(3-hexylthiophene):methanofullerene bulk-heterojunction photovoltaic cells," *Applied Physics Letters*, vol. 90, pp. 043504–043506, jan 2007.

[27] J. Jo, S.-I. Na, S.-S. Kim, T.-W. Lee, Y. Chung, S.-J. Kang, D. Vak, and D.-Y. Kim, "Three-Dimensional Bulk Heterojunction Morphology for Achieving High Internal Quantum Efficiency in Polymer Solar Cells," *Advanced Functional Materials*, vol. 19, pp. 2398–2406, aug 2009.

[28] L. Ma, W. H. Lee, Y. D. Park, J. S. Kim, H. S. Lee, and K. Cho, "High performance polythiophene thin-film transistors doped with very small amounts of an electron acceptor," *Applied Physics Letters*, vol. 92, no. 6, pp. 1–4, 2008.

[29] K. Kim, J. Liu, M. A. G. Namboothiry, and D. L. Carroll, "Roles of donor and acceptor nanodomains in 6% efficient thermally annealed polymer photovoltaics," *Applied Physics Letters*, vol. 90, p. 163511, apr 2007.

[30] E. Verploegen, R. Mondal, C. J. Bettinger, S. Sok, M. F. Toney, and Z. Bao, "Effects of thermal annealing upon the morphology of polymer-fullerene blends," *Advanced Functional Materials*, vol. 20, pp. 3519–3529, oct 2010.

[31] A. L. Ayzner, C. J. Tassone, S. H. Tolbert, and B. J. Schwartz, "Reappraising the Need for Bulk Heterojunctions in Polymer-Fullerene Photovoltaics: The Role of Carrier Transport in All-Solution-Processed P3HT/PCBM Bilayer Solar Cells," *The Journal of Physical Chemistry C*, vol. 113, pp. 20050–20060, nov 2009.

[32] V. S. Gevaerts, L. J. A. Koster, M. M. Wienk, and R. A. J. Janssen, "Discriminating Between Bilayer and Bulk Heterojunction Polymer:Fullerene Solar Cells Using the External Quantum Efficiency," *ACS Applied Materials & Interfaces*, vol. 3, pp. 3252–3255, sep 2011.

[33] J. S. Moon, C. J. Takacs, Y. Sun, and A. J. Heeger, "Spontaneous Formation of Bulk Heterojunction Nanostructures: Multiple Routes to Equivalent Morphologies," *Nano Letters*, vol. 11, pp. 1036–1039, mar 2011.

[34] P. Cheng, J. Hou, Y. Li, and X. Zhan, "Layer-by-layer solution-processed low-bandgap polymer-PC61BM solar cells with high efficiency," *Advanced Energy Materials*, vol. 4, p. 1301349, jun 2014.

[35] N. D. Treat, M. A. Brady, G. Smith, M. F. Toney, E. J. Kramer, C. J. Hawker, and M. L. Chabinyc, "Interdiffusion of PCBM and P3HT reveals miscibility in a photovoltaically active blend," *Advanced Energy Materials*, vol. 1, pp. 82–89, jan 2011.

[36] A. L. Ayzner, S. C. Doan, B. Tremolet De Villers, and B. J. Schwartz, "Ultrafast studies of exciton migration and polaron formation in sequentially solution-processed conjugated polymer/fullerene quasi-bilayer photovoltaics," *Journal of Physical Chemistry Letters*, vol. 3, no. 16, pp. 2281–2287, 2012.

[37] S. A. Hawks, J. C. Aguirre, L. T. Schelhas, R. J. Thompson, R. C. Huber, A. S. Ferreira, G. Zhang, A. A. Herzing, S. H. Tolbert, and B. J. Schwartz, "Comparing Matched Polymer:Fullerene Solar Cells Made by Solution-Sequential Processing and Traditional Blend Casting: Nanoscale Structure and Device Performance," *The Journal of Physical Chemistry C*, vol. 118, pp. 17413–17425, aug 2014.

[38] G. Zhang, R. C. Huber, A. S. Ferreira, S. D. Boyd, C. K. Luscombe, S. H. Tolbert, and B. J. Schwartz, "Crystallinity Effects in Sequentially Processed and Blend-Cast Bulk-Heterojunction Polymer/Fullerene Photovoltaics," *The Journal of Physical Chemistry C*, vol. 118, pp. 18424–18435, aug 2014.

[39] A. S. Ferreira, J. C. Aguirre, S. Subramaniyan, S. A. Jenekhe, S. H. Tolbert, and B. J. Schwartz, "Understanding How Polymer Properties Control OPV Device Performance: Regioregularity, Swelling, and Morphology Optimization Using Random Poly(3-butylthiophene-co -3-octylthiophene) Polymers," *The Journal of Physical Chemistry C*, vol. 120, pp. 22115–22125, oct 2016.

[40] P. E. Schwenn, K. Gui, A. M. Nardes, K. B. Krueger, K. H. Lee, K. Mutkins, H. Rubinstein-Dunlop, P. E. Shaw, N. Kopidakis, P. L. Burn, and P. Meredith, "A small molecule non-fullerene electron acceptor for organic solar cells," *Advanced Energy Materials*, vol. 1, pp. 73–81, jan 2011.

[41] A. Loiudice, A. Rizzo, G. Latini, C. Nobile, M. de Giorgi, and G. Gigli, "Graded vertical phase separation of donor/acceptor species for polymer solar cells," *Solar Energy Materials and Solar Cells*, vol. 100, pp. 147–152, may 2012.

[42] A. M. Nardes, A. L. Ayzner, S. R. Hammond, A. J. Ferguson, B. J. Schwartz, and N. Kopidakis, "Photoinduced charge carrier generation and decay in sequentially deposited polymer/-fullerene layers: Bulk heterojunction vs planar interface," *Journal of Physical Chemistry C*, vol. 116, no. 13, pp. 7293–7305, 2012.

[43] D. H. Kim, J. Mei, A. L. Ayzner, K. Schmidt, G. Giri, A. L. Appleton, M. F. Toney, and Z. Bao, "Sequentially solution-processed, nanostructured polymer photovoltaics using selective solvents," *Energy & Environmental Science*, vol. 7, no. 3, p. 1103, 2014.

[44] J. C. Aguirre, S. A. Hawks, A. S. Ferreira, P. Yee, S. Subramaniyan, S. A. Jenekhe, S. H. Tolbert, and B. J. Schwartz, "Sequential Processing for Organic Photovoltaics: Design Rules for Morphology Control by Tailored Semi-Orthogonal Solvent Blends," *Advanced Energy Materials*, vol. 5, p. 1402020, jun 2015.

[45] S. Liu, P. You, J. Li, J. Li, C.-S. Lee, B. S. Ong, C. Surya, and F. Yan, "Enhanced efficiency of polymer solar cells by adding a high-mobility conjugated polymer," *Energy & Environmental Science*, vol. 8, pp. 1463–1470, 2015.

[46] K. H. Lee, P. E. Schwenn, A. R. Smith, H. Cavaye, P. E. Shaw, M. James, K. B. Krueger, I. R. Gentle, P. Meredith, and P. L. Burn, "Morphology of all-solution-processed "bilayer" organic solar cells," *Advanced Materials*, vol. 23, pp. 766–770, feb 2011.

[47] B. a. Collins, E. Gann, L. Guignard, X. He, C. R. McNeill, and H. Ade, "Molecular Miscibility of Polymer-Fullerene Blends," *The Journal of Physical Chemistry Letters*, vol. 1, pp. 3160–3166, nov 2010.

[48] C. Tao, M. Aljada, P. E. Shaw, K. H. Lee, H. Cavaye, M. N. Balfour, R. J. Borthwick, M. James, P. L. Burn, I. R. Gentle, and P. Meredith, "Controlling hierarchy in solution-processed polymer solar cells based on crosslinked P3HT," *Advanced Energy Materials*, vol. 3, pp. 105–112, jan 2013.

[49] C. Piliego, T. W. Holcombe, J. D. Douglas, C. H. Woo, P. M. Beaujuge, and J. M. J. Fréchet, "Synthetic Control of Structural Order in N -Alkylthieno[3,4-c]pyrrole-4,6-dione-Based Polymers for Efficient Solar Cells," *Journal of the American Chemical Society*, vol. 132, pp. 7595–7597, jun 2010.

[50] C. Cabanetos, A. El Labban, J. A. Bartelt, J. D. Douglas, W. R. Mateker, J. M. Fréchet, M. D. McGehee, and P. M. Beaujuge, "Linear side chains in benzo[1,2-b:4,5-b']dithiophene-thieno[3,4-c] pyrrole-4,6-dione polymers direct self-assembly and solar cell performance," *Journal of the American Chemical Society*, vol. 135, pp. 4656–4659, mar 2013.

[51] J. Rivnay, R. Steyrleuthner, L. H. Jimison, A. Casadei, Z. Chen, M. F. Toney, A. Facchetti, D. Neher, and A. Salleo, "Drastic control of texture in a high performance n-type polymeric semiconductor and implications for charge transport," *Macromolecules*, vol. 44, pp. 5246–5255, jul 2011.

[52] X. Zhang, L. J. Richter, D. M. Delongchamp, R. J. Kline, M. R. Hammond, I. McCulloch, M. Heeney, R. S. Ashraf, J. N. Smith, T. D. Anthopoulos, B. Schroeder, Y. H. Geerts, D. A. Fischer, and M. F. Toney, "Molecular packing of high-mobility diketo pyrrolo-pyrrole polymer semiconductors with branched alkyl side chains," *Journal of the American Chemical Society*, vol. 133, pp. 15073–15084, sep 2011.

[53] F. Liu, Y. Gu, J. W. Jung, W. H. Jo, and T. P. Russell, "On the morphology of polymer-based photovoltaics," *Journal of Polymer Science Part B: Polymer Physics*, vol. 50, pp. 1018–1044, aug 2012.

[54] A. Saeki, Y. Koizumi, T. Aida, and S. Seki, "Comprehensive approach to intrinsic charge carrier mobility in conjugated organic molecules, macromolecules, and supramolecular architectures," *Accounts of Chemical Research*, vol. 45, pp. 1193–1202, aug 2012.

[55] G. H. Lu, L. G. Li, and X. N. Yang, "Achieving Perpendicular Alignment of Rigid Polythiophene Backbones to the Substrate by Using Solvent-Vapor Treatment," *Advanced Materials*, vol. 19, pp. 3594–3598, nov 2007.

[56] K. M. Coakley, B. S. Srinivasan, J. M. Ziebarth, C. Goh, Y. Liu, and M. D. McGehee, "Enhanced hole mobility in regioregular polythiophene infiltrated in straight nanopores," *Advanced Functional Materials*, vol. 15, pp. 1927–1932, dec 2005.

[57] M. Aryal, K. Trivedi, and W. W. Hu, "Nano-Confinement Induced Chain Alignment in Ordered P3HT Nanostructures Defined by Nanoimprint Lithography," *ACS Nano*, vol. 3, pp. 3085–3090, oct 2009.

[58] H. Sirringhaus, P. J. Brown, R. H. Friend, M. M. Nielsen, K. Bechgaard, B. M. Langeveld-Voss, A. J. Spiering, R. A. Janssen, E. W. Meijer, P. Herwig, and D. M. De Leeuw, "Two-dimensional charge transport in self-organized, high-mobility conjugated polymers," *Nature*, vol. 401, pp. 685–688, oct 1999.

[59] M. R. Hammond, R. J. Kline, A. A. Herzing, L. J. Richter, D. S. Germack, H. W. Ro, C. L. Soles, D. A. Fischer, T. Xu, L. Yu, M. F. Toney, and D. M. Delongchamp, "Molecular order in high-efficiency polymer/fullerene bulk heterojunction solar cells," *ACS Nano*, vol. 5, pp. 8248–8257, sep 2011.

[60] M. S. Chen, J. R. Niskala, D. a. Unruh, C. K. Chu, O. P. Lee, and J. M. J. Fréchet, "Control of polymer-packing orientation in thin films through synthetic tailoring of backbone coplanarity," *Chemistry of Materials*, vol. 25, no. 20, pp. 4088–4096, 2013.

[61] I. Osaka, T. Kakara, N. Takemura, T. Koganezawa, and K. Takimiya, "Naphthodithiophene–Naphthobisthiadiazole Copolymers for Solar Cells: Alkylation Drives the Polymer Backbone Flat and Promotes Efficiency," *Journal of the American Chemical Society*, vol. 135, pp. 8834–8837, jun 2013.

[62] I. Osaka, M. Saito, T. Koganezawa, and K. Takimiya, "Thiophene-Thiazolothiazole Copolymers: Significant Impact of Side Chain Composition on Backbone Orientation and Solar Cell Performances," *Advanced Materials*, vol. 26, pp. 331–338, jan 2014.

[63] J. M. Szarko, J. Guo, Y. Liang, B. Lee, B. S. Rolczynski, J. Strzalka, T. Xu, S. Loser, T. J. Marks, L. Yu, and L. X. Chen, "When function follows form: Effects of donor copolymer side chains on film morphology and BHJ solar cell performance," *Advanced Materials*, vol. 22, pp. 5468–5472, dec 2010.

[64] C. M. Proctor, J. A. Love, and T.-Q. Nguyen, "Mobility Guidelines for High Fill Factor Solution-Processed Small Molecule Solar Cells," *Advanced Materials*, vol. 26, pp. 5957–5961, sep 2014.

[65] H.-y. Chen, J. Hou, S. Zhang, Y. Liang, G. Yang, Y. Yang, L. Yu, Y. Wu, and G. Li, "Polymer solar cells with enhanced open-circuit voltage and efficiency," *Nature Photonics*, vol. 3, pp. 649–653, nov 2009.

[66] J. Hou, H.-Y. Chen, S. Zhang, R. I. Chen, Y. Yang, Y. Wu, and G. Li, "Synthesis of a Low Band Gap Polymer and Its Application in Highly Efficient Polymer Solar Cells," *Journal of the American Chemical Society*, vol. 131, pp. 15586–15587, nov 2009.

[67] V. M. Le Corre, A. R. Chatri, N. Y. Doumon, and L. J. A. Koster, "Charge Carrier Extraction in Organic Solar Cells Governed by Steady-State Mobilities," *Advanced Energy Materials*, vol. 7, no. 22, pp. 1–7, 2017.

[68] H. Y. Chen, S. H. Lin, J. Y. Sun, C. H. Hsu, S. Lan, and C. F. Lin, "Morphologic improvement of the PBDTTT-C and PC71BM blend film with mixed solvent for high-performance inverted polymer solar cells," *Nanotechnology*, vol. 24, p. 484009, dec 2013.

[69] S. A. Hawks, F. Deledalle, J. Yao, D. G. Rebois, G. Li, J. Nelson, Y. Yang, T. Kirchartz, and J. R. Durrant, "Relating Recombination, Density of States, and Device Performance in an Efficient Polymer:Fullerene Organic Solar Cell Blend," *Advanced Energy Materials*, vol. 3, pp. 1201–1209, sep 2013.

[70] Y. Ning, L. Lv, Y. Lu, C. Zhang, Y. Fang, A. Tang, Y. Hu, Z. Lou, F. Teng, and Y. Hou, "Effects of photo-induced defects on the performance of PBDTTT-C/PC70BM solar cells," *physica status solidi (RRL) - Rapid Research Letters*, vol. 9, pp. 120–124, feb 2015.

[71] Y. M. Yang, W. Chen, L. Dou, W.-h. Chang, H.-S. Duan, B. Bob, G. Li, and Y. M. Yang, "High-performance multiple-donor bulk heterojunction solar cells," *Nature Photonics*, vol. 9, no. 3, pp. 190–198, 2015.

[72] A. Zusan, B. Gieseking, M. Zerson, V. Dyakonov, R. Magerle, and C. Deibel, "The Effect of Diiodooctane on the Charge Carrier Generation in Organic Solar Cells Based on the Copolymer PBDTTT-C," *Scientific Reports*, vol. 5, p. 8286, jul 2015.

[73] J. Kong, S. Song, M. Yoo, G. Y. Lee, O. Kwon, J. K. Park, H. Back, G. Kim, S. H. Lee, H. Suh, and K. Lee, "Long-term stable polymer solar cells with significantly reduced burn-in loss.," *Nature communications*, vol. 5, p. 5688, 2014.

[74] J. C. Bijleveld, V. S. Gevaerts, D. Di Nuzzo, M. Turbiez, S. G. J. Mathijssen, D. M. de Leeuw, M. M. Wienk, and R. A. J. Janssen, "Efficient Solar Cells Based on an Easily Accessible Diketopyrrolopyrrole Polymer," *Advanced Materials*, vol. 22, pp. E242–E246, sep 2010.

[75] X. Guo, M. Zhang, W. Ma, L. Ye, S. Zhang, S. Liu, H. Ade, F. Huang, and J. Hou, "Enhanced photovoltaic performance by modulating surface composition in bulk heterojunction polymer solar cells based on PBDTTT-C-T/PC71BM," *Advanced Materials*, vol. 26, pp. 4043–4049, jun 2014.

[76] L. Chang, I. E. Jacobs, M. P. Augustine, and A. J. Moulé, "Correlating dilute solvent interactions to morphology and OPV device performance," *Organic Electronics*, vol. 14, pp. 2431–2443, oct 2013.

[77] S. J. Lou, J. M. Szarko, T. Xu, L. Yu, T. J. Marks, and L. X. Chen, "Effects of Additives on the Morphology of Solution Phase Aggregates Formed by Active Layer Components of High-Efficiency Organic Solar Cells," *Journal of the American Chemical Society*, vol. 133, pp. 20661–20663, dec 2011.

[78] J. Li, G. Zhang, D. M. Holm, I. E. Jacobs, B. Yin, P. Stroeve, M. Mascal, and A. J. Moulé, "Introducing Solubility Control for Improved Organic P-Type Dopants," *Chemistry of Materials*, vol. 27, no. 16, pp. 5765–5774, 2015.

[79] L. Lu and L. Yu, "Understanding Low Bandgap Polymer PTB7 and Optimizing Polymer Solar Cells Based on It," *Advanced Materials*, vol. 26, pp. 4413–4430, jul 2014.

[80] Z. Xiao, Y. Yuan, B. Yang, J. Vanderslice, J. Chen, O. Dyck, G. Duscher, and J. Huang, "Universal formation of compositionally graded bulk heterojunction for efficiency enhancement in organic photovoltaics," *Advanced Materials*, vol. 26, no. 19, pp. 3068–3075, 2014.

[81] L. Ye, Y. Jing, X. Guo, H. Sun, S. Zhang, M. Zhang, L. Huo, and J. Hou, "Remove the Residual Additives Toward Enhanced Efficiency with Higher Reproducibility in Polymer Solar Cells," *Journal of Physical Chemistry C*, vol. 117, no. 29, pp. 14920–14928, 2013.

[82] B. J. Tremolet De Villers, K. A. O'Hara, D. P. Ostrowski, P. H. Biddle, S. E. Shaheen, M. L. Chabinyc, D. C. Olson, and N. Kopidakis, "Removal of Residual Diiodooctane Improves Photostability of High-Performance Organic Solar Cell Polymers," *Chemistry of Materials*, vol. 28, no. 3, pp. 876–884, 2016.

[83] P. N. Murgatroyd, "Theory of space-charge-limited current enhanced by Frenkel effect," *Journal of Physics D: Applied Physics*, vol. 3, no. 2, pp. 151–156, 1970.

[84] J. C. Blakesley, F. A. Castro, W. Kylberg, G. F. Dibb, C. Arantes, R. Valaski, M. Cremona, J. S. Kim, and J.-S. Kim, "Towards reliable charge-mobility benchmark measurements for organic semiconductors," *Organic Electronics*, vol. 15, pp. 1263–1272, jun 2014.

[85] S. Foster, F. Deledalle, A. Mitani, T. Kimura, K.-B. Kim, T. Okachi, T. Kirchartz, J. Oguma, K. Miyake, J. R. Durrant, S. Doi, and J. Nelson, "Electron Collection as a Limit to Polymer:PCBM Solar Cell Efficiency: Effect of Blend Microstructure on Carrier Mobility and Device Performance in PTB7:PCBM," *Advanced Energy Materials*, vol. 4, p. 1400311, oct 2014.

[86] E. F. Manley, J. Strzalka, T. J. Fauvell, N. E. Jackson, M. J. Leonardi, N. D. Eastham, T. J. Marks, and L. X. Chen, "In Situ GIWAXS Analysis of Solvent and Additive Effects on PTB7 Thin Film Microstructure Evolution During Spin Coating," *Advanced Materials*, vol. 29, p. 1703933, nov 2017.

[87] D. T. Scholes, P. Y. Yee, J. R. Lindemuth, H. Kang, J. Onorato, R. Ghosh, C. K. Luscombe, F. C. Spano, S. H. Tolbert, and B. J. Schwartz, "The Effects of Crystallinity on Charge Transport and the Structure of Sequentially Processed F4TCNQ-Doped Conjugated Polymer Films," *Advanced Functional Materials*, vol. 27, pp. 1–13, nov 2017.

[88] D. T. Scholes, S. A. Hawks, P. Y. Yee, H. Wu, J. R. Lindemuth, S. H. Tolbert, and B. J. Schwartz, "Overcoming Film Quality Issues for Conjugated Polymers Doped with F4TCNQ by Solution Sequential Processing: Hall Effect, Structural, and Optical Measurements," *Journal of Physical Chemistry Letters*, vol. 6, no. 23, pp. 4786–4793, 2015.

[89] B. X. Dong, B. Huang, A. Tan, and P. F. Green, "Nanoscale orientation effects on carrier transport in a low-band-gap polymer," *Journal of Physical Chemistry C*, vol. 118, no. 31, pp. 17490–17498, 2014.

[90] B. Lüssem, M. Riede, and K. Leo, *Doping of organic semiconductors*, vol. 210. 2013.

[91] Y. Zhang, H. Zhou, J. Seifter, L. Ying, A. Mikhailovsky, A. J. Heeger, G. C. Bazan, and T. Q. Nguyen, "Molecular doping enhances photoconductivity in polymer bulk heterojunction solar cells," *Advanced Materials*, vol. 25, no. 48, pp. 7038–7044, 2013.

[92] A. M. Glaudell, J. E. Cochran, S. N. Patel, and M. L. Chabinyc, "Impact of the doping method on conductivity and thermopower in semiconducting polythiophenes," *Advanced Energy Materials*, vol. 5, no. 4, 2015.

[93] S. N. Patel, A. M. Glaudell, K. A. Peterson, E. M. Thomas, K. A. O'Hara, E. Lim, and M. L. Chabinyc, "Morphology controls the thermoelectric power factor of a doped semiconducting polymer," *Science Advances*, vol. 3, no. 6, pp. 24–26, 2017.

[94] G. Zuo, O. Andersson, H. Abdalla, and M. Kemerink, "High thermoelectric power factor from multilayer solution-processed organic films," *Applied Physics Letters*, vol. 112, no. 8, pp. 2–6, 2018.

[95] J. Hynynen, D. Kiefer, and C. Müller, "Influence of crystallinity on the thermoelectric power factor of P3HT vapour-doped with F4TCNQ," *RSC Advances*, vol. 8, no. 3, pp. 1593–1599, 2018.

[96] E. Lim, K. A. Peterson, G. M. Su, and M. L. Chabinyc, "Thermoelectric Properties of Poly(3-hexylthiophene) (P3HT) Doped with 2,3,5,6-Tetrafluoro-7,7,8,8-tetracyanoquinodimethane (F4TCNQ) by Vapor-Phase Infiltration," *Chemistry of Materials*, vol. 30, no. 3, pp. 998–1010, 2018.

[97] A. Hamidi-Sakr, L. Biniek, J. L. Bantignies, D. Maurin, L. Herrmann, N. Leclerc, P. Lévêque, V. Vijayakumar, N. Zimmermann, and M. Brinkmann, "A Versatile Method to Fabricate Highly In-Plane Aligned Conducting Polymer Films with Anisotropic Charge Transport and Thermoelectric Properties: The Key Role of Alkyl Side Chain Layers on the Doping Mechanism," *Advanced Functional Materials*, vol. 27, no. 25, pp. 1–13, 2017.

[98] J. D. Yuen, A. S. Dhoot, E. B. Namdas, N. E. Coates, M. Heeney, I. McCulloch, D. Moses, and A. J. Heeger, "Electrochemical doping in electrolyte-gated polymer transistors," *Journal of the American Chemical Society*, vol. 129, no. 46, pp. 14367–14371, 2007.

[99] J. F. Chang, J. Clark, N. Zhao, H. Sirringhaus, D. W. Breiby, J. W. Andreasen, M. M. Nielsen, M. Giles, M. Heeney, and I. McCulloch, "Molecular-weight dependence of interchain polaron delocalization and exciton bandwidth in high-mobility conjugated polymers," *Physical Review B - Condensed Matter and Materials Physics*, vol. 74, no. 11, pp. 1–12, 2006.

[100] C. K. Chiang, S. C. Gau, C. R. Fincher, Y. W. Park, A. G. MacDiarmid, and A. J. Heeger, "Polyacetylene, (CH)x: N-type and p-type doping and compensation," *Applied Physics Letters*, vol. 33, no. 1, pp. 18–20, 1978.

[101] V. V. Kislyuk, O. P. Dimitriev, A. A. Pud, J. Lautru, and I. Ledoux-Rak, "In-situ conductivity and UV-VIS absorption monitoring of iodine doping-dedoping processes in poly(3-hexylthiophene) (P3HT)," *Journal of Physics: Conference Series*, vol. 286, no. 1, 2011.

[102] P. Pingel and D. Neher, "Comprehensive picture of p-type doping of P3HT with the molecular acceptor F4TCNQ," *Physical Review B*, vol. 87, no. 11, pp. 1–9, 2013.

[103] P. Pingel, M. Arvind, L. Kölln, R. Steyrleuthner, F. Kraffert, J. Behrends, S. Janietz, and D. Neher, "p-Type Doping of Poly(3-hexylthiophene) with the Strong Lewis Acid Tris(pentafluorophenyl)borane," *Advanced Electronic Materials*, vol. 2, p. 1600204, oct 2016.

[104] A. Mityashin, Y. Olivier, T. Van Regemorter, C. Rolin, S. Verlaak, N. G. Martinelli, D. Beljonne, J. Cornil, J. Genoe, and P. Heremans, "Unraveling the mechanism of molecular doping in organic semiconductors," *Advanced Materials*, vol. 24, no. 12, pp. 1535–1539, 2012.

[105] I. E. Jacobs, E. W. Aasen, J. L. Oliveira, T. N. Fonseca, J. D. Roehling, J. Li, G. Zhang, M. P. Augustine, M. Mascal, and A. J. Moulé, "Comparison of solution-mixed and sequentially processed P3HT:F4TCNQ films: effect of doping-induced aggregation on film morphology," *J. Mater. Chem. C*, vol. 4, no. 16, pp. 3454–3466, 2016.

[106] J. Hynynen, D. Kiefer, L. Yu, R. Kroon, R. Munir, A. Amassian, M. Kemerink, and C. Müller, "Enhanced Electrical Conductivity of Molecularly p-Doped Poly(3-hexylthiophene) through Understanding the Correlation with Solid-State Order," *Macromolecules*, vol. 50, no. 20, pp. 8140–8148, 2017.

[107] A. R. Chew, R. Ghosh, Z. Shang, F. C. Spano, and A. Salleo, "Sequential Doping Reveals the Importance of Amorphous Chain Rigidity in Charge Transport of Semi-Crystalline Polymers," *The Journal of Physical Chemistry Letters*, pp. 4974–4980, 2017.

[108] K. Kang, S. Watanabe, K. Broch, A. Sepe, A. Brown, I. Nasrallah, M. Nikolka, Z. Fei, M. Heeney, D. Matsumoto, K. Marumoto, H. Tanaka, S. I. Kuroda, and H. Sirringhaus, "2D coherent charge transport in highly ordered conducting polymers doped by solid state diffusion," *Nature Materials*, vol. 15, no. 8, pp. 896–902, 2016.

[109] W. Gao and A. Kahn, "Controlled p-doping of zinc phthalocyanine by coevaporation with tetrafluorotetracyanoquinodimethane: A direct and inverse photoemission study," *Applied Physics Letters*, vol. 79, pp. 4040–4042, dec 2001.

[110] R. B. King, "Three-Dimensional Aromaticity in Polyhedral Boranes and Related Molecules," *Chemical Reviews*, vol. 101, pp. 1119–1152, may 2001.

[111] T. Peymann, C. B. Knobler, S. I. Khan, and M. F. Hawthorne, "Dodeca(benzyloxy)dodecaborane, B12(OCH2Ph)12: A stable derivative of hypercloso-B12H12," *Angewandte Chemie - International Edition*, vol. 40, pp. 1664–1667, may 2001.

[112] T. Peymann, C. B. Knobler, and M. F. Hawthorne, "An unpaired electron incarcerated within an icosahedral borane cage: Synthesis and crystal structure of the blue, air-stable {[closo-B12(CH3)12]·}-radical," *Chemical Communications*, vol. 12, no. 20, pp. 2039–2040, 1999.

[113] N. Van, I. Tiritiris, R. F. Winter, B. Sarkar, P. Singh, C. Duboc, A. Muñoz-Castro, R. Arratia-Pérez, W. Kaim, and T. Schleid, "Oxidative Perhydroxylation of [closo-B12H12]2- to

the Stable Inorganic Cluster Redox System [B12(OH)12]2-/.-: Experiment and Theory," *Chemistry - A European Journal*, vol. 16, no. 37, pp. 11242–11245, 2010.

[114] O. K. Farha, R. L. Julius, M. W. Lee, R. E. Huertas, C. B. Knobler, and M. F. Hawthorne, "Synthesis of stable dodecaalkoxy derivatives of hypercloso-B 12H12," *Journal of the American Chemical Society*, vol. 127, no. 51, pp. 18243–18251, 2005.

[115] J. C. Axtell, L. M. A. Saleh, E. A. Qian, A. I. Wixtrom, and A. M. Spokoyny, "Synthesis and Applications of Perfunctionalized Boron Clusters," *Inorganic Chemistry*, vol. 57, no. 5, pp. 2333–2350, 2018.

[116] D. Jung, L. M. A. Saleh, Z. J. Berkson, M. F. El-Kady, J. Y. Hwang, N. Mohamed, A. I. Wixtrom, E. Titarenko, Y. Shao, K. McCarthy, J. Guo, I. B. Martini, S. Kraemer, E. C. Wegener, P. Saint-Cricq, B. Ruehle, R. R. Langeslay, M. Delferro, J. L. Brosmer, C. H. Hendon, M. Gallagher-Jones, J. Rodriguez, K. W. Chapman, J. T. Miller, X. Duan, R. B. Kaner, J. I. Zink, B. F. Chmelka, and A. M. Spokoyny, "A molecular cross-linking approach for hybrid metal oxides," *Nature Materials*, vol. 17, no. 4, pp. 341–348, 2018.

[117] M. S. Messina, J. C. Axtell, Y. Wang, P. Chong, A. I. Wixtrom, K. O. Kirlikovali, B. M. Upton, B. M. Hunter, O. S. Shafaat, S. I. Khan, J. R. Winkler, H. B. Gray, A. N. Alexandrova, H. D. Maynard, and A. M. Spokoyny, "Visible-Light-Induced Olefin Activation Using 3D Aromatic Boron-Rich Cluster Photooxidants," *Journal of the American Chemical Society*, vol. 138, pp. 6952–6955, jun 2016.

[118] O. Khatib, B. Lee, J. Yuen, Z. Q. Li, M. Di Ventra, A. J. Heeger, V. Podzorov, and D. N. Basov, "Infrared signatures of high carrier densities induced in semiconducting poly(3-hexylthiophene) by fluorinated organosilane molecules," *Journal of Applied Physics*, vol. 107, no. 12, 2010.

[119] C. Y. Kao, B. Lee, L. S. Wielunski, M. Heeney, I. McCulloch, E. Garfunkel, L. C. Feldman, and V. Podzorov, "Doping of conjugated polythiophenes with alkyl silanes," *Advanced Functional Materials*, vol. 19, no. 12, pp. 1906–1911, 2009.

[120] T. J. Aubry, A. S. Ferreira, P. Y. Yee, J. C. Aguirre, S. A. Hawks, M. T. Fontana, B. J. Schwartz, and S. H. Tolbert, "Processing Methods for Obtaining a Face-On Crystalline Domain Orientation in Conjugated Polymer-Based Photovoltaics," *The Journal of Physical Chemistry C*, vol. 122, pp. 15078–15089, jun 2018.

[121] P. Reiser, L. Müller, V. Sivanesan, R. Lovrincic, S. Barlow, S. R. Marder, A. Pucci, W. Jaegermann, E. Mankel, and S. Beck, "Dopant Diffusion in Sequentially Doped Poly(3-hexylthiophene) Studied by Infrared and Photoelectron Spectroscopy," *The Journal of Physical Chemistry C*, vol. 122, pp. 14518–14527, jul 2018.

[122] Z. Liang, Y. Zhang, M. Souri, X. Luo, A. M. Boehm, R. Li, Y. Zhang, T. Wang, D. Y. Kim, J. Mei, S. R. Marder, and K. R. Graham, "Influence of dopant size and electron affinity on the electrical conductivity and thermoelectric properties of a series of conjugated polymers," *Journal of Materials Chemistry A*, vol. 6, no. 34, pp. 16495–16505, 2018.

[123] L. Müller, D. Nanova, T. Glaser, S. Beck, A. Pucci, A. K. Kast, R. R. Schröder, E. Mankel, P. Pingel, D. Neher, W. Kowalsky, and R. Lovrincic, "Charge-Transfer-Solvent Interaction Predefines Doping Efficiency in p-Doped P3HT Films," *Chemistry of Materials*, vol. 28, no. 12, pp. 4432–4439, 2016.

[124] M. Kivala, C. Boudon, J.-P. Gisselbrecht, B. Enko, P. Seiler, I. B. Müller, N. Langer, P. D. Jarowski, G. Gescheidt, and F. Diederich, "Organic Super-Acceptors with Efficient Intramolecular Charge-Transfer Interactions by [2+2] Cycloadditions of TCNE, TCNQ, and F 4 -TCNQ to Donor-Substituted Cyanoalkynes," *Chemistry - A European Journal*, vol. 15, pp. 4111–4123, apr 2009.

[125] L. J. Van der Pauw, "A Method of Measuring the Resistivity and Hall Coefficient on Lamellae of Arbitraty Shape," *Phys. Tech. Rev.*, vol. 1958, no. I, pp. 220–224, 1958.

[126] V. A. Kolesov, C. Fuentes-Hernandez, W. F. Chou, N. Aizawa, F. A. Larrain, M. Wang, A. Perrotta, S. Choi, S. Graham, G. C. Bazan, T. Q. Nguyen, S. R. Marder, and B. Kippelen, "Solution-based electrical doping of semiconducting polymer films over a limited depth," *Nature Materials*, vol. 16, no. 4, pp. 474–481, 2017.

[127] J. C. Goeltz, C. J. Hanson, and C. P. Kubiak, "Rates of electron self-exchange reactions between oxo-centered ruthenium clusters are determined by orbital overlap," *Inorganic Chemistry*, vol. 48, no. 11, pp. 4763–4767, 2009.

[128] J. C. Goeltz, E. E. Benson, and C. P. Kubiak, "Electronic structural effects in self-exchange reactions," *Journal of Physical Chemistry B*, vol. 114, no. 45, pp. 14729–14734, 2010.

[129] T. M. Porter, G. C. Canzi, S. A. Chabolla, and C. P. Kubiak, "Tuning Electron Delocalization and Transfer Rates in Mixed-Valent Ru3O Complexes through "push-Pull" Effects," *Journal of Physical Chemistry A*, vol. 120, no. 32, pp. 6309–6316, 2016.

[130] N. C. Miller, E. Cho, R. Gysel, C. Risko, V. Coropceanu, C. E. Miller, S. Sweetnam, A. Sellinger, M. Heeney, I. McCulloch, J.-L. Brédas, M. F. Toney, and M. D. McGehee, "Factors Governing Intercalation of Fullerenes and Other Small Molecules Between the Side Chains of Semiconducting Polymers Used in Solar Cells," *Advanced Energy Materials*, vol. 2, pp. 1208–1217, oct 2012.

[131] C. M. Pochas and F. C. Spano, "New insights on the nature of two-dimensional polarons in semiconducting polymers: Infrared absorption in poly(3-hexylthiophene)," *Journal of Chemical Physics*, vol. 140, no. 24, 2014.

[132] R. Ghosh, C. M. Pochas, and F. C. Spano, "Polaron Delocalization in Conjugated Polymer Films," *Journal of Physical Chemistry C*, vol. 120, no. 21, pp. 11394–11406, 2016.

[133] R. Ghosh, A. R. Chew, J. Onorato, V. Pakhnyuk, C. K. Luscombe, A. Salleo, and F. C. Spano, "Spectral Signatures and Spatial Coherence of Bound and Unbound Polarons in P3HT Films: Theory Versus Experiment," *The Journal of Physical Chemistry C*, p. acs.jpcc.8b03873, 2018.

[134] J. Lindemuth, "Variable temperature Hall measurements on low-mobility materials," *Spie*, vol. 8470, no. October 2012, p. 84700G, 2012.

[135] Y. Chen, H. T. Yi, and V. Podzorov, "High-Resolution ac Measurements of the Hall Effect in Organic Field-Effect Transistors," *Physical Review Applied*, vol. 5, no. 3, pp. 1–9, 2016.

[136] F. Werner, "Hall measurements on low-mobility thin films," *Journal of Applied Physics*, vol. 122, no. 13, 2017.

[137] H. T. Yi, Y. N. Gartstein, and V. Podzorov, "Charge carrier coherence and Hall effect in organic semiconductors," *Scientific Reports*, vol. 6, no. March, pp. 1–11, 2016.

[138] B. D. Fahlman, *Semiconductors*, pp. 263–371. Dordrecht: Springer Netherlands, 2018.

[139] H. Méndez, G. Heimel, A. Opitz, K. Sauer, P. Barkowski, M. Oehzelt, J. Soeda, T. Okamoto, J. Takeya, J. B. Arlin, J. Y. Balandier, Y. Geerts, N. Koch, and I. Salzmann, "Doping of organic semiconductors: Impact of dopant strength and electronic coupling," *Angewandte Chemie - International Edition*, vol. 52, no. 30, pp. 7751–7755, 2013.

[140] H. Ma, H.-L. Yip, F. Huang, and A. K.-Y. Jen, "Interface Engineering for Organic Electronics," *Advanced Functional Materials*, vol. 20, no. 9, pp. 1371–1388, 2010.

[141] T. J. Aubry, J. C. Axtell, V. M. Basile, K. J. Winchell, J. R. Lindemuth, T. M. Porter, J. Liu, A. N. Alexandrova, C. P. Kubiak, S. H. Tolbert, A. M. Spokoyny, and B. J. Schwartz, "Dodecaborane-Based Dopants Designed to Shield Anion Electrostatics Lead to Increased Carrier Mobility in a Doped Conjugated Polymer," *Advanced Materials*, vol. 31, p. 1805647, mar 2019.

[142] R. Ghosh, C. K. Luscombe, M. Hambsch, S. C. B. Mannsfeld, A. Salleo, and F. C. Spano, "Anisotropic Polaron Delocalization in Conjugated Homopolymers and Donor–Acceptor Copolymers," *Chemistry of Materials*, vol. 31, no. 17, pp. 7033–7045, 2019.

[143] Q. Pei, G. Zuccarello, M. Ahlskog, and O. Inganäs, "Electrochromic and highly stable poly(3,4-ethylenedioxythiophene) switches between opaque blue-black and transparent sky blue," *Polymer*, vol. 35, no. 7, pp. 1347–1351, 1994.

[144] I. E. Jacobs, E. W. Aasen, D. Nowak, J. Li, W. Morrison, J. D. Roehling, M. P. Augustine, and A. J. Moulé, "Direct-Write Optical Patterning of P3HT Films Beyond the Diffraction Limit," *Advanced Materials*, vol. 29, no. 2, 2017.

[145] M. T. Fontana, D. A. Stanfield, D. T. Scholes, K. J. Winchell, S. H. Tolbert, and B. J. Schwartz, "Evaporation vs Solution Sequential Doping of Conjugated Polymers: F 4 TCNQ Doping of Micrometer-Thick P3HT Films for Thermoelectrics," *The Journal of Physical Chemistry C*, vol. 123, no. 37, pp. 22711–22724, 2019.

[146] D. T. Scholes, P. Y. Yee, G. R. McKeown, S. Li, H. Kang, J. R. Lindemuth, X. Xia, S. C. King, D. S. Seferos, S. H. Tolbert, and B. J. Schwartz, "Designing Conjugated Polymers for Molecular Doping: The Roles of Crystallinity, Swelling, and Conductivity in Sequentially-Doped Selenophene-Based Copolymers," *Chemistry of Materials*, vol. 31, no. 1, pp. 73–82, 2019.

[147] J. Aihara, "Three-dimensional aromaticity of polyhedral boranes," *Journal of the American Chemical Society*, vol. 100, pp. 3339–3342, may 1978.

[148] P. Pingel, R. Schwarzl, and D. Neher, "Effect of molecular p-doping on hole density and mobility in poly(3-hexylthiophene)," *Applied Physics Letters*, vol. 100, no. 14, pp. 1–4, 2012.

[149] B. Nell, K. Ortstein, O. V. Boltalina, and K. Vandewal, "Influence of Dopant-Host Energy Level Offset on Thermoelectric Properties of Doped Organic Semiconductors," *Journal of Physical Chemistry C*, vol. 122, no. 22, pp. 11730–11735, 2018.

[150] Y. Karpov, T. Erdmann, I. Raguzin, M. Al-Hussein, M. Binner, U. Lappan, M. Stamm, K. L. Gerasimov, T. Beryozkina, V. Bakulev, D. V. Anokhin, D. A. Ivanov, F. Günther, S. Gemming, G. Seifert, B. Voit, R. Di Pietro, and A. Kiriy, "High Conductivity in Molecularly p-Doped Diketopyrrolopyrrole-Based Polymer: The Impact of a High Dopant Strength and Good Structural Order," *Advanced Materials*, pp. 6003–6010, 2016.

[151] H. Méndez, G. Heimel, S. Winkler, J. Frisch, A. Opitz, K. Sauer, B. Wegner, M. Oehzelt, C. Röthel, S. Duhm, D. Többens, N. Koch, and I. Salzmann, "Charge-transfer crystallites as molecular electrical dopants," *Nature Communications*, vol. 6, 2015.

[152] A. I. Wixtrom, Y. Shao, D. Jung, C. W. Machan, S. N. Kevork, E. A. Qian, J. C. Axtell, S. I. Khan, C. P. Kubiak, and A. M. Spokoyny, "Rapid synthesis of redox-active dodecaborane B 12 (OR) 12 clusters under ambient conditions," *Inorganic Chemistry Frontiers*, vol. 3, no. 5, pp. 711–717, 2016.

[153] A. I. Wixtrom, Z. A. Parvez, M. D. Savage, E. A. Qian, D. Jung, S. I. Khan, A. L. Rheingold, and A. M. Spokoyny, "Tuning the electrochemical potential of perfunctionalized dodecaborate clusters through vertex differentiation," *Chemical Communications*, vol. 54, no. 46, pp. 5867–5870, 2018.

[154] M. G. Voss, D. T. Scholes, J. R. Challa, and B. J. Schwartz, "Ultrafast transient absorption spectroscopy of doped P3HT films: Distinguishing free and trapped polarons," *Faraday Discussions*, vol. 216, pp. 339–362, 2019.

[155] F. A. Larrain, C. Fuentes-Hernandez, W. F. Chou, V. A. Rodriguez-Toro, T. Y. Huang, M. F. Toney, and B. Kippelen, "Stable solvent for solution-based electrical doping of semiconducting polymer films and its application to organic solar cells," *Energy and Environmental Science*, vol. 11, no. 8, pp. 2216–2224, 2018.

[156] J. K. Keum, J. F. Browning, K. Xiao, M. Shao, C. E. Halbert, and K. Hong, "Morphological origin for the stratification of P3HT:PCBM blend film studied by neutron reflectometry," *Applied Physics Letters*, vol. 103, no. 22, pp. 3–7, 2013.

[157] S. B. Kirschner, N. P. Smith, K. A. Wepasnick, H. E. Katz, B. J. Kirby, J. A. Borchers, and D. H. Reich, "X-ray and neutron reflectivity and electronic properties of PCBM-poly(bromo)styrene blends and bilayers with poly(3-hexylthiophene)," *Journal of Materials Chemistry*, vol. 22, no. 10, pp. 4364–4370, 2012.

[158] K. H. Lee, Y. Zhang, P. L. Burn, I. R. Gentle, M. James, A. Nelson, and P. Meredith, "Correlation of diffusion and performance in sequentially processed P3HT/PCBM heterojunction films by time-resolved neutron reflectometry," *Journal of Materials Chemistry C*, vol. 1, no. 14, pp. 2593–2598, 2013.

[159] P. Y. Yee, D. T. Scholes, B. J. Schwartz, and S. H. Tolbert, "Dopant-Induced Ordering of Amorphous Regions in Regiorandom P3HT," *The Journal of Physical Chemistry Letters*, vol. 10, no. 17, pp. 4929–4934, 2019.

[160] I. E. Jacobs, C. Cendra, T. F. Harrelson, Z. I. Bedolla Valdez, R. Faller, A. Salleo, and A. J. Moulé, "Polymorphism controls the degree of charge transfer in a molecularly doped semiconducting polymer," *Materials Horizons*, vol. 5, no. 4, pp. 655–660, 2018.

[161] J. H. Burke and M. J. Bird, "Energetics and Escape of Interchain-Delocalized Ion Pairs in Nonpolar Media," *Advanced Materials*, vol. 31, no. 12, pp. 1–7, 2019.

[162] "TURBOMOLE V6.6 2014, a development of University of Karlsruhe and Forschungszentrum Karlsruhe GmbH, 1989-2007, TURBOMOLE GmbH, since 2007; available from http://www.turbomole.com.."

[163] J. Tao, J. P. Perdew, V. N. Staroverov, and G. E. Scuseria, "Climbing the density functional ladder: Nonempirical meta–generalized gradient approximation designed for molecules and solids," *Physical Review Letters*, vol. 91, no. 14, pp. 3–6, 2003.

[164] F. Weigend and R. Ahlrichs, "{B}alanced Basis Sets of Split Valence, Triple Zeta Valence and Quadruple Zeta Valence Quality for {H} to {R}n: {D}esign and Assessment of Accuracy.," *Phys. Chem. Chem. Phys.*, vol. 7, no. 18, pp. 3297–3305, 2005.

[165] F. Weigend, "Accurate Coulomb-fitting basis sets for H to Rn," *Physical Chemistry Chemical Physics*, vol. 8, no. 9, pp. 1057–1065, 2006.

[166] V. N. Staroverov, G. E. Scuseria, J. Tao, and J. P. Perdew, "Comparative assessment of a new nonempirical density functional: Molecules and hydrogen-bonded complexes," *Journal of Chemical Physics*, vol. 119, no. 23, pp. 12129–12137, 2003.

[167] T. H. Dunning, "Gaussian basis sets for use in correlated molecular calculations. I. The atoms boron through neon and hydrogen," *The Journal of Chemical Physics*, vol. 90, no. 2, pp. 1007–1023, 1989.

[168] E. R. Davidson, L. E. McMurchie, and S. J. Day, "The B_K method: Application to methylene," *The Journal of Chemical Physics*, vol. 74, no. 10, pp. 5491–5496, 1981.

[169] M. J. Frisch, G. W. Trucks, H. B. Schlegel, G. E. Scuseria, M. A. Robb, J. R. Cheeseman, G. Scalmani, V. Barone, G. A. Petersson, H. Nakatsuji, X. Li, M. Caricato, A. V. Marenich, J. Bloino, B. G. Janesko, R. Gomperts, B. Mennucci, H. P. Hratchian, J. V. Ortiz, A. F. Izmaylov, J. L. Sonnenberg, D. Williams-Young, F. Ding, F. Lipparini, F. Egidi, J. Goings, B. Peng, A. Petrone, T. Henderson, D. Ranasinghe, V. G. Zakrzewski, J. Gao, N. Rega, G. Zheng, W. Liang, M. Hada, M. Ehara, K. Toyota, R. Fukuda, J. Hasegawa, M. Ishida,

T. Nakajima, Y. Honda, O. Kitao, H. Nakai, T. Vreven, K. Throssell, J. A. Montgomery Jr., J. E. Peralta, F. Ogliaro, M. J. Bearpark, J. J. Heyd, E. N. Brothers, K. N. Kudin, V. N. Staroverov, T. A. Keith, R. Kobayashi, J. Normand, K. Raghavachari, A. P. Rendell, J. C. Burant, S. S. Iyengar, J. Tomasi, M. Cossi, J. M. Millam, M. Klene, C. Adamo, R. Cammi, J. W. Ochterski, R. L. Martin, K. Morokuma, O. Farkas, J. B. Foresman, and D. J. Fox, "Gaussian~16 {R}evision {D}.01," 2016.

[170] S. F. Nelsen, R. F. Ismagilov, K. E. Gentile, M. A. Nagy, H. Q. Tran, Q. Qu, D. W. T. Halfen, A. L. Odegard, and J. R. Pladziewicz, "Indirect determination of self-exchange electron transfer rate constants," *Journal of the American Chemical Society*, vol. 120, no. 32, pp. 8230–8240, 1998.

[171] M.-S. Chan, J. B. DeRoos, and A. C. Wahl, "Rate of electron transfer between tris(3,4,7,8-tetramethyl-1,10-phenanthroline)iron(II) and -(III) ions from nuclear magnetic resonance studies," *The Journal of Physical Chemistry*, vol. 77, no. 18, pp. 2163–2165, 1973.

[172] P. R. Hoffman and K. G. Caulton, "Solution structure and dynamics of five-coordinate d6 complexes," *J. Am. Chem. Soc.*, vol. 97, no. 15, pp. 4221–4228, 1975.

[173] A. L. Efros and B. I. Shklovskii, "Coulomb gap and low temperature conductivity of disordered systems," *Journal of Physics C: Solid State Physics*, vol. 8, no. 4, 1975.

[174] N. F. Mott, "Conduction in glasses containing transition metal ions," *Journal of Non-Crystalline Solids*, vol. 1, no. 1, pp. 1–17, 1968.

[175] C. O. Yoon, M. Reghu, D. Moses, A. J. Heeger, Y. Cao, T. A. Chen, X. Wu, and R. D. Rieke, "Hopping transport in doped conducting polymers in the insulating regime near the metal-insulator boundary: polypyrrole, polyaniline and polyalkylthiophenes," *Synthetic Metals*, vol. 75, no. 3, pp. 229–239, 1995.

[176] S. Wang, M. Ha, M. Manno, C. Daniel Frisbie, and C. Leighton, "Hopping transport and the Hall effect near the insulator-metal transition in electrochemically gated poly(3-hexylthiophene) transistors," *Nature Communications*, vol. 3, pp. 1210–1217, 2012.

[177] M. Doucet, R. M. Ferraz Leal, and T. C. Hobson, "Web interface for reflectivity fitting," *SoftwareX*, vol. 7, pp. 287–293, 2018.

[178] J. Müllerová, M. Kaiser, V. Nádaždy, P. Šiffalovič, and E. Majková, "Optical absorption study of P3HT: PCBM blend photo-oxidation for bulk heterojunction solar cells," *Solar Energy*, vol. 134, pp. 294–301, 2016.